Załącznik nr 1/1
do Zarządzenia Rektora PG nr 30/2022 z 14 kwietnia 2022 r.

POLITECHNIKA GDAŃSKA

The author of the doctoral dissertation: M.Eng. Deepak Vyas
Scientific discipline: automation, electronics, electrical engineering and space technologies

DOCTORAL DISSERTATION

Title of doctoral dissertation: Investigation and synthesis of selected control systems of multi-phase interior permanent magnet synchronous machine

Title of doctoral dissertation (in Polish): Badanie i synteza wybranych układów sterowania wielofazową maszyną z magnesami trwałymi

Supervisor *signature*	Second supervisor *signature*
Prof. D.Sc. Ph.D. Eng. Marcin Morawiec	
Auxiliary supervisor *signature*	Cosupervisor *signature*

Gdańsk, year 2025

POLITECHNIKA GDAŃSKA

STATEMENT

The author of the doctoral dissertation: M.Eng. Deepak Vyas

I, the undersigned, declare that I am aware that in accordance with the provisions of Art. 27 (1) and (2) of the Act of 4th February 1994 on Copyright and Related Rights (Journal of Laws of 2021, item 1062), the university may use my doctoral dissertation entitled:
The pulse width modulation strategy for a five-phase three-level NPC voltage source inverter with DC-link voltage balancing ability.
for scientific or didactic purposes.[1][1]

Gdańsk,..... .....
signature of the PhD student

Aware of criminal liability for violations of the Act of 4th February 1994 on Copyright and Related Rights and disciplinary actions set out in the Law on Higher Education and Science(Journal of Laws 2021, item 478),[2] as well as civil liability, I declare, that the submitted doctoral dissertation is my own work.

I declare, that the submitted doctoral dissertation is my own work performed under and in cooperation with the supervision of Ph.D., D. Sc., Eng. Prof. Marcin Morawiec.

This submitted doctoral dissertation has never before been the basis of an official procedure associated with the awarding of a PhD degree.

All the information contained in the above thesis which is derived from written and electronic sources is documented in a list of relevant literature in accordance with Art. 34 of the Copyright and Related Rights Act.

I confirm that this doctoral dissertation is identical to the attached electronic version.

Gdańsk,..... .....
signature of the PhD student

I, the undersigned, agree to include an electronic version of the above doctoral dissertation in the open, institutional, digital repository of Gdańsk University of Technology.

Gdańsk,..... .....
signature of the PhD student

**delete where appropriate*

[1] Art 27. 1. Educational institutions and entities referred to in art. 7 sec. 1 points 1, 2 and 4–8 of the Act of 20 July 2018 – Law on Higher Education and Science, may use the disseminated works in the original and in translation for the purposes of illustrating the content provided for didactic purposes or in order to conduct research activities, and to reproduce for this purpose disseminated minor works or fragments of larger works.

2. If the works are made available to the public in such a way that everyone can have access to them at the place and time selected by them, as referred to in para. 1, is allowed only for a limited group of people learning, teaching or conducting research, identified by the entities listed in paragraph 1.

POLITECHNIKA GDAŃSKA

DESCRIPTION OF DOCTORAL DISSERTATION

The Author of the doctoral dissertation: Deepak Vyas

Title of doctoral dissertation: Investigation and synthesis of selected control systems of multi-phase interior permanent magnet synchronous machine

Title of doctoral dissertation in Polish: Badanie i synteza wybranych układów sterowania wielofazową maszyną z magnesami trwałymi

Language of doctoral dissertation: English

Supervisor: Marcin Morawiec

Date of doctoral defense:

Keywords of doctoral dissertation in Polish: Maszyna wielofazowa, sterowanie ze zmiennymi multiskalarnymi, sterowanie bezczujnikowe, obserwator prędkości, iniekcja trzeciej harmonicznej.

Keywords of doctoral dissertation in English: Multiphase machine, Multiscalar control, sensorless control, speed observer, third harmonic injection.

Summary of doctoral dissertation in Polish: Rozprawa doktorska przedstawia syntezę wybranych metod sterowania bezczujnikowego wielofazowej maszyny synchronicznej z magnesami trwałymi. Badania ograniczono do maszyny o liczbie faz 3 i 5. Proponowane rozwiązania sterowania opracowano w stacjonarnym układzie współrzędnych przy użyciu transformacji multiskalarnej dla zdefiniowanych wektorów strumienia i prądu. Proponowane struktury sterowania pięciofazowej maszyny synchronicznej z magnesami trwałymi zbadano przy użyciu klasycznego podejścia sterowania ze sprzężeniem zwrotnym i regulatorami proporcjonalno-całkowymi, predykcyjnego i backstepping. Aby zwiększyć wartość momentu elektromagnetycznego zaproponowano injekcję trzeciej harmonicznej dla układu z maszyną pięciofazową. Ponadto proponowane rozwiązania sterowania zapewniają niezależne sterowanie podsystemami elektromechanicznym i elektromagnetycznym w każdej płaszczyźnie wektorowej układu. Aby zapewnić analizę porównawczą, proponowane rozwiązania sterowania porównano również z istniejącymi układami sterowania. Na koniec zaprezentowano wyniki symulacji i wyniki eksperymentów w celu walidacji wydajności proponowanych struktur sterowania dla pięciofazowego układu napędowego.

Summary of doctoral dissertation in English: The doctoral dissertation presents a synthesis of selected sensorless control methods for a multiphase permanent magnet synchronous machine. The research is limited to the machine with 3 and 5 phases. The proposed control solutions are developed using multiscalar transformation for defined flux and current vectors in a stationary coordinate system. The proposed control structures of a five-phase permanent magnet synchronous machine are studied using classical feedback control approaches with proportional-integral, predictive, and backstepping controllers. To increase the value of electromagnetic torque, third harmonic injection is proposed for the five-phase machine system. Moreover, the proposed control solutions provide independent control of the electromechanical and electromagnetic subsystems in each vector plane of the system. The proposed control solutions are compared with existing control systems to provide a comparative analysis. Finally, simulation and experimental results are presented to validate the performance of the proposed control structures for the five-phase drive system.

ACKNOWLEDGEMENTS

By the grace of GOD, I have received the opportunity to extend my heartfelt thanks to everyone who has supported me throughout this Ph.D. journey. First and foremost, I wish to express my deepest gratitude to my Ph.D. supervisor, Professor Marcin Morawiec, whose inspiring mentorship and steadfast encouragement have been pivotal in navigating and triumphs of my doctoral research. I am deeply appreciative of his patience and understanding, especially during challenging phases of my work, and his ability to inspire me to strive for excellence. His mentorship has not only enriched my academic experience but has also left a lasting impact on my personal growth. Thank you for believing in my abilities and for providing me with the opportunities and resources to succeed. I am truly fortunate to have had the privilege of working under your supervision.

In addition to my supervisor, I also express my sincere gratitude to other employer of the Department of Electric Drive Automation and Energy Conversion for their encouragement, support, stimulating discussions during my Ph.D. journey.

I acknowledge my sincere gratitude to the Gdańsk University of Technology for providing financial support during my doctoral research work.

I owe a debt of gratitude to my parents Shree Gautambhai Vyas and Smt. Parulben Vyas, my brother Hardik Vyas for their endless support, encouragement, patience and care.

I sincerely acknowledge the ethical support from parents-in-law Shree Natvarlal Vyas and Smt. Bhavanaben Vyas.

I wish to express my deepest gratitude my beloved wife, Smt. Riddhi Vyas, whose unwavering love, patience, and support have been my greatest source of strength throughout this journey. Her understanding and sacrifices, especially during the demanding phases of my research, have been instrumental in helping me stay focused and motivated. This accomplishment would not have been possible without her presence by my side.

TABLE OF CONTENTS

LIST OF SYMBOLS

Symbol	Meaning
L_d	Direct axis inductance
L_q	Quadrature axis inductance
u_s	Stator voltage
i_s	Stator current
L_s	Stator inductance
ψ_f	Permanent magnet flux
p	No. of poles
p_n	No. of pole pairs
T_e	Electro-magnetic torque
T_L	Load torque
J	Moment of inertia
B	Damping friction
ω_r	Rotor speed
θ_r	Rotor angle
x_{11}, x_{12}, x_{21}, x_{22}	Multiscalar variables
(i)	Index of control system (1st or 2nd plane)
$\hat{x}$	Estimated variable
$\tilde{x}$	Estimation error
x^*	Reference value
$u_{s\alpha}$, $u_{s\beta}$	Stator voltage components in stationary coordinates system
$i_{s\alpha}$, $i_{s\beta}$	Stator current components in stationary coordinates system
u_{sd}, u_{sq}	Stator voltage components in rotating coordinates system
i_{sd}, i_{sq}	Stator current components in rotating coordinates system
$\psi_{s\alpha}$, $\psi_{s\beta}$	Stator flux components in stationary coordinates system
$\psi_{f\alpha}$, $\psi_{f\beta}$	Permanent magnet flux components in stationary coordinates system
ψ_{sd}, ψ_{sq}	Stator flux components in rotating coordinates system
T_s	Sample time
L_0, L_2	Components of magnetizing inductance
L_1, L_2, L_3	Inductances
e_α, e_β	EMF components in stationary coordinates system
λ_α, λ_β	Rotor flux vector in stationary coordinates system
i_{sa}, $i_{sb,}$ i_{sc}, i_{sd}, i_{se}	Phase currents
k_p	Proportional gain of PI controller
k_i	Integral gain of PI controller
ω_n	Natural frequency
ζ	Damping ratio
u_{dc}	DC-link voltage
θ_e	Electrical angle
ψ_f^α	Active flux linkage

LIST OF ABBREVIATIONS

Abbreviations	Meaning
IEA	International Energy Agency
PMSM	Permanent Magnet Synchronous Machine
SPMSM	Surface-mounted Permanent Magnet Synchronous Motor
IPMSM	Interior Permanent Magnet Synchronous Motor
EMF	Electromotive Force
HF	High Frequency
CLF	Control of Lyapunov Function
PLL	Phase Locked Loop
INFORM	Indirect Flux Detection by On-line Reactance Measurement
FPWMI	Fundamental Pulse Width Modulation Integrated Method
SMO	Sliding Mode Observer
EKF	Extended Kalman Filter
MRAS	Model Reference Adaptive Systems
AI	Artificial Intelligence
MRAC	Model Reference Adaptive Control
SMC	Sliding Mode Control
PWM	Pulse Width Modulation
FOC	Field-Oriented Control
EEMF	Extended Electromotive Force
DTC	Direct Torque Control
MPC	Model Predictive Control
MTPA	Maximum Torque Per Ampere
PTC	Predictive Torque Control
SBL	Stability Boundary Locator
PPR	Pulses Per Revolution
VSC	Voltage Source Converter
SVM	Space Vector Modulation
DSP	Digital Signal Processor
ADC	Analog to Digital Converter
PI	Proportional Integral
EV	Electric Vehicle
FPGA	Field-Programmable Gate Array

CHAPTER 1: INTRODUCTION

1.1 Preliminary discussion

Electric machines play a crucial role in the industrial development. Electric motors consume up to 53% of global energy based on the report of International Energy Agency (IEA). Efficient and reliable motion control of electric drives remains the key challenge for researchers. Compared to constant speed drive, variables speed drive is favored due various reasons such as energy saving and speed and position control for excellent dynamic response.

Permanent magnet synchronous machine (PMSM) is widely popular and utilized because of its numerous benefits such as high torque density, fast transient response, high reliability, less maintenance cost, compact structure, high airgap flux density, high acceleration and deceleration rates, high efficiency, high power factor and simplicity and ruggedness [1]-[5]. The stator structure of PMSM remains the same as other AC machine, the rotor structure of PMSM is different than the traditional AC machine. In Fig. 1.1, rotor structures of PMSM are shown. Surface-mounted permanent magnet synchronous motors (SPMSM) where permanent magnets are mounted on the surface of the rotor and interior permanent magnet synchronous motors (IPMSM) where magnets are embedded inside the rotor core, are mainly two types of PMSM motors [6], [7]. Compared to SPMSM, IPMSM provide reluctance torque and better field weakening control [8], [9].

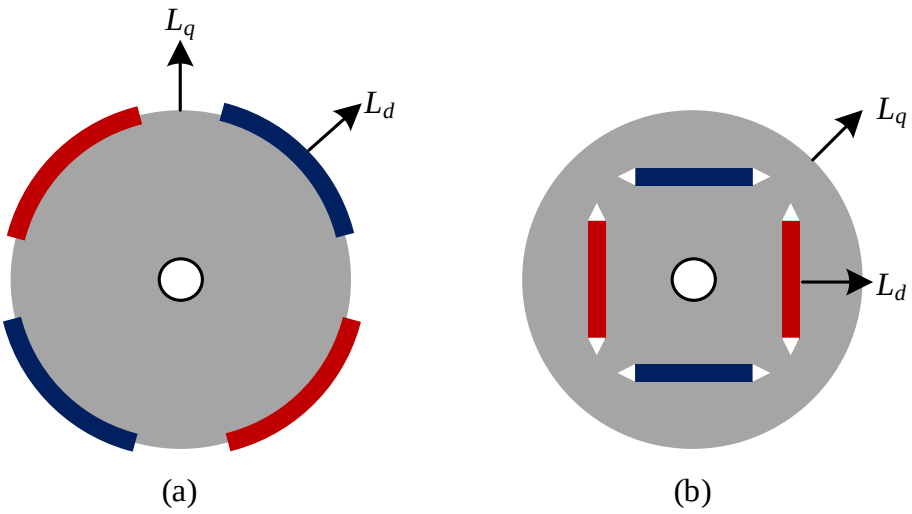

Fig. 1.1 Rotor structure (a) SPMSM (b) IPMSM

Permanent magnets are important element in PMSM. Permanent magnets contribute to field excitation by eliminating the field winding and additional supply which also reduces the corresponding losses. Residual flux density (B), coercive force (H), and maximum energy product are the important magnetic parameters of permanent magnet [10]. Alnico, Ferrite, Cobalt-Samarium, and Neodymium-Iron-Boron are the available magnetic materials [11], [12]. In Appendix - A, B-H curve of different magnetic martials is shown. Compared to other magnetic material, Neodymium-Iron-Boron magnet (NdFeB) provides better maximum remanence and coercive force and large energy product.

PMSM are widely utilized in various application due to their high performance and efficiency. To make it more applicable and cost-effective, advanced control techniques such as position sensorless control methods are preferred. In the next section, detailed review on position sensorless method is provided.

1.2 Review on Position Sensorless Methods

To obtain good dynamic and steady state response of the PMSM drive using the closed loop control, the information of angular position of the rotor is essential. Position sensor such as resolver and encoder can be employed for rotor position measurement but due to high cost, maintenance issues and lower reliability, sensorless control techniques are preferred which results in downsizing the system size, cost effective and increases the system reliability. In addition, it can also be used as additional support in sensor-based control system. When sensor struggle to sense the position of rotor, sensorless system can ensured proper working operation of IPMSM drive. This prevents subsequent failure of other system components caused by the failure of the sensors.

Moreover, estimated speed and estimated position can be used for condition monitoring of the IPMSM drive. This reduces the failure, maintenance cost and increase the reliability of IPMSM drive systems. Sensorless control of AC machine have been examined and studied for a long time and enough quality literature can be found with different control methods for different machine. This work is specifically focused on sensorless control of polyphase IPMSM drive system. Researchers across the globe has contributed a lot in the development of sensorless control of IPMSM [13]-[19]. The

various sensorless control methods can be classified into three main categories as shown in Fig. 1.2.

Sensorless control techniques for IPMSM drive can be classified based on zero and low speed range and medium and high-speed range (speed above 10% of the rated speed) [20], [21], [22]. In recent years, saliency-based approach has been developed significantly which made possible to start-up machine in closed-loop using estimated initial angular position at zero and low speed.

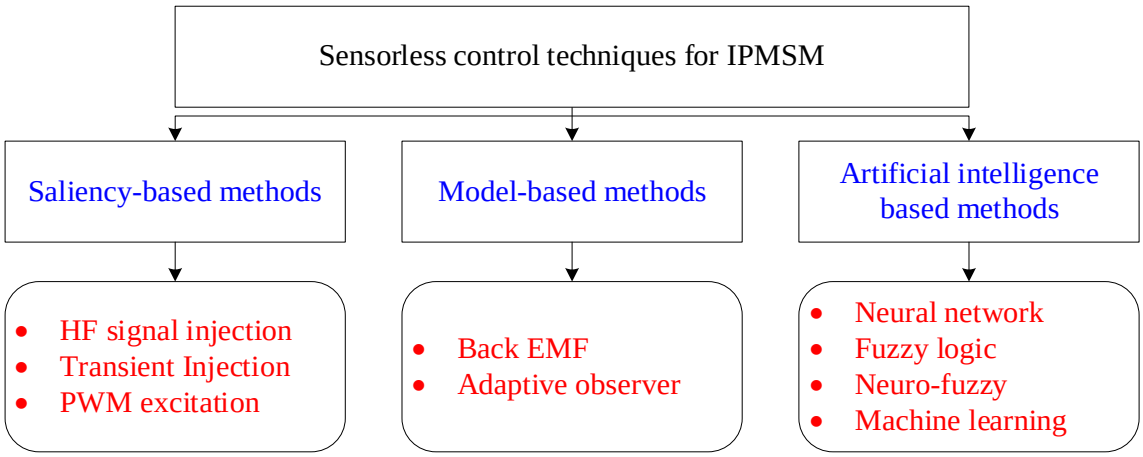

Fig. 1.2 Classification of sensorless methods for IPMSM

The model-based methods struggle at low speed due to significant low amplitude of back electro-motive force (EMF). Hence, the signal used for estimation is very weak and can be easily contaminated by the measurement noises or nonlinear effect of inverter. Moreover, voltage drop due to stator resistance have a very significant impact at low speed. In addition, the signal can be lost in heavy load conditions due to magnetic saturation; this problem is still open for research [15]. For medium and high-speed application, model-based methods are mostly preferred as amplitude of back EMF is high and other nonlinearities are negligible during medium and high-speed operation. Moreover, sensorless control techniques based on artificial intelligence have also been introduced [23], [24].

1.2.1 Saliency-based sesnorless control methods

The machine anisotropic property makes feasible to implement saliency based sensorless methods which makes possible to estimate initial angular position at zero and low speed in other words, saliency-based methods, machine winding inductances are the function of rotor position due to saliency, rotor position can be obtained from inductance variation which is essential for sensorless control implementation.

Interaction between the rotor saliency and stator teeth varies with magnetic airgap flux due to which self-inductance and mutual inductance also changes with respect to the rotor position. To obtain estimated angular position, injection of signals with high frequency (HF) becomes necessary. Saliency based signal injection technique can be broadly classified into 3 main types: continuous carrier (HF) signal injection [25], transient voltages pulses injection [26], and inherent pulse width modulation (PWM) excitation with no additional injection [27].

Signal injection methods have undergone serious development since the early 1990 [25], [28], [29]. As explained earlier, this method exploits machine anisotropies, especially based on magnetic saliency and the saturation phenomenon. The continuous injection of HF career signal is continuously superimposed to the fundamental excitation.

The rotating HF carrier injection method was first proposed by Prof. R. D. Lorenz for induction motor and then for a PMSM. In the beginning, both rotating current and voltage vectors were examined but due to high bandwidth requirement for the current regulators even larger than career frequency then voltage-based injection was preferred [30]. A constant amplitude voltage vector rotating with high frequency is superimposed to the fundamental voltage vector in stationary reference frame. The range of frequency can be from 500Hz to 3kHz. By interfering with the spatial saliency, the injected HF voltages give rise to position dependent high frequency signal. By using the demodulator, HF current is extracted to received rotor position information. While the fundamental current component is supplied as feedback to current controller after extracting HF current components. Special, demodulation techniques employed to decode the value of rotor position such phase locked loop (PLL), phasor transformation and observer.

The pulsating HF signal injection method was proposed in [31] for PMSM drive. as compared to rotating vector injection, the pulsating HF signal injection provided faster dynamic response, reduced computation time, intrinsic cancellation of filter lags during signal processing [32]. Corely and Lorentz applied pulsating HF voltage injection in q-axis on an IPMSM, but q-axis injection scheme resulted in noise and high torque ripples, later HF injection on d-axis was proposed which eliminated the disadvantages of q-axis injection method [33]-[36]. This technique was very popular in industrial

applications [37]. A specific pulsating HF injection method for stationary coordinate was proposed in [38], [39].

Rotating and pulsating sinusoidal carrier signal injection-based sensorless methods have been profoundly used. Both have same physical principle and low implementation cost. The only limitation of both techniques was limited dynamic bandwidth of the system due to signal demodulation process. The defined drawback was eliminated by square wave signal injection technique which also provides higher dynamics and eliminates requirements of low pass filters for signal demodulation [40]. Square wave injection method is less sensitive to the machine geometry compared to sinusoidal injection-based methods. Square wave-based demodulation technique does not allow more than two points per period of the injected signal to be stamped [28] .

Alternative approach to estimate the position by using saliency property is implement an impulse voltage vector to the machine and process the transient response of the current. Blaschke introduced transient excitation technique to estimate machine parameter and initial rotor position [41]. Prof. Schroedl proposed indirect flux detection by on-line reactance measurement (INFORM) for various types of AC machine [42]. In INFORM method, for a specific period of time fundamental PWM pattern required to interrupted. The reason for interruption is to inject test voltages designed manually which consist of basic six active vectors and two zero vectors. Ogasawara and Akagi rearranged PWM modulator and all six vectors to minimal time during each switching period which made possible to measure current at zero and low speed operation [43]. The major disadvantages of this method were introduction of disturbances in current due to transient voltage vector and it required additional sensor.

Fundamental PWM-Integrated method (FPWMI) method does not require injection of additional transient voltages or HF signal injection, it only relies on the inherent fundamental PWM induced effects [42]-[45]. This method gives flexibility to avoid any problem arises due to signal injection such as additional current ripple and higher switching loss. Compared to INFORM method, FPWMI provided better dynamic responses than the INFORM method [46].

1.2.2 Model-based sensorless control methods

For medium and high-speed operation, model-based methods are preferred in which angular position of the rotor is estimated using the flux linkages or back electromotive

force. In model-based techniques, open loop estimators and close loop observers are two popular approaches. In the closed loop control, the law has to prepared to force the estimation error to zero. Estimation of the EMF and flux have significant impact on position rotor position and speed, it can be reviewed by implemented reference frame, mathematical model, and error convergence techniques [46]-[48]. The model methods can be applied either in stationary coordinates system or rotating coordinates system. The general diagram of speed and position estimation using model-based methods is presented in Fig. 1.3.

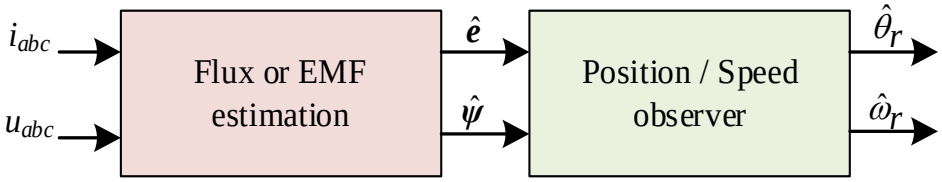

Fig. 1.3 General structure of speed and position estimation using model-based methods

Estimation of speed and position using open loop observer simple and straight forward. This method behaves same as real-time dynamic models of the PMSMs as it requires the same control inputs and run parallel. Information of angular position, and speed can be derived from the rotor flux of the back-EMF. Reference model [51], adaptive observer structures [52], extended Kalman filter [53], sliding mode observer [22], Luenberger observer are popular methods derived from machine fundamental models to estimate angular speed and position [19]. Over of back-EMF techniques and observer-based techniques are given below.

In the case of salient structure of PMSM, the information of angular position exists not only in EMF, but also in stator inductances. Hence, traditional model based sensorless control structure cannot be implemented directly. To resolve the issue, mathematical model based on the extended EMF concept [54], [55] and active flux model [54]- [56] have been reported.

In the past decade, back-EMF technique is widely used, in this approach, back-EMF is extracted from the machine fundamental model equation. Irrespective of the saliency ration in machine, back-EMF contains the information of rotor angular position [59], [60], [61], [62]. The main drawback of the back-EMF method is directly proportional to the speed, hence at low speed operation the value of back-EMF is extremely small

due to which detection capability is reduces as speed range is less than 10% of rated speed.

In addition, voltage drop due to stator resistance and nonlinearity of the inverter becomes dominant compared to back-EMF impacts at low speed which results in position information gets too small to detect [13], [15], [19]. Moreover, any uncertainty of the machine parameters directly affects in the back-EMF calculation which can lead to inaccurate estimation of speed and position. Back EMF can be obtained to extract the information of angular position of the rotor either using open loop and closed loop observers [63]. Cross coupling between d-axis and q-axis also affects the estimation performance [59].

Due to advancement in electronics, processors, and FPGAs (Field-Programmable Gate Array), it has become possible to implement the state space-based observer structure [64]. Moreover, the observer structure gives an edge to estimate and measure the variables which cannot be possible to measured directly.

Taylor linearization based high gain observer were very popular around 1980s [62]-[64], but due the poor performance at wide region of state space, observer based on nonlinear techniques such as sliding mode observer (SMO) and nonlinear Luenberger observer became popular during 1900s [68], [69]. Luenberger observer and extended Luenberger observer was proposed in [70], [71]. In this observer structure, prediction term follows the dynamics of EMF and a correction term with a nonlinear gain coefficient is added. The primary benefit of this type observer is that it ensures convergence at wide region of the state space.

Sliding mode observer prepared using the variable structure design. In SMO, sign function based discontinuous gain is added in correction term. SMO is widely used to reconstruct the rotor position and rotor speed in PMSM drive [71]- [75]. The disadvantage of SMO is that due to discontinuous function, it causes undesirable chattering. To eliminate the chattering effect, different modifications were proposed in [72]. Extended sliding mode-disturbance observer was proposed in [75], where lumped uncertainties were estimated directly and major disturbances were compensated. In this proposition, only rotor speed was estimated, angular position was measured using the sensor.

Kalman filter for linear system and the extended Kalman filter (EKF) for nonlinear system comes under the second approach which is stochastic observer [53], [77]. In this method, objective to minimize the covariance of the error between the real state space vector and estimated one by considering measurement noises and modelling errors. EKF provides better estimation accuracy and less affected by measurement noise. The limitation in EKF is computation task is very complex which makes difficult to implement in practice. Adaptive control and Model reference adaptive systems (MRAS) is also another alternative for adaptive observer structure [52], [77]-[79]. Compared to EKF, implementation of MRAS is less complex which is the one of main reasons of its popularity in sensorless control of drives [81], [82].

1.2.3 Artificial intelligence-based sensorless control methods

Since 1990, artificial intelligence (AI) based algorithm are being develop for the application of sensorless control [83], [84], [85], [86], [87], [88]. As compared to previous mentioned techniques, AI based eliminate the requirement of a physical model of the machine. They can approximate any function, irrespective of its linearity. This technique can be more beneficial if datasets are available for learning. AI based algorithms were firstly implemented in with vector-controlled motor drives [85], [89]. It was concluded that this method reduces tuning efforts required by controller and provide better results. In [23], [90], PI controller was replaced by AI based MRAS to solve the problem of discretization instability in field weakening region. AI based algorithms are also used for estimation of angular position [24], [84], [86], [91], [92]. This type of estimators allows the estimation of position without using the fundamental machine model, which cannot be possible in model-based conventional scheme. Among the different AI techniques, the fuzzy logic is complicated and simple to apply [93]. Torque ripple reduction using fuzzy logic base algorithm reported in [94].

In the next section, detailed discussion on multiphase machine is provided considering the benefits, evolution, research gap in the existing research trends.

1.3 Multiphase Machine

Multiphase machines are receiving significant attention owing to their benefits over three-phase machines such as reduced power per phase rating, improved reliability, increment in torque density, higher fault tolerance capability, and lower torque ripple. Multiphase machine drives provide higher power range by employing low-power

switching devices [95], [96], [97]. Compared to three phase drives, the fault tolerance capability is one of the most desired properties of multiphase machine drives in industrial applications [98]. A five-phase IPMSM provides various advantages such as: higher torque density, fast dynamic response, good power factor and high reliability [99]. Multiphase machines are used in electromobility, electric aircraft, ship propulsion, and electric vehicle (EV) [100], [101].

In multiphase machine, it is possible to inject harmonics current to increase the output electromagnetic torque. Compared to three-phase machine, output torque can be increased up to 15% in five-phase machine [102], [105]-107]. Generally, harmonic order lower than the number of phases are mostly used to increase the output torque, if harmonics order higher than number of phases are injected then losses are increased and torque ripple is also increased. In seven-phase machine, 3^{rd} and 5^{th} harmonics can be injected, in nine-phase machine, 3^{rd}, 5^{th} and 7^{th} harmonics can be injected to improve torque density. In multiphase machine, independent vector planes exist for five-phase machine 2-planes, for seven-phase machine 3-planes, for fifteen phase machine 7-planes [103].

Design of windings in Five-phase IPMSM can be done in two ways: distributed winding and concentrated winding. In distributed winding, coil is shared with several slots which allows to ensure proper flux distribution with less harmonics components, while in concentrated winding coil is wounded in one single slot [104],[105], due to which flux curve results as quasi-rectangular as it contains harmonic components. Spatial displacement between two consecutive stator phases is $\alpha = 72°$ in the five-phase IPMSM.

The winding of investigated five-phase IPMSM is concentrated type as it offers enhancement in output torque by injecting third harmonic current[104],[105]. In the Appendix – B, single plate of state and rotor of five-phase IPMSM is depicted. The five-phase has 3 pole pairs and 30 slots in the stator and slots per pole per phase is 1.

In Fig. 1.4, properly synchronized rotor flux distribution is presented for five-phase IPMSM. As per Fig. 1.4, by injecting 3^{rd} harmonic current with fundamental current, resulting flux has quasi-trapezoidal wave shape [106]. It can be observer that the peak value of fundamental sine wave (green) is higher than the resulting wave (red), but

maximum amplitude duration of quasi-trapezoidal wave (red) is longer which helps to utilizes magnetic circuit better.

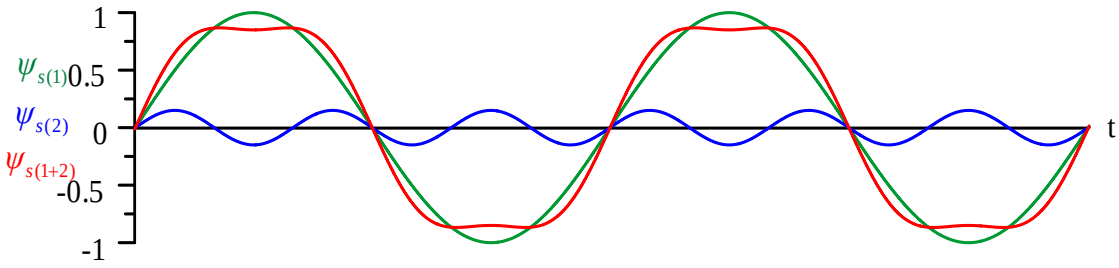

Fig. 1.4 Flux distribution with 3rd harmonic injection in five-phase IPMSM

In the 1960s, Ward and Harer presented first article on theoretical and experimental analysis on five-phase induction machine [107]. It was reported in the article that as phase number was increased from three to five, amplitude was decreased and torque ripple frequency was increased. In the 1980s, Jahns examined the fault-tolerant performance and reliability of multiphase drive system [108]. However, research on multiphase machine was not popular in that time as due to technical restriction. In the 1990s, technological development in the field of power electronics, microcontrollers, and adjustable-speed drive led to research implementation on multiphase machines.

Currently, most of the research on sensorless control is dedicated three phase machines drives. In addition, research on multiphase machine is majorly focused on improving the fault-tolerant capability [104], [118], [120]-[125]. Moreover, control strategies of three phase machine applications have been extended to control multiphase machine [96], [100], [101], [116]. The control approach of a multiphase machine incorporates simultaneous control of two virtual machine in one physical motor to ensure a higher value of torque generation by fundamental current and injected third harmonic current [102], [106], [117], [118].

Advanced control structures such as vector control also known as field-oriented control (FOC) where state variables are transformed to rotating reference coordinates (dq), direct torque control and model predictive control (MPC) are most commonly used in control applications of multiphase machines. Researchers worldwide explained these control approaches well in the existing literature for three-phase and five-phase machines [109], [119]-[123] [124] [125].

The main drawback of the vector control scheme is that while changing the flux linkage, the decoupling between the electromagnetic and electromechanical part is not achieved in the presence of nonlinearities defined in [126], [127]. It fails to decouple the system entirely in the presence of nonlinearity due to the machine state variable transformation to the rotating coordinates and plausible intervention between the two controlled subsystems of the multiphase machine. In the direct torque control (DTC) structure, hysteresis controllers are required and switching table also needs to be prepared which increases complexity of the control system [128].

For fast dynamic response and to reduce the number of proportional integral controllers, backstepping technique with feedback control for five-phase induction machine was proposed in [118]. MPC with disturbance observer was proposed to minimize steady-state error and harmonics in current for six-phase PMSM [129]. MPC with the Luenberger observer was reported to enhance the robustness and the steady state performance for multiphase PMSM [119]. This proposition also reduced the mismatch of flux and inductance. For a nine phase IPMSM, high frequency injections with Luenberger observer were implemented to estimate angular rotor position without generating any high frequency torque ripple [120]. Considering single phase fault, estimation of inductance for dual three phase PMSM using extended Kalman filter was proposed and up to 2% estimation error, fast convergence and accurate estimation under different operating conditions are key contribution [115].

Fig. 1.5 shows that from the year 2014 to 2024 overall 579 research articles were published on PMSM in the IEEE Xplore. Out of 579 research articles, 502 research articles were focused on the research on three-phase PMSM and remaining 77 articles were dedicated to multiphase PMSM. Moreover, year wise research publication in reputed IEEE journals from 2014 to 2024 is shown in Fig. 1.6. Most of these research articles on multiphase machine focused towards the fault tolerant performance. It can be observed from Fig. 1.5 and Fig. 1.6 that research on multiphase machine is significantly less specially in the direction of control system of multiphase machine due to high complexity.

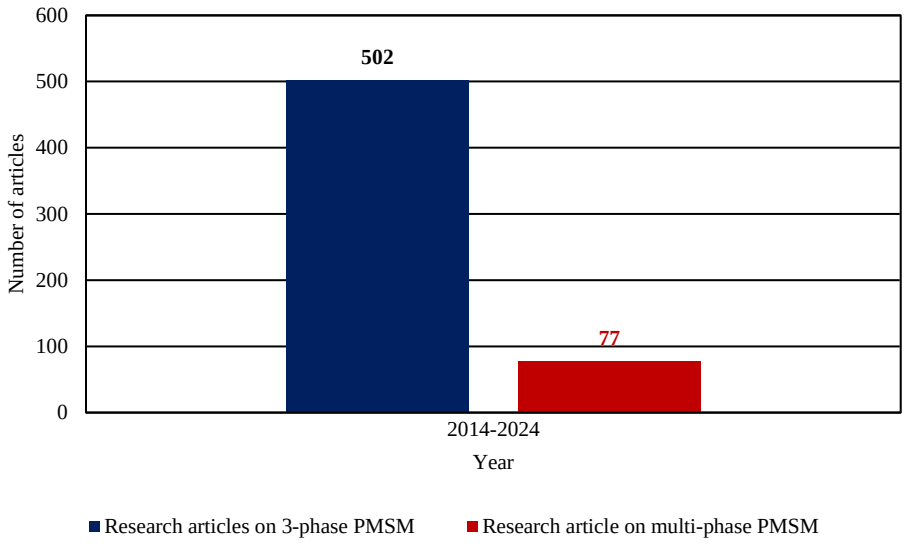

Fig. 1.5 Research articles on 3-phase PMSM and multiphase PMSM

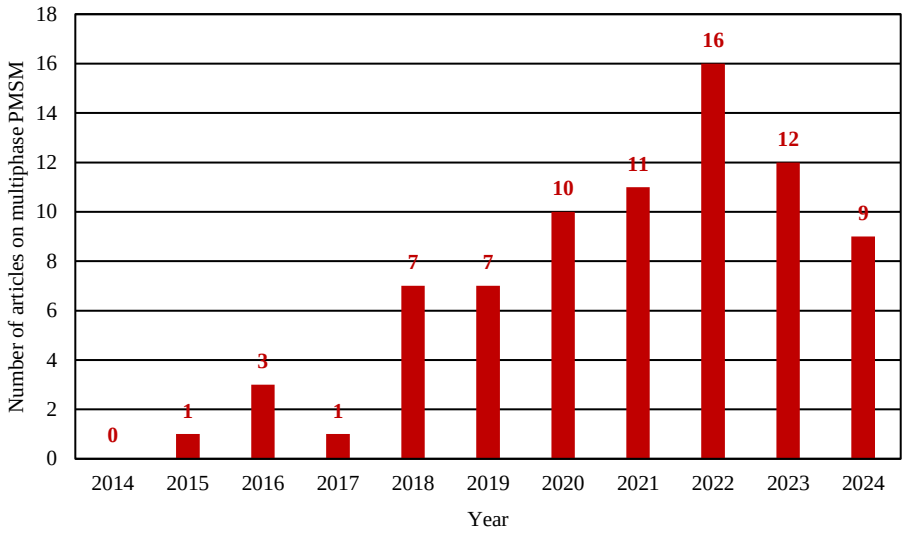

Fig. 1.6 Research articles on multiphase PMSM per year

1.4 Originality of the research and research objectives

Based on the literature review presented in section 1.3, existing literature lacks analysis and discussion on the advanced control systems in which nonlinear state variables transformation is considered. The control solution of five-phase IPMSM based on nonlinear state variables transformation ensures effective separation between electromechanical and electromagnetic subsystems. In the classical FOC structure, electromagnetic torque production depends on interaction between flux component ψ_{sd} in d-axis and torque controlling current i_{sq} component in q-axis and reluctance torque relies on product between direct i_{sd} and quadrature i_{sq} axis current, hence accurate

decoupling between flux control system and torque control system is not obtained in the presence of the nonlinearity [126], [127].

The author of this thesis proposes control strategy using nonlinear transformation of chosen state variables of IPMSM (three-phase and five-phase) to *x* - multiscalar form presented by Krzeminski in [121]. The multiscalar transformation ensure separate control of electromechanical and electromagnetic subsystem. The author of this thesis applies multiscalar transformation in combination with predictive and backstepping approach. To increase output torque in five-phase IPMSM, the third harmonic current is injected with the fundamental current. An adaptive observer structure is employed to estimate the state variables to eliminate the noise and gain drift in the measured parameters due to mechanical sensors. Initially, the proposed control solutions were verified on experimental setup with three-IPMSM drive with fundamental components only.

The three-phase IPMSM available in the laboratory set up contains spatial harmonics and non-sinusoidal distribution of EMF as shown in [122]. The problem of spatial harmonics and non-sinusoidal distribution of EMF is considered as additional disturbances in the sensorless control system. The research work carried out in this doctoral thesis is limited to three-phase IPMSM and five-phase IPMSM.

Based on the above discussion, the principal research objectives of the doctoral dissertation can be briefly summarized for three-phase IPMSM and five-phase IPMSM:

1.4.1 Three-phase IPMSM drive

- To design different state observer structures based on mathematical structures of three-phase IPMSM.
- To design the appropriate form of the stabilizing functions considering the problem machine asymmetry.
- To conduct the stability analysis of three-phase linearized observer error structures close to an equilibrium points in rotating coordinate system.
- To verify the performance of observer structure in simulation and experimental investigation.
- To perform comparative analysis of different observer structure.

The doctoral research aims to conduct original theoretical, simulation and experimental research on multiscalar variables based sensorelss control of multiphase IPMSM drive. The proposed control structures of five-phase IPMSM are also compared with the existing control solution of multiphase IPMSM machines.

1.4.2 Five-phase IPMSM drive

- To design an adaptive observer structure based on the mathematical model of the five-phase IPMSM.
- To conduct the stability analysis based on the linearized observer error structure near an equilibrium point in (*d-q*) reference frame.
- To study and examine existing sensorless control algorithms of five-phase IPMSM.
- To develop various control technique based on multiscalar transformation for fundamental plane and second plane to inject 3rd harmonic current to increase output torque up to 10% fundamental torque.
- To conduct closed loop stability analysis of the proposed sensorless control system of five-phase IPMSM.
- To examine the effectiveness of the proposed sensorless control scheme of five-phase IPMSM by simulation and experimental verification under wide speed operation range and loading conditions.
- To investigate similarities and difference between the existing sensorless control scheme and proposed sensorless control solution of five-phase IPMSM to perform the comparative analysis.

1.5 Research Hypothesis

In this thesis author proposes control system structure using multiscalar transformation 1) $\boldsymbol{\psi}_{\mathbf{f(i)}},\mathbf{i}_{\mathbf{s(i)}}$ vectors (1st strategy) 2) $\boldsymbol{\psi}_{\mathbf{s(i)}},\mathbf{i}_{\mathbf{s(i)}}$ vectors (2nd strategy). The research thesis of the doctoral work is formulated as:

I. Proposed multiscalar transformation utilized in stationary coordinate system of five-phase IPMSM for the defined vectors: $\boldsymbol{\psi}_{\mathbf{f(i)}},\mathbf{i}_{\mathbf{s(i)}}$ *vectors and* $\boldsymbol{\psi}_{\mathbf{s(i)}},\mathbf{i}_{\mathbf{s(i)}}$ *vectors, allows to determine static state feedback control laws for both control strategies.*

II. *In the proposed control system structures the classical proportional-integral (PI), predictive and backstepping controllers are considered. In addition, these control approaches ensure independent control of the state variables in the electromechanical and electromagnetic subsystems even if the 3rd harmonic is injected.*

III. *In the proposed control system structure using the* $\boldsymbol{\psi}_{f(i)}, \mathbf{i}_{s(i)}$ *vectors and* $\boldsymbol{\psi}_{s(i)}, \mathbf{i}_{s(i)}$ *vectors in stationary coordinate of five-phase IPMSM allows the utilization of 3rd harmonic injection to enhance the output torque value.*

CHAPTER 2: MATHEMATICAL MODEL OF INTERIOR PERMANENT MAGNET SYNCHRONOUS MACHINE

2.1 Overview

The selection of accurate and appropriate mathematical model of the machine is an important task in the implementation of sensorless control. The mathematical model of the machine is needed for various important reasons such as: design of controller, the selection of controller parameters, simulation analysis, and implementation of digital control. The selection of reference frame also plays a vital part in the modelling of any machine, as reference frame are like observer platforms in which each of platforms provide a specific view of the system at hand as well as the changes in the system equation. Mathematical model of the machine can be prepared in two different reference frames: stationary reference frame and rotating reference frame. The stationary reference frame is fixed with stator and rotating reference frame is fixed to rotor. Before proceeding to design observer structures and control systems, mathematical model of interior permanent magnet synchronous motor is presented.

2.2 Mathematical model of three-phase IPMSM

The mathematical model of IPMSM is prepared using the space vector theory. Fig. 2.1 shows that mathematical model of IPMSM can be prepared in different reference frame. The stator windings are placed 120° degrees apart from each other, θ_r is the rotor angle, which is the angle between magnetic axis of stator winding 'a' and rotor magnetic flux (i.e., *d*-axis). The positive direction is taken in anti-clockwise as shown in Fig. 2.1, where angular velocity of rotor ω_r is in positive direction.

Following assumptions are considered for the modelling of IPMSM.

- Stator winding produces sinusoidal mmf distribution.
- Space harmonics are neglected in air-gaps.
- Air-gap reluctance has a constant component as well as sinusoidally varying component.
- Balanced three-phase supply voltage is considered.

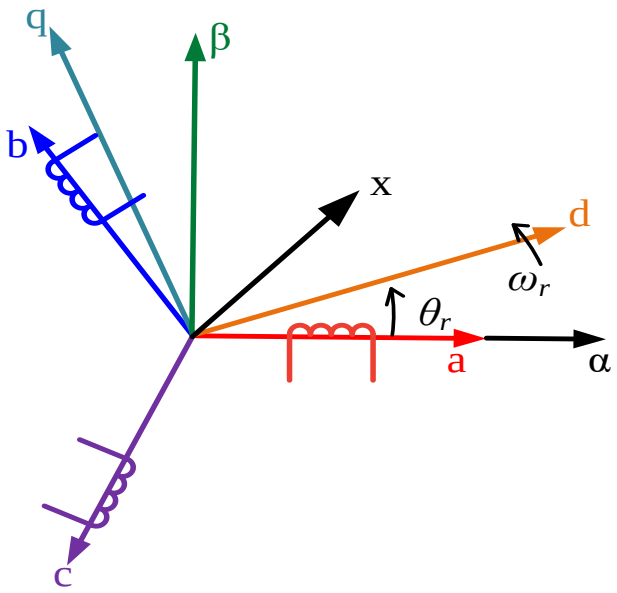

Fig. 2.1. Different reference frames

- Saturation is neglected, although it can be taken into account by parameter changes.
- The back emf is sinusoidal.
- Eddy currents and hysteresis loses are negligible.

The IPMSM machine has permanent magnet in the rotor hence the need of excitation winding is eliminated which simplifies the mathematical model of IPMSM in natural coordinate system. The following vector equations represents the machine model in natural coordinates [9], [130] .

$$\mathbf{u}_s = \mathbf{R}_s \mathbf{i}_s + \frac{d\boldsymbol{\psi}_s}{d\tau} \tag{2.1}$$

$$\boldsymbol{\psi}_s = \mathbf{L}_s \mathbf{i}_s + \boldsymbol{\psi}_f \tag{2.2}$$

$$T_e = \frac{dW}{\partial\theta_r} = P_n \left(\frac{1}{2} \mathbf{i}_s^T \frac{\partial \mathbf{L}_s}{\partial\theta_r} \mathbf{i}_s + \frac{\partial \boldsymbol{\psi}_f}{\partial\theta_r} \mathbf{i}_s \right) \tag{2.3}$$

$$T_e - T_L = J \frac{d\omega_r}{d\tau} + B\omega_r \tag{2.4}$$

Where $\mathbf{u}_s$ and $\mathbf{i}_s$ are the stator voltage and current vectors, $\mathbf{R}_s$ and $\mathbf{L}_s$ are the stator resistance and inductance matrices, $\boldsymbol{\psi}_s$ is the stator magnetic flux vector, $\boldsymbol{\psi}_f$ is

permanent magnet flux vector, θ_r is the rotor angular position, p_n is the number of pole pairs, J is the moment of inertia, B is viscous friction coefficient.

2.2.1 Mathematical model of IPMSM in rotating reference frame

The mathematical model of IPMSM is often determined in the rotating reference frame using the Park transfromation [8], [9]. The primary reason of using rotating reference frame is that it is possible to control reference frame quantites seprately, which is the basic aim of vector control scheme. Using the (d-q) coordinate system, dynamical model of the IPMSM based on stator currents in (d-q) reference frame is well known in the literature.

$$\frac{di_{sd}}{d\tau} = -\frac{R_s}{L_d} i_{sd} + \frac{1}{L_d} \omega_r L_q i_{sq} + \frac{1}{L_d} u_{sd} \tag{2.5}$$

$$\frac{di_{sq}}{d\tau} = -\frac{R_s}{L_q} i_{sq} - \frac{1}{L_q} \omega_r \left(L_d i_{sd} + \psi_f \right) + \frac{1}{L_q} u_{sq} \tag{2.6}$$

$$\frac{d\omega_r}{d\tau} = \frac{1}{J} (\psi_f i_{sq} + (L_d - L_q) i_{sd} i_{sq} - T_L) \tag{2.7}$$

$$\frac{d\theta_r}{d\tau} = \omega_r \tag{2.8}$$

Where i_{sd} and i_{sq} are vector components of currents, u_{sd} and u_{sq} are vector components of voltages, R_s is stator resistance, L_d and L_q are inductance in d-axis and q-axis, respectively. J is inertia, and T_L is load torque.

2.2.2 Rotor flux vector-based modeling of IPMSM

The following mathematical model of the IPMSM can be obtained in stationary reference frame [122], [123].

$$\frac{di_{s\alpha}}{d\tau} = \frac{\omega_r}{L_d} \lambda_\beta + (-R_s i_{s\alpha} + u_{s\alpha}) L_1 + (-R_s i_{s\beta} + u_{s\beta}) L_3 \tag{2.9}$$

$$\frac{di_{s\beta}}{d\tau} = -\frac{\omega_r}{L_d} \lambda_\alpha + (-R_s i_{s\alpha} + u_{s\alpha}) L_3 + (-R_s i_{s\beta} + u_{s\beta}) L_4 \tag{2.10}$$

$$\frac{d\omega_r}{d\tau} = \frac{1}{J} (\psi_{f\alpha} i_{s\beta} - \psi_{f\beta} i_{s\alpha} - T_L) \tag{2.11}$$

$$\frac{d\theta_r}{d\tau} = \omega_r \tag{2.12}$$

Where

$$\lambda_\alpha = \frac{L_d}{L_q}\psi_{f\alpha} - (1-\frac{L_d}{L_q})(L_0 i_{\alpha 2} + L_2 i_{s\alpha}), \tag{2.13}$$

$$\lambda_\beta = \frac{L_d}{L_q}\psi_{f\beta} + (1-\frac{L_d}{L_q})(L_0 i_{\beta 2} - L_2 i_{s\beta}), \tag{2.14}$$

$$\begin{aligned} L_0 &= 0.5(L_d + L_q), \\ L_2 &= 0.5(L_d - L_q), \\ L_1 &= L_d^{-1}\cos^2\theta_r + L_q^{-1}\sin^2\theta_r, \\ L_3 &= 0.5(L_d^{-1} - L_q^{-1})\sin 2\theta_r, \\ L_4 &= L_d^{-1}\sin^2\theta_r + L_q^{-1}\cos^2\theta_r \end{aligned} \tag{2.15}$$

$$\begin{aligned} i_{s\alpha 2} &= i_{s\alpha}\cos(2\theta_r) + i_{s\beta}\sin(2\theta_r) \\ i_{s\beta 2} &= -i_{s\alpha}\sin(2\theta_r) + i_{s\beta}\cos(2\theta_r) \end{aligned} \tag{2.16}$$

The dynamical model of IPMSM considering the extended electromotive force (EEMF) can be modeled by state space equation in stationary reference frame as is presented in (2.17) - (2.20). In the EEMF model e_α and e_β are the vector components of EMF. It is assumed that the parameters of the machine are considered unchanging in time.

$$\frac{\mathrm{d}i_{s\alpha}}{\mathrm{d}\tau} = \frac{1}{L_q}e_\beta + \omega_r\lambda_\beta + (-R_s i_{s\alpha} + u_{s\alpha})L_1 + (-R_s i_{s\beta} + u_{s\beta})L_3, \tag{2.17}$$

$$\frac{\mathrm{d}i_{s\beta}}{\mathrm{d}\tau} = -\frac{1}{L_q}e_\alpha + \omega_r\lambda_\alpha + (-R_s i_{s\alpha} + u_{s\alpha})L_3 + (-R_s i_{s\beta} + u_{s\beta})L_4, \tag{2.18}$$

$$\frac{\mathrm{d}e_\alpha}{\mathrm{d}\tau} = \frac{\mathrm{d}\omega_r}{\mathrm{d}\tau}\psi_{f\alpha} - \omega_r e_\beta, \tag{2.19}$$

$$\frac{\mathrm{d}e_\beta}{\mathrm{d}\tau} = \frac{\mathrm{d}\omega_r}{\mathrm{d}\tau}\psi_{f\beta} + \omega_r e_\alpha, \tag{2.20}$$

$$\lambda_\alpha = (\frac{1}{L_d} - \frac{1}{L_q})(\frac{1}{L_d}L_0 i_{\alpha 2} + \frac{1}{L_d}L_2 i_{s\alpha}), \tag{2.21}$$

$$\lambda_\beta = (\frac{1}{L_d} - \frac{1}{L_q})(\frac{1}{L_d}L_0 i_{\beta 2} - \frac{1}{L_d}L_2 i_{s\beta}), \tag{2.22}$$

Where R_s is stator resistance, L_d and L_q are winding inductances, J is inertia, T_L and T_e are load and electromagnetic torque, respectively. $u_{s\alpha,\beta}$, $i_{s\alpha,\beta}$ and $\psi_{f\alpha,\beta}$ are the vector components of stator voltage current and permanent magnet flux, respectively. ω_r and

θ_r rotor angular speed and position of the rotor. λ_α and λ_β are defined as rotor flux vector component. Where parameters L_0, L_2 and functions L_1, L_3, L_4 and the park transformation of stator current are defined in (2.15) and (2.16), respectively.

2.2.3 Active flux-based modeling of IPMSM

The active flux concept-based machine model transforms salient AC motor into the non-salient one [56], [57]. This transformation reduces the burden of analysis and design of the position sensorless control system. The active flux linkage can be explained for the IPMSM in (2.24). To understand the active flux concept in details, the vector diagram of active flux concept in stationary and rotating coordinate system is presented Fig. 2.2.

$$T_e = \frac{3}{2} p_n \left[\psi_f + \left(L_d - L_q \right) i_{sd} \right] i_{sq} \tag{2.23}$$

$$\psi_f^a = \psi_f + \left(L_d - L_q \right) i_{sd}, \quad L_d < L_q \tag{2.24}$$

$$T_e = \frac{3}{2} p_n \psi_f^a i_{sq} \tag{2.25}$$

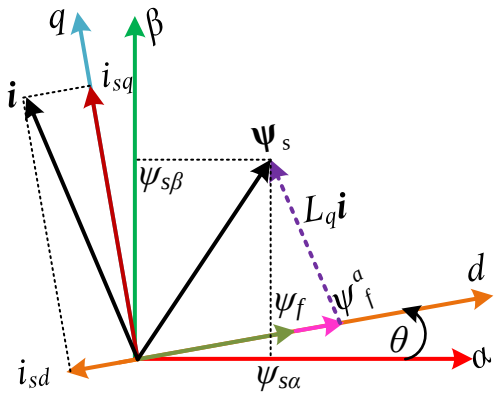

Fig. 2.2 Vector representation of active flux in rotating and stationery coordinate system

where T_e is the electromagnetic torque, p_n is number of pole pairs, ψ_f^a is the active flux linkage. The active flux linkage includes permanent magnet flux linkage and the flux linkage generated by rotor saliency. The direction of active flux linkage is towards the d-axis. The linear equation of torque appears in (2.25) when ψ_f^a is fixed, toque can be controlled directly by i_{sq}.

$$\boldsymbol{\psi}_f^a = \boldsymbol{\psi}_s - L_q \mathbf{i}_s \tag{2.26}$$

The voltage equation of IPMSM in the vector form is given in (2.27),

$$\mathbf{u}_s = \mathbf{R}_s \mathbf{i}_s + \frac{d}{d\tau}\left(\boldsymbol{\psi}_f^a + L_q \mathbf{i}_s\right) \tag{2.27}$$

$$\boldsymbol{\psi}_s = \int \left(\mathbf{u}_s - \mathbf{R}_s \mathbf{i}_s\right) d\tau \tag{2.28}$$

$$\boldsymbol{\psi}_f^a = \int \left(\mathbf{u}_s - \mathbf{R}_s \mathbf{i}_s\right) d\tau - L_q \mathbf{i}_s \tag{2.29}$$

As per (2.26), simple relationship between stator flux and active flux is visible where inductance L_q is the only motor parameters affected. The active flux model of the IPMSM allows to omit the inductance L_d, which simplify the overall model of IPMSM as described in [56], [57].

Based on the idea of active flux concept, the IPMSM model can be described in stationary reference frame by the following differential equation (2.30) – (2.33). This doctoral thesis aims to prove that based on active flux model of IPMSM in stationary reference frame, it is possible to control IPMSM drive with suitable accuracy compared to the control system which is based on *d-q* model where multiscalar the transformation was proposed by Krzemiński [123].

$$\frac{di_{s\alpha}}{d\tau} = -\frac{1}{L_q} R_s i_{s\alpha} + \frac{1}{L_q} \omega_r \psi_{f\beta} + \frac{1}{L_q} u_{s\alpha} \tag{2.30}$$

$$\frac{di_{s\beta}}{d\tau} = -\frac{1}{L_q} R_s i_{s\beta} - \frac{1}{L_q} \omega_r \psi_{f\alpha} + \frac{1}{L_q} u_{s\beta} \tag{2.31}$$

$$\frac{d\omega_r}{d\tau} = \frac{1}{J}(\psi_{f\alpha} i_{s\beta} - \psi_{f\beta} i_{s\alpha} - T_L) \tag{2.32}$$

$$\frac{d\theta_r}{d\tau} = \omega_r \tag{2.33}$$

$$\begin{aligned} \psi_{s\alpha} &= \psi_{f\alpha} + L_q i_{s\alpha} \\ \psi_{s\beta} &= \psi_{f\beta} + L_q i_{s\beta} \end{aligned} \tag{2.34}$$

Similarly, by applying state space in stationary reference frame dynamic model of IPMSM can be prepared using EEMF as (2.35) - (2.38).

$$\frac{\mathrm{d}i_{s\alpha}}{\mathrm{d}\tau} = -\frac{1}{L_q} R_s i_{s\alpha} + \frac{1}{L_q} e_\beta + \frac{1}{L_q} u_{s\alpha}, \tag{2.35}$$

$$\frac{\mathrm{d}i_{s\beta}}{\mathrm{d}\tau} = -\frac{1}{L_q} R_s i_{s\beta} - \frac{1}{L_q} e_\alpha + \frac{1}{L_q} u_{s\beta}, \tag{2.36}$$

$$\frac{\mathrm{d}e_\alpha}{\mathrm{d}\tau} = \frac{\mathrm{d}\omega_r}{\mathrm{d}\tau} \psi_{f\alpha} - \omega_r e_\beta, \tag{2.37}$$

$$\frac{\mathrm{d}e_\beta}{\mathrm{d}\tau} = \frac{\mathrm{d}\omega_r}{\mathrm{d}\tau} \psi_{f\beta} + \omega_r e_\alpha, \tag{2.38}$$

In the mathematical model, stator resistance is defined as R_s; magnetic anisotropy can be ignored by considering the rotor pole salient IPMSM into fictitious rotor non-salient pole IPMSM, which reduces the complexity in the estimation process of speed and position. The inductance of the rotor of the IPMSM can be considered as L_q. $u_{s\alpha,\beta}$, $i_{s\alpha,\ \beta}$ and $\psi_{f\alpha,\beta}$ are the vector components of supplied voltage and current to stator terminals, and flux components of a permanent magnet, respectively. J, T_L, and T_e are known as the machine's inertia, load torque, and electromagnetic torque. Angular speed is ω_r, and angular position is θ_r. In the extended model, electromotive force (EMF) is introduced. $e_{\alpha,\beta}$ is the vector components of EMF. The EMF **e** vector contains the information of angular position, which will be useful in the EEMF model.

The mathematical model described in (2.30) – (2.33) redcues the overall complexity and less machine parametrer dependent compared to classical model given in [8], [9]. Moreover, the active flux model shows a great similarity and equivalence between the IPMSM and SPMSM with the real magnet flux for IPMSM in the (α-β). The sensorless control applied to SPMSM can directly applied IPMSM by using the active flux model. In addition, the model is independent on motor inductance matrix parameter.

2.3 Mathematical model of five-phase IPMSM

The modelling concepts of three phase electrical machine also applies to five phase machines. In five-phase machine phase displacement between two consecutive winding is 72°. Due to injection of current harmonic, machine model can be transformed from natural reference frame (five-phase) to two stationary orthogonal planes for fundamental components and third harmonic components, respectively [103], [105], [131], [132].

2.3.1 Mathematical of five-phase IPMSM in rotating reference frame

The mathematical model of five-phase IPMSM [132], [133], [134] in synchronous rotating frame is expressed using the following differential equation (2.39) – (2.42).

$$\frac{di_{sd(i)}}{d\tau} = -\frac{R_s}{L_{d(i)}} i_{sd(i)} + \frac{1}{L_{d(i)}} \omega_{r(i)} L_{q(i)} i_{sq(i)} + \frac{1}{L_{d(i)}} u_{sd(i)} \tag{2.39}$$

$$\frac{di_{sq(i)}}{d\tau} = -\frac{R_s}{L_{q(i)}} i_{sq(i)} - \frac{1}{L_{q(i)}} \omega_{r(i)} \left(L_{d(i)} i_{sd(i)} + \psi_{f(i)} \right) + \frac{1}{L_{q(i)}} u_{sq(i)} \tag{2.40}$$

$$\frac{d\omega_{r(i)}}{d\tau} = \frac{1}{J} \left(\sum_{i=1}^{N} \psi_{f(i)} i_{sq(i)} + (L_{d(i)} - L_{q(i)}) i_{sd(i)} i_{sq(i)} - T_L \right) \tag{2.41}$$

$$\frac{d\theta_{r(i)}}{d\tau} = \omega_{r(i)} \tag{2.42}$$

Where, vector component of voltages $u_{sd(i)}$, $u_{sq(i)}$ and currents $i_{sd(i)}$,$i_{sq(i)}$ for each planes, R_s is stator resistance, $L_{d(i)}$ and $L_{q(i)}$ are inductance in d-axis and q-axis, respectively. J is inertia, T_L is load torque. It is important to mention that, index i defines reference plane for N-phase IPMSM.

For an odd phase number, $i = 0.5(N\text{-}1)$ and for even phase, $i = 0.5N\text{ -}1$. The variables of first coordinate systems which is responsible for fundamental current injection is represented using the index (1) and variables of second coordinate system which is responsible for third harmonic current injection into system is denoted using the index (2). In Fig. 2.3, representation of fundamental variables in the first plane and third harmonics variables in the second plane are depicted in using vector plane in rotating coordinates system.

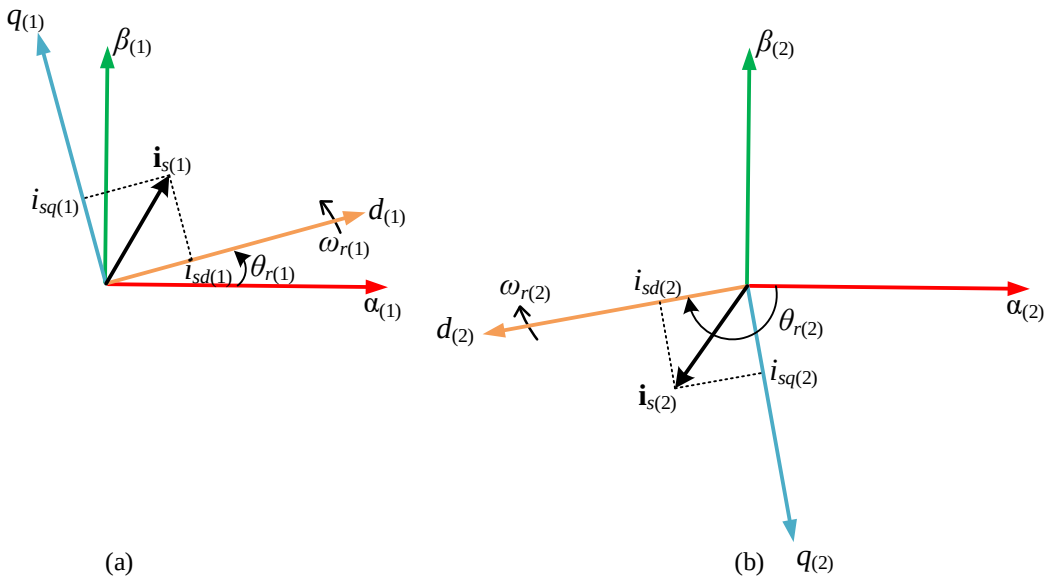

Fig. 2.3 Rotating coordinates systems (a) First plane system (b) Second plane system

2.3.2 Active flux-based modeling of five-phase IPMSM

The mathematical model defined for three-phase machine using active flux concept (2.30) – (2.33) can be extended for the five-phase IPMSM. The differential equations of the mathematical model of the *N*-phase IPMSM in stationary reference frame for fundamental plane and third harmonic plane have the following form (2.43) – (2.46).

$$\frac{di_{s\alpha(i)}}{d\tau} = -\frac{1}{L_{q(i)}} R_s i_{s\alpha(i)} + \frac{1}{L_{q(i)}} \omega_{r(i)} \psi_{f\beta(i)} + \frac{1}{L_{q(i)}} u_{s\alpha(i)} \tag{2.43}$$

$$\frac{di_{s\beta(i)}}{d\tau} = -\frac{1}{L_{q(i)}} R_s i_{s\beta(i)} - \frac{1}{L_{q(i)}} \omega_{r(i)} \psi_{f\alpha(i)} + \frac{1}{L_{q(i)}} u_{s\beta(i)} \tag{2.44}$$

$$\frac{d\omega_{r(i)}}{d\tau} = \frac{1}{J}\left(\sum_{i=1}^{N} (\psi_{f\alpha(i)} i_{s\beta(i)} - \psi_{f\beta(i)} i_{s\alpha(i)}) - T_L \right) \tag{2.45}$$

$$\frac{d\theta_{r(i)}}{d\tau} = \omega_{r(i)} \tag{2.46}$$

$$\psi_{s\alpha(i)} = L_{q(i)} i_{s\alpha(i)} + \psi_{f\alpha(i)} \tag{2.47}$$

$$\psi_{s\beta(i)} = L_{q(i)} i_{s\beta(i)} + \psi_{f\beta(i)} \tag{2.48}$$

Where R_s is stator resistance, $L_{q(i)}$ is q-axis inductance, $\omega_{r(i)}$ is rotor speed, T_L is load torque, J is the rotor moment of inertia, $u_{s\alpha(i)}$ and $u_{s\beta(i)}$ are stator voltage components, $i_{s\alpha(i)}$ and $i_{s\beta(i)}$ are the stator current components, $\psi_{f\alpha(i)}$ and $\psi_{f\beta(i)}$ are the permanent magnet flux components for first plane and second plane respectively. It is assumed that machine parameters for five-phase IPMSM is known and constant.

The presented mathematical model of the three phase IPMSM defined in 2.2.2 and 2.2.3 and five-phase IPMSM defined in 2.3.2 are considered to design the observer structures as illustrated in the Chapter 3.

CHAPTER 3: OBSERVER STRUCTURE OF INTERIOR PERMANENT MAGNET SYNCHRONOUS MACHINE

3.1 Overview

In the last decade, sensorless control has drawn major attention from researchers across academia as well as industries which has helped to develop new sensorless control methods for a wide speed range of the IPMSM drive [13], [15], [16]. Sensorless control also known as self-sensing unit, is primarily used to lessen the cost and size of the system while improving the reliability compared to mechanical sensors. Moreover, sensorless speed control techniques are also preferred in explosive, corrosive or chemically aggressive environments due to unreliable performance of the encoder. This Chapter presents the formulation observer structures based on the mathematical model of the three-phase IPMSM and five-phase IPMSM presented in Chapter 2. Before the discussion of observer structure of IPMSM, the generalized form of observer structure is explained.

3.2 Full-order observer structure

The generalized form of a system model can be expressed using (3.1) and (3.2). Here, $\boldsymbol{x}$ represents vector of state variables, $\boldsymbol{u}$ is the vector of control inputs, $\boldsymbol{y}$ is the output of the system. $\boldsymbol{A, B, C}$ contains the constant parameters of the system model [135].

$$\dot{\boldsymbol{x}} = \boldsymbol{Ax} + \boldsymbol{Bu} \tag{3.1}$$

$$\boldsymbol{y} = \boldsymbol{Cx} \tag{3.2}$$

The full order observer for (3.1) and (3.2) can be computed using the following differential equation (3.3) and (3.4). Here, observer tuning gains are defined in matrix $\boldsymbol{G}$. Error between the estimated variables and measured variables is represented using the

$$\dot{\hat{\boldsymbol{x}}} = \boldsymbol{A}\hat{\boldsymbol{x}} + \boldsymbol{Bu} + \boldsymbol{G}(\hat{\boldsymbol{y}} - \boldsymbol{y}) \tag{3.3}$$

$$\hat{\boldsymbol{y}} = \boldsymbol{C}\hat{\boldsymbol{x}} \tag{3.4}$$

$$\tilde{\boldsymbol{x}} = \hat{\boldsymbol{x}} - \boldsymbol{x} \tag{3.5}$$

The dynamics of the observer estimation error can be determined using the (3.6) and further simplified as (3.7).

$$\dot{\tilde{\boldsymbol{x}}} = \dot{\hat{\boldsymbol{x}}} - \dot{\boldsymbol{x}} \tag{3.6}$$

$$\dot{\tilde{\boldsymbol{x}}} = (\boldsymbol{A}+\boldsymbol{GC})\tilde{\boldsymbol{x}} \tag{3.7}$$

Assuming that the eigenvalues of the matrix $\mathbf{F} = \boldsymbol{A}+\boldsymbol{GC}$ have the negative values and as $t\rightarrow\infty$ the error in state variable estimation $\tilde{\boldsymbol{X}}(t)\rightarrow 0$ decays to zero and according to Lyapunov stability theorem, the observer structure will be asymptotical stable:

$$\dot{\tilde{\boldsymbol{x}}} = e^{\mathbf{F}t}\tilde{\boldsymbol{x}}(t) \tag{3.8}$$

Based on the generalized theory of observer structure, section 3.3 and section 3.4 covers observer design of three-phase IPMSM and five-phase IPMSM, respectively.

3.3 Speed and position observer structure of three-phase IPMSM

Firstly, observer structure based on adaptive mechanism will be discussed then extended emf (EEMF) based observer structure using non-adaptive estimation law will be discussed. In this thesis, observer structure based on (α-β) reference frame is implemented for adaptive observer structure as well as EEMF-based non-adaptive structure. In the observer structure, the symbol "^" is used to define the estimated state variable and "~" is used to define as the error between estimated and measured state variable.

3.3.1 Rotor flux vector-based adaptive observer structure

Firstly, adaptive observer structure based on the rotor flux vector [122] will be presented, followed by the non-adaptive speed and position observer structure. This considered model is based on (α-β) reference frame connected to the stator and compares the performance with the EEMF non-adaptive observer structure (2.9) - (2.10). The observer model contains L_1, L_3, and L_4 introduced to which are the rotor position functions, making this observer structure non-symmetrical. The observer structure can be designed using the mathematical model of IPMSM (2.9) - (2.12). The symbols such as "^" and "~" are used for estimated and error values.

$$\frac{d\hat{i}_{s\alpha}}{d\tau} = \frac{\hat{\omega}_r}{L_d}\hat{\lambda}_\beta + (-R_s\hat{i}_{s\alpha} + u_{s\alpha})L_1 + (-R_s\hat{i}_{s\beta} + u_{s\beta})L_3 + v_\alpha \tag{3.9}$$

$$\frac{d\hat{i}_{s\beta}}{d\tau} = -\frac{\hat{\omega}_r}{L_d}\hat{\lambda}_\alpha + (-R_s\hat{i}_{s\alpha} + u_{s\alpha})L_3 + (-R_s\hat{i}_{s\beta} + u_{s\beta})L_4 + v_\beta \tag{3.10}$$

$$\frac{d\hat{\theta}_r}{d\tau} = \hat{\omega}_r + v_\theta \tag{3.11}$$

where

$$\hat{\lambda}_\alpha = \frac{L_d}{L_q}\hat{\psi}_{f\alpha} - (1 - \frac{L_d}{L_q})(L_0\hat{i}_{\alpha 2} + L_2\hat{i}_{s\alpha}) \tag{3.12}$$

$$\hat{\lambda}_\beta = \frac{L_d}{L_q}\hat{\psi}_{f\beta} + (1 - \frac{L_d}{L_q})(L_0\hat{i}_{\beta 2} - L_2\hat{i}_{s\beta}) \tag{3.13}$$

It can be seen that in (3.9) - (3.11), stabilizing functions are introduced $v_{\alpha,}$ v_β and v_θ. The final form of stabilizing function can be derived with the help of Lyapunov stability criteria. In the observer model, $u_{s\alpha,\beta}$ is stator voltage vector components which is considered to be the known value. Component of rotor flux can be estimated using (3.12) - (3.13). It is assumed that the function L_1, L_3, L_4, $i_{\alpha 2}$, $i_{\beta 2}$, $\psi_{f\alpha,\beta}$ defined in observer structure from (3.9) to (3.13) are calculated using the estimated value of rotor position and stator current vector components.

$$\begin{aligned}
L_0 &= 0.5(L_d + L_q),\\
L_2 &= 0.5(L_d - L_q),\\
L_1 &= L_d^{-1}\cos^2\hat{\theta}_r + L_q^{-1}\sin^2\hat{\theta}_r,\\
L_3 &= 0.5(L_d^{-1} - L_q^{-1})\sin 2\hat{\theta}_r,\\
L_4 &= L_d^{-1}\sin^2\hat{\theta}_r + L_q^{-1}\cos^2\hat{\theta}_r
\end{aligned} \tag{3.14}$$

$$\begin{aligned}
\hat{i}_{s\alpha 2} &= \hat{i}_{s\alpha}\cos 2\hat{\theta}_r + \hat{i}_{s\beta}\sin 2\hat{\theta}_r,\\
\hat{i}_{s\beta 2} &= -\hat{i}_{s\alpha}\sin 2\hat{\theta}_r + \hat{i}_{s\beta}\cos 2\hat{\theta}_r
\end{aligned} \tag{3.15}$$

$$\begin{aligned}
\hat{\psi}_{f\alpha} &= \psi_f\cos\hat{\theta}_r,\\
\hat{\psi}_{f\beta} &= \psi_f\sin\hat{\theta}_r
\end{aligned} \tag{3.16}$$

The error between estimated and measured parameters can be calculated using (3.17).

$$\begin{aligned}
\tilde{i}_{s\alpha} &= \hat{i}_{s\alpha} - i_{s\alpha},\ \tilde{i}_{s\beta} = \hat{i}_{s\beta} - i_{s\beta},\\
\tilde{\omega}_r &= \hat{\omega}_r - \omega_r,\ \tilde{\theta}_r = \hat{\theta}_r - \theta_r
\end{aligned} \tag{3.17}$$

The stabilizing functions in the observer structure defined in (3.9) - (3.11) will be formed using the Lyapunov stability criteria. As per the Lyapunov stability criteria, a

positively determined candidate function should be defined first. The chosen quadratic Lyapunov function has the following form.

$$V = \frac{1}{2}\left((\tilde{i}_{s\alpha}^2 + \tilde{i}_{s\beta}^2) + \tilde{\theta}_r^2\right) \tag{3.18}$$

The derivative of the defined Lyapunov function should be negatively determined as (3.19)

$$\begin{aligned} \dot{V} = \tilde{i}_{s\alpha} & \begin{pmatrix} \frac{1}{L_d}(\hat{\omega}_r(\hat{\lambda}_\beta - \tilde{\lambda}_\beta) - \tilde{\omega}_r(\hat{\lambda}_\beta - \tilde{\lambda}_\beta) \\ -R_s(\tilde{i}_{s\alpha}L_1 + \tilde{i}_{s\beta}L_3) + v_\alpha \end{pmatrix} + \\ \tilde{i}_{s\beta} & \begin{pmatrix} -\frac{1}{L_d}(\hat{\omega}_r(\hat{\lambda}_\alpha - \tilde{\lambda}_\alpha) - \tilde{\omega}_r(\hat{\lambda}_\alpha - \tilde{\lambda}_\alpha) \\ -R_s(\tilde{i}_{s\alpha}L_3 + \tilde{i}_{s\beta}L_4) + v_\beta \end{pmatrix} + \\ \tilde{\theta}_r & (\tilde{\omega}_r + v_\theta) \ \leq \ 0 \end{aligned} \tag{3.19}$$

The given observer structure is asymptotically stable if obtained stabilizing functions have the following form and c_α, c_λ, $c_\theta > 0$ are introduced to the stabilizing functions in (3.20), (3.21), and (3.22).

$$v_\alpha = -c_a R_s L_1 \tilde{i}_{s\alpha} + c_\lambda \frac{1}{L_d}\hat{\omega}_r \hat{\lambda}_\beta \tilde{i}_{s\alpha} \tag{3.20}$$

$$v_\beta = -c_a R_s L_4 \tilde{i}_{s\beta} - c_\lambda \frac{1}{L_d}\hat{\omega}_r \hat{\lambda}_\alpha \tilde{i}_{s\beta} \tag{3.21}$$

$$v_\theta = -c_\theta \tilde{\theta}_r \tag{3.22}$$

To estimate speed using adaptive mechanism, the positively defined Lyapunov function can be extended as (3.23), based on the derivative of the Lyapunov function given in (3.24), speed can be estimated using (3.25).

$$V_1 = \frac{1}{\gamma}\tilde{\omega}_r^2 \tag{3.23}$$

$$\dot{V}_1 = \tilde{\omega}_r \frac{1}{L_d}\left(-\hat{\lambda}_\beta \tilde{i}_{s\alpha} + \hat{\lambda}_\alpha \tilde{i}_{s\beta} + \frac{1}{\gamma}\dot{\tilde{\omega}}_r\right) \ \leq \ 0 \tag{3.24}$$

$$\dot{\hat{\omega}}_r = \gamma \frac{1}{L_d}(\hat{\lambda}_\beta \tilde{i}_{s\alpha} - \hat{\lambda}_\alpha \tilde{i}_{s\beta}), \ \gamma > 0 \tag{3.25}$$

In (3.25), position error is needed to implement the stabilizing function v_θ. In sensorless control operation, the implementation of speed and position error has certain limitations as these parameters are not measured. Hence, position error $\tilde{\theta}_r$ can be approximated using the defined the error between the rotor flux vectors $\tilde{\theta}_\lambda$.

$$v_\theta = -c_\theta \tilde{\theta}_\lambda, \tag{3.26}$$

Vectors rotate at synchronous speed of the flux vector of the permanent magnets, which is equivalent to the rotor angular speed. The position of the rotor is the same as the position of the flux vector of permanent magnets. Hence, the position error between the rotor flux vectors can be estimated firstly from (3.12) - (3.13) and secondly from (2.13) - (2.14). Vector $\lambda_{\alpha,\beta}$ (2.13) and (2.14) can be calculated using in which it can be assumed that $\theta_r \approx \hat{\theta}_r$ and the measured currents are used for calculation. $\tilde{\theta}_\lambda$ can be seen in Fig. 3.1. The value $\tilde{\theta}_\lambda$ is close to 0, and after amplifying, the value can be $\tilde{\theta}_r \approx \tilde{\theta}_\lambda$. Value $\tilde{\theta}_\lambda$ can be projected by

$$\tilde{\theta}_\lambda = \tan^{-1}(\varphi), \tag{3.27}$$

$$\varphi = \frac{(\lambda_\alpha \hat{\lambda}_\beta - \lambda_\beta \hat{\lambda}_\alpha)}{(\lambda_\alpha \hat{\lambda}_\alpha + \hat{\lambda}_\beta \lambda_\beta)} \tag{3.28}$$

$$\tilde{\theta}_\lambda = \begin{Bmatrix} \tilde{\theta}_\lambda - \pi/2, & \varphi \geq 0 \\ \tilde{\theta}_\lambda + \pi/2, & \varphi < 0 \end{Bmatrix} \tag{3.29}$$

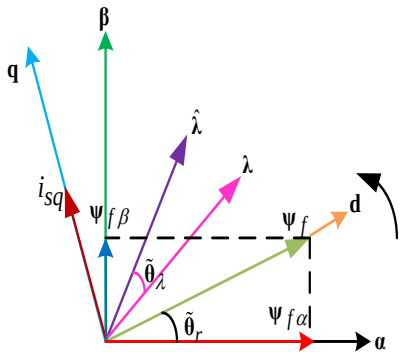

Fig. 3.1. The space vector representation of IPMSM in the α-β plane

To improve rotor speed estimation during the zero-speed crossing, stabilization function based on dot product of rotor flux vector components and stator current vector components is proposed and rotor speed can be estimated using the added new stabilizing function given in (3.30).

$$\dot{\hat{\omega}}_r = \gamma \frac{1}{L_d}(\hat{\lambda}_\beta \tilde{i}_{s\alpha} - \hat{\lambda}_\alpha \tilde{i}_{s\beta} - k_c s_\omega) \tag{3.30}$$

$$s_\omega = (\hat{\lambda}_\alpha \tilde{i}_{s\alpha} + \hat{\lambda}_\beta \tilde{i}_{s\beta}) \tag{3.31}$$

3.3.2 Rotor flux vector-based non-adaptive observer structure

In this section, the observer structure is presented which is based on non-adaptive speed estimation. In this structure observer structure, EMF components are introduced in (3.34), and (3.35). Based on the added EMF the observer differential equations are extended to (3.32) - (3.37). It is important to mention about the observability of system before proposing an observer structure. The observability rank is 4 and determinant of the observability matrix is nonsingular which satisfy the criteria of observability. Hence, the system is observable [136]. The form of the observer structure is given below.

$$\frac{\mathrm{d}\hat{i}_{s\alpha}}{\mathrm{d}\tau} = \frac{1}{L_q}\hat{e}_\beta + \hat{\omega}_r\hat{\lambda}_\beta + (-R_s\hat{i}_{s\alpha} + u_{s\alpha})L_1 + (-R_s\hat{i}_{s\beta} + u_{s\beta})L_3 + v_\alpha, \tag{3.32}$$

$$\frac{\mathrm{d}\hat{i}_{s\beta}}{\mathrm{d}\tau} = -\frac{1}{L_q}\hat{e}_\alpha + \hat{\omega}_r\hat{\lambda}_\alpha + (-R_s\hat{i}_{s\alpha} + u_{s\alpha})L_3 + (-R_s\hat{i}_{s\beta} + u_{s\beta})L_4 + v_\beta, \tag{3.33}$$

$$\frac{\mathrm{d}\hat{e}_\alpha}{\mathrm{d}\tau} = \frac{\mathrm{d}\hat{\omega}_r}{\mathrm{d}\tau}\psi_{f\alpha} - \hat{\omega}_r\hat{e}_\beta + v_{e\alpha}, \tag{3.34}$$

$$\frac{\mathrm{d}\hat{e}_\beta}{\mathrm{d}\tau} = \frac{\mathrm{d}\hat{\omega}_r}{\mathrm{d}\tau}\psi_{f\beta} + \hat{\omega}_r\hat{e}_\alpha + v_{e\beta}, \tag{3.35}$$

$$\hat{\lambda}_\alpha = (\frac{1}{L_d} - \frac{1}{L_q})(\frac{1}{L_d}L_0\hat{i}_{\alpha 2} + \frac{1}{L_d}L_2\hat{i}_{s\alpha}), \tag{3.36}$$

$$\hat{\lambda}_\beta = (\frac{1}{L_d} - \frac{1}{L_q})(\frac{1}{L_d}L_0\hat{i}_{\beta 2} - \frac{1}{L_d}L_2\hat{i}_{s\beta}), \tag{3.37}$$

Estimation error can be defined as (3.38).

$$\begin{aligned} &\tilde{i}_{s\alpha} = \hat{i}_{s\alpha} - i_{s\alpha},\ \tilde{i}_{s\beta} = \hat{i}_{s\beta} - i_{s\beta}, \\ &\tilde{e}_\alpha = \hat{e}_\alpha - e_\alpha,\ \tilde{e}_\beta = \hat{e}_\beta - e_\beta, \\ &\tilde{\omega}_r = \hat{\omega}_r - \omega_r,\ \tilde{\theta}_r = \hat{\theta}_r - \theta_r \end{aligned} \tag{3.38}$$

The new added input variables in the observer structures are v_α, v_β, $v_{e\alpha}$, and $v_{e\beta}$ are considered stabilizing functions. With the help of this stabilizing function, the observer structure can converge to the real value of the machine under the assumption that all

machine parameters are known and constant in nature. In (3.34) and (3.35), the derivative of rotor speed can be approximated, considering the $d\hat{\omega}_r/d\tau \approx \Delta\hat{\omega}_r/\Delta\tau$,. Moreover, this term does not impact accuracy while estimating rotor speed and position. As used in earlier observer structures, the Lyapunov theorem will significantly help define the stabilizing function.

As per the Lyapunov function, a first positively determined function is defined, and the function's derivative should be negatively determined $\dot{V} \leq 0$, which can be seen in (3.39)and (3.40), respectively.

$$V = \frac{1}{2}(\tilde{i}_{s\alpha}^2 + \tilde{i}_{s\beta}^2), \tag{3.39}$$

$$\begin{aligned} \dot{V} = \tilde{i}_{s\alpha} & \left(\begin{array}{l} \frac{1}{L_q}\tilde{e}_\beta + (\hat{\omega}_r(\hat{\lambda}_\beta - \tilde{\lambda}_\beta) - \tilde{\omega}_r(\hat{\lambda}_\beta - \tilde{\lambda}_\beta) + \\ (-R_s\tilde{i}_{s\alpha} + u_{s\alpha})L_1 + (-R_s\tilde{i}_{s\beta} + u_{s\beta})L_3 + v_\alpha \end{array} \right) \\ + \quad \tilde{i}_{s_\beta} & \left(\begin{array}{l} -\frac{1}{L_q}\tilde{e}_\alpha + (\hat{\omega}_r(\hat{\lambda}_\alpha - \tilde{\lambda}_\alpha) - \tilde{\omega}_r(\hat{\lambda}_\alpha - \tilde{\lambda}_\alpha) + \\ (-R_s\tilde{i}_{s\alpha} + u_{s\alpha})L_3 + (-R_s\tilde{i}_{s\beta} + u_{s\beta})L_4 + v_\beta, \end{array} \right) \leq 0 \end{aligned} \tag{3.40}$$

The proposed observer structure is asymptotic and stable if the stabilizing function has the following form: Gains c_α, $c_{e\alpha}$, and $c_{e\beta}$ are > 0.

$$v_\alpha = -c_\alpha R_s L_1 \tilde{i}_{s\alpha} \tag{3.41}$$

$$v_\beta = -c_\alpha R_s L_4 \tilde{i}_{s\beta} \tag{3.42}$$

$$v_{e\alpha} = c_{e\alpha}\frac{1}{L_q}\tilde{i}_{s\beta}, \tag{3.43}$$

$$v_{e\beta} = -c_{e\beta}\frac{1}{L_q}\tilde{i}_{s\alpha}, \tag{3.44}$$

The estimated angular speed and position value can be determined from the dependence of EEMF and permanent magnet flux components [137]. It is worth mentioning that $\hat{\psi}_{f\alpha}^2 + \hat{\psi}_{f\beta}^2 \neq 0$ flux components tend to have real values in finite time, and estimated speed converges exponentially to their real value.

$$\hat{\omega}_r = \frac{\hat{e}_\alpha\hat{\psi}_{f\alpha} + \hat{e}_\beta\hat{\psi}_{f\beta}}{\hat{\psi}_{f\alpha}^2 + \hat{\psi}_{f\beta}^2} \tag{3.45}$$

$$\hat{\theta}_r = a\tan(\hat{e}_\beta, \hat{e}_\alpha) \tag{3.46}$$

3.3.3 Active flux-based adaptive observer structure

Based on the active flux-based mathematical model defined in (2.30) - (2.33), the observer structure can be prepared in the following the form (3.47) - (3.49).

$$\frac{d\hat{i}_{s\alpha}}{d\tau} = -\frac{1}{L_q} R_s \hat{i}_{s\alpha} + \frac{1}{L_q} \hat{\omega}_r \hat{\psi}_{f\beta} + \frac{1}{L_q} u_{s\alpha} + v_a \tag{3.47}$$

$$\frac{d\hat{i}_{s\beta}}{d\tau} = -\frac{1}{L_q} R_s \hat{i}_{s\beta} - \frac{1}{L_q} \hat{\omega}_r \hat{\psi}_{f\alpha} + \frac{1}{L_q} u_{s\beta} + v_\beta \tag{3.48}$$

$$\frac{d\hat{\theta}_r}{d\tau} = \hat{\omega}_r + v_\theta \tag{3.49}$$

$v_{\alpha,\beta}$ and v_θ are the added stabilizing functions in the observer structure. The final form of the stabilizing functions can be computed using the Lyapunov stability theorem. It can be seen in the observer model that $u_{s\alpha,\beta}$ the input state voltage vector components. $\hat{i}_{s\alpha,\beta}$, $\hat{\psi}_{s\alpha,\beta}$ and $\hat{\psi}_{f\alpha,\beta}$ are defined as the vector components of estimated currents, estimated components of stator flux and permanent magnet flux in (α-β) reference frame which are calculated using estimated angular position as well as estimated angular speed.

$$\begin{aligned} \hat{\psi}_{f\alpha} &= \psi_f \cos\hat{\theta}_r \\ \hat{\psi}_{s\alpha} &= L_q \hat{i}_{s\alpha} + \hat{\psi}_{f\alpha} \end{aligned} \tag{3.50}$$

$$\begin{aligned} \hat{\psi}_{f\beta} &= \psi_f \sin\hat{\theta}_r \\ \hat{\psi}_{s\beta} &= L_q \hat{i}_{s\beta} + \hat{\psi}_{f\beta} \end{aligned} \tag{3.51}$$

The error between the estimated state variable and measured value can be obtained from the following form.

$$\begin{aligned} &\tilde{i}_{s\alpha} = \hat{i}_{s\alpha} - i_{s\alpha},\ \tilde{i}_{s\beta} = \hat{i}_{s\beta} - i_{s\beta}, \\ &\tilde{\omega}_r = \hat{\omega}_r - \omega_r,\ \tilde{\theta}_r = \hat{\theta}_r - \theta_r \end{aligned} \tag{3.52}$$

By implementing stability analysis using the Lyapunov stability theorem the proposed observer structure can be stabilized. As per the Lyapunov stability criteria, firstly a positively determined candidate function should be defined. The chosen quadratic Lyapunov function has following form.

$$V = \frac{1}{2}\left((\tilde{i}_{s\alpha}^2 + \tilde{i}_{s\beta}^2) + \tilde{\theta}_r^2\right) \tag{3.53}$$

In the next step, derivative of defined Lyapunov function in (3.53) must be negatively determined which means $\dot{V} \leq 0$.

$$\begin{aligned} \dot{V} = \tilde{i}_{sa}\left(-\frac{R}{L_q}\tilde{i}_{s\alpha} + \frac{1}{L_q}(\hat{\omega}_r(\hat{\psi}_{f\beta} - \psi_{f\beta}) - \tilde{\omega}_r(\hat{\psi}_{f\beta} - \psi_{f\beta})) + v_\alpha\right) + \\ \tilde{i}_{s\beta}\left(-\frac{R}{L_q}\tilde{i}_{s\beta} - \frac{1}{L_q}(\hat{\omega}_r(\hat{\psi}_{f\alpha} - \psi_{f\alpha}) - \tilde{\omega}_r(\hat{\psi}_{f\alpha} - \psi_{f\alpha})) + v_\beta\right) + \\ \tilde{\theta}_r(\tilde{\omega}_r + v_\theta) \leq 0 \end{aligned} \tag{3.54}$$

By introducing c_α & $c_\theta > 0$ in the stabilizing functions v_α, v_β and v_θ the proposed observer structure becomes asymptotically stable and the stabilizing functions have the following form:

$$v_\alpha = -c_\alpha \frac{R_s}{L_q}\tilde{i}_{s\alpha} \tag{3.55}$$

$$v_\beta = -c_\alpha \frac{R_s}{L_q}\tilde{i}_{s\beta} \tag{3.56}$$

$$v_\theta = -c_\theta \tilde{\theta}_r \tag{3.57}$$

The positively defined Lyapunov function can be extended in ordered to obtained estimated speed. The extended positively defined Lyapunov function and its derivative are given in (3.58) and (3.59), respectively

$$V_1 = \frac{1}{\gamma}\tilde{\omega}_r^2 \tag{3.58}$$

$$\dot{V}_1 = \tilde{\omega}_r\left(\frac{1}{\gamma}\dot{\tilde{\omega}}_r + (\hat{\psi}_{f\beta}\tilde{i}_{s\alpha} - \hat{\psi}_{f\alpha}\tilde{i}_{s\beta})\right) \tag{3.59}$$

With the help of adaptive mechanism, the value of estimated speed can be calculated from (3.59) and expressed in (3.60) by assuming that $\dot{\tilde{\omega}}_r \approx \dot{\hat{\omega}}_r$.

$$\dot{\hat{\omega}}_r = -\gamma(\hat{\psi}_{f\beta}\tilde{i}_{s\alpha} - \hat{\psi}_{f\alpha}\tilde{i}_{s\beta}),\ \gamma > 0 \tag{3.60}$$

It can be seen that in (3.57) angular position error exists. However, the angular position error cannot be implemented as in sensorless control system angular position

as well as speed are not measured. Hence, instead of $\tilde{\theta}_r$ approximated value of this error $\tilde{\theta}_\psi$ can be used and (3.57) can be rewritten as

$$v_\theta = -c_\theta \tilde{\theta}_\psi \tag{3.61}$$

Hence, the position error between the stator flux vectors can be estimated firstly from (3.50), (3.51) and secondly from (2.34) as follows [122]. In calculation of stator flux components (2.34), measured currents are used and measured position is replaced by estimated position using the assumption that $\theta_r \approx \hat{\theta}_r$.

$$\tilde{\theta}_\psi = \tan^{-1}(\varphi) \tag{3.62}$$

Where

$$\varphi = \frac{\psi_{s\alpha}\hat{\psi}_{s\beta} - \psi_{s\beta}\hat{\psi}_{s\alpha}}{\psi_{s\alpha}\hat{\psi}_{s\alpha} + \psi_{s\beta}\hat{\psi}_{s\beta}}, \text{ and } \psi_{s\alpha}\hat{\psi}_{s\alpha} + \psi_{s\beta}\hat{\psi}_{s\beta} \neq 0 \tag{3.63}$$

From (3.60), the estimated value of rotor speed can be obtained. Stator current deviation and the vector components of permanent magnet flux are used to calculated the estimated speed. It can be seen that it is a cross product of these vectors. Mutual position of these vectors is changing at different working instance of the IPMSM. Scalar product of these vectors is zero if it is assumed that these vectors are perpendicular. In practice, scalar product cannot become zero due to tuning gains of the observer. Moreover, error in estimation of the speed will be dependent on the scalar product of these two vectors. Hence, to increase the robustness of the observer structure, improved estimation law is proposed in this thesis. The improved estimation law is based on the cross and scalar product of the permanent magnet flux and stator current errors. Here, Gain k_c plays an important part when machine passes through zero speed. The improved estimation law is as follow:

$$\dot{\hat{\omega}}_r = \gamma(\hat{\psi}_{f\alpha}\tilde{i}_{s\beta} - \hat{\psi}_{f\beta}\tilde{i}_{s\alpha} + k_c s_\omega),\ \gamma > 0, k_c > 0 \tag{3.64}$$

$$s_\omega = (\hat{\psi}_{f\alpha}\tilde{i}_{s\alpha} + \hat{\psi}_{f\beta}\tilde{i}_{s\beta}) \tag{3.65}$$

3.3.4 Active flux-based non-adaptive observer structure

The EEMF based observer structure for the estimation of speed and position considering the non-adaptive is prepared based on the dynamic model (2.35) - (2.38) and given as

$$\frac{d\hat{i}_{s\alpha}}{d\tau} = -\frac{1}{L_q} R_s \hat{i}_{s\alpha} + \frac{1}{L_q} \hat{e}_\beta + \frac{1}{L_q} u_{s\alpha} + v_a \tag{3.66}$$

$$\frac{d\hat{i}_{s\beta}}{d\tau} = -\frac{1}{L_q} R_s \hat{i}_{s\beta} - \frac{1}{L_q} \hat{e}_\alpha + \frac{1}{L_q} u_{s\beta} + v_\beta \tag{3.67}$$

$$\frac{d\hat{e}_\alpha}{d\tau} = \frac{\mathrm{d}\hat{\omega}_r}{\mathrm{d}\tau} \hat{\psi}_{f\alpha} - \hat{\omega}_r \hat{e}_\beta + v_{e\alpha} \tag{3.68}$$

$$\frac{\mathrm{d}\hat{e}_\beta}{\mathrm{d}\tau} = \frac{\mathrm{d}\hat{\omega}_r}{\mathrm{d}\tau} \hat{\psi}_{f\beta} + \hat{\omega}_r \hat{e}_\alpha + v_{e\beta} \tag{3.69}$$

It can be seen that stabilizing functions v_α, v_β, $v_{e\alpha}$, and $v_{e\beta}$ are introduced to the observer structures. Without stabilizing functions, it is not possible for observer to converge to the real value of the machine, hence, stabilizing functions have significant importance. By considering $\mathrm{d}\hat{\omega}_r / \mathrm{d}\tau \approx \Delta\hat{\omega}_r / \Delta\tau$, the derivative of speed given in (3.68) and (3.69) can be approximated. The final form of the stabilizing function can be achieved using the Lyapunov theorem. Error of estimation and measured value can be defined as (3.70). Positively determined Lyapunov function and its derivative which is negatively determined $\dot{V} \leq 0$ are given (3.71) and (3.72).

$$\begin{aligned} &\tilde{i}_{s\alpha} = \hat{i}_{s\alpha} - i_{s\alpha},\ \tilde{i}_{s\beta} = \hat{i}_{s\beta} - i_{s\beta}, \\ &\tilde{e}_\alpha = \hat{e}_\alpha - e_\alpha,\ \tilde{e}_\beta = \hat{e}_\beta - e_\beta, \\ &\tilde{\omega}_r = \hat{\omega}_r - \omega_r,\ \tilde{\theta}_r = \hat{\theta}_r - \theta_r \end{aligned} \tag{3.70}$$

$$V = \frac{1}{2}(\tilde{i}_{s\alpha}^2 + \tilde{i}_{s\beta}^2), \tag{3.71}$$

$$\dot{V} = \tilde{i}_{sa}\left(-\frac{R}{L_q}\tilde{i}_{s\alpha} + \frac{1}{L_q}\tilde{e}_\beta + v_\alpha\right) + \tilde{i}_{s\beta}\left(-\frac{R}{L_q}\tilde{i}_{s\beta} - \frac{1}{L_q}\tilde{e}_\alpha + v_\beta\right) \tag{3.72}$$

The proposed observer structure is asymptotic stable if v_α, v_β, $v_{e\alpha}$, and $v_{e\beta}$ have the following form.

$$v_\alpha = -c_\alpha \frac{R_s}{L_q} \tilde{i}_{s\alpha} \tag{3.73}$$

$$v_\beta = -c_\alpha \frac{R_s}{L_q} \tilde{i}_{s\beta} \tag{3.74}$$

$$v_{e\alpha} = c_{e\alpha} \frac{1}{L_q} \tilde{i}_{s\beta} \tag{3.75}$$

$$v_{e\beta} = -c_{e\beta} \frac{1}{L_q} \tilde{i}_{s\alpha} \tag{3.76}$$

Where gains c_α, $c_{e\alpha}$ and $c_{e\beta}$ are > 0.

Estimation of angular speed using non-adaptive approach (3.77) can be performed using dependences of EEMF and components of permanent magnet flux [137]. Similarly, angular position can be estimated using the angle observer between the EEMF (3.79).

$$\hat{\omega}_r = \frac{\hat{e}_\alpha \hat{\psi}_{f\alpha} + \hat{e}_\beta \hat{\psi}_{f\beta} - k_f s_\omega}{\hat{\psi}_{f\alpha}^2 + \hat{\psi}_{f\beta}^2}, k_f > 0 \tag{3.77}$$

$$s_\omega = \hat{e}_\alpha \hat{\psi}_{f\beta} - \hat{e}_\beta \hat{\psi}_{f\alpha} \tag{3.78}$$

$$\hat{\theta}_r = a\tan(\hat{e}_\beta, \hat{e}_\alpha) \tag{3.79}$$

3.4 Speed and position observer structure of five-phase IPMSM

In this section, observer structures of five-phase IPMSM is presented in stationary reference frame. Adaptive observer structures are prepared based on the defined mathematical model of the five-phase IPMSM. In the multiphase observer structure, index *i* refers to reference plane of the system. For fundamental plane, *i* = 1 and for second plane *i* = 2. In the observer structure, estimated quantities are denoted using "^" and the error between the estimated and measured variable is defined using "~".

3.4.1 Active flux-based adaptive observer structure of five-phase IPMSM

From the dynamical model of the multiphase IPMSM (2.43) - (2.46), an observer structure can be prepared in a stationary reference frame for each plane. The final form of the observer structure has the following form (3.80) - (3.82).

$$\frac{\mathrm{d}\hat{i}_{s\alpha(i)}}{\mathrm{d}\tau} = -\frac{1}{L_{q(i)}} R_s \hat{i}_{s\alpha(i)} + \frac{1}{L_{q(i)}} \hat{\omega}_{r(i)} \hat{\psi}_{f\beta(i)} + \frac{1}{L_{q(i)}} u_{s\alpha(i)} + v_{\alpha(i)} \tag{3.80}$$

$$\frac{\mathrm{d}\hat{i}_{s\beta(i)}}{\mathrm{d}\tau} = -\frac{1}{L_{q(i)}} R_s \hat{i}_{s\beta(i)} - \frac{1}{L_{q(i)}} \hat{\omega}_{r(i)} \hat{\psi}_{f\alpha(i)} + \frac{1}{L_{q(i)}} u_{s\beta(i)} + v_{\beta(i)} \tag{3.81}$$

$$\frac{\mathrm{d}\hat{\theta}_{(i)}}{\mathrm{d}\tau} = \hat{\omega}_{r(i)} + v_{\theta(i)} \tag{3.82}$$

$$\begin{aligned} \hat{\psi}_{f\alpha(i)} &= \psi_{f(i)} \cos\hat{\theta}_{r(i)} \\ \hat{\psi}_{s\alpha(i)} &= L_{q(i)}\hat{i}_{s\alpha(i)} + \hat{\psi}_{f\alpha(i)} \end{aligned} \tag{3.83}$$

$$\begin{aligned} \hat{\psi}_{f\beta(i)} &= \psi_{f(i)} \sin\hat{\theta}_{r(i)} \\ \hat{\psi}_{s\beta(i)} &= L_{q(i)}\hat{i}_{s\beta(i)} + \hat{\psi}_{f\beta(i)} \end{aligned} \tag{3.84}$$

The estimation error can be computed using (3.85).

$$\begin{aligned} &\tilde{i}_{s\alpha(i)} = \hat{i}_{s\alpha(i)} - i_{s\alpha(i)},\ \tilde{i}_{s\beta(i)} = \hat{i}_{s\beta(i)} - i_{s\beta(i)}, \\ &\tilde{\omega}_{r(i)} = \hat{\omega}_{r(i)} - \omega_{r(i)},\ \tilde{\theta}_{r(i)} = \hat{\theta}_{r(i)} - \theta_{r(i)} \end{aligned} \tag{3.85}$$

The estimated quantities are: stator current components $\hat{i}_{s\alpha(i)}$ and $\hat{i}_{s\beta(i)}$, permanent magnet flux components $\widehat{\psi}_{f\alpha(i)}$ and $\widehat{\psi}_{f\beta(i)}$, stator flux components $\widehat{\psi}_{s\alpha(i)}$ and $\widehat{\psi}_{s\beta(i)}$, angular speed of the rotor $\widehat{\omega}_{r(i)}$, angular position of the rotor $\hat{\theta}_{r(i)}$. To stabilize the observer structure asymptotically, the following stabilizing functions are added $v_{\alpha(i)}$, $v_{\beta(i)}$ and $v_{\theta(i)}$. The form of the stabilizing functions is calculated using the Lyapunov stability criteria.

To apply the Lyapunov theorem, based on the current error and position error, positive function is defined in (3.86). The derivative of defined function should be negative to obtain the asymptotic stability of the system as expressed in (3.87).

$$V_{(i)} = \frac{1}{2}\left((\tilde{i}^2_{s\alpha(i)} + \tilde{i}^2_{s\beta(i)}) + \tilde{\theta}^2_{r(i)}\right) \tag{3.86}$$

$$\begin{aligned} \dot{V}_{(i)} = {} & \tilde{i}_{sa(i)}\left(-\frac{R}{L_{q(i)}}\tilde{i}_{s\alpha(i)} + \frac{1}{L_{q(i)}}(\hat{\omega}_{r(i)}(\hat{\psi}_{f\beta(i)} - \psi_{f\beta(i)}) - \tilde{\omega}_{r(i)}(\hat{\psi}_{f\beta(i)} - \psi_{f\beta(i)})) + v_{\alpha(i)}\right) + \\ & \tilde{i}_{s\beta(i)}\left(-\frac{R}{L_{q(i)}}\tilde{i}_{s\beta(i)} - \frac{1}{L_{q(i)}}(\hat{\omega}_{r(i)}(\hat{\psi}_{f\alpha(i)} - \psi_{f\alpha(i)}) - \tilde{\omega}_{r(i)}(\hat{\psi}_{f\alpha(i)} - \psi_{f\alpha(i)})) + v_{\beta(i)}\right) + \\ & \tilde{\theta}_{r(i)}(\tilde{\omega}_{r(i)} + v_{\theta(i)}) \ \leq \ 0 \end{aligned}$$

(3.87)

The defined observer structure is asymptotically stable for each plane by selecting the following stabilizing functions $v_{\alpha(i)}$, $v_{\beta(i)}$ and $v_{\theta(i)}$. In the defined stabilizing functions, tuning gains $c_{\alpha(i)}$, $c_{\theta(i)} > 0$.

$$v_{\alpha(i)} = -c_{\alpha(i)} \frac{R_s}{L_q(i)} \tilde{i}_{s\alpha(i)} \tag{3.88}$$

$$v_{\beta(i)} = -c_{\alpha(i)} \frac{R_s}{L_q(i)} \tilde{i}_{s\beta(i)} \tag{3.89}$$

$$v_{\theta(i)} = -c_{\theta(i)} \tilde{\theta}_{r(i)} \tag{3.90}$$

The defined positive function (3.86) is extended to estimate the speed using the classical adaptive control law. The extended form and its derivative is defined in (3.91) and (3.92), respectively.

$$V_{1(i)} = \frac{1}{\gamma(i)} \tilde{\omega}_{r(i)}^2 \tag{3.91}$$

$$\dot{V}_{1(i)} = \tilde{\omega}_{r(i)} \left(\frac{1}{\gamma(i)} \dot{\tilde{\omega}}_{r(i)} + (\hat{\psi}_{f\beta(i)} \tilde{i}_{s\alpha(i)} - \hat{\psi}_{f\alpha(i)} \tilde{i}_{s\beta(i)}) \right) \tag{3.92}$$

By using the adaptive control mechanism, angular speed of the machine can be estimated using the (3.93)

$$\dot{\hat{\omega}}_{r_{(i)}} = -\gamma_{(i)} (\hat{\psi}_{f\beta_{(i)}} \tilde{i}_{s\alpha_{(i)}} - \hat{\psi}_{f\alpha_{(i)}} \tilde{i}_{s\beta_{(i)}}), \ \gamma_{(i)} > 0 \tag{3.93}$$

Similar to 3-phase observer structure, position error exist in the defined stabilizing functions in (3.90). The position error $\tilde{\theta}_{r(i)}$ can be approximated using the error $\tilde{\theta}_{\psi(i)}$ and stabilizing functions can be updated as (3.94)

$$v_{\theta(i)} = -c_{\theta(i)} \tilde{\theta}_{\psi(i)} \tag{3.94}$$

To apply updated stabilizing function (3.94), error between stator flux components required to be calculated. Stator flux components $\hat{\psi}_{s\alpha(i)}$ and $\hat{\psi}_{s\beta(i)}$ defined in (3.83) - (3.84) are calculated using the estimated position and estimated currents. In the next step, based on assumption that $\theta_{r(i)} \approx \hat{\theta}_{r(i)}$, measured stator flux components defined in (2.47) - (2.48) are calculated using the estimated position $\hat{\theta}_{r(i)}$, and measured currents components $i_{s\alpha(i)}$, $i_{s\beta(i)}$.

$$\tilde{\theta}_{\psi(i)} = \tan^{-1}(\varphi_{(i)}) \tag{3.95}$$

Where

$$\varphi_{(i)} = \frac{\psi_{s\alpha(i)}\hat{\psi}_{s\beta(i)} - \psi_{s\beta(i)}\hat{\psi}_{s\alpha(i)}}{\psi_{s\alpha(i)}\hat{\psi}_{s\alpha(i)} + \psi_{s\beta(i)}\hat{\psi}_{s\beta(i)}}, \text{ and } \psi_{s\alpha(i)}\hat{\psi}_{s\alpha(i)} + \psi_{s\beta(i)}\hat{\psi}_{s\beta(i)} \neq 0 \quad (3.96)$$

Similarly, speed estimation law is also improved by adding the stabilizing function $s_{\omega(i)}$, the stabilizing function is prepared using vector dot product between permanent magnet flux components and stator current components as defined in (3.98). The updated speed adaptive law improved the estimation during the zero crossing. The tuning gains $k_{c(i)}$ & $\gamma_{(i)}$ must be > 0.

$$\dot{\hat{\omega}}_{r(i)} = \gamma_{(i)}(\hat{\psi}_{f\alpha(i)}\tilde{i}_{s\beta(i)} - \hat{\psi}_{f\beta(i)}\tilde{i}_{s\alpha(i)} + k_{c(i)}s_{\omega(i)}),\ \gamma_{(i)} > 0, k_{c(i)} > 0 \quad (3.97)$$

$$s_{\omega(i)} = (\hat{\psi}_{f\alpha(i)}\tilde{i}_{s\alpha(i)} + \hat{\psi}_{f\beta(i)}\tilde{i}_{s\beta(i)}) \quad (3.98)$$

3.5 Stability analysis of the observer structures

In this section, stability analysis of speed and position observer structures is presented. In the observer structure added stabilizing functions are selected based on the fact that the Lyapunov condition $\dot{V} \leq 0$ is satisfied. The Lyapunov condition ensures the asymptotic stability of the observer structure when defined constant tuning gains are > 0. The observer structures tuning gains can be identified from the model of the observer errors linearized near an equilibrium point in *d-q* coordinate system as presented in [105], [118], [122]. In the following subsections stability analysis is presented for rotor flux-based observer structure and active flux-based observer structure.

3.5.1 Stability analysis of rotor flux vector-based adaptive observer structure of three-phase IPMSM

The stability analysis of rotor flux vector-based observer (3.9) - (3.11) is discussed in details [105], [118], [122]. The model of the observer errors is considered in rotating reference frame *d-q*. The error vector $\tilde{\mathbf{x}}$ is presented in (3.99). Error vector contains information of current errors: $\tilde{i}_{sd}$, $\tilde{i}_{sq}$, speed error $\tilde{\omega}_r$, position error $\tilde{\theta}_r$.

$$\tilde{\mathbf{X}} = \begin{bmatrix} \tilde{i}_{sd} & \tilde{i}_{sq} & \tilde{\omega}_r & \tilde{\theta}_r \end{bmatrix}^T \quad (3.99)$$

The matrix **A** of the observer systems cab be prepared as follows,

$$\mathbf{A} = \begin{bmatrix} -a_1(1+c_\alpha) & a_2\omega_r^*(1+c_\lambda) & a_2 i_{sq}^* & 0 \\ -a_3\omega_r^*(1+c_\lambda) & -a_4(1+c_\alpha) & -a_3 i_{sd}^* & 0 \\ -\gamma(a_2 i_{sq}^* - k_c\psi_{sd}^*) & \gamma(a_3 i_{sd}^* + k_c\psi_{sq}^*) & 0 & 0 \\ 0 & 0 & 1 & -c_\theta \end{bmatrix} \tag{3.100}$$

$$a_1 = \frac{R_s}{L_d},\ a_2 = \frac{L_q}{L_d},\ a_3 = \frac{L_d}{L_q},\ a_4 = \frac{R_s}{L_q} \tag{3.101}$$

The value of i_{sq}^* can be computed using (3.102), and the value of i_{sd}^*, and ω_r^* are chosen based selected equilibrium points. The stability analysis is performed using the defined tuning gains and chosen working points:

$$i_{sq}^* = \frac{T_L}{(\psi_f + (L_d - L_q)i_{sd}^*)} \tag{3.102}$$

In Fig. 3.2 (a), c_α = 1.0 p.u. to 10.0 p.u. and c_θ = 0.0 p.u., for ω_r = 1.0 p.u., γ = 0.2 p.u., k_c = 0.05 p.u., c_λ = 0.05 p.u., T_L = 1.0 p.u.

In Fig. 3.2 (b), c_θ = 0.05 p.u. to 2.0 p.u., for ω_r = 1.0 p.u., c_α = 3 p.u., γ = 0.2 p.u., k_c = 0.05 p.u., c_λ = 0.05 p.u., T_L = 1.0 p.u.

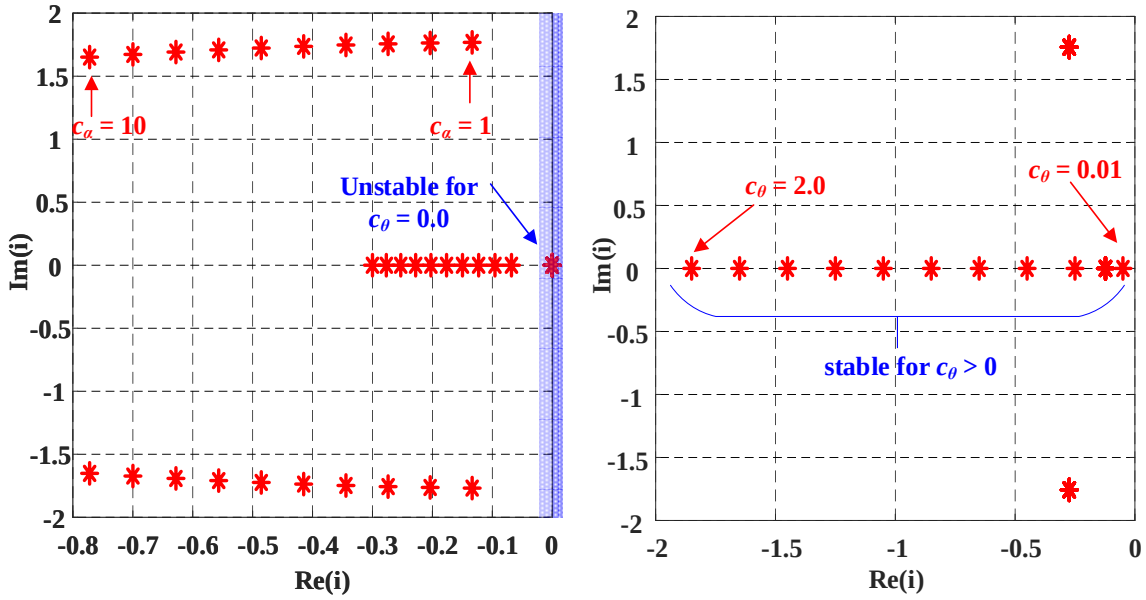

Fig. 3.2 The spectrum of matrix **A** of the linearized observer system (a) for c_α = 1 p.u. to 10.0 p.u and c_θ = 0 (b) for c_θ = 0.0 p.u. to 2.0 p.u.,

In Fig. 3.2 (a), stability analysis plot is presented when c_α was changed from 1.0 p.u. to 10.0 p.u. and c_θ was 0.0 p.u. As can be seen from Fig. 3.2 (a), the position error tuning gain c_θ affects stability of the linearized system, at c_θ = 0, system is unstable and as tuning gain c_α is increasing from 1 p.u. to 10 p.u eigen values of the matrix **A** travels

further in left side of the s-plane. However, due to imaginary poles oscillations can be experienced in the system. In Fig. 3.2 (b), c_θ was varied from 0.01 p.u to 2.0 p.u. and c_α = 3.0 p.u., the linearized system was stable for the chosen operating points when c_θ > 0. At c_θ = 0.01 p.u., eigen value were close to zero but in left half the plane, when c_θ increases from 0.01, eigen values drifted further left and system stability margin increases.

In Fig. 3.3 (a), ω_r = -1.0 p.u. to 1.0 p.u. for c_α = 3.0 p.u., c_θ = 0.07 p.u., γ = 0.2 p.u., k_c = 0.05 p.u., c_λ = 0.05 p.u., T_L = 1.0 p.u.

In Fig. 3.3 (b), k_c = 0.01 p.u. to 2.0 p.u., for ω_r = 1.0 p.u., c_α = 3 p.u., γ = 0.2 p.u., c_θ = 0.07 p.u., c_λ = 0.05, T_L = 1.0 p.u.

In Fig. 3.3 (a), with the selected operating points and tuning gains angular speed was changed from -1.0 p.u. to 1.0 p.u. Eigen values of the system matrix **A** lies in the left half of plane and system is stable. In Fig. 3.3 (b), tuning k_c was changed from 0.01 p.u. to 2.0 p.u. The linearized system remains stable throughout the change in value of k_c.

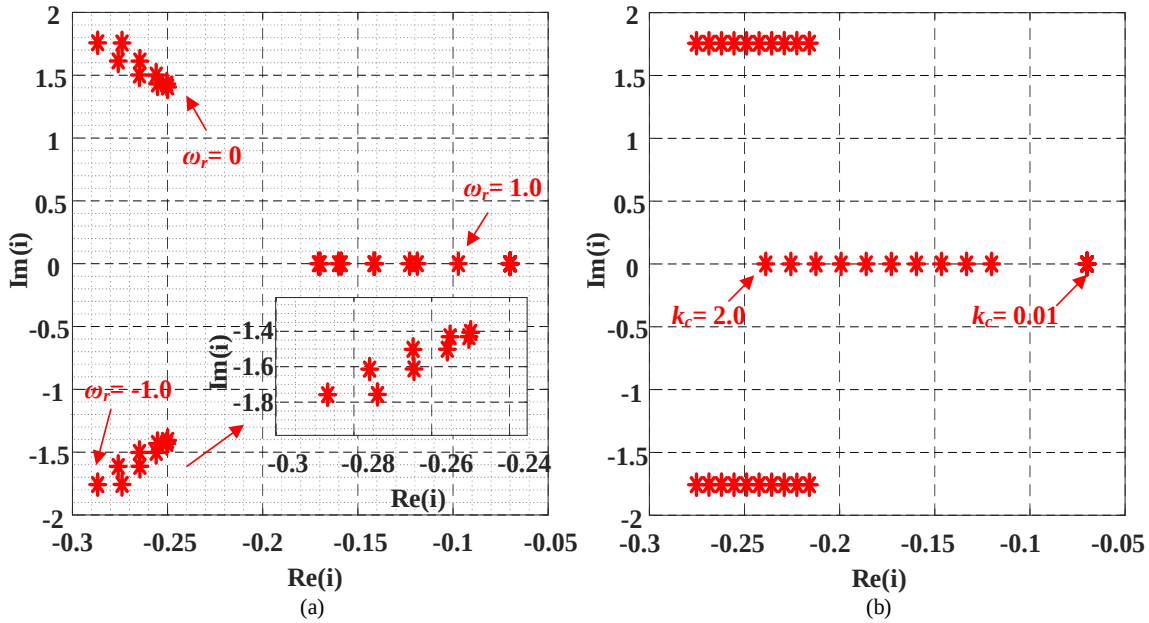

Fig. 3.3 The spectrum of matrix **A** of the linearized observer system (a) for ω_r = -1.0 p.u. to 1.0 p.u. (b) for k_c = 0.01 p.u. to 2.0 p.u.

In Fig. 3.4 (a), c_λ = 0.01 p.u. to 2.0 p.u., for ω_r = 1.0 p.u., c_α = 3 p.u., γ = 0.2 p.u., c_θ = 0.07 p.u., k_c = 0.05, T_L = 1.0 p.u.

In Fig. 3.4 (b), γ = 0.01. to 2.0 p.u. for c_α = 3.0 p.u., c_θ = 0.07 p.u., ω_r = 1.0 p.u., k_c = 0.05 p.u., c_λ = 0.05 p.u., T_L = 1.0 p.u.

In Fig. 3.4 (a), c_λ was altered from 0.01 p.u. to 2.0 p.u., and in Fig. 3.4 (b), γ was changed from 0.01 p.u. to 2.0 p.u. In both cases, the linearized observer system, was stable. When c_λ and γ = 0.01 p.u., the eigen value of the matrix **A** were close to zero and as the value of both tuning gains increased eigen value travelled further in left half of the plane.

For the defined operating points and selected tuning gains, linearized observer structure is stable. For c_θ = 0.0 p.u, observer structure is unstable which shows the significant of the proposed stabilizing functions (3.26), in order to increase the stability range $c_\alpha > 1$ and $k_c > 0$.

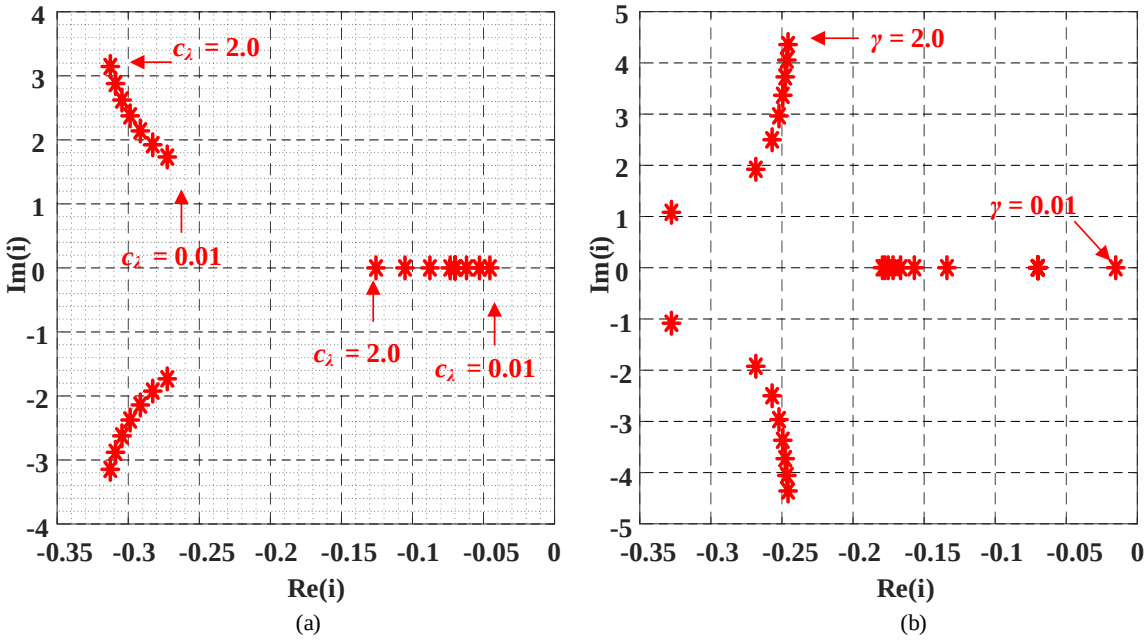

Fig. 3.4 The spectrum of matrix **A** of the linearized observer system (a) for c_λ = 0.0 p.u. to 2.0 p.u., (b) for γ = 0.01 p.u. to 2.0 p.u.

3.5.2 Stability analysis of rotor flux vector-based non-adaptive observer structure of three-phase IPMSM

The stability analysis of non-adaptive rotor flux vector-based observer structure (3.32) - (3.35) is depicted here. In (3.103), error vector $\tilde{\mathbf{x}}$ consisting current errors $\tilde{i}_{sd}$, $\tilde{i}_{sq}$ and EMF errors $\tilde{e}_d$, $\tilde{e}_q$ in rotating coordinates are presented. The system matrix **A** is presented in (3.104). The value of i_{sd}^*, and ω_r^* are selected based on chosen working points and i_{sq}^* can be obtained using (3.106).

$$\tilde{\mathbf{X}} = \begin{bmatrix} \tilde{i}_{sd} & \tilde{i}_{sq} & \tilde{e}_d & \tilde{e}_q \end{bmatrix}^T \tag{3.103}$$

$$\mathbf{A} = \begin{bmatrix} -a_1(1+c_\alpha) & 0 & 0 & a_2 \\ 0 & -a_3(1+c_\alpha) & -a_4 & 0 \\ -R_s\omega_r^* & c_{e\alpha}a_4 & 0 & \omega_r^{2*} \\ -c_{e\beta}a_3 & -R_s\omega_r^* & -\omega_r^{2*} & 0 \end{bmatrix} \tag{3.104}$$

$$a_1 = \frac{R_s}{L_d},\ a_2 = \frac{1}{L_d},\ a_3 = \frac{R_s}{L_q},\ a_4 = \frac{1}{L_q} \tag{3.105}$$

$$i_{sq}^* = \frac{T_L}{(\psi_f + (L_d - L_q)i_{sd}^*)} \tag{3.106}$$

The following value of tuning gains and working points are selected to conduct the stability analysis.

In Fig. 3.5 (a), c_α = 1.0 p.u. to 10.0 p.u. for ω_r = 1.0 p.u., $c_{e\alpha}$ = 0.7 p.u., $c_{e\beta}$ = 0.7 p.u., T_L = 1.0 p.u.

In Fig. 3.5 (b), $c_{e\alpha}$ = 0.1 p.u. to 1.0 p.u. for ω_r = 1.0 p.u., c_α = 3. p.u., $c_{e\beta}$ = 0.7 p.u., T_L = 1.0 p.u.

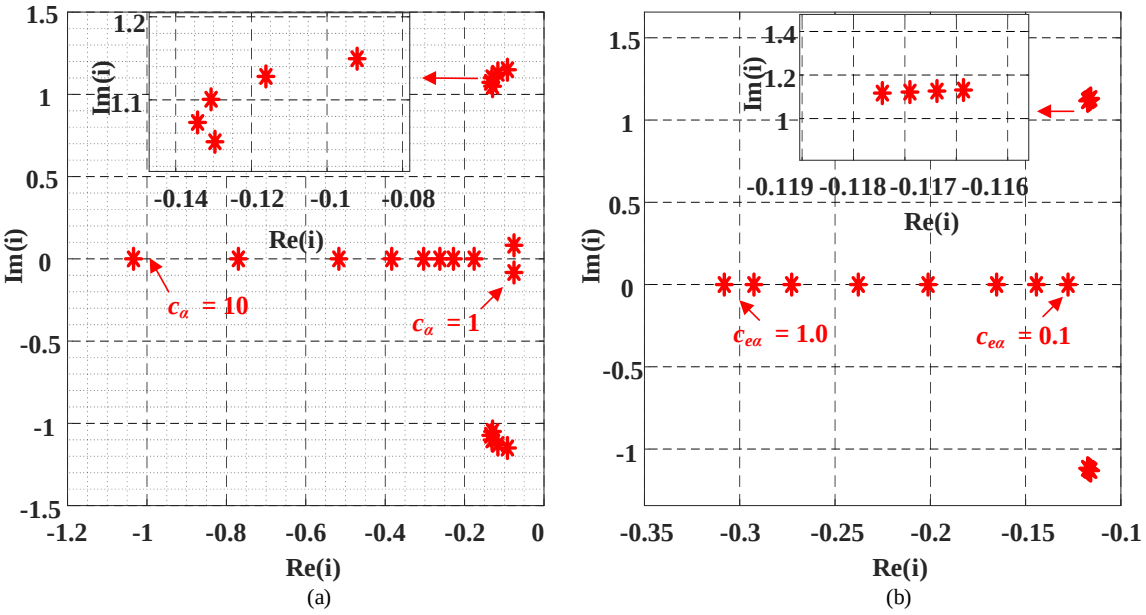

Fig. 3.5 The spectrum of matrix **A** of the linearized observer system (a) for c_α = 1 p.u. to 10.0 p.u. (b) for $c_{e\alpha}$ = 0.1 p.u. to 1.0 p.u.

In Fig. 3.5 (a), tuning gain c_α was varied from 1.0 p.u to 10.0 p.u. For lower value of c_α, linearized system was stable but eigen values of matrix A were close to zero

value, as c_α was increased eigenvalues drifted further in left half. In Fig. 3.5 (b), $c_{e\alpha}$ was changed from 0.1 p.u. to 1.0 p.u. As seen from the Fig. 3.5 (b), $c_{e\alpha}$ has effect on the position of the eigen values. For $c_{e\alpha}$ = 0.1 p.u., poles are closer to zero and $c_{e\alpha}$ = 1.0 p.u. poles are moving away in the left side of complex plain.

In Fig. 3.6 (a), $c_{e\beta}$ = 0.1 p.u. to 1.0 p.u. for ω_r = 1.0 p.u., c_α = 3.0 p.u., $c_{e\alpha}$ = 0.7 p.u., T_L = 1.0 p.u.

In Fig. 3.6 (b), ω_r = -1.0 p.u. to 1.0 p.u., c_α = 3.5 p.u., $c_{e\alpha}$ = 0.9 p.u., $c_{e\beta}$ = 0.9 p.u., T_L = 1.0 p.u.

The spectrum of matrix **A** of the linearized observer system is presented when $c_{e\beta}$ is changing from 0.1 p.u. to 1.0 p.u. in Fig. 3.6 (a) and angular speed ω_r is changing from -1.0 p.u. to 1.0 p.u. in Fig. 3.6 (b). In both cases, eigen values of linearized system were in left half and system was stable.

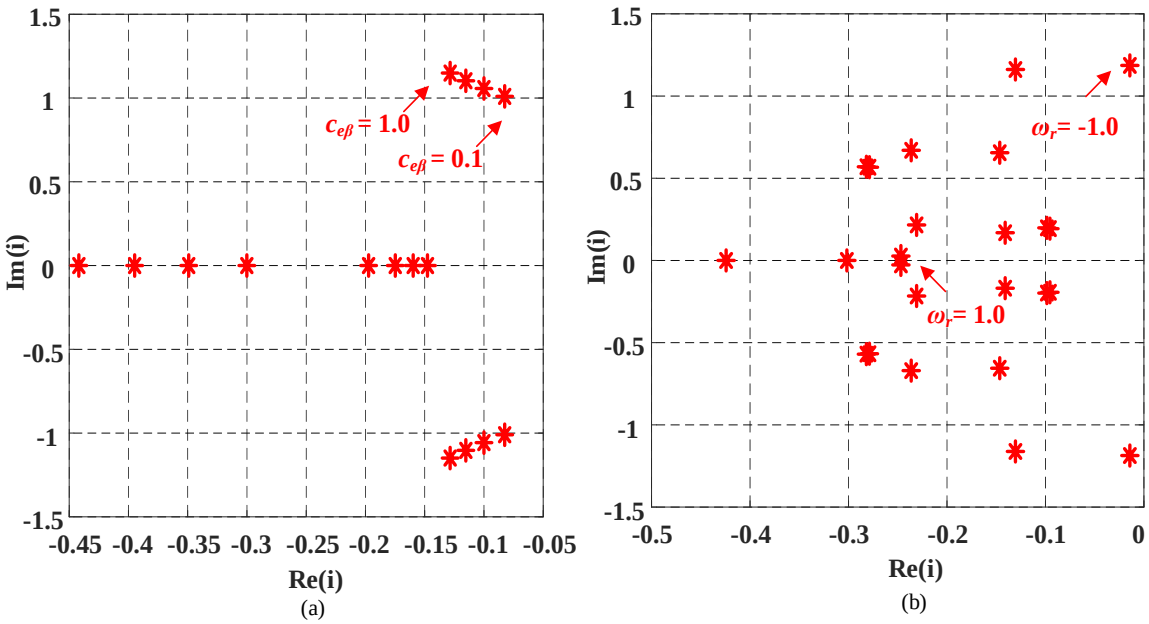

Fig. 3.6 The spectrum of matrix **A** of the linearized observer system (a) for $c_{e\beta}$ = 0.1 p.u. to 1.0 p.u. (b) for ω_r = -1.0 p.u. to 1.0 p.u.

3.5.3 Stability analysis of active flux-based adaptive observer structure of three-phase IPMSM

In the defined observer structure (3.47) - (3.49) and (3.64), the correction terms v_α, v_β and v_θ with constant tuning gains c_α, c_θ, γ, and k_c are added. The tuning gains can be identified by linearizing the observer errors model near an equilibrium point in (d-q) reference frame.

The observer error model is presented in rotating coordinates system as below (3.107)- (3.110).

$$\frac{d\tilde{i}_{sd}}{d\tau} = \left(-\frac{R_s}{L_d} - c_a \frac{R_s}{L_d} \right) \tilde{i}_{sd} + \frac{1}{L_d} (\hat{\omega}_r \hat{\psi}_{sq} - \omega_r \psi_{sq}) \tag{3.107}$$

$$\frac{d\tilde{i}_{sq}}{d\tau} = \left(-\frac{R_s}{L_q} - c_a \frac{R_s}{L_q} \right) \tilde{i}_{sq} - \frac{1}{L_q} (\hat{\omega}_r \hat{\psi}_{sd} - \omega_r \psi_{sd}) \tag{3.108}$$

$$\frac{d\tilde{\omega}_r}{d\tau} = \gamma \left(\frac{1}{L_q} \hat{\psi}_{sd} \tilde{i}_{sq} - \frac{1}{L_d} \hat{\psi}_{sq} \tilde{i}_{sd} + k_c (\hat{\psi}_{sd} \tilde{i}_{sd} + \hat{\psi}_{sq} \tilde{i}_{sq}) \right) \tag{3.109}$$

$$\frac{d\tilde{\theta}_r}{d\tau} = \tilde{\omega}_r + c_\theta \tilde{\theta}_r \tag{3.110}$$

The vector of deviations $\tilde{\mathbf{x}}$ defined in (3.111) and the matrix **A** is defined as (3.112)

$$\tilde{\mathbf{X}} = \begin{bmatrix} \tilde{i}_{sd} & \tilde{i}_{sq} & \tilde{\omega}_r & \tilde{\theta}_r \end{bmatrix}^T \tag{3.111}$$

$$\mathbf{A} = \begin{bmatrix} -a_1(1+c_\alpha) & a_2 \omega_r^* & a_2 i_{sq}^* & 0 \\ -a_3 \omega_r^* & -a_4(1+c_\alpha) & -a_3 i_{sd}^* & 0 \\ -\gamma(a_2 i_{sq}^* - k_c \psi_{sd}^*) & \gamma(a_3 i_{sd}^* + k_c \psi_{sq}^*) & 0 & 0 \\ 0 & 0 & 1 & -c_\theta \end{bmatrix} \tag{3.112}$$

Where i_{sd}^* and i_{sq}^* imply the values determined from working point. The i_{sd}^* = -0.05 p.u. and ω_r^* are chosen from different working points. The working point for i_{sq}^* can be calculated from (3.114).

$$a_1 = \frac{R_s}{L_d},\ a_2 = \frac{L_q}{L_d},\ a_3 = \frac{L_d}{L_q},\ a_4 = \frac{R_s}{L_q} \tag{3.113}$$

$$i_{sq}^* = \frac{T_L}{(\psi_f + (L_d - L_q) i_{sd}^*)} \tag{3.114}$$

The stability analysis of active flux-based adaptive observer is performed as a result the following parameters and the equilibrium point changes.

In Fig. 3.7 (a), c_α = 0.1 p.u. to 5.0 p.u. and c_θ = 0.0 p.u., for ω_r = 1.0 p.u., γ = 0.12 p.u., k_c = 0.05 p.u., T_L = 0.7 p.u.

In Fig. 3.7 (b), c_α = 0.1 p.u. to 5.0 p.u. and c_θ = 0.1 p.u. to 0.5 p.u., for ω_r = 1.0 p.u., γ = 0.12 p.u., k_c = 0.05 p.u., T_L = 0.7 p.u.

In Fig. 3.8 (a), ω_r = -1.0 p.u to 1.0 p.u. for c_α = 3.5 p.u. and c_θ = 0.1 p.u., γ = 0.12 p.u., k_c = 0.05 p .u., T_L = 1.0 p.u.

In Fig. 3.8 (b), k_c = 0.01 p.u. to 2.0 p.u. for ω_r = 1.0 p.u. for c_α = 3.5 p.u., c_θ = 0.1 p.u., γ = 0.12 p.u., T_L = 1.0 p.u.

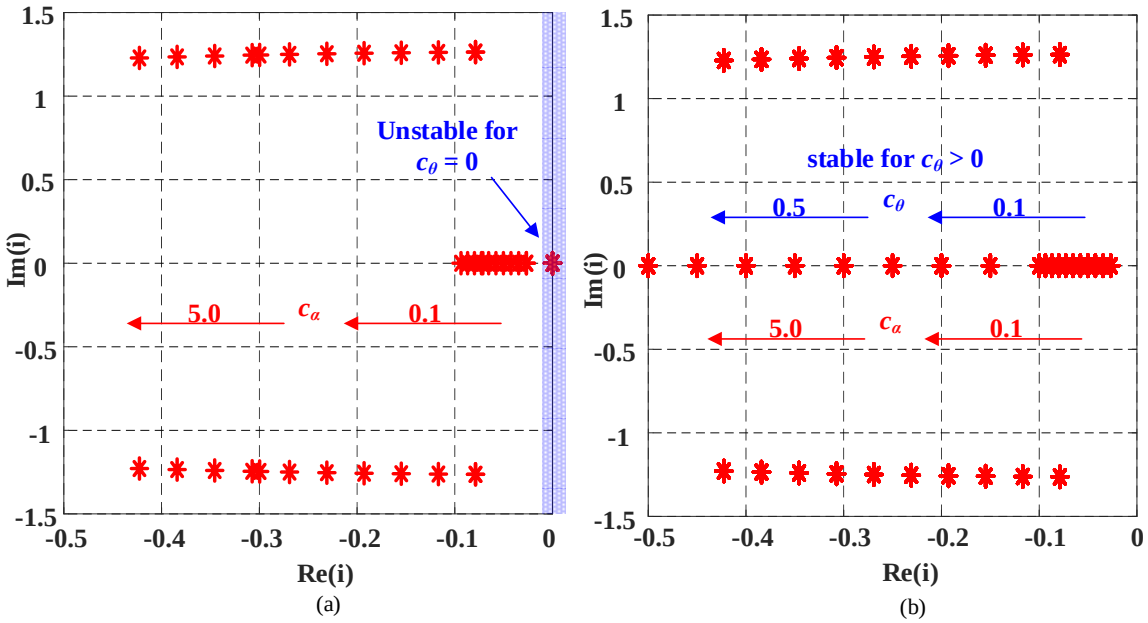

Fig. 3.7 The spectrum of matrix **A** of the linearized observer system (a) for c_α = 0.1 p.u. to 5 p.u. and c_θ = 0.0 p.u. (b) for c_α = 0.1 p.u. to 5 p.u. and c_θ = 0.1 p.u.to 0.5 p.u.

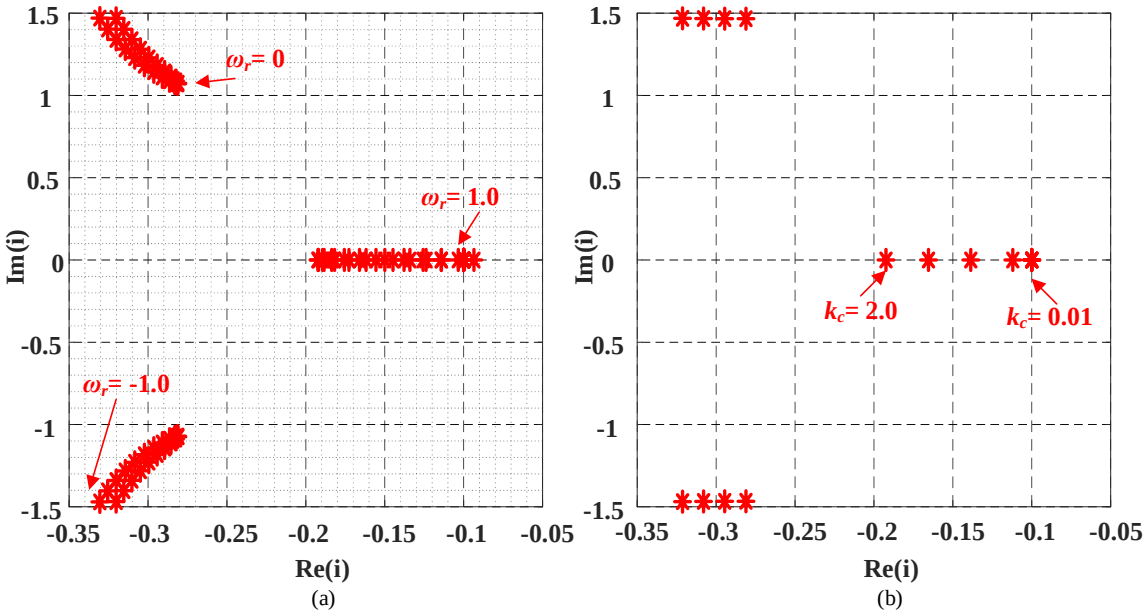

Fig. 3.8 The spectrum of matrix **A** of the linearized observer system (a) for ω_r = -1.0 p.u. to 1.0 p.u. (b) for k_c = 0.01 p.u. to 2.0 p.u.

It is worth noticing that in Fig. 3.7 (a), when c_α is changing from 0.1 p.u. to 5 p.u. and position error equation (3.61) is omitted c_θ = 0.0 p.u. in the linearized system, due

to open integrator form one pole of the system matrix **A** lies at zero which means the linearized system has undamped oscillation and system is unstable. In Fig. 3.7 (b), c_α is varying from 0.1 p.u. to 5 p.u. and $c_\theta > 0.0$ p.u. and varying from 0.1 p.u. to 0.5 p.u. all poles of the system lies in the left half of the plane and system is stable.

In Fig. 3.8, eigen values of matrix **A** is shown for two cases. In Fig. 3.8 (a), rotor speed ω_r is changed from -1.0 p.u. to 1.0 using defined tuning gains. It can be observed that the linearized system is stable for the defined tuning gains. In Fig. 3.8 (b), rotor speed ω_r was set around 1.0 p.u and applied load torque T_L was 1.0 p.u. and gain k_c was changed from 0.01 to 2.0 p.u. It can be observed that eigen values of the system matrix **A** moves further in left half plane and overall system remain stable.

In Fig. 3.9 (a), γ = 0.01 p.u to 2.0 p.u. for c_α = 3.5 p.u. and c_θ = 0.05 p.u., ω_r= 1.0 p.u., k_c = 0.05 p.u., T_L = 1.0 p.u.

In Fig. 3.9 (b), ω_r = 0.1 p.u to 1.0 p.u. and c_θ = 0 to 2.0 p.u., for c_α = 3.5 p.u., γ = 0.12, k_c = 0.05 p.u., T_L = 1.0 p.u.

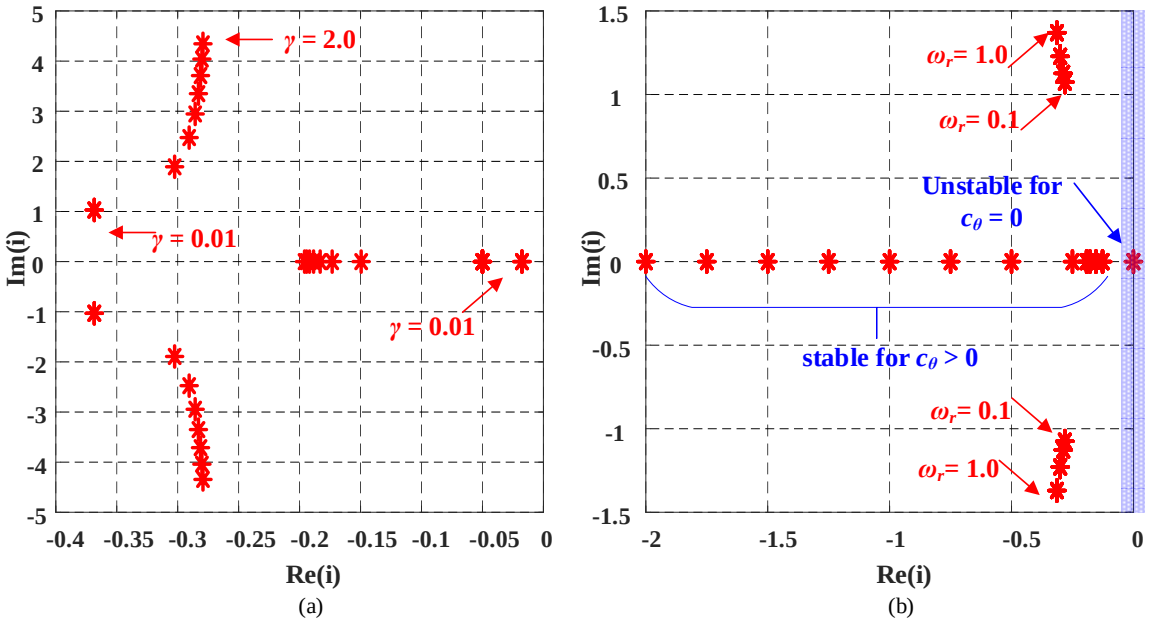

Fig. 3.9 The spectrum of matrix **A** of the linearized observer system (a) for γ = 0.01 p.u. to 2.0 p.u. (b) for ω_r = 0.1 p.u. to 1.0 p.u and c_θ = 0.0 p.u. to 2.0 p.u.,

In Fig. 3.9 (a), the tuning gain γ used in adaptive speed estimation was changed from 0.01 p.u. to 2.0 p.u. For γ = 0.01, one of the poles of the system is closer to zero and as the value of γ increases poles are drifting away from zero and increases overall stability. For γ = 2.0 p.u. systems poles are away from zero but due to imaginary value

of poles oscillation can occurs. In Fig. 3.9 (b), rotor speed ω_r was varied from 0.1 p.u. to 1.0 p.u. and c_θ was also changed from 0 p.u. to 2.0 p.u. If proposed stabilizing functions (3.61) is not added in the system, then the system remains unstable as one pole will remain at zero due to open integrator. When c_θ > 0.0 p.u, system is stable and as rotor speed is increases from 0.1 p.u. poles are moving imaginary planes as shown .

3.5.4 Stability analysis of active flux-based non-adaptive observer structure of three-phase IPMSM

The stability analysis of non-adaptive observer structure (3.66) - (3.69) is presented here. The error vector $\tilde{\mathbf{x}}$ consisting current errors: $\tilde{i}_{sd}$, $\tilde{i}_{sq}$ and EMF errors: $\tilde{e}_d$, $\tilde{e}_q$ is defined in (3.115).

$$\tilde{\mathbf{X}} = \begin{bmatrix} \tilde{i}_{sd} & \tilde{i}_{sq} & \tilde{e}_d & \tilde{e}_q \end{bmatrix}^T \tag{3.115}$$

By using the observer errors for dq coordinates, the matrix **A** of the observer system can be determined as follows:

$$\mathbf{A} = \begin{bmatrix} -a_1(1+c_\alpha) & 0 & 0 & a_2 \\ 0 & -a_3(1+c_\alpha) & -a_4 & 0 \\ -R_s\omega_r^* & c_{e\alpha}a_4 & 0 & \omega_r^{2*} \\ -c_{e\beta}a_3 & -R_s\omega_r^* & -\omega_r^{2*} & 0 \end{bmatrix} \tag{3.116}$$

Where $$a_1 = \frac{R_s}{L_d},\ a_2 = \frac{1}{L_d},\ a_3 = \frac{R_s}{L_q},\ a_4 = \frac{1}{L_q} \tag{3.117}$$

The Value of i_{sd}^*, i_{sq}^* and ω_r^* are obtained using the chosen working points. The i_{sd}^* = -0.05 p.u. and i_{sq}^* can calculated from (3.118)

$$i_{sq}^* = \frac{T_L}{(\psi_f + (L_d - L_q)i_{sd}^*)} \tag{3.118}$$

The following equilibrium points and tuning gains are used to conduct the stability analysis.

In Fig. 3.10 (a), c_α = 0.1 p.u. to 5.0 p.u. for ω_r = 1.0 p.u., $c_{e\alpha}$ = 0.9 p.u., $c_{e\beta}$ = 0.9 p.u., T_L = 1.0 p.u.

In Fig. 3.10 (b), $c_{e\alpha}$ = 0.1 p.u. to 1.0 p.u. for ω_r = 1.0 p.u., c_α = 3.1 p.u., $c_{e\beta}$ = 0.9 p.u., T_L = 1.0 p.u.

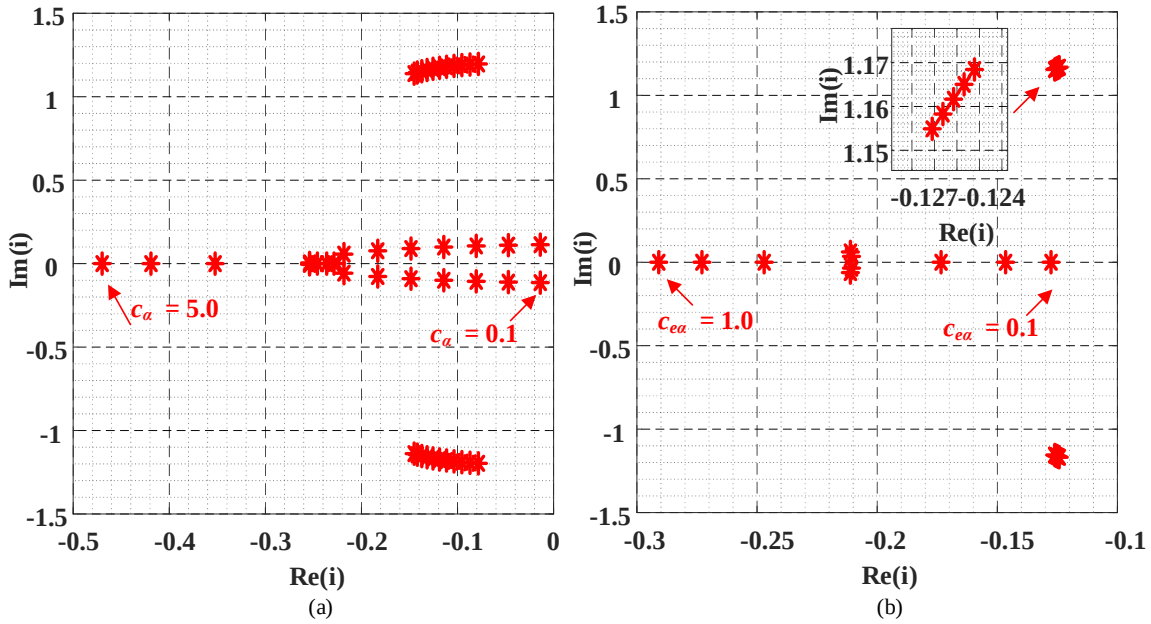

Fig. 3.10 The spectrum of matrix **A** of the linearized observer system (a) for c_α = 0.1 p.u. to 5.0 p.u. (b) for $c_{e\alpha}$ = 0.1 p.u. to 1.0 p.u.

In Fig. 3.11 (a), $c_{e\beta}$ = 0.1 p.u. to 1.0 p.u. for ω_r = 1.0 p.u., c_α = 3.1 p.u., $c_{e\alpha}$ = 0.9 p.u., T_L = 1.0 p.u.

In Fig. 3.11 (b), ω_r = -1.0 p.u. to 1.0 p.u., c_α = 3.1 p.u., $c_{e\alpha}$ = 0.9 p.u., $c_{e\beta}$ = 0.9 p.u., T_L = 1.0 p.u.

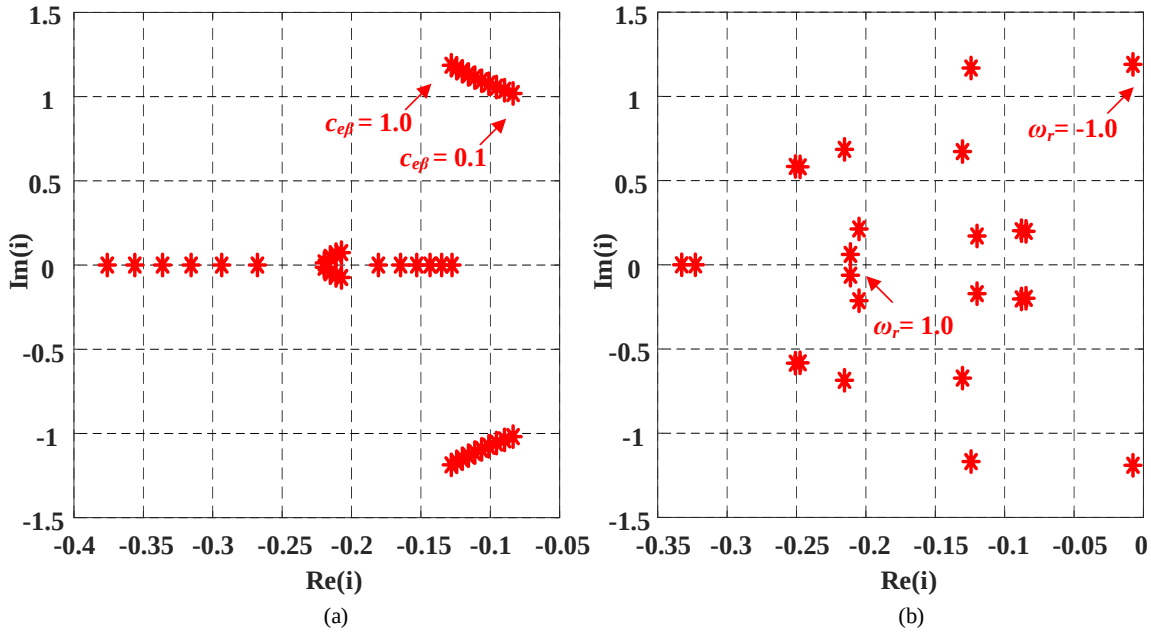

Fig. 3.11 The spectrum of matrix **A** of the linearized observer system (a) for $c_{e\beta}$ = 0.1 p.u. to 1.0 p.u. (b) for ω_r = -1.0 p.u. to 1.0 p.u.

In Fig. 3.10 (a), the tuning gain c_α was changed from 0.1 p.u. to 5.0 p.u. and in Fig. 3.10 (b), the tuning gain $c_{e\alpha}$ was varied from 0.1 p.u. to 1.0 p.u. It can be observed that at c_α = 0.1 p.u. and $c_{e\alpha}$ = 0.1, poles are closer to zero, and as the value of tuning gain increases the poles are drifting away and increases the stability of the linearized system.

In Fig. 3.11 (a), the tuning gain $c_{e\beta}$ is changed from 0.1 p.u. to 1.0 p.u. As the tuning gain value of $c_{e\beta}$ is increasing, poles are drifting away from zero, but due to imaginary poles the effect of oscillation can occur. In Fig. 3.11 (b), rotor speed was changed from -1.0 p.u to 1.0 p.u using the defined tuning gains. It can be noticed that system is stable but when speed is -1.0 p.u., system is closer to zero and stability margin is less.

3.5.5 Stability analysis of active flux-based adaptive observer structure of five-phase IPMSM

The stability analysis of five-phase active flux-based adaptive observer structure (3.80) - (3.82) is presented here. The deviation vector $\tilde{\mathbf{X}}_{(i)}$ and system matrix $\mathbf{A}_{(i)}$ are presented in (3.119) and (3.120), respectively.

$$\tilde{\mathbf{X}}_{(i)} = \begin{bmatrix} \tilde{i}_{sd(i)} & \tilde{i}_{sq(i)} & \tilde{\omega}_{r(i)} & \tilde{\theta}_{r(i)} \end{bmatrix}^T \tag{3.119}$$

$$\mathbf{A}_{(i)} = \begin{bmatrix} -a_{1(i)}(1+c_{\alpha(i)}) & a_{2(i)}\omega^*_{r(i)} & a_{2(i)}i^*_{sq(i)} & 0 \\ -a_{3(i)}\omega^*_{r(i)} & -a_{4(i)}(1+c_{\alpha(i)}) & -a_{3(i)}i^*_{sd(i)} & 0 \\ -\gamma_{(i)}(a_{2(i)}i^*_{sq(i)} - k_{c(i)}\psi^*_{sd(i)}) & \gamma_{(i)}(a_{3(i)}i^*_{sd(i)} + k_{c(i)}\psi^*_{sq(i)}) & 0 & 0 \\ 0 & 0 & 1 & -c_{\theta(i)} \end{bmatrix}$$

(3.120)

Where $$a_1 = \frac{R_s}{L_{d(i)}},\ a_2 = \frac{L_{q(i)}}{L_{d(i)}},\ a_3 = \frac{L_{d(i)}}{L_{q(i)}},\ a_4 = \frac{R_s}{L_{q(i)}} \tag{3.121}$$

The value of $i^*_{sd(i)}, \omega^*_{r(i)}$ are selected based on chosen working points. $i^*_{sq(i)}$ can calculated using (3.122). The selected values of $i^*_{sd(1)}$ = -0.1 p.u. and $i^*_{sd(2)}$ =0.0 p.u.

$$i^*_{sq(i)} = \frac{T_L}{(\psi_{f(i)} + (L_{d(i)} - L_{q(i)})i^*_{sd(i)})} \tag{3.122}$$

In Fig. 3.12 (a), $c_{\alpha(1)}$ = 1.0 p.u. to 10.0 p.u. for $\omega_{r(1)}$ = 1.0 p.u., $\gamma_{(1)}$ = 0.3 p.u., $k_{c(1)}$ = 0.1 p.u., $c_{\theta(1)}$ = 0.1 p.u., T_L = 1.0 p.u.

In Fig. 3.12 (b), $c_{\alpha(2)}$ = 1.0 p.u. to 10.0 p.u. for $\omega_{r(2)}$ = -3.0 p.u., $\gamma_{(2)}$ = 0.3 p.u., $k_{c(2)}$ = 0.1 p.u., $c_{\theta(2)}$ = 0.1 p.u.

In Fig. 3.13 (a), $\omega_{r(1)}$ = -1.0 p.u. to 1.0 p.u. and $c_{\theta(1)}$ = 0.0 p.u., for $c_{\alpha(1)}$ = 3 p.u., $\gamma_{(1)}$ = 0.3 p.u., $k_{c(1)}$ = 0.1 p.u., T_L = 1.0 p.u.

In Fig. 3.13 (b), $\omega_{r(2)}$ = 3.0 p.u. to -3.0 p.u. and $c_{\theta(2)}$ = 0.0 p.u., for $c_{\alpha(2)}$ = 5 p.u., $\gamma_{(2)}$ = 0.3 p.u., $k_{c(2)}$ = 0.1 p.u.

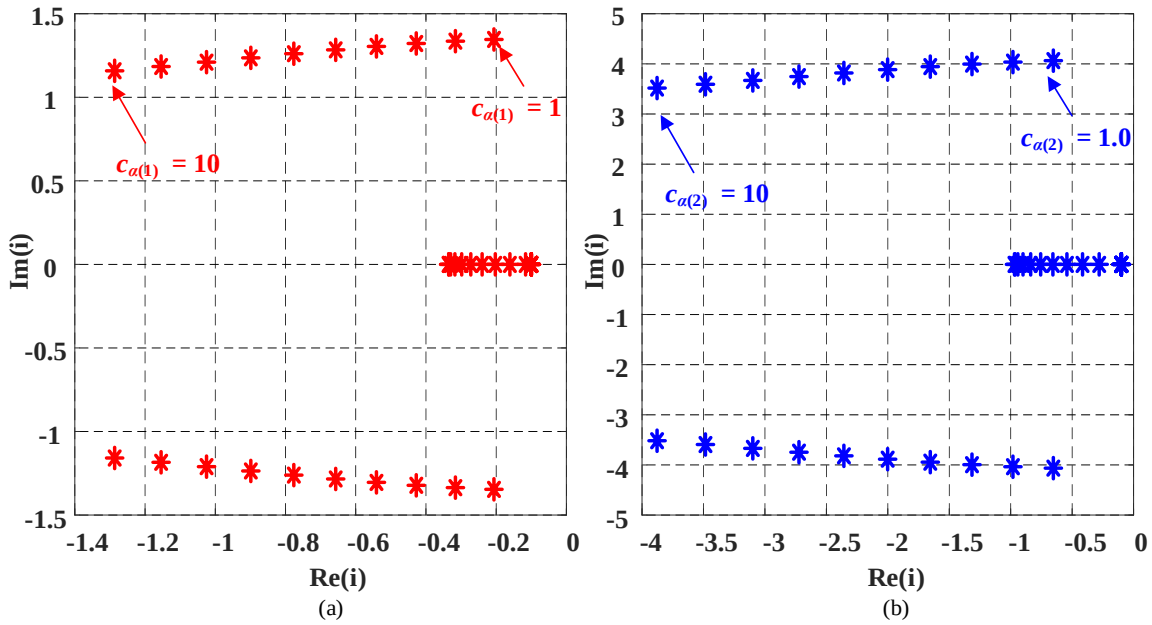

Fig. 3.12 The spectrum of matrix **A** of the linearized observer system (a) for $c_{\alpha(1)}$ = 1 p.u. to 10.0 p.u. (b) for $c_{\alpha(2)}$ = 1 p.u. to 10.0 p.u.

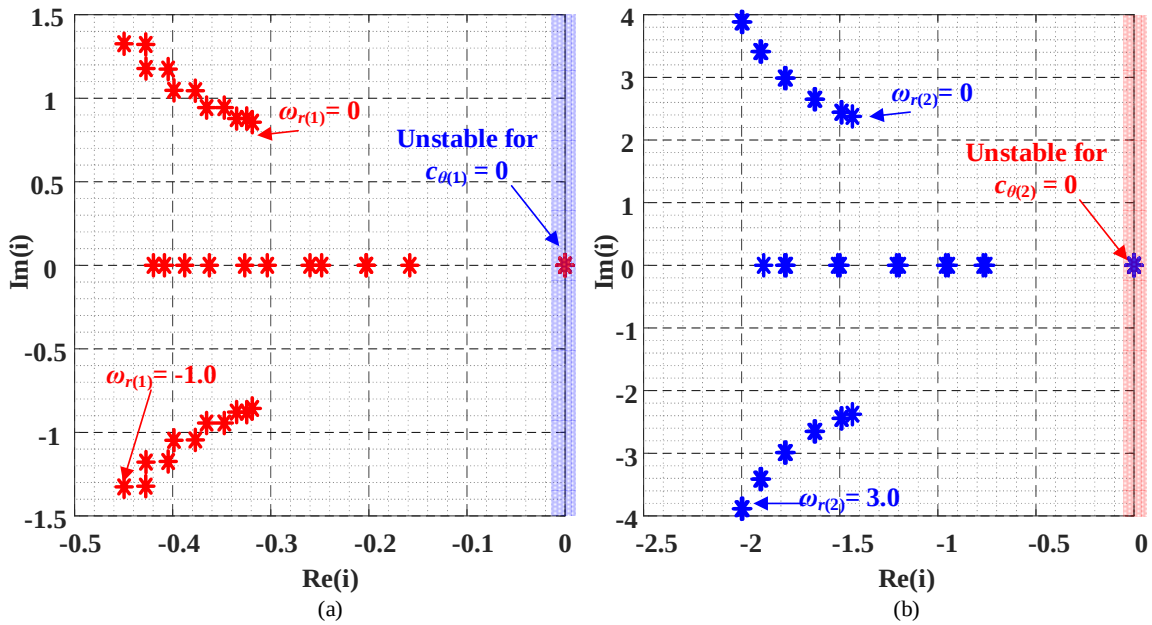

Fig. 3.13 The spectrum of matrix **A** of the linearized observer system (a) for $\omega_{r(1)}$ = -1.0 p.u. to 1.0 p.u and $c_{\theta(1)}$ = 0 (b) for $\omega_{r(2)}$ = 3.0 p.u. to -3.0 p.u and $c_{\theta(2)}$ =0.

In Fig. 3.12, stability plot is presented where tuning gain $c_{a(i)}$ in each plane was changed from 1.0 p.u. to 10.0 p.u. With the increment in tuning gains $c_{a(i)}$, the eigen values of the matrix $\mathbf{A}_{(i)}$ drifting away in the left half plane. Due to complex conjugate roots, oscillation can occur. In Fig. 3.13 (a), rotor speed was changed from -1.0 p.u. to 1.0 p.u in first plane and 3.0 p.u. to -3.0 p.u. in second plane and tuning gain $c_{\theta(i)} = 0$ for both planes. As can be seen from Fig. 3.13, due to omission of $c_{\theta(i)}$, the linearized system is unstable as one pole always remain at zero value due to open integrator.

In Fig. 3.14 (a), $\omega_{r(1)}$ = -1.0 p.u. to 1.0 p.u. and $c_{\theta(1)}$ = 0.1 p.u., for $c_{\alpha(1)}$ = 3 p.u., $\gamma_{(1)}$ = 0.3 p.u., $k_{c(1)}$ = 0.1 p.u., T_L = 1.0 p.u.

In Fig. 3.14 (b), $\omega_{r(2)}$ = 3.0 p.u. to -3.0 p.u. and $c_{\theta(2)}$ = 0.1 p.u., for $c_{\alpha(2)}$ = 5 p.u., $\gamma_{(2)}$ = 0.3 p.u., $k_{c(2)}$ = 0.1 p.u.

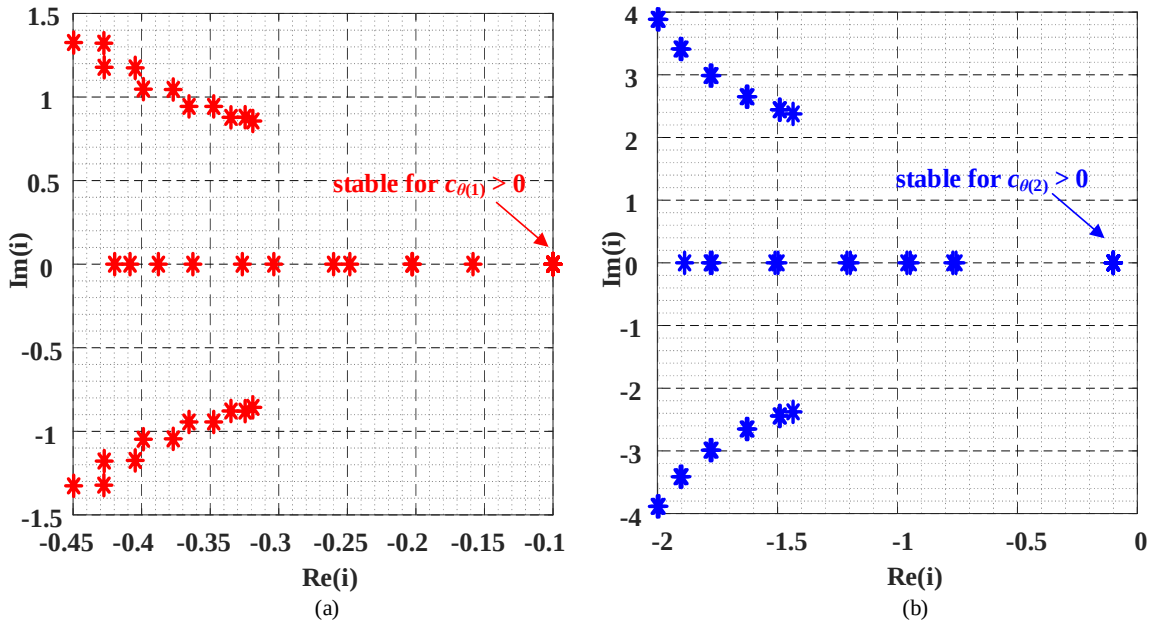

Fig. 3.14 The spectrum of matrix **A** of the linearized observer system (a) for $\omega_{r(1)}$ = -1.0 p.u. to 1.0 p.u and $c_{\theta(1)}$ = 0.1 p.u. (b) for $\omega_{r(2)}$ = 3.0 p.u. to -3.0 p.u and $c_{\theta(2)}$ =0.1 p.u.

In Fig. 3.14, $c_{\theta(i)}$ was included and kept at 0.1 p.u. for the same working points. The linearized system was stable, which shows the importance of the proposed stabilization function defined in (3.94).

In Fig. 3.15 (a), $k_{c(1)}$ = 0.1 p.u. to 5.0 p.u. and for $c_{\alpha(1)}$ = 3 p.u., $\gamma_{(1)}$ = 0.3 p.u., $\omega_{r(1)}$ = 1.0 p.u., $c_{\theta(1)}$ = 0.1 p.u., T_L = 1.0 p.u.

In Fig. 3.15 (b), $k_{c(2)}$ = 0.1 p.u. to 5.0 p.u. and for $c_{\alpha(2)}$ = 5 p.u., $\gamma_{(2)}$ = 0.3 p.u., $\omega_{r(2)}$ = -3.0 p.u., $c_{\theta(2)}$ = 0.1 p.u.,

In Fig. 3.16 (a), $\gamma_{(1)}$ = 0.1 p.u. to 5.0 p.u. and for $c_{\alpha(1)}$ = 3 p.u., $k_{c(1)}$ = 0.1 p.u., $\omega_{r(1)}$ = 1.0 p.u., $c_{\theta(1)}$ = 0.1 p.u., T_L = 1.0 p.u.

In Fig. 3.16 (b), $\gamma_{(2)}$ = 0.1 p.u. to 5.0 p.u. and for $c_{\alpha(2)}$ = 5 p.u., $k_{c(2)}$ = 0.1 p.u., $\omega_{r(2)}$ = -3.0 p.u., $c_{\theta(2)}$ = 0.1 p.u.,

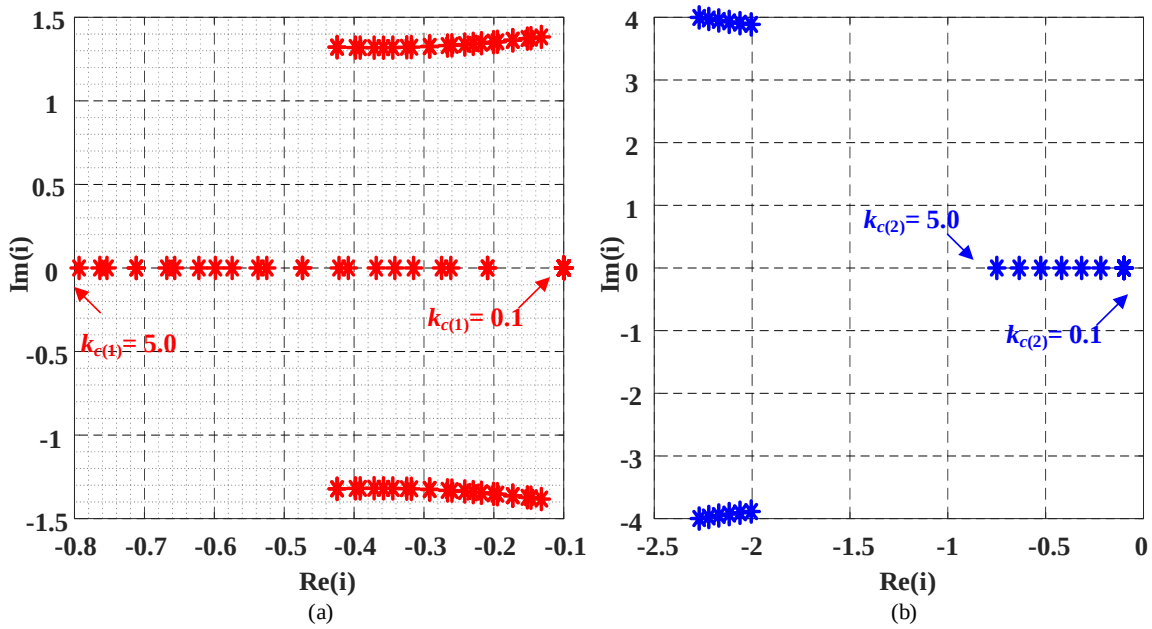

Fig. 3.15 The spectrum of matrix **A** of the linearized observer system (a) for $k_{c(1)}$ = 0.1 p.u. to 5.0 p.u (b) for $k_{c(2)}$ = 0.1 p.u. to 5.0 p.u

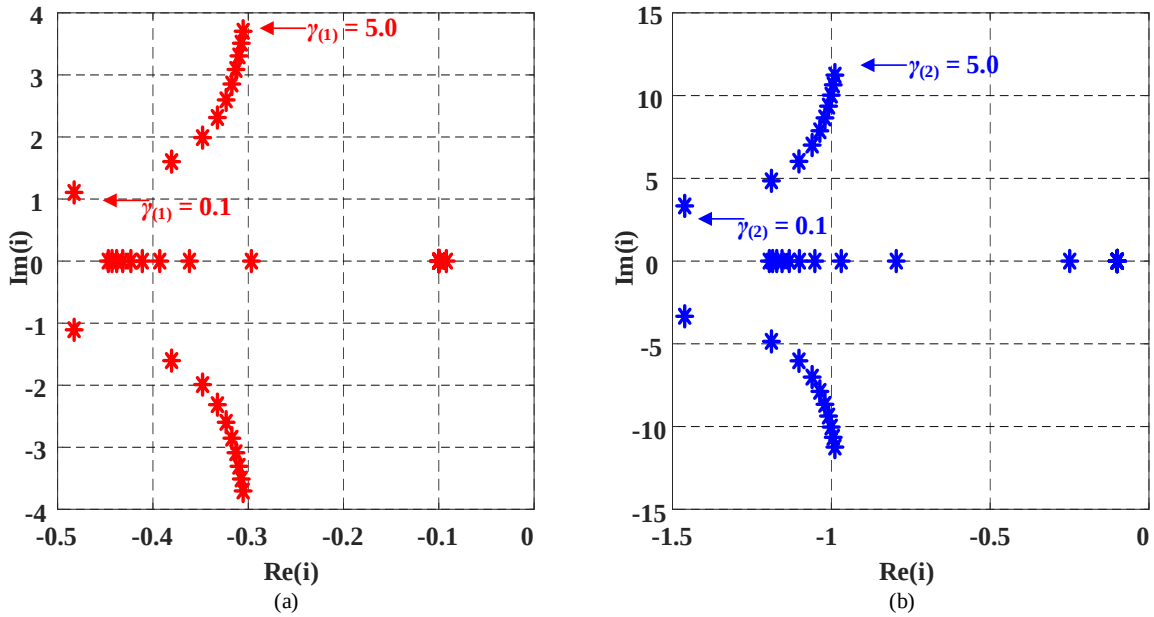

Fig. 3.16 The spectrum of matrix **A** of the linearized observer system (a) for $\gamma_{(1)}$ = 0.1 p.u. to 5.0 p.u (b) for $\gamma_{(2)}$ = 0.1 p.u. to 5.0 p.u

In Fig. 3.15, the eigen values of linearized observer structure is presented for fundamental plane and second plane. In the presented plot, tuning $k_{c(i)}$ was varied from

0.1 p.u to 5.0 p.u. In Fig. 3.16, the stability analysis is depicted for the case of $\gamma_{(i)}$ changing from 0.1 p.u. to 5.0 p.u. In both Fig. 3.15 and Fig. 3.16, eigen values of the linearized observer structure were in left half of complex plain and system was stable in each plane for the given operating points.

In this chapter, complete description of the design of adaptive and non-adaptive observer structure of three-phase IPMSM is provided. The observer structures of three-phase IPMSM and five-phase IPMSM are prepared using the mathematical model explained in Chapter 2. To estimate the state variables of the fundamental plane and second plane in five-phase IPMSM, adaptive active flux concept-based observer structure was extended as defined in 3.4.1.

Furthermore, stability analysis of three-phase observer structures and five-phase observer structures are provided to ensure the proper selection of tuning gains and stabilizing functions. To conduct the stability analysis, observer error model was transformed rotating coordinates systems. Based on the stability plots, it can be identified that without using the proposed stabilizing functions in position estimation system remains unstable as one pole always lies at origin.

In the next chapter, detailed discussion on control structure of three-phase IPMSM and proposed control solutions based on $\boldsymbol{\psi_{f(i)}, i_{s(i)}}$ vectors (1st strategy) and $\boldsymbol{\psi_{s(i)}, i_{s(i)}}$ vectors (2nd strategy) of five-phase IPMSM are provided.

CHAPTER 4: CONTROL STRUCTURE OF POLY-PHASE INTERIOR PERMANENT MAGNET SYNCHRONOUS MACHINE

4.1 Overview

In this chapter, control structures of poly-phase interior permanent magnet synchronous machine are discussed in details. For three-phase IPMSM drive classical FOC control structure is explained. The estimation accuracy of adaptive and non-adaptive observer structures described in Section – 3.3, was verified using the classical FOC structure.

In the following, proposed control system structures: 1) $\boldsymbol{\psi}_{\mathbf{f(i)}}, \mathbf{i}_{\mathbf{s(i)}}$ vectors based control solution 2) $\boldsymbol{\psi}_{\mathbf{s(i)}}, \mathbf{i}_{\mathbf{s(i)}}$ vectors based control solution of five-phase IPMSM are presented in stationary coordinate system $(\alpha - \beta)_{(i)}$. To obtain effective control of five-phase IPMSM, proposed control system utilizes the classical PI, MPC and backstepping control approaches using the nonlinear transformation. The control approach of a multiphase machine incorporates simultaneous control of two virtual machines in one single physical motor to ensure a higher value of torque generation by fundamental current and injected third harmonic current. Firstly, control scheme implemented for three-phase IPMSM is explained, then proposed control structure for multiphase IPMSM are explained.

4.2 Control structure of three-phase IPMSM

4.2.1 Field-oriented control of three-phase IPMSM

In this thesis, a classical control scheme known as field-oriented control or vector control is employed. The field-oriented control allows the satisfactory control performance of IPMSM as the DC machine [8], [9]. To achieve good dynamic and steady state response of the drive, field-oriented control is preferred over direct torque control. The torque equation defined in (2.23), can be written in per unit as (4.1). For accurate control of electromagnetic torque, flux controlling current i_{sd} and torque controlling current i_{sq} should be examined as shown in (4.1).

$$T_e = \psi_f i_{sq} + \left(L_d - L_q\right) i_{sd} i_{sq} \tag{4.1}$$

In present time, i_{sd}^{*} = 0 control and maximum torque per ampere (MTPA) control are the widely used vector control modes. To examine the performance of three-phase observer structures in the closed loop system, the i_{sd}^{*} = 0 mode was used as first control strategy in this thesis. In addition, i_{sd}^{*} = 0 control structure avoids the usage of machine parameters whereas MTPA heavily relies on ψ_f, L_d, and L_q. The space vector diagram of i_{sd}^{*} = 0 control is presented in Fig. 4.1.

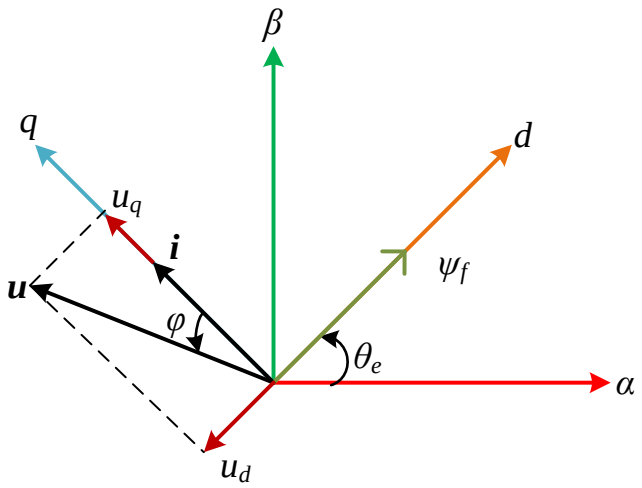

Fig. 4.1 Space vector representation of i_{sd}^{*} = 0 control mode

As flux controlling current i_{sd} is kept at zero value, the simplified equation of electromagnetic torque is given in (4.2).

$$T_e = \psi_f i_{sq} \tag{4.2}$$

The block diagram of the control scheme is depicted in Fig. 4.2. As shown in Fig. 4.2, the Clarke transformation is used to convert 3 phase voltages and currents components into 2 phase reference frames for the observer structure implementation. Estimated parameters such as currents, speed, and angular position are defined using the symbol "^". Estimated current components $\hat{i}_{s\alpha}$ and $\hat{i}_{s\beta}$ from the observer are transformed to d-q reference frame $\hat{i}_{sd}$ and $\hat{i}_{sq}$ using the estimated angular position $\hat{\theta}_r$ to implement field-oriented control (FOC).

In field-oriented control, two control loops are formed. The outer loop uses one speed controller and the inner loop requires two current controllers. Controllers in field-oriented control compare reference values of speed ω_r^{*} and currents i_{sd}^{*} and i_{sq}^{*}, with the estimated values of speed $\hat{\omega}_r$ and currents $\hat{i}_{sd}$ and $\hat{i}_{sq}$, and based on the error signals, it

generates the reference control signals u_{sd}^{*} and u_{sq}^{*}. The generated reference signals in rotating coordinates are transformed to stationary coordinates $u_{s\alpha}^{*}$ and $u_{s\beta}^{*}$ to supply the reference input voltages to inverter to generate the desired gate pulse to drive the IPMSM drive.

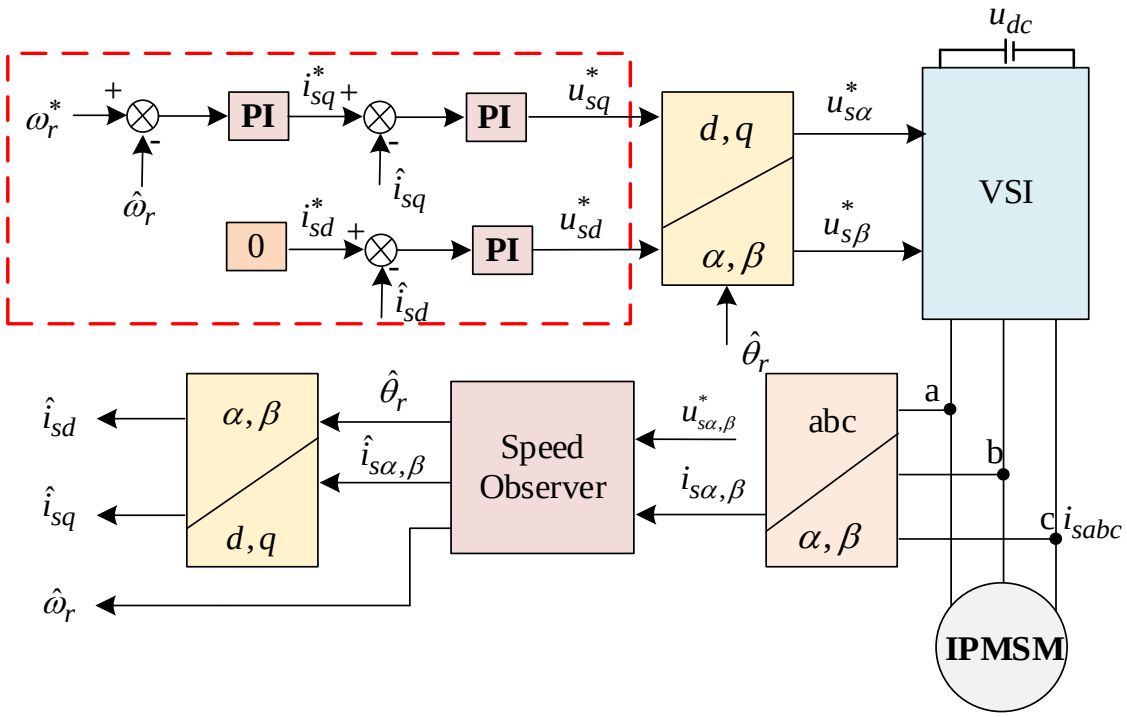

Fig. 4.2 The block diagram of field-oriented control scheme of three-phase IPMSM

4.3 Control structure of five-phase IPMSM

4.3.1 Field-oriented control of five-phase IPMSM

The block diagram of sensorless field-oriented control of five-phase IPMSM is presented in Fig. 4.3. To implement observer structure in two independent stationary orthogonal planes: fundamental plane $(\alpha\text{-}\beta)_1$ and third harmonic plane $(\alpha\text{-}\beta)_2$ extended the Clarke transformation is used to transform 5 phase currents into 2 phase reference frame $(\alpha\text{-}\beta)_{(i)}$. Estimated variables: speed, angular position, and currents are used to implement sensor-less control scheme. Estimated currents in the stationary reference frame $(\alpha\text{-}\beta)_{(i)}$ are transformed to the rotating reference frame $(d\text{-}q)_{(i)}$ using estimated angular position to implement a field-oriented control scheme.

The FOC structure was implemented on 5.5 kW five-phase IPMSM to provide a comparative analysis with the proposed control structure [44], [105], [112], [126], [131], [134]. The control of fundamental and third harmonic variables is shown in the

red and green dotted box, respectively. For accurate speed control of the five-phase IPMSM, PI controller was implemented in the first plane. Depending on the speed error, reference value of torque representing current $i^*_{sq(1)}$ generates in the first plane. In the next step, based on the error between reference torque producing current $i^*_{sq(1)}$ and estimated current $\hat{i}_{sq(1)}$, q-axis reference voltage $u^*_{sq(1)}$ is generated in the first plane to minimize the speed error and torque error.

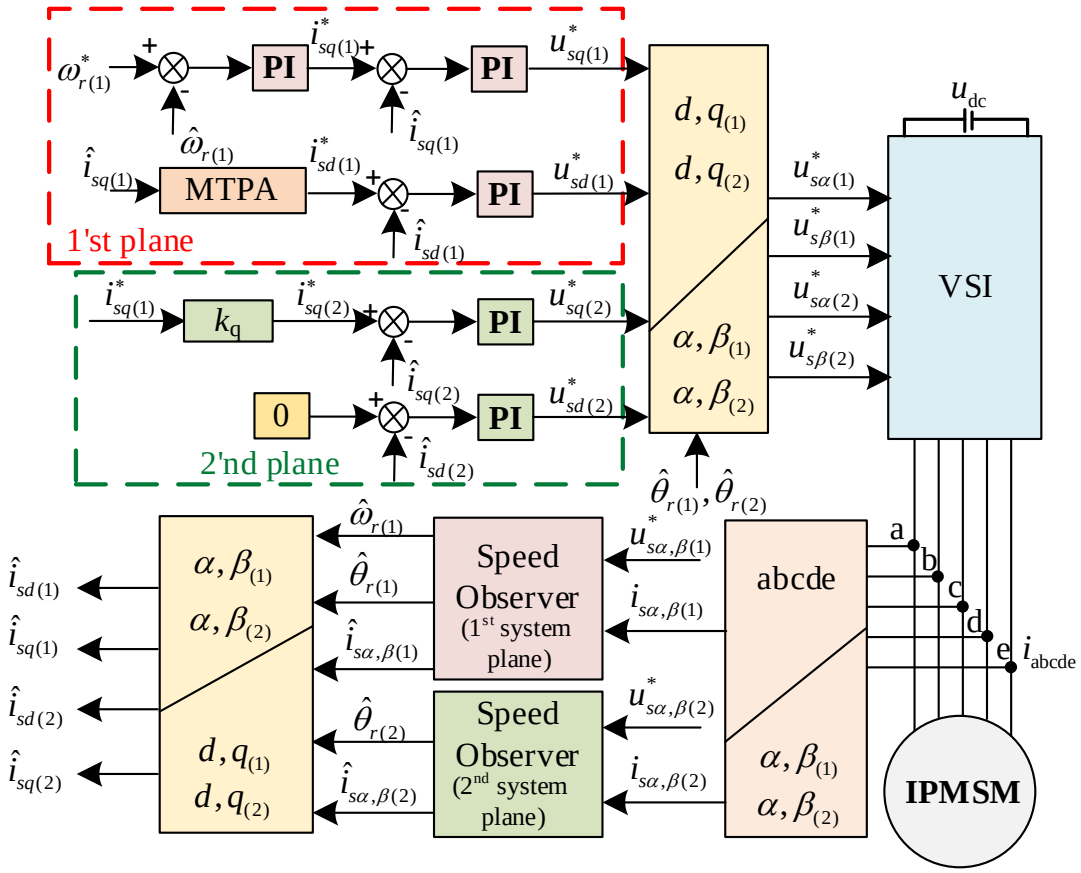

Fig. 4.3 The block diagram of field-oriented control scheme of five-phase IPMSM

To extract reluctance torque, the reference value of flux controlling current $i^*_{sd(1)}$ was computed using maximum torque per ampere algorithm (MTPA) [8], [9] as expressed in (4.3). Similar to q-axis, reference voltage $u^*_{sd(1)}$ is generated in d-axis to minimize the error between the reference value of $i^*_{sd(1)}$and actual value of $\hat{i}_{sd(1)}$. The generated reference voltages $u^*_{sd,q(1)}$ in rotating coordinates are transformed to stationary coordinates $u^*_{s\alpha,\beta(1)}$ using estimated angular position $\hat{\theta}_{r(1)}$ to apply to the inverter to drive the five-phase IPMSM drive [8], [9], [138].

$$i_{sd(1)}^{*} = \frac{-\psi_{f(1)} + \sqrt{\psi_{f(1)}^{2} + 8(L_{d(1)} - L_{q(1)})^{2} i_{sq(1)}^{2}}}{4(L_{d(1)} - L_{q(1)})} \tag{4.3}$$

In the second plane, reference value of $i_{sd(2)}^{*}= 0$, reference of torque controlling $i_{sd(2)}^{*}$ current can be computed from the fundamental plane as the machine model of five-phase IPMSM in first plane and second plane are in conjunction [102]. To supply the reference voltages to the inverter, the generated control signals $u_{sd,q(2)}^{*}$ in second plane are transformed to stationary reference frame $u_{s\alpha,\beta(2)}^{*}$ using estimated angular position $\hat{\theta}_{r(2)}$.

4.3.2 Proposed control structure ($\boldsymbol{\psi}_{\mathbf{f}(i)}$,$\mathbf{i}_{\mathbf{s}(i)}$) vectors based of five-phase IPMSM

In the proposed control structure, multiscalar variables are prepared using stator flux vector $\boldsymbol{\psi}_{\mathbf{s}(i)}$ and stator current vector $\mathbf{i}_{\mathbf{s}(i)}$. The selected variables in each plane are: $x_{11(i)}$ is rotor angular speed, $x_{12(i)}$ is electromagnetic torque, $x_{21(i)}$ is square of stator flux, $x_{22(i)}$ is flux controlling variable. In general form multiscalar variables can expressed in the rotating coordinate system as (4.4) - (4.7).

$$x_{11(i)} = \omega_{r(i)} \tag{4.4}$$

$$x_{12(i)} = \psi_{sd(i)} i_{sq(i)} - \psi_{sq(i)} i_{sd(i)} \tag{4.5}$$

$$x_{21(i)} = \psi_{sd(i)}^{2} + \psi_{sq(i)}^{2} \tag{4.6}$$

$$x_{22(i)} = \psi_{sd(i)} i_{sd(i)} + \psi_{sq(i)} i_{sq(i)} \tag{4.7}$$

In this proposed control solution, author assumes that stator flux $\boldsymbol{\psi}_{\mathbf{s}(i)}$ vector is equal to permanent magnet flux vector $\boldsymbol{\psi}_{\mathbf{f}(i)}$ which allows to form new transformation using permanent magnet flux vector $\boldsymbol{\psi}_{\mathbf{f}(i)}$ and stator current vector $\mathbf{i}_{\mathbf{s}(i)}$. The new multiscalar variables are prepared in the stationary reference frame: $x_{11(i)}$ is rotor angular speed, $x_{12(i)}$ is vector product of permanent magnet flux vector $\boldsymbol{\psi}_{\mathbf{f}(i)}$ and stator current vector $\mathbf{i}_{\mathbf{s}(i)}$, $x_{21(i)}$ is square of permanent magnet flux, $x_{22(i)}$ is scalar product of permanent magnet flux vector $\boldsymbol{\psi}_{\mathbf{f}(i)}$ and stator current vector $\mathbf{i}_{\mathbf{s}(i)}$. The selected variables are defined in (4.8) - (4.11) using the permanent magnet flux vector $\boldsymbol{\psi}_{\mathbf{f}(i)}$ and stator current vector $\mathbf{i}_{\mathbf{s}(i)}$.

$$x_{11(i)} = \omega_{r(i)} \tag{4.8}$$

$$x_{12(i)} = \psi_{f\alpha(i)} i_{s\beta(i)} - \psi_{f\beta(i)} i_{s\alpha(i)} \tag{4.9}$$

$$x_{21(i)} = \psi_{f\alpha(i)}^2 + \psi_{f\beta(i)}^2 \tag{4.10}$$

$$x_{22(i)} = \psi_{f\alpha(i)} i_{s\alpha(i)} + \psi_{f\beta(i)} i_{s\beta(i)} \tag{4.11}$$

After taking time derivative of selected variables and substituting the current and flux derivative, multiscalar model of the control system is prepared as defined in.

$$\frac{dx_{11(i)}}{d\tau} = \frac{1}{J} x_{12(i)} - \frac{1}{J} T_L \tag{4.12}$$

$$\frac{dx_{12(i)}}{d\tau} = -\frac{1}{T_{v(i)}} x_{12(i)} - \frac{1}{L_q} x_{11(i)} x_{21(i)} - x_{11(i)} x_{22(i)} + \underbrace{\frac{1}{L_q} (u_{s\beta(i)} \psi_{f\alpha(i)} - u_{s\alpha(i)} \psi_{f\beta(i)})}_{u_{1(i)}}$$

(4.13)

$$\frac{dx_{22(i)}}{d\tau} = -\frac{1}{T_{v(i)}} x_{22(i)} + x_{11(i)} x_{12(i)} + \underbrace{\frac{1}{L_{q(i)}} (u_{s\beta(i)} \psi_{f\beta(i)} + u_{s\alpha(i)} \psi_{f\alpha(i)})}_{u_{2(i)}} \tag{4.14}$$

Where $T_{v(i)}$ is time constant (4.15),

$$T_{v(i)} = \frac{L_{q(i)}}{R_s} \tag{4.15}$$

It can be observed that nonlinear terms appear in (4.13) and (4.14). Hence, to implement the proposed control structure in the fundamental and second planes, the nonlinear state feedback linearization process must be performed in the following step [121]. The nonlinear signals $m_{1(i)}$ and $m_{2(i)}$ are computed from the PI controllers of $x_{12(i)}$ and $x_{22(i)}$, respectively. The control variables $u_{1(i)}$ and $u_{2(i)}$ are obtained from (4.13) and (4.14), respectively. To generate the gate pulse in the inverter gate driver, the required reference voltages $u^*_{s\alpha,\beta(i)}$ in stationary coordinates need to be supplied. The reference input voltages in stationary coordinates can be computed from the obtained control signals $u_{1(i)}$ and $u_{2(i)}$.

$$u_{s\alpha(i)} = L_{q(i)} \left(\frac{u_{2(i)} \psi_{f\alpha(i)} - u_{1(i)} \psi_{f\beta(i)}}{x_{21(i)}} \right) \tag{4.16}$$

$$u_{s\beta(i)} = L_{q(i)} \left(\frac{u_{2(i)} \psi_{f\beta(i)} + u_{1(i)} \psi_{f\alpha(i)}}{x_{21(i)}} \right) \tag{4.17}$$

The following linear model of the machine can be formed after completing the process of nonlinear state feedback linearization and decoupling process. The fully decoupled model of the machine is presented in (4.18) - (4.20). Mechanical subsystem is represented using (4.18) and (4.19). The electromagnetic subsystem is presented in (4.20).

$$\frac{dx_{11(i)}}{dt} = \frac{1}{J} x_{12(i)} - \frac{1}{J} T_L \tag{4.18}$$

$$\frac{dx_{12(i)}}{dt} = \frac{1}{T_{v(i)}} \left(-x_{12(i)} + m_{1(i)} \right) \tag{4.19}$$

$$\frac{dx_{22(i)}}{dt} = \frac{1}{T_{v(i)}} \left(-x_{22(i)} + m_{2(i)} \right) \tag{4.20}$$

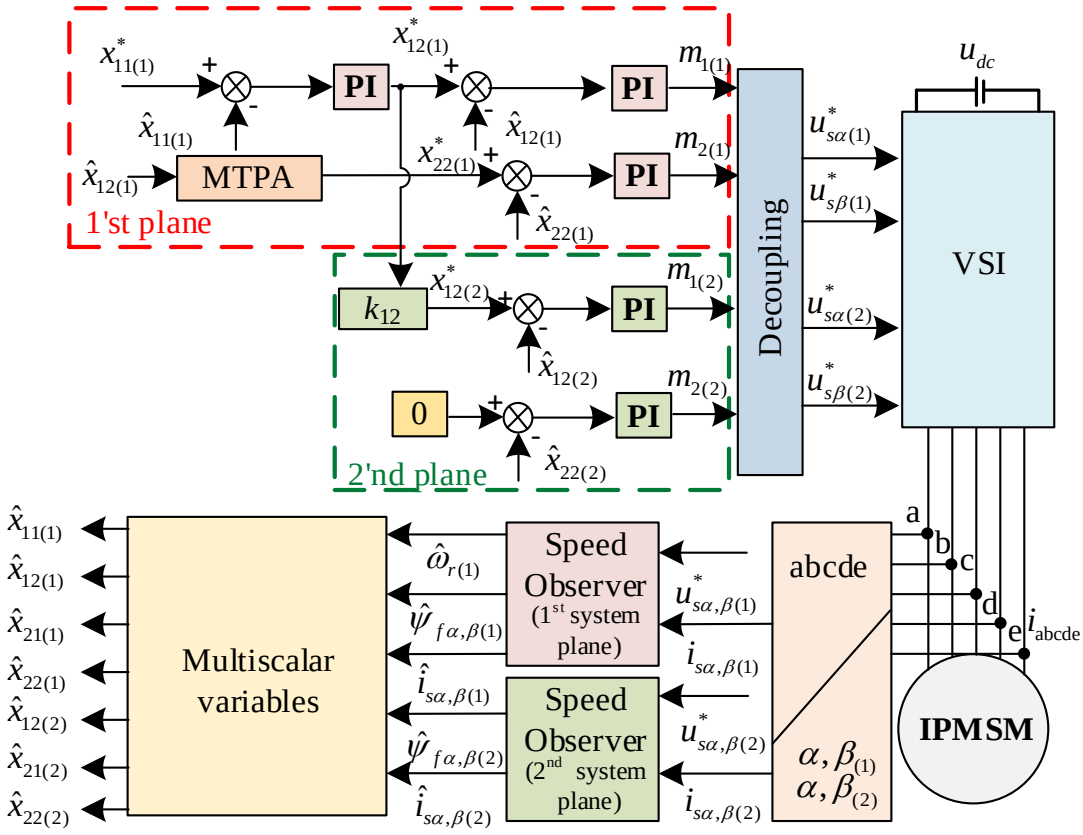

Fig. 4.4 The block diagram of $(\psi_{f(i)}, i_{s(i)})$ vector based control structure of five-phase IPMSM

In Fig. 4.4, the block diagram of the proposed control structure is visible. The input stator current components in the natural reference frame (abcde) are requisite to transform to stationary reference $(\alpha\text{-}\beta)_{(i)}$ frame through the Clarke transformation for observer structure implementation. The instantaneous value of stator voltages and currents are used in the estimator in each plane, to reconstruct the machine variables.

In the next step, multiscalar variables are calculated using the estimated variables to implement the proposed control structure. In the first plane, the speed controller is used to regulate the speed of the machine and generate the reference value of electromagnetic torque $x^*_{12(1)}$ depending on the speed error. Moreover, electromagnetic torque controller and flux controller generate signals $m_{1(i)}$ and $m_{2(i)}$ for each plane. These nonlinear signals are used as nonlinear state feedback to linearize the defined multiscalar model of the control system of the five-phase IPMSM. After the decoupling process, when the system model considered to be linear and the reference voltage signals are computed from the control signal appearing in the multiscalar model.

It is important to acknowledge that the reference value of $x^*_{12(2)}$ can be computed using the $x^*_{12(1)}$. The ratio between the third harmonic torque to fundamental torque is considered to be around 10 % from the presented FFT analysis in Chapter 5.

$$x^*_{12(2)} = k_{12} x^*_{12(1)} \tag{4.21}$$

Where the value of k_{12} was selected from the range of 0.1 to 0.15. The $x^*_{12(2)}$ defined (4.21) is also considered during the implementation of the other proposed control structures.

In addition, after the linearizing and decoupling process, the machine model considered as linear and independent control of the mechanical subsystem and electromagnetic subsystem becomes possible. It is essential to mention that variables are not required to transform to rotating coordinates in the proposed control structure. Hence, the proposed control structure eliminates the need of the Park transformation. Moreover, proper decoupling between the electromagnetic subsystem and the mechanical subsystem is not obtained in the FOC scheme due to the presence of nonlinearities, while the proposed control structure provides accurate decoupling between the electromagnetic subsystem and the electromechanical subsystem.

Fig. 4.5(a) presents the variation of different torque components produced by the motor corresponding to torque angle. The reluctance torque in IPMSM is directly influenced by the torque angle as described in [9]. As SPMSM offer uniform reluctance path, total developed torque and electromagnetic torque is equal, while in IPMSM permanent magnets are embedded inside the rotor, creating saliency which allow the IPMSM to produce both electromagnetic torque and reluctance torque, which increases

total developed torque. Fig. 4.5(b), locus of the constant torque in the current vector plane is presented. From Fig. 4.5(b), it can be observed that the amplitude of current vector will be always lower at θ_{MTPA} compared to amplitude at θ_1 and θ_2.

After substituting the current vector components in the defined multiscalar variable in rotating reference frame in (4.5). The torque angle at which maximum torque can be obtained can computed using (4.22).

$$\frac{\partial x_{12}}{\partial \theta_e} = \psi_f I_s \cos\theta_e + (L_d - L_q) I_s^2 \cos 2\theta_e = 0 \tag{4.22}$$

The calculated $x^*_{22(1)}$ is defined in (4.23) for the first plane, in the second plane $x^*_{22(2)}$ was set equal to zero as produced reluctance torque in the second plane is very small.

$$x^*_{22(1)} = \frac{-\psi_{f(1)} + \sqrt{\psi^2_{f(1)} + 8(L_{d(1)} - L_{q(1)})^2 x^2_{12(1)}}}{4(L_{d(1)} - L_{q(1)})} \tag{4.23}$$

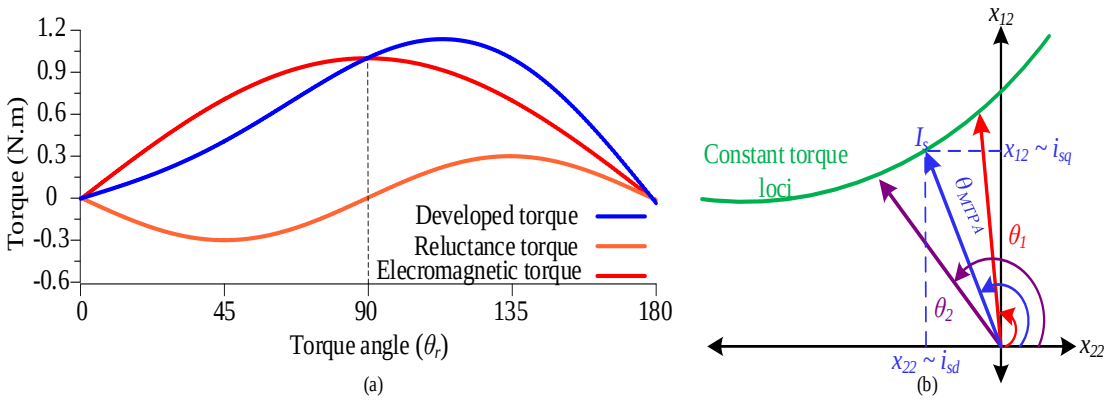

Fig. 4.5 (a) Torque vs torque angle (b) Locus of the constant torque in the current vector plane

Proposed control structure

The proposed control using $\boldsymbol{\psi}_{\mathbf{f}(i)}, \mathbf{i}_{\mathbf{s}(i)}$ vectors will be investigated using the simulation and experimental assessment. In the next section, proposed control structure – 1 using $\boldsymbol{\psi}_{\mathbf{s}(i)}, \mathbf{i}_{\mathbf{s}(i)}$ vectors is explained in details.

4.3.3 Proposed ($\boldsymbol{\psi}_{\mathbf{s}(i)}, \mathbf{i}_{\mathbf{s}(i)}$) vector based control structure 1 of five-phase IPMSM

In the proposed control scheme, multiscalar model of the control system is prepared with equal state variables *x*. The stator current vector $\mathbf{i}_{\mathbf{s}(i)}$ and stator flux vector $\boldsymbol{\psi}_{\mathbf{s}(i)}$ can be transformed into the scalar and vectors by the inner and external product operation. The new state variables considering $\boldsymbol{\psi}_{\mathbf{s}(i)}, \mathbf{i}_{\mathbf{s}(i)}$ vector for five-phase IPMSM are angular

rotor speed $x_{11(i)}$, vector product of stator flux vector and stator current vector $x_{12(i)}$, which is proportional to the motor torque component, the square of the stator flux $x_{21(i)}$ and scalar product of stator flux and stator current vector $x_{22(i)}$ which is flux controlling variable, respectively. The chosen state variables are represented as:

$$x_{11(i)} = \omega_{r(i)} \tag{4.24}$$

$$x_{12(i)} = \psi_{s\alpha(i)} i_{s\beta(i)} - \psi_{s\beta(i)} i_{s\alpha(i)} \tag{4.25}$$

$$x_{21(i)} = \psi_{s\alpha(i)}^2 + \psi_{s\beta(i)}^2 \tag{4.26}$$

$$x_{22(i)} = \psi_{s\alpha(i)} i_{s\alpha(i)} + \psi_{s\beta(i)} i_{s\beta(i)} \tag{4.27}$$

There are 4 state variables in each plane. The multiscalar model of the control system of five-phase IPMSM drive is presented here by taking the time derivative of multiscalar variables from (4.24) to (4.27) and substituting the derivative of currents and fluxes from the motor model; the final form is given as:

$$\frac{dx_{11(i)}}{dt} = \frac{1}{J} x_{12(i)} - \frac{1}{J} T_L \tag{4.28}$$

$$\frac{dx_{12(i)}}{dt} = -\frac{1}{T_{v(i)}} x_{12(i)} - \frac{1}{L_{q(i)}} x_{11(i)} (\psi_{s(i)} \odot \psi_{f(i)}) + q_{s(i)} + \underbrace{\frac{1}{L_{q(i)}} (\psi_{s\alpha(i)} u_{s\beta(i)} - \psi_{s\beta(i)} u_{s\alpha(i)})}_{u_{1(i)}} \tag{4.29}$$

$$\frac{dx_{21(i)}}{dt} = 2(-R_s x_{22(i)} + u_{s\alpha(i)} \psi_{s\alpha(i)} + u_{s\beta(i)} \psi_{s\beta(i)}) \tag{4.30}$$

$$\begin{aligned} \frac{dx_{22(i)}}{dt} &= -\frac{1}{T_{v(i)}} x_{22(i)} - R_s i_{s(i)}^2 + \frac{1}{L_{q(i)}} x_{11(i)} (\psi_{s(i)} \otimes \psi_{f(i)}) + p_{s(i)} \\ &+ \underbrace{\frac{1}{L_{q(i)}} (\psi_{s\alpha(i)} u_{s\alpha(i)} + \psi_{s\beta(i)} u_{s\beta(i)})}_{u_{2(i)}} \end{aligned} \tag{4.31}$$

Where $T_{v(i)}$ is the motor electromagnetic time constant and other various terms that appear in differential equations from (4.29) to (4.31) are given as:

$$T_{v(i)} = \frac{L_{q(i)}}{R_s} \tag{4.32}$$

$$(\psi_{s(i)} \odot \psi_{f(i)}) = (\psi_{s\alpha(i)} \psi_{f\alpha(i)} + \psi_{s\beta(i)} \psi_{f\beta(i)}) \tag{4.33}$$

$$(\psi_{s(i)} \otimes \psi_{f(i)}) = (\psi_{s\alpha(i)}\psi_{f\beta(i)} - \psi_{s\beta(i)}\psi_{f\alpha(i)}) \tag{4.34}$$

$$p_{s(i)} = u_{s\alpha(i)}i_{s\alpha(i)} + u_{s\beta(i)}i_{s\beta(i)} \tag{4.35}$$

$$q_{s(i)} = u_{s\alpha(i)}i_{s\beta(i)} - i_{s\alpha(i)}u_{s\beta(i)} \tag{4.36}$$

$$i_{s(i)}^2 = (i_{s\alpha(i)}^2 + i_{s\beta(i)}^2) \tag{4.37}$$

In the next step, the feedback linearization process must be completed as given in [121]. To linearize the nonlinear system, new signals $m_{1(i)}$ and $m_{2(i)}$ are computed using PI controllers of $x_{12(i)}$ and $x_{22(i)}$ as shown in Fig. 4.6. The state feedback linearized control can be obtained from (4.29) and (4.31), as follows:

$$u_{1(i)} = \frac{1}{T_{v(i)}} m_{1(i)} + \frac{1}{L_{q(i)}} x_{11(i)} (\psi_{s(i)} \odot \psi_{f(i)}) - q_{s(i)} \tag{4.38}$$

$$u_{2(i)} = \frac{1}{T_{v(i)}} m_{2(i)} + R_s i_{s(i)}^2 - \frac{1}{L_{q(i)}} x_{11(i)} (\psi_{s(i)} \otimes \psi_{f(i)}) - p_{s(i)} \tag{4.39}$$

Voltage components in (α-β)$_{(i)}$ coordinate can be obtained from $u_{1(i)}$ and $u_{2(i)}$ defined in (4.29) and (4.31), respectively.

$$u_{s\alpha(i)} = L_{q(i)} \left(\frac{u_{2(i)}\psi_{sa(i)} - u_{1(i)}\psi_{s\beta(i)}}{x_{21(i)}} \right) \tag{4.40}$$

$$u_{s\beta(i)} = L_{q(i)} \left(\frac{u_{2(i)}\psi_{s\beta(i)} + u_{1(i)}\psi_{s\alpha(i)}}{x_{21(i)}} \right) \tag{4.41}$$

By using state feedback control law, two linear subsystems are shown from (4.42) to (4.45). Electro-mechanical subsystem is shown in (4.42) and (4.43) while electromagnetic subsystem is depicted in (4.44) and (4.45).

$$\frac{dx_{11(i)}}{dt} = \frac{1}{J} x_{12(i)} - \frac{1}{J} T_L \tag{4.42}$$

$$\frac{dx_{12(i)}}{dt} = \frac{1}{T_{v(i)}} \left(-x_{12(i)} + m_{1(i)} \right) \tag{4.43}$$

$$\frac{dx_{21(i)}}{dt} = 2(-R_s x_{22(i)} + u_{s\alpha(i)}\psi_{s\alpha(i)} + u_{s\beta(i)}\psi_{s\beta(i)}) \tag{4.44}$$

$$\frac{dx_{22(i)}}{dt} = \frac{1}{T_{v(i)}}\left(-x_{22(i)} + m_{2(i)}\right) \tag{4.45}$$

The control system structure 1 based on stator current $\mathbf{i}_{s(i)}$ and stator flux $\boldsymbol{\psi}_{s(i)}$ is depicted in Fig. 4.6. From Fig. 4.6, two subsystems are controlled by cascaded controllers. Controllers are marked in red for the first plane and in green for the second plane of the five-phase IPMSM. It can be observed that seven controllers are needed to implement the control scheme.

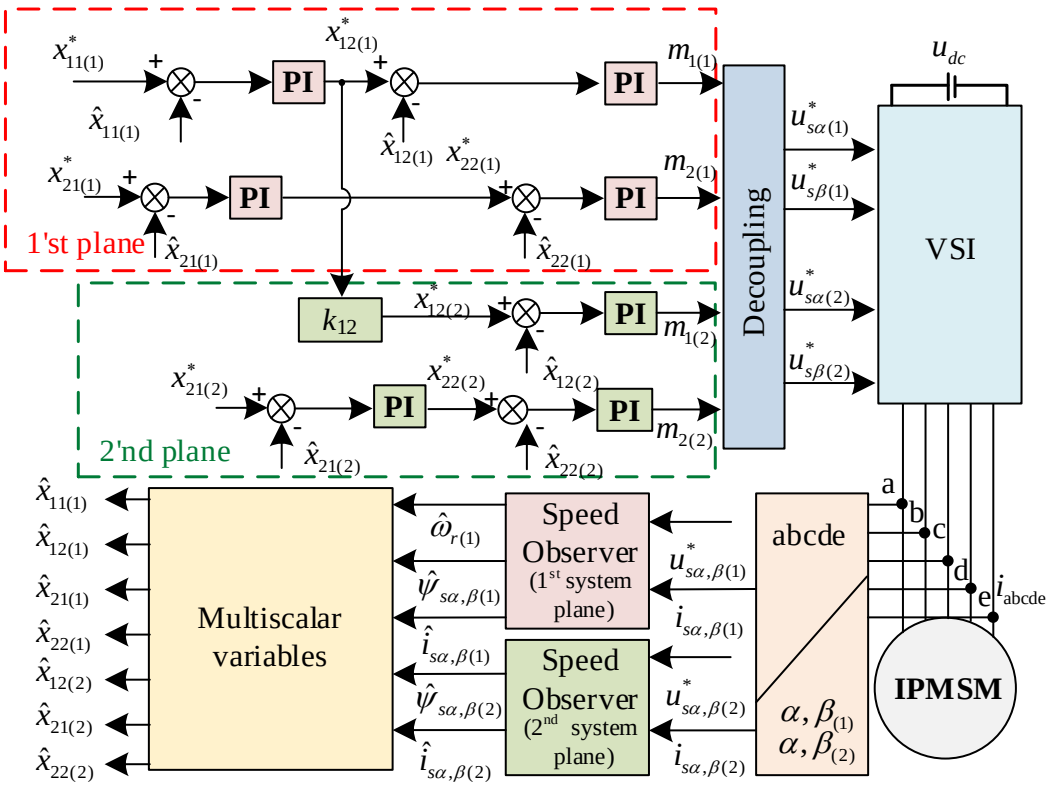

Fig. 4.6 The block diagram of $(\boldsymbol{\psi}_{s(i)},\mathbf{i}_{s(i)})$ vector based control structure 1 of five-phase IPMSM

To provide the comparison analysis, proposed control structure – 2 using the $(\boldsymbol{\psi}_{s(i)},\mathbf{i}_{s(i)})$ vectors is discussed in the following section.

4.3.4 Proposed $(\boldsymbol{\psi}_{s(i)},\mathbf{i}_{s(i)})$ vectors based control structure 2 of five-phase IPMSM

The block diagram of the proposed $(\boldsymbol{\psi}_{s(i)},\mathbf{i}_{s(i)})$ vector based control structure 2 is presented in Fig. 4.7. The multiscalar model of the proposed control structure for five-phase IPMSM can be prepared by differentiating the multiscalar variables from (4.24) to (4.26) and represented as

$$\frac{dx_{11(i)}}{dt} = \frac{1}{J}x_{12(i)} - \frac{1}{J}T_L \tag{4.46}$$

$$\frac{dx_{12(i)}}{dt} = -\frac{1}{T_{v(i)}} x_{12(i)} - \frac{1}{L_{q(i)}} x_{11(i)} (\psi_{s(i)} \odot \psi_{f(i)}) + q_{s(i)} + \underbrace{\frac{1}{L_{q(i)}} (\psi_{s\alpha(i)} u_{s\beta(i)} - \psi_{s\beta(i)} u_{s\alpha(i)})}_{u_{1(i)}}$$

(4.47)

$$\frac{dx_{21(i)}}{dt} = -2R_s x_{22(i)} + \underbrace{2(\psi_{s\alpha(i)} u_{s\alpha(i)} + \psi_{s\beta(i)} u_{s\beta(i)})}_{u_{2(i)}} \tag{4.48}$$

Here, control signal $u_{2(i)}$ is obtained from (4.48) and $x_{22(i)}$ variable is controlled internally from $x_{21(i)}$ controller as per the requirement of IPMSM drive hence, the use of (4.31) to compute control signal $u_{2(i)}$ is unnecessary and control system becomes simpler and the number of controllers required are reduced.

In the proposed control structure, new control signals $m_{1(i)}$ and $m_{2(i)}$ from the PI controllers are used for the linearization process as shown in Fig. 4.7. $u_{1(i)}$ and $u_{2(i)}$ are the control variables appearing in the nonlinear model of IPMSM (4.47) and (4.48), respectively. The final control variables in stationary frame defined in (4.49) and (4.50) can be determined from $u_{1(i)}$ and $u_{2(i)}$.

$$u_{s\alpha(i)} = -\frac{1}{2x_{21(i)}} (2L_{q(i)} u_{1(i)} \psi_{s\beta(i)} - u_{2(i)} \psi_{s\alpha(i)}) \tag{4.49}$$

$$u_{s\beta(i)} = \frac{1}{2x_{21(i)}} (2L_{q(i)} u_{1(i)} \psi_{s\alpha(i)} + u_{2(i)} \psi_{s\beta(i)}) \tag{4.50}$$

By using the state feedback control law, two linear and fully decoupled subsystems are obtained: electro-mechanical subsystem defined in (4.51) - (4.52) and electro-magnetic subsystem defined in (4.53).

$$\frac{dx_{11(i)}}{dt} = \frac{1}{J} x_{12(i)} - \frac{1}{J} T_L \tag{4.51}$$

$$\frac{dx_{12(i)}}{dt} = \frac{1}{T_{v(i)}} \left(-x_{12(i)} + m_{1(i)} \right) \tag{4.52}$$

$$\frac{dx_{21(i)}}{dt} = 2R_s \left(-x_{22(i)} + m_{2(i)} \right) \tag{4.53}$$

It is important to mention that discussion on control system using the stator current vector and stator flux vector only available for three-phase machines in the literature.

This control strategy is close to the constant mutual flux linkage control, instead of constant mutual flux, stator flux is kept constant. Under this assumption, stator current coefficient could be $i_{sd(i)} \neq 0$. Variable $x_{22(i)}$ defined in (4.27) is proportional to $i_{sd(i)}$: ($x_{22(i)} \sim i_{sd(i)} \neq 0$).

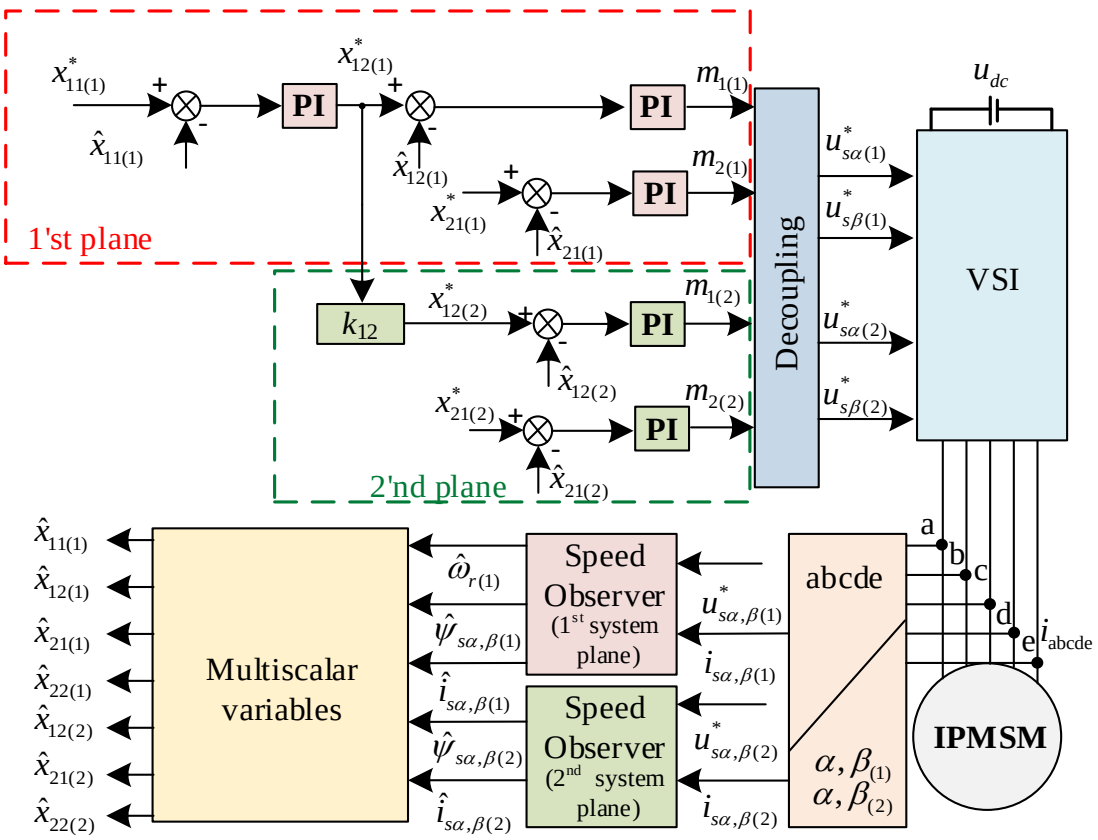

Fig. 4.7 The block diagram of $(\psi_{s(i)}, i_{s(i)})$ vector based control structure 2 of five-phase IPMSM

The block diagram of the proposed control system is shown in Fig. 4.7. From the DC link voltage, stator voltage can be determined using the PWM algorithm or directly from the command voltage in the case of using the voltage modulator. The five-phase measured currents are transformed to the stationary reference frame $(\alpha\text{-}\beta)_{(i)}$ for each plane using the Clarke transformation. The measured currents are connected to the observer structure in $(\alpha\text{-}\beta)_{(i)}$ coordinates to reconstruct the state variables. Motor variables are calculated using the instantaneous quantities of stator currents and voltages. Based on estimated state variables, multiscalar variables are calculated and defined in (4.24) to (4.26) for each vector plane. After differentiating multiscalar variables, the multiscalar model of the control system is prepared, defined in (4.46) - (4.48).

The speed controller is employed to control the speed and generate torque reference for the first plane represented by $x^{*}_{12(1)}$. Similar to FOC, reference torque for the second plane can be calculated from the first plane as machine models in the first plane and in the second plane are connected internally [102]. In the proposed technique, the torque controller $x_{12(i)}$ and square of flux controller $x_{21(i)}$ in each plane generate feedback signal $m_{1(i)}$ and $m_{2(i)}$, which is used to linearize the system model. After the decoupling process, reference voltage components can be calculated using the control signals $u_{1(i)}$ and $u_{2(i)}$. The general block diagram of multiscalar control scheme is presented in Fig. 4.8.

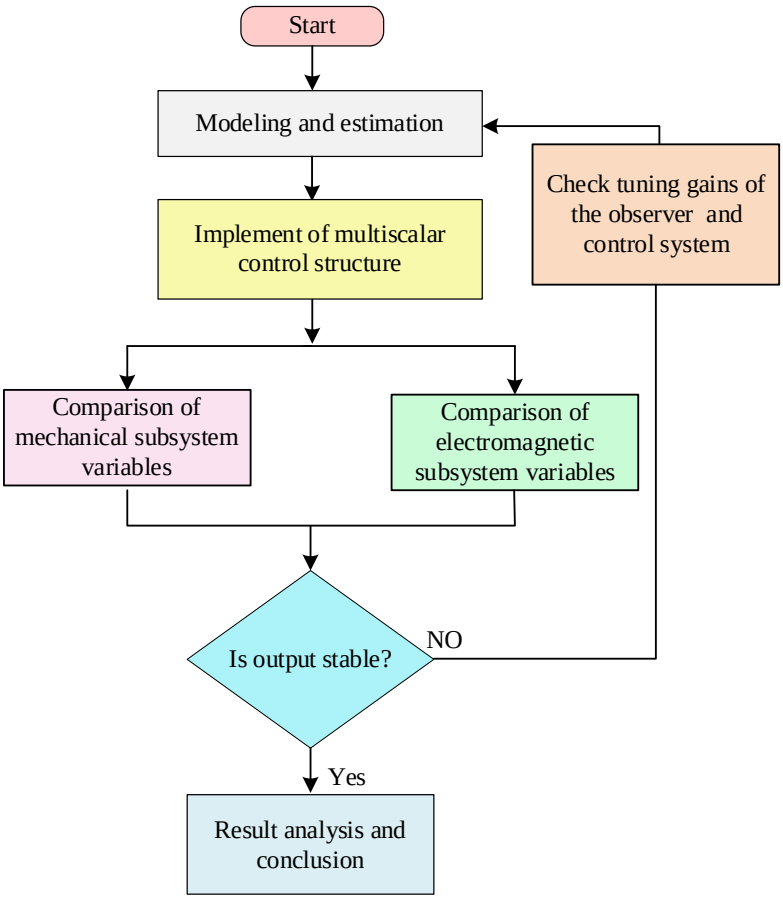

Fig. 4.8 General block diagram of multiscalar control structure

Control of the electro-mechanical subsystem remains the same for control structure – 1 and structure – 2 for stator flux and stator current vector. However, when it comes to the control of electro-magnetic subsystem, control technique – 2 eliminates the need $x_{22(i)}$ controller and it is controlled directly by $x_{21(i)}$ controller, which simplify the overall control structure. If control structure – 1 is not simplified, $x_{22(i)}$ controller is needed to maintain stator flux constant, which increases system complexity. The necessity of transformation to $(d\text{-}q)_{(i)}$ coordinate system is also eliminated by the proposed control

technique for five-phase IPMSM. The proposed control method requires total 5 controllers as shown in Fig. 4.7.

In the following section, advanced control structure of five-phase IPMSM is proposed. The proposed control structure involves predictive control using multiscalar variable for 1st plane and multiscalar model-based control for 2nd plane.

4.3.5 Proposed predictive control using multi-scalar variables for 1st plane and multi-scalar model-based control for 2nd plane of five-phase IPMSM

The conceptualization behind the multi-scalar is that the inner and external product of the stator current vector ($\mathbf{i}_{s(i)}$) and stator flux vector ($\boldsymbol{\psi}_{s(i)}$) can be transformed into scalars [105], [126], [127], [131]. For the fundamental plane $\boldsymbol{i}$ = 1, in the nonlinear control such as five-phase IPMSM, these four are state variables in each plane

$$x_{11(i)} = \omega_{r(i)} \tag{4.54}$$

$$x_{12(i)} = \psi_{s\alpha(i)} i_{s\beta(i)} - \psi_{s\beta(i)} i_{s\alpha(i)} \tag{4.55}$$

$$x_{21(i)} = \psi^2_{s\alpha(i)} + \psi^2_{s\beta(i)} \tag{4.56}$$

$$x_{22(i)} = \psi_{s\alpha(i)} i_{s\alpha(i)} + \psi_{s\beta(i)} i_{s\beta(i)} \tag{4.57}$$

$x_{11(i)}$ is rotor speed, $x_{12(i)}$ is an external product of stator flux and current which represents the motor torque, $x_{21(i)}$ is the square of stator flux, and $x_{22(i)}$ is the inner product of stator flux and stator currents. The proposed control strategy for five-phase IPMSM is depicted in Fig. 4.9.

The control objective is prepared for the fundamental plane based on multi-scalar variables. Predictive control is employed to control the multi-scalar variables of the 1st plane. Multi-scalar model-based control is proposed for 2nd plane to control the flux and torque components. It can be observed from Fig. 4.9. that park transformation is not required in the second plane to control the third harmonic components.

To discretize (3.80) and (3.81), the forward Euler method can be used, and the stator current at instant (k + 1) can be predicted as (4.58)-(4.59):

$$i^{(k+1)}_{s\alpha(i)} = (1 - \frac{T_s}{T_{v(i)}}) i^{(k)}_{s\alpha(i)} + \frac{T_s}{L_{q(i)}} \omega_{r(i)} \psi_{f\beta(i)} + \frac{T_s}{L_{q(i)}} u^{(k)}_{sa(i)} \tag{4.58}$$

$$i_{s\beta(i)}^{(k+1)} = (1-\frac{T_s}{T_{v(i)}})i_{s\beta(i)}^{(k)} - \frac{T_s}{L_{q(i)}}\omega_{r(i)}\psi_{f\alpha(i)} + \frac{T_s}{L_{q(i)}}u_{s\beta(i)}^{(k)} \quad (4.59)$$

Where $T_{v(i)} = \frac{L_{q(i)}}{R_s}$, based on (4.58) and (4.59) the predicted current value, stator flux can be predicted for the same current vector

$$\psi_{s\alpha(i)}^{(k+1)} = (L_{q(i)}i_{s\alpha(i)}^{(k)} + \psi_{f\alpha(i)}) \quad (4.60)$$

$$\psi_{s\beta(i)}^{(k+1)} = (L_{q(i)}i_{s\beta(i)}^{(k)} + \psi_{f\beta(i)}) \quad (4.61)$$

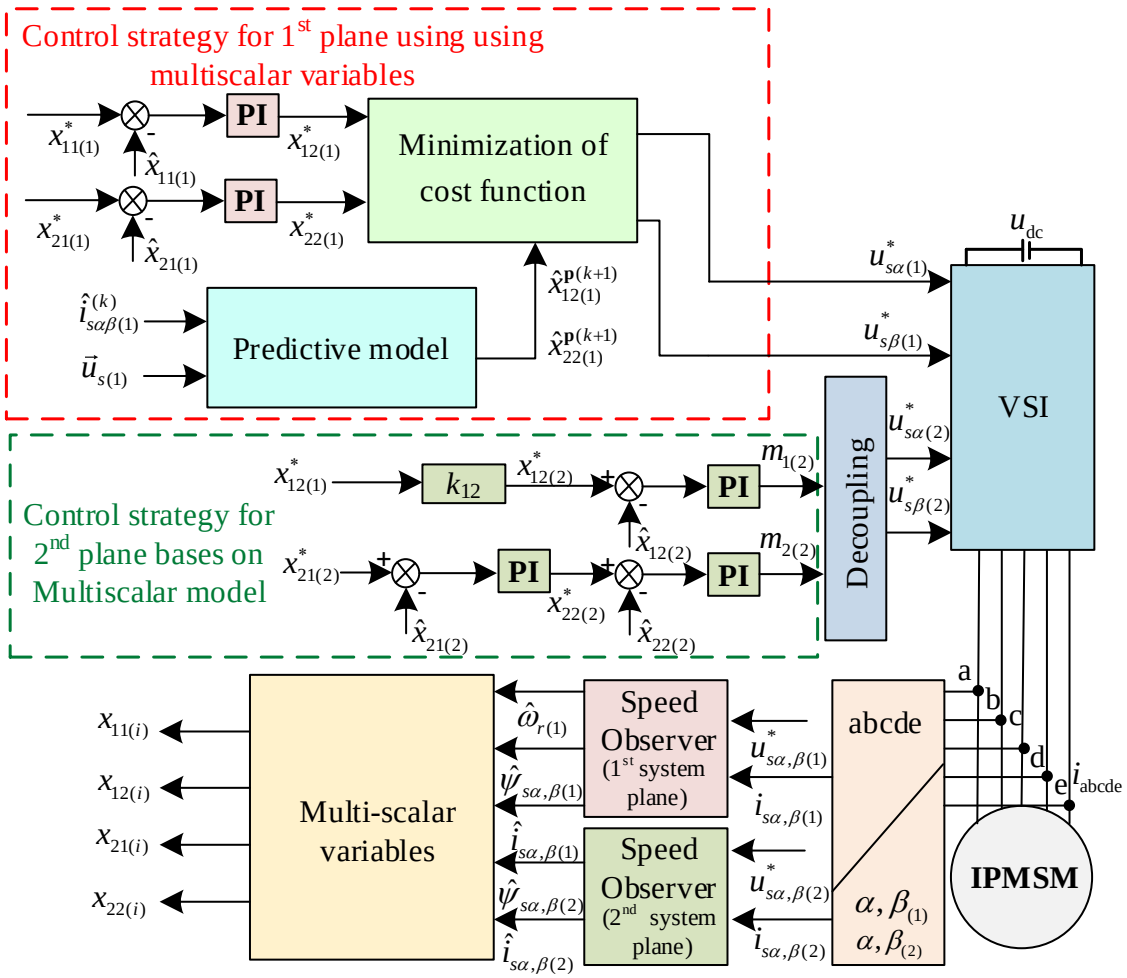

Fig. 4.9 The control diagram of the proposed predictive multiscalar based control of five-phase IPMSM

After substituting the predicted value of stator currents and stator flux in (4.55) and (4.57), multi-scalar variables: $x_{12(i)}$ which represents torque, and $x_{22(i)}$ which is the flux controlling variable, can also be predicted and given as

$$x_{12(i)}^{(k+1)} = \psi_{s\alpha(i)}^{(k+1)}i_{s\beta(i)}^{(k+1)} - \psi_{s\beta(i)}^{(k+1)}i_{s\alpha(i)}^{(k+1)} \quad (4.62)$$

$$x_{22(i)}^{(k+1)} = \psi_{s\alpha(i)}^{(k+1)} i_{s\alpha(i)}^{(k+1)} + \psi_{s\beta(i)}^{(k+1)} i_{s\beta(i)}^{(k+1)} \tag{4.63}$$

The unit and dimension of (4.62) and (4.63) are the same; hence, the weighting factor can be eliminated, and the following cost function is proposed.

$$g = ((x_{12(i)}^{*} - x_{12(i)}^{\mathbf{P}(k+1)}) + (x_{22(i)}^{*} - x_{22(i)}^{\mathbf{P}(k+1)}))^2 \tag{4.64}$$

The reference value of torque $x_{12(1)}^{*}$ is generated using a speed controller, and the reference value of flux controlling variable $x_{22(1)}^{*}$ is obtained from the flux controller $x_{21(1)}^{*}$. In the proposed scheme, the value of stator flux is kept constant, hence $x_{22(i)} \neq 0$ for the proposed control scheme. The flowchart of the proposed PTC based on multi-scalar variables is shown in Fig. 4.10.

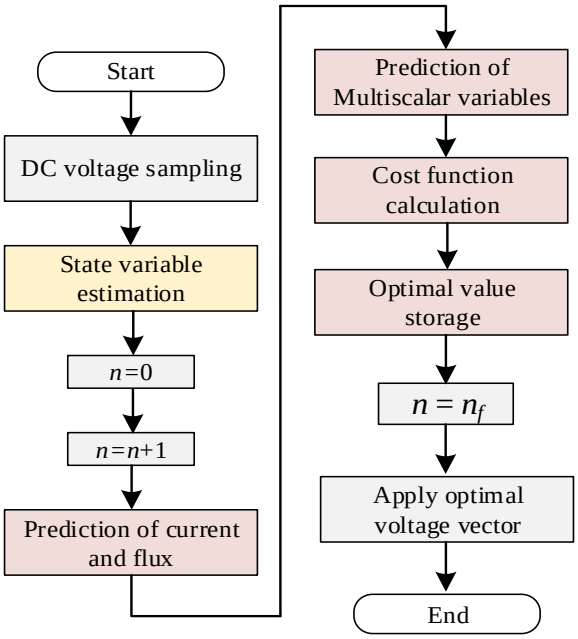

Fig. 4.10 Flowchart of the proposed control diagram of proposed predictive control using multi-scalar variables for 1st plane

Following the above procedure, a predictive controller can be designed for the fundamental plane of the five-phase IPMSM, as shown in the red dashed box in Fig. 4.9. At the instant of *k*, estimated current signals from the adaptive observer are used instead of measured current signals. Implementing multi-scalar variable-based PTC does not require angle transformation. It is important to mention that in the proposed control solution, measure speed $\omega_{r(i)}$, position $\theta_{r(i)}$, permanent magnet flux components $\psi_{f\alpha,\beta(i)}$, stator flux components $\psi_{s\alpha,\beta(i)}$, and stator current components $i_{s\alpha,\beta(i)}$ are replaced with estimated speed $\hat{\omega}_{r(i)}$, position $\hat{\theta}_{r(i)}$, permanent magnet flux components $\hat{\psi}_{f\alpha,\beta(i)}$,

stator flux components $\hat{\psi}_{s\alpha,\beta(i)}$ and stator current components $\hat{i}_{s\alpha,\beta(\mathrm{i})}$ for fundamental plane and second plane to avoid the issue of noise and gain drift due to mechanical sensor. It is assumed that machine parameters are known and constant in nature.

To conduct comparative inspection, proposed control structure is compared with classical predictive FOC control system. In the next section, classical predictive FOC system is explained.

4.3.6 Classical predictive current control based FOC for 1st plane and classical FOC for 2nd plane of five-phase IPMSM

For control of five-phase IPMSM, the traditional control schemes: MPC for the fundamental plane, which is also known as traditional predictive torque control (PTC), and PI controller-based FOC for 3rd harmonic plane is shown in Fig. 4.11.

In the fundamental plane, the PI controller is implemented for accurate speed control and produce reference current for $i^*_{sq(1)}$. For sampling time T_s, the derivative of stator currents can be approximated using Euler approximation, and the final form of predictive currents model in the rotating reference frame can be obtained, based on the voltage vectors generated by the inverter in the stationary reference frame are the rotating vectors in $(d\text{-}q)_{(i)}$ reference frame and stator currents can be predicted, which is well known in the literature[139]. The predictive current controller tracks the reference current generated by the PI controller. The voltage vector, which minimizes the defined cost function in (4.65) will be applied for the whole sampling period [140].

$$g = ((i^*_{sd(i)} - i^{\mathbf{P}(k+1)}_{sd(i)}) + (i^*_{sq(i)} - i^{\mathbf{P}(k+1)}_{sq(i)}))^2 \tag{4.65}$$

In the second plane, PI controllers control the flux and torque components of the currents. In the second plane, the reference current $i^*_{sq(2)}$ is calculated optimally from the fundamental reference current $i^*_{sq(1)}$ [102]. In the control scheme, measured currents in the natural reference frame are transformed into the stationary reference frame to implement the observer structure. The observer structure estimates the defined state variables in the stationary reference frame. State variables are converted into the rotating reference frame for control system implementation using an estimated angular position. To implement the classical control structure for the five-phase IPMSM drive, it is necessary to transform state variables in $(d\text{-}q)_{(i)}$ reference frame as shown in Fig. 4.11.

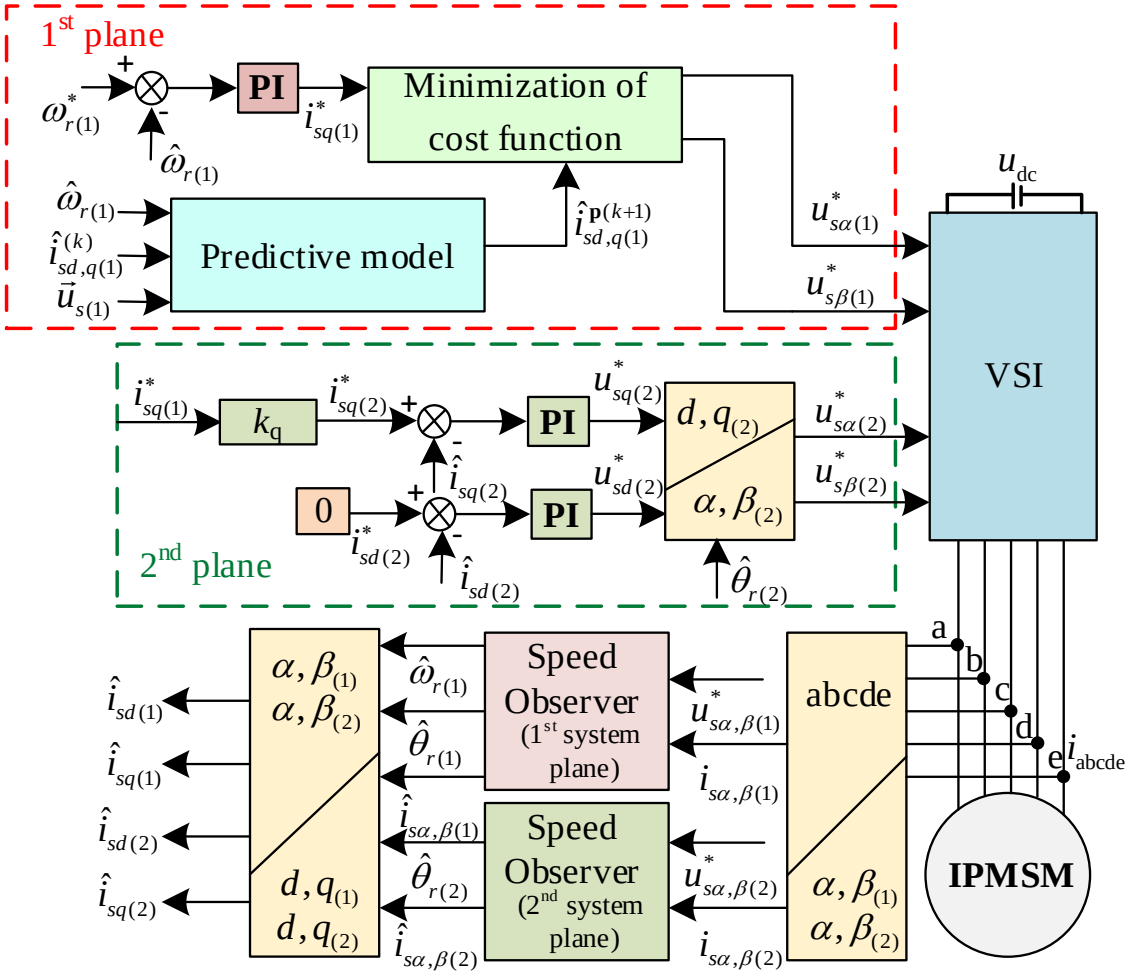

Fig. 4.11 The control diagram of classical predictive current control based FOC for 1st plane and classical FOC for 2nd plane

In the next section, backstepping multiscalar control of five-phase IPMSM is discussed in details.

4.3.7 Proposed control of five-phase IPMSM using the backstepping technique

Taking into account the mathematical model of five-phase IPMSM (2.43) - (2.46) in stationary coordinates system, the $x_{(i)}$ – coordinate transformation for multiphase IPMSM are defined as follows:

$$x_{11(i)} = \omega_{r(i)} \tag{4.66}$$

$$x_{12(i)} = \frac{1}{J}(\psi_{f\alpha(i)} i_{s\beta(i)} - \psi_{f\beta(i)} i_{s\alpha(i)} - T_L) \tag{4.67}$$

$$x_{21(i)} = \psi_{f\alpha(i)}^2 + \psi_{f\beta(i)}^2 \tag{4.68}$$

$$x_{22(i)} = \psi_{f\alpha(i)} i_{s\alpha(i)} + \psi_{f\beta(i)} i_{s\beta(i)} \tag{4.69}$$

After differentiating (4.66) - (4.69), the machine model provides the following form,

$$\frac{dx_{11(i)}}{dt} = \frac{1}{J} x_{12(i)} - \frac{1}{J} T_L \tag{4.70}$$

$$\frac{dx_{12(i)}}{d\tau} = -\frac{1}{T_{v(i)}} x_{12(i)} - \frac{1}{L_q} x_{11(i)} x_{21(i)} - x_{11(i)} x_{22(i)} + \underbrace{\frac{1}{L_{q(i)}} (u_{s\beta(i)} \psi_{f\alpha(i)} - u_{s\alpha(i)} \psi_{f\beta(i)})}_{u_{1(i)}}$$

(4.71)

$$\frac{dx_{22(i)}}{d\tau} = -\frac{1}{T_{v(i)}} x_{22(i)} + x_{11(i)} x_{12(i)} + \underbrace{\frac{1}{L_{q(i)}} (u_{s\beta(i)} \psi_{f\beta(i)} + u_{s\alpha(i)} \psi_{f\alpha(i)})}_{u_{2(i)}} \tag{4.72}$$

The strict feed-back form is demonstrated in obtained model in (4.70) - (4.72)[141]. Implementation of the control system with backstepping control is well explained in literature [78], [141]. The reference signal of rotor speed is denoted by $x^*_{11(i)}$ is smooth and bounded. Using the classical backstepping control approach, controller can be designed. In the first step, it is important to calculate reference value of $x^*_{12(i)}$ to oblige $x_{11(i)}$ to track the reference value of speed $x^*_{11(i)}$. Similar to vector control scheme where $i^*_{sd(i)}$= 0, here $x^*_{22(i)}$ was forced to zero to obtain the final control input. In the next step, to converge reference value $x^*_{12(i)}$ and $x^*_{22(i)}$, the control inputs $u_{1(i)}$ and $u_{2(i)}$ require to be computed hence, all system tracking errors are minimized zero value.

The speed tracking error is defined as (4.73), the dynamics of speed error $e_{1(i)}$ can be obtained as (4.75) by differentiating (4.73) and substituting (4.70).

$$e_{11(i)} = x^*_{11(i)} - x_{11(i)} \tag{4.73}$$

$$\dot{e}_{11(i)} = \dot{x}^*_{11(i)} - \dot{x}_{11(i)} \tag{4.74}$$

$$\dot{e}_{11(i)} = \dot{x}^*_{11(i)} - \left(\frac{1}{J} x_{12(i)} - \frac{1}{J} T_L \right) \tag{4.75}$$

The first Lyapunov function $V_{e11(i)}$ is given as (4.76) and its derivative after substituting (4.75), presented as (4.77):

$$V_{e11(i)} = \frac{1}{2} e^2_{11(i)} \tag{4.76}$$

$$\dot{V}_{e11(i)} = -k_{11(i)}e_{11(i)}^2 + e_{11(i)}\left(k_{11(i)}e_{11(i)} - \frac{1}{J}x_{12(i)} + \frac{1}{J}T_L\right) \tag{4.77}$$

In the next step, the virtual control $x_{12(i)}^*$ can be computed as (4.78), it can be observed that the load torque is estimated by integral action, hence it is represented using the "^".

$$x_{12(i)}^* = k_{11(i)}e_{11(i)}J + \hat{T}_L \tag{4.78}$$

In the next step, the control variables should be computed, therefore, other tracking errors in the system are defined as (4.79) and (4.80)

$$e_{12(i)} = x_{12(i)}^* - x_{12(i)} \tag{4.79}$$

$$e_{22(i)} = x_{22(i)}^* - x_{22(i)} \tag{4.80}$$

From (4.79) and (4.78), (4.82) can be calculated, and in the next step the backstep through the integrator (4.74) takes place,

$$e_{12(i)} = k_{11(i)}e_{11(i)}J + \hat{T}_L - x_{12(i)} \tag{4.81}$$

$$x_{12(i)} = k_{11(i)}e_{11(i)}J + \hat{T}_L - e_{12(i)} \tag{4.82}$$

$$\dot{e}_{11(i)} = -k_{11(i)}e_{11(i)} + \frac{1}{J}e_{12(i)} - \frac{1}{J}\tilde{T}_L \tag{4.83}$$

The load torque error can be obtained from (4.84), $\hat{T}_{L(i)}$ is the real value of load torque such that $\dot{T}_{L(i)} = 0$.

$$\tilde{T}_{L(i)} = \hat{T}_{L(i)} - T_{L(i)} \tag{4.84}$$

Using the (4.71) and (4.72), the dynamics of tracking errors (4.79) and (4.80) can be calculated.

$$\dot{e}_{12(i)} = \dot{x}_{12(i)}^* - \dot{x}_{12(i)} \tag{4.85}$$

$$\begin{aligned}\dot{e}_{12(i)} = &\left(-k_{11(i)}^2 e_{11(i)} + k_{11(i)}e_{12(i)} - k_{11(i)}\tilde{T}_L\right) + \dot{\hat{T}}_L + \frac{1}{T_{v(i)}}x_{12(i)} \\ &+ \frac{1}{L_q}x_{11(i)}x_{21(i)} + x_{11(i)}x_{22(i)} - \underbrace{\frac{1}{L_{q(i)}}(u_{s\beta(i)}\psi_{f\alpha(i)} - u_{s\alpha(i)}\psi_{f\beta(i)})}_{u_{1(i)}}\end{aligned} \tag{4.86}$$

$$\dot{e}_{22(i)} = \dot{x}^{*}_{22(i)} - \dot{x}_{22(i)} \tag{4.87}$$

$$\dot{e}_{22(i)} = \frac{1}{T_{v(i)}} x_{22(i)} - x_{11(i)} x_{12(i)} - \underbrace{\frac{1}{L_{q(i)}} (u_{s\beta(i)} \psi_{f\beta(i)} + u_{s\alpha(i)} \psi_{f\alpha(i)})}_{u_{2(i)}} \tag{4.88}$$

The Lyapunov candidate function is defined in (4.89), calculates the tracking errors for the completed system. Here, *N* is the number of phases and can be determined using (4.91)

$$V_{(i)} = \sum_{i=1}^{N} \left(0.5 \left(e_{11(i)}^2 + e_{12(i)}^2 + e_{22(i)}^2 \right) + \frac{0.5}{\gamma_{l(i)}} \tilde{T}_{L(i)}^2 \right) \tag{4.89}$$

$$\dot{V}_{(i)} = \sum_{i=1}^{N} \left(\begin{array}{l} -k_{11(i)} e_{11(i)}^2 - k_{12(i)} e_{12(i)}^2 - k_{22(i)} e_{22(i)}^2 + e_{12(i)} ((k_{12(i)} + k_{11(i)}) e_{12(i)} \\ + limit_{12(i)} ((-k_{11(i)}^2 J + \frac{1}{J}) e_{11(i)}) + \dot{\tilde{T}}_{L(i)} + \frac{R_s}{L_{q(i)}} x_{12(i)} + \frac{1}{L_{q(i)}} x_{11(i)} \psi_{f(i)}^2 \\ + x_{11(i)} x_{22(i)} - u_{1(i)}) + e_{22(i)} (k_{22(i)} e_{22(i)} + \frac{R_s}{L_{q(i)}} x_{22(i)} - x_{11(i)} x_{12(i)} - u_{2(i)}) + \\ \tilde{T}_{L(i)} (\frac{1}{\gamma_{l(i)}} \dot{\tilde{T}}_{L(i)} - \frac{1}{J} e_{11(i)} - k_{11(i)} e_{12(i)}) \le 0 \end{array} \right)$$

(4.90)

$$N = \begin{cases} 0.5(N-1), & N \text{ is odd} \\ 0.5N - 1, & N \text{ is even} \end{cases} \tag{4.91}$$

Moreover, it is important to mention the limitations of the set variables. In conventional linear controllers, based on the working points of the drive, the controller output or dynamic of the variables is limited by constant value or dynamically changed. In such a control system, where control variables are obtained using the Lyapunov criteria, the limitations in the set variables control structure are absent. The dynamics of the reference variables can be limited by the first-order inertia elements [78], [141]. The use of an inertia element on the reference signal slows down the reaction of the electromagnetic torque variable. The electromagnetic torque reaction is proportional to the time constant of the inertia element. The objective of limiting the electromagnetic torque reference signal can be possible without compromising the dynamics by limiting inertial elements. The block diagram of the proposed backstepping control structure of five-phase IPMSM is presented in the Fig. 4.12.

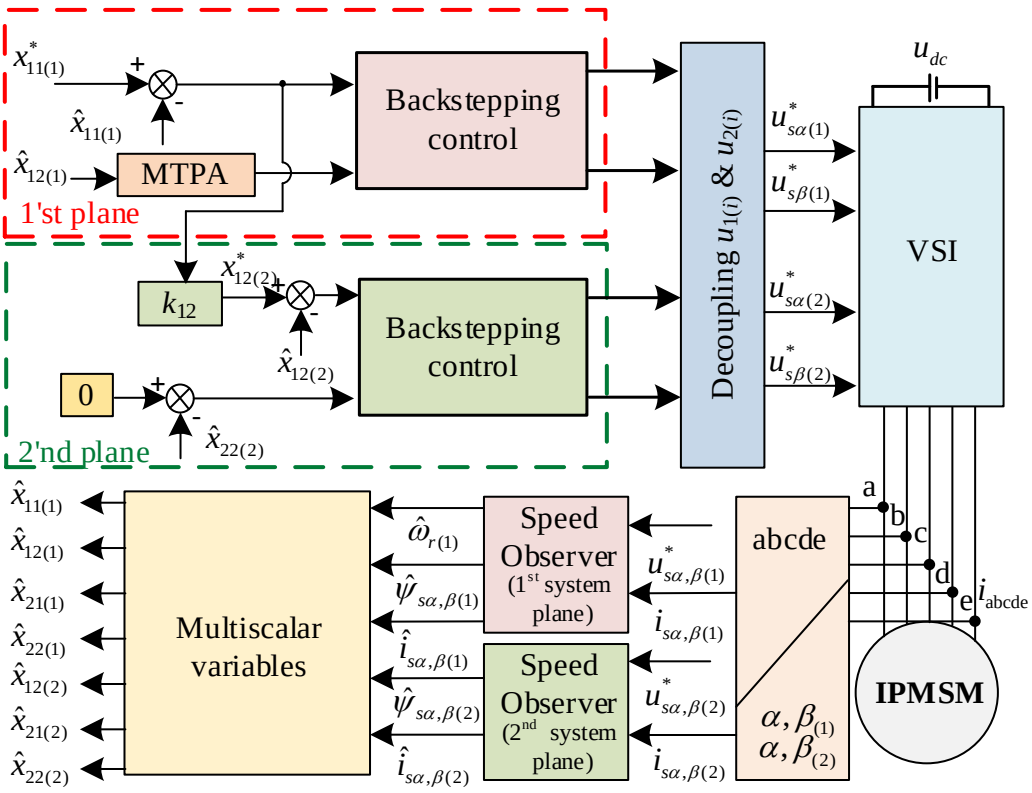

Fig. 4.12 The control diagram of the proposed backstepping of five-phase IPMSM

The reference value of $x^*_{12(i)}$ appearing in (4.79) can be limited using (4.92), where $x_{12\lim(i)}$ is the set value of torque limitation, $i^2_{s\max(i)}$ is the square of the maximum current. In the proposed control $limit_{12(i)}$ was introduced in (4.90), the value of $limit_{12(i)}$ was either 0 or 1 as per the requirement of set limiting variables [78], [142]. The limitations of the variables can be applied as per (4.93) and (4.94).

$$x_{12\lim(i)} = \sqrt{i^2_{s\max(i)} x_{21(i)} - x^2_{22(i)}} \tag{4.92}$$

$$if\ (x^*_{12} > x_{12(i)\lim})\ then \begin{Bmatrix} limit_{12(i)} = 0 \\ e_2 = x_{12(i)\lim} - x_{12(i)} \end{Bmatrix}, \tag{4.93}$$

$$if\ (x^*_{12} < -x_{12(i)\lim})\ then \begin{Bmatrix} limit_{12(i)} = 0 \\ e_2 = -x_{12(i)\lim} - x_{12(i)} \end{Bmatrix}\ else\ limit_{12(i)} = 1. \tag{4.94}$$

From the differential equation (4.90), control variables $u_{1(i)}$ and $u_{2(i)}$ can be obtained as (4.95) - (4.96). The value of load torque can be estimated from (4.97)

$$u_{1(i)} = (k_{12(i)} + k_{11(i)})e_{12(i)} + limit_{12(i)}((-k_{11(i)}^2 J + \frac{1}{J})e_{11(i)}) + \dot{\hat{T}}_L + \frac{R_s}{L_q(i)} x_{12(i)} + \frac{1}{L_{q(i)}} x_{11(i)} \psi_{f(i)}^2 + x_{11(i)} x_{22(i)} \quad (4.95)$$

$$u_{2(i)} = k_{22(i)} e_{22(i)} + \frac{R_s}{L_{q(i)}} x_{22(i)} - x_{11(i)} x_{12(i)} \quad (4.96)$$

$$\dot{\hat{T}}_{L(i)} = \gamma_{l(i)} (\frac{1}{J} e_{11(i)} + k_{11(i)} e_{12(i)}) \quad (4.97)$$

The obtained control variables $u_{1(i)}$ and $u_{2(i)}$ ensure the system stability and final form of the system is represented using (4.98)

$$\dot{V}_{(i)} = -\sum_{i=1}^{N} \left(k_{11(i)} e_{11(i)}^2 + k_{12(i)} e_{12(i)}^2 + k_{22(i)} e_{22(i)}^2 \right) \quad (4.98)$$

The control variables are transformed to stationary voltage components $u_{s\alpha(i)}$ and $u_{s\beta(i)}$ to supply to the five-phase inverter, given as (4.99) - (4.100).

$$u_{s\alpha(i)} = L_{q(i)} \left(\frac{u_{2(i)} \psi_{sa(i)} - u_{1(i)} \psi_{s\beta(i)}}{x_{21(i)}} \right) \quad (4.99)$$

$$u_{s\beta(i)} = L_{q(i)} \left(\frac{u_{2(i)} \psi_{s\beta(i)} + u_{1(i)} \psi_{s\alpha(i)}}{x_{21(i)}} \right) \quad (4.100)$$

Simulation and experimental analysis of the proposed backstepping multiscalar control structure is provided in the Chapter – 5. In the following section, process of gain selection is explained for $(\boldsymbol{\psi}_{\mathbf{f(i)}}, \mathbf{i}_{\mathbf{s(i)}})$ vector based control structure.

4.4 Gain selection of PI in the linearized control structures

4.4.1 Gain selection of the $(\boldsymbol{\psi}_{\mathbf{f(i)}}, \mathbf{i}_{\mathbf{s(i)}})$ vector based control structure

To ensure the stability of the closed loop system, the design of PI coefficients is an important task in control system. Different approaches are demonstrated in the literature [143]. The selected tuning gains $k_{p(i)}$ and $k_{i(i)}$ must ensure the following design objectives: ensure the closed loop stability of the drive system, reject disturbances, obtain fast tracking of reference points, and an appropriate degree of flexibility to process change. Fig. 4.13 shows the cascaded PI control structure of speed loop and electromagnetic torque loop and Fig. 4.14 depicts the flux controlling loop where one PI controller is used. The control loop presented in Fig. 4.13 shows the control of the

electromechanical subsystem variables and in Fig. 4.14, the control of the electromagnetic subsystem variable is shown. Firstly, PI coefficients of the inner loop is obtained as shown in Fig. 4.13, then the coefficients of the outer loop PI will be computed.

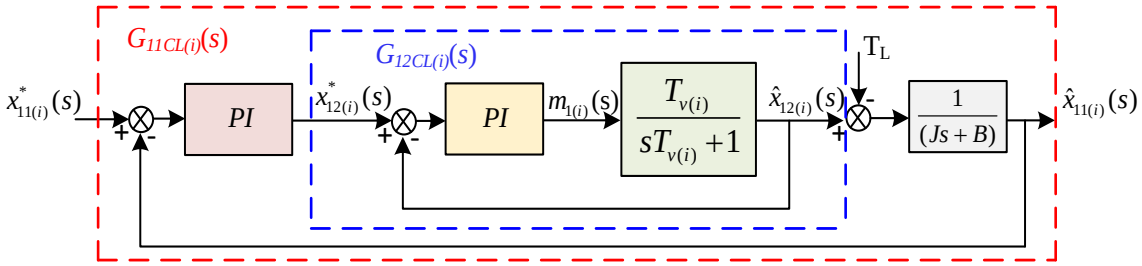

Fig. 4.13 Cascade PI controllers for electromagnetic torque loop and speed loop

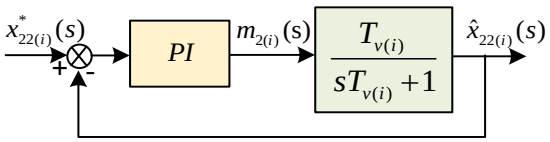

Fig. 4.14 Flux controlling loop

The analytical representation of open loop transfer function of torque loop is presented in (4.101).

$$G_{12OL(i)}(s) = PI\left(\frac{T_{v(i)}}{sT_{v(i)}+1}\right) \tag{4.101}$$

$$G_{12OL(i)}(s) = \left(k_{p12(i)} + \frac{k_{i12(i)}}{s}\right)\left(\frac{T_{v(i)}}{sT_{v(i)}+1}\right) \tag{4.102}$$

To design the torque, speed and flux controller, unity feedback is assumed. The close loop transfer function of torque loop matches to standard canonical form as presented in (4.103), where ω_n is natural frequency and ζ is damping ratio. The following designed specification are used to design the control system: 2% settling in less than a second (t_s), peak duration of less than 0.50 seconds (t_p), and 5% or less maximum overshoot.

$$G_{12CL(i)}(s) = \frac{G_{12OL(i)}(s)}{1+G_{12OL(i)}(s)} \approx \frac{\omega_n^2}{s^2+2\zeta\omega_n s+\omega_n^2} \tag{4.103}$$

$$G_{12CL(i)}(s) = \frac{(k_{p12(i)}s + k_{i12(i)})}{s^2 + (T_{v(i)}^{-1} + k_{p12(i)})s + k_{i12(i)}} \tag{4.104}$$

By using the same approach of open loop $G_{12OL(i)}$, and closed loop $G_{12CL(i)}$ transfer functions of torque loop, the open loop $G_{22OL(i)}$, and closed loop $G_{22CL(i)}$ transfer functions of flux controlling loop can also be prepared as (4.105) - (4.106). It can be observed that the open loop transfer function and closed loop transfer function of the flux controlling loop has the same form (4.105) and (4.106).

$$G_{22OL(i)}(s) = PI\left(\frac{T_{v(i)}}{sT_{v(i)}+1}\right) \tag{4.105}$$

$$G_{22CL(i)}(s) = \frac{(k_{p22(i)}s + k_{i22(i)})}{s^2 + (T_{v(i)}^{-1} + k_{p22(i)})s + k_{i22(i)}} \tag{4.106}$$

After solving the closed loop equation of torque controlling loop (4.104) and flux controlling loop (4.106) in MATLAB for different value of $k_{p(i)}$ and $k_{i(i)}$. The value of $k_{p(i)}$ was changed from the range of 1 to 10 and $k_{i(i)}$ was changed from 0.0001 to 0.1. The following proportional controller gains and integral controller gains are identified for torque controlling loop and flux controlling loop for first plane and second plane.

$$\begin{aligned} k_{p12(1)}, k_{p12(2)} &= 5 \\ k_{p22(1)}, k_{p22(2)} &= 2.5 \end{aligned} \tag{4.107}$$

$$\begin{aligned} k_{i12(1)}, k_{i12(2)} &= 0.01 \\ k_{i22(1)}, k_{i22(2)} &= 0.01 \end{aligned} \tag{4.108}$$

After identification PI gains of torque controlling loop, tuning gains of the speed controller is identified. First, the open loop transfer function of speed loop is represented in (4.109) and after substituting required variables in the open loop transfer function it can be expressed as (4.111).

$$G_{11OL(i)}(s) = PI\ G_{12CL(i)}(s)\left(\frac{1}{Js+B}\right) \tag{4.109}$$

$$G_{11OL(i)}(s) = \left(k_{p11(i)} + \frac{k_{i11(i)}}{s}\right)\left(\frac{(k_{p12(i)}s + k_{i12(i)})}{s^2 + (T_{v(i)}^{-1} + k_{p12(i)})s + k_{i12(i)}}\right)\left(\frac{1}{Js+B}\right) \tag{4.110}$$

$$G_{11OL(i)}(s) = \left(\frac{k_{p11(i)}k_{p12(i)}s^2 + (k_{p11(i)}k_{i12(i)} + k_{11i(i)}k_{p12(i)})s + k_{11i(i)}k_{i12(i)}}{Js^4 + (J(T_{v(i)}^{-1} + k_{p12(i)}) + B)s^3 + (Jk_{i12(i)} + B(T_{v(i)}^{-1} + k_{p12(i)}))s^2 + Bk_{i12(i)}s}\right) \tag{4.111}$$

The closed loop characteristic equation of the speed loop can be written as (4.112), where $H(s)$ is the unity feedback of the system.

$$G_{11CL(i)}(s) = \frac{G_{11OL(i)}(s)}{1 + G_{11OL(i)}(s)} \tag{4.112}$$

By solving (4.112) in MATLAB for different values of $k_{p11(1)}$ and $k_{i11(1)}$ shown in Table 4.1, bode plot analysis of the closed loop transfer function of the speed loop can be conducted. The bode plot of the closed loop transfer function of the speed loop is presented in Fig. 4.15.

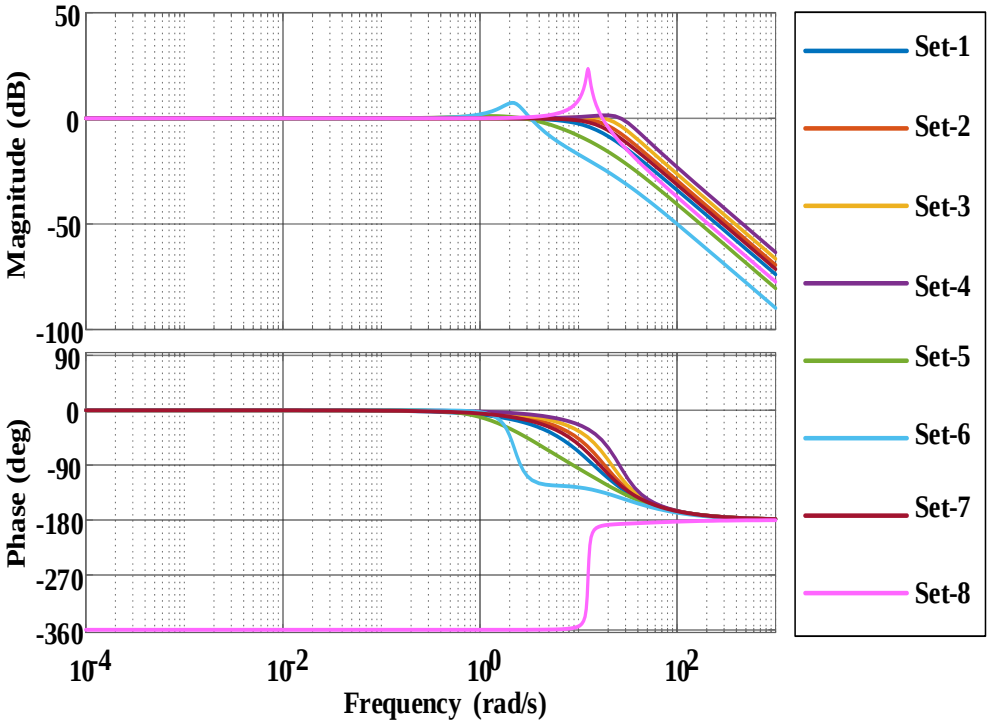

Fig. 4.15 Bode plot of speed loop

Table 4.1 Set of tuning gains for speed loop

Gains	Set-1	Set-2	Set-3	Set-4	Set-5	Set-6	Set-7	Set-8
$k_{p11(1)}$	10	7	2.5	1.5	3.5	1	8	0.5
$k_{i11(1)}$	0.001	0.005	0.002	0.0001	0.05	0.09	0.001	0.01

Based on the obtained phase margin (PM) and gain margin (GM), the conclusion about close loop system stability is made. To ensure the stability, phase margin and gain margin must be positive, if the either margin is zero then the system is marginally stable, if any of the margin is less than zero than system is unstable.

The step response of the speed loop is demonstrated in Fig. 4.16. The stability margin and step response performance values are given in Table 4.2.

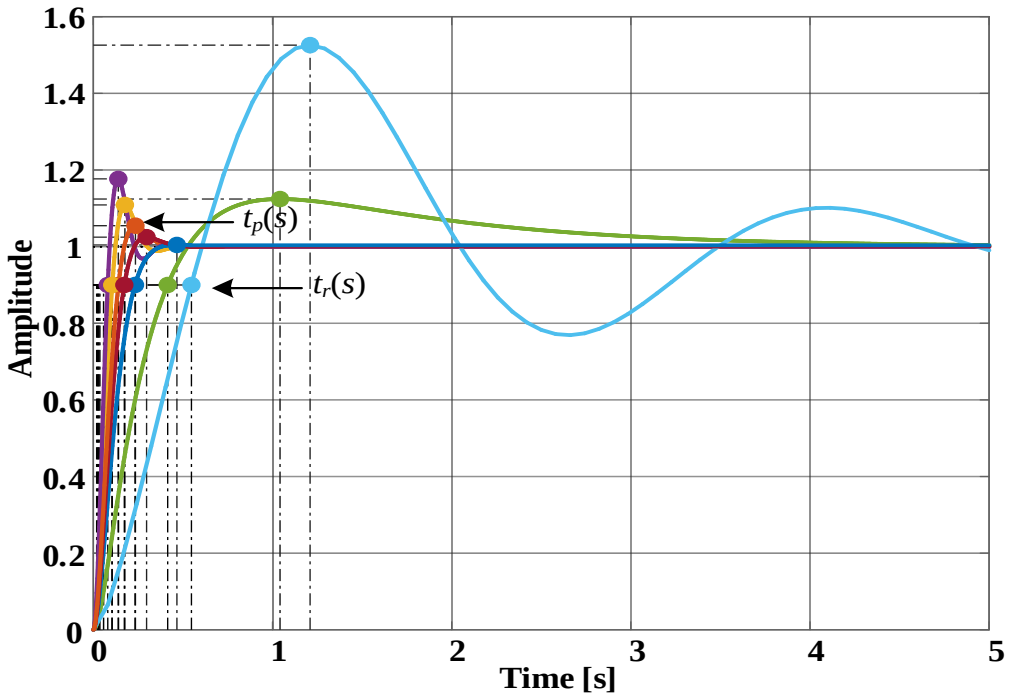

Fig. 4.16 Step response of the speed loop

Table 4.2 Performance value for different set of PI gains

Parameter	Set-1	Set-2	Set-3	Set-4	Set-5	Set-6	Set-7	Set-8
PM	174.5	147.6	109.3	86.1	138.4	67.2	175.2	-9.3
GM	∞	∞	∞	∞	∞	∞	∞	∞
Stable	Yes	Yes	Yes	Yes	Yes	Yes	Yes	No
$t_r(s)$	0.196	0.112	0.082	0.061	0.357	0.443	0.141	NaN
$t_s(s)$	0.313	0.330	0.271	0.315	3.320	6.078	0.342	NaN
Mp%	0.447	5.466	10.900	17.683	12.427	52.59	2.488	NaN
Peak value	1.004	1.054	1.109	1.176	1.124	1.525	1.024	Inf
$t_p(s)$	0.466	0.235	0.176	0.139	1.042	1.209	0.297	Inf

It can be observed form Table 4.2, for different values of $k_{p11(1)}$ and $k_{i11(1)}$, Set – 1 to Set – 7 provide positive gain margin and phase margin hence system is stable. For Set – 8, system has infinite gain margin but phase margin is negative around -9.3° hence the closed loop system is unstable for the given case. Moreover, it is important to mention that from $k_{p11(1)}$ and $k_{i11(1)}$, Set – 2 to Set – 6 is able to achieve the stable performance of the closed loop system but it failed to meet desired performance criteria

as can be seen in Table 4.2. It can be observed that maximum peak overshoot is more than 5% for Set – 2 to Set – 6. For Set – 1 and Set – 7, maximum peak overshoot was around 0.447% and 2.488%, respectively. Other criteria such as settling time and rise time were also met by Set – 1 and Set – 7. The closed loop transfer function of the speed loop and flux control loop remains the same for stator current vector $\mathbf{i_{s(i)}}$ and stator flux vector $\boldsymbol{\psi}_{\mathbf{s(i)}}$ based nonlinear feedback control structure. Hence, the performed stability analysis remains the same for stator current vector $\mathbf{i_{s(i)}}$ and stator flux vector $\boldsymbol{\psi}_{\mathbf{s(i)}}$ based nonlinear feedback control structure. The stability analysis of electrotechnical loop remains the same, the only change is visible is in square of the stator flux loop, instead of $k_{p22(1)}$ and $k_{i22(1)}$, $k_{p21(1)}$ and $k_{i21(1)}$ is obtained in the similar way. The square of stator flux loop is shown in the Fig. 4.17.

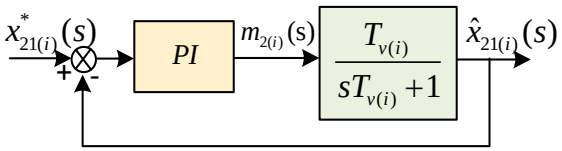

Fig. 4.17 Square of stator flux loop

In the next section, gain tuning process of backstepping multiscalar control of five-phase IPMSM is explained.

4.4.2 Gain tuning of the backstepping multiscalar control technique of five-phase IPMSM

The dynamics of the tracking errors defined in the nonlinear state feedback control structure can be rewritten as per the given the form (4.113) - (4.116).

$$\dot{e}_{11(i)} = -k_{11(i)}e_{11(i)} + \frac{1}{J}e_{12(i)} - \frac{1}{J}\tilde{T}_{L(i)} \tag{4.113}$$

$$\dot{e}_{12(i)} = -k_{12(i)}e_{12(i)} \tag{4.114}$$

$$\dot{e}_{22(i)} = -k_{22(i)}e_{22(i)} \tag{4.115}$$

$$\dot{\tilde{T}}_{L(i)} = \gamma_{l(i)}\left(\frac{1}{J}e_{11(i)} + k_{11(i)}e_{12(i)}\right) \tag{4.116}$$

The error dynamics can be rearranged as per matrix $\mathbf{E_{e(i)}}$ defined in (4.117), where $k_{11(i)}$ to $k_{22(i)}$ and $\gamma_{l(i)} > 0$.

$$\mathbf{E}_{e(i)} = \begin{bmatrix} -k_{11(i)} & \frac{1}{J} & 0 & -\frac{1}{J} \\ 0 & -k_{12(i)} & 0 & 0 \\ 0 & 0 & -k_{22(i)} & 0 \\ \frac{\gamma_{l(i)}}{J} & \gamma_{l(i)} k_{11(i)} & 0 & 0 \end{bmatrix} \tag{4.117}$$

In Fig. 4.18, the spectrum of $\mathbf{E}_{e(i)}$ are presented. In Fig. 4.18 (a), $k_{11(i)}$ was changed from 0.01 to 1.0 p.u and in Fig. 4.18 (b), $k_{12(i)}$ was also changed from 0.01 to 1.0 p.u. eigen values of the matrix $\mathbf{E}_{e(i)}$ lies in the left half of the *s*-plane which ensure the stability of the system.

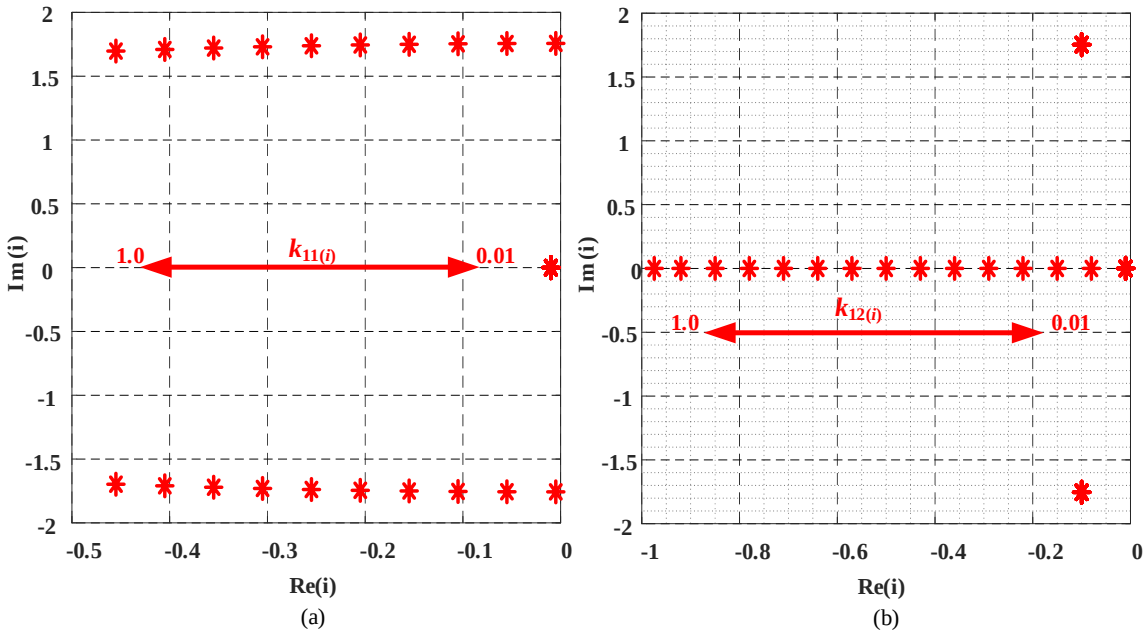

Fig. 4.18 Spectrum of Matrix $\mathbf{E}_{e(i)}$ (a) $k_{11(i)}$ varies from 0.01 to 1.0 p.u. (b) $k_{12(i)}$ varies from 0.01 to 1.0 p.u.

The tuning gains $k_{22(i)}$ was also varied from 0.01 to 1.0 p.u., but it provided similar performance as shown in Fig. 4.18 (b). It can be observed from Fig. 4.18, that as the values of tuning gains increased from 0.01 to 1.0 p.u, eigen values of the matrix $\mathbf{E}_{e(i)}$ are drifting away from the origin.

In summary, this chapter deals with sensorless control structures of three-phase IPMSM and five-phase IPMSM. First, classical FOC control structure ($i_{sd}^{*} = 0$) of three-phase IPMSM was discussed. Later, the description of control structure of five-phase IPMSM begins with the explanations of FOC with MTPA of five-phase IPMSM.

After discussion of existing control scheme, proposed control solutions considering the $\boldsymbol{\psi}_{f(i)}, \mathbf{i}_{s(i)}$ vectors and $\boldsymbol{\psi}_{s(i)}, \mathbf{i}_{s(i)}$ vectors are explained. Using $\boldsymbol{\psi}_{s(i)}, \mathbf{i}_{s(i)}$ vectors two type

control structure are proposed. Furthermore, advanced control structure such as predictive multilscalar control using $\boldsymbol{\psi}_{s(i)}, \mathbf{i}_{s(i)}$ vectors and backstepping multiscalar control using the $\boldsymbol{\psi}_{f(i)}, \mathbf{i}_{s(i)}$ vectors are proposed and explained in details.

Following that, tuning gains of the proposed control systems were identified using bode plot analysis and the step response of the multiscalar control system using $\boldsymbol{\psi}_{f(i)}, \mathbf{i}_{s(i)}$ vectors is presented using MATLAB. The gain tuning process of the backstepping multiscalar control is also presented in this doctoral thesis.

In the next chapter, to validate the closed loop performance of the designed observer structures and proposed control systems of five-phase IPMSM are verified using the simulation as well as experimental tests.

CHAPTER 5: SIMULATION AND EXPERIMENTAL INVESTIGATIONS

5.1 Overview

In this chapter, discussion of simulation and experimental results of three phase IPMSM drive and five-phase IPMSM drive are provided. The analysis begins with simulation and experimental results of adaptive observer structure and non-adaptive of three-phase IPMSM drive. To verify the performance of adaptive and nonadaptive observer structures at different speed range in simulation and experimental stand, classical FOC structure was employed. Moreover, the comparative analysis between the adaptive and non-adaptive observer structure is provided.

In the following, performance of five-phase IPMSM drive using the proposed control structures: $\boldsymbol{\psi}_{f(i)}, \mathbf{i}_{s(i)}$ vectors and $\boldsymbol{\psi}_{s(i)}, \mathbf{i}_{s(i)}$ vectors are depicted using the simulation and experimental results. The proposed multiscalar transformation-based control structures are applied using the classical PI, predictive control and backstepping control. Proposed control solutions using nonlinear transformation is compared with the FOC structure and MPC based FOC structure. This chapter of the thesis is focused on benefits of using the proposed control strategies of five-phase IPMSM drive such as improved control flexibility, enhanced electromagnetic torque using 3^{rd} harmonic injection, fault-tolerant operation. In addition, the comparative analysis between the conventional control schemes and proposed control scheme is provided.

5.2 Simulation results of 3-phase IPMSM drive

The simulation work was carried out in WinSim where simulation program was written in the C language and was developed in the department. The simulation code was extended for the declaration of machine model of IPMSM, state observer, control system and transformation. The use of C programming language provides quick transition to the practical DSP program during the experimental work. The nominal parameters of three-phase machine are defined in Appendix - A The depicted results are provided in the per unit system.

5.2.1 Simulation results of rotor flux vector-based adaptive observer and non-adaptive observer using classical FOC structure

Simulation results of drive starting up to nominal speed and reversing from 1.0 p.u to -1.0 p.u. using the adaptive and non-adaptive rotor flux vector-based observer structure are presented in Fig. 5.1 and Fig. 5.2, respectively.

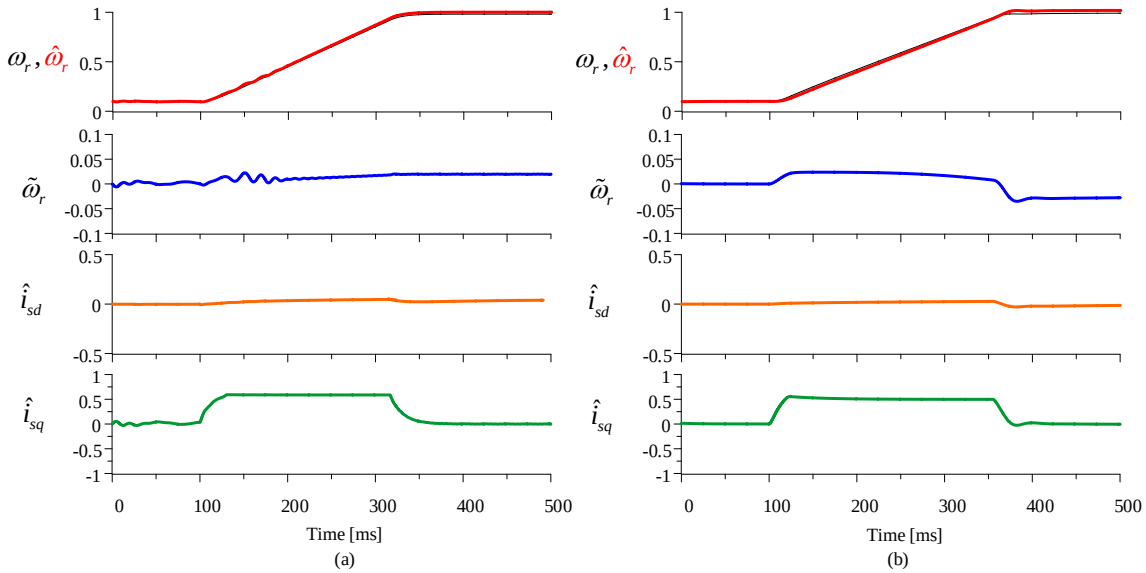

Fig. 5.1 Simulation results of 3-phase IPMSM drive starting up to 1.0 p.u. (a) Adaptive observer structure (b) Non-adaptive observer structure

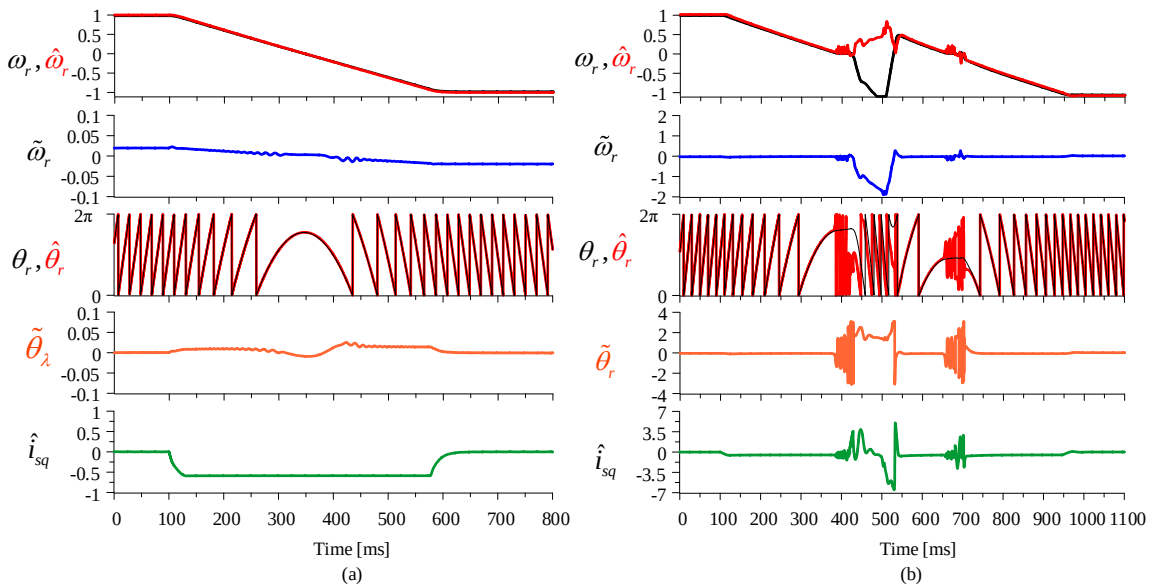

Fig. 5.2 Simulation results of 3-phase IPMSM drive reversing from 1.0 p.u to -1.0 p.u. (a) Adaptive observer structure (b) Non-adaptive observer structure

In Fig. 5.1, three-phase IPMSM drive performance is visible for drive starting up to 1.0 p.u. The simulation performance of the rotor flux vector-based adaptive and non-adaptive observer is similar to Fig. 5.3 for the same state variables. Error between the measured speed and estimated speed was less than 0.015 p.u. for adaptive observer

structure and 0.04 p.u. for non-adaptive observer structure. The direct axis current $\hat{i}_{sd}$ was almost zero during this test and the quadrature axis current $\hat{i}_{sq}$ increased from 0.0 p.u to 0.6 p.u during the dynamic state and again decreased to 0.0 p.u. as drive reaches the steady state.

In Fig. 5.2, simulation analysis is conducted for the case of drive reversal, where three-phase IPMSM drive is reversing from 1.0 p.u. to -1.0 p.u. using the adaptive observer in Fig. 5.2 (a) and using the non-adaptive observer structure in Fig. 5.2 (b). It can be observed from Fig. 5.2, that adaptive observer structure provides satisfactory performance during the reversal test, while non-adaptive observer struggle to estimate rotor speed and position during the zero crossing. The primary reasons for the poor performance of non-adaptive observer structures are nonlinearity of the inverter, significant voltage drop at low speed and lower amplitude of back EMF. The information of position error $\tilde{\theta}_{\lambda}$ in adaptive observer structure is computed using the defined stabilizing function (3.27).

5.2.2 Simulation results of active flux-based adaptive observer and non-adaptive observer using classical FOC structure

In Fig. 5.3 and Fig. 5.4, simulation results of active flux based adaptive observer and non-adaptive observer are presented for 2 cases: 1) drive starting up to nominal speed 2) reversing from 1.0 p.u. to -1.0 p.u. In Fig. 5.3, dynamic performance of three-phase IPMSM drive is presented for the first case. Measured speed ω_r, estimated speed $\hat{\omega}_r$, speed estimation error $\tilde{\omega}_r$, current components in rotating coordinates $\hat{i}_{sd,q}$ are shown. As shown in Fig. 5.3, three-phase IPMSM drive starts to accelerates from 0.1 p.u to 1.0 p.u. When drive starts acceleration, torque component $\hat{i}_{sq}$ increases from 0.0 p.u and reaches to defined limit 0.6 p.u during the dynamic state. When IPMSM drive reaches to steady state, electromagnetic torque decreases to 0.0 p.u due to no-load condition. In addition, flux controlling current component $\hat{i}_{sd}$ remains almost to 0.0 p.u. The speed estimation error was less than 0.05 p.u. for adaptive observer structure and non-adaptive observer structure during the transient state of three-phase IPMSM drive.

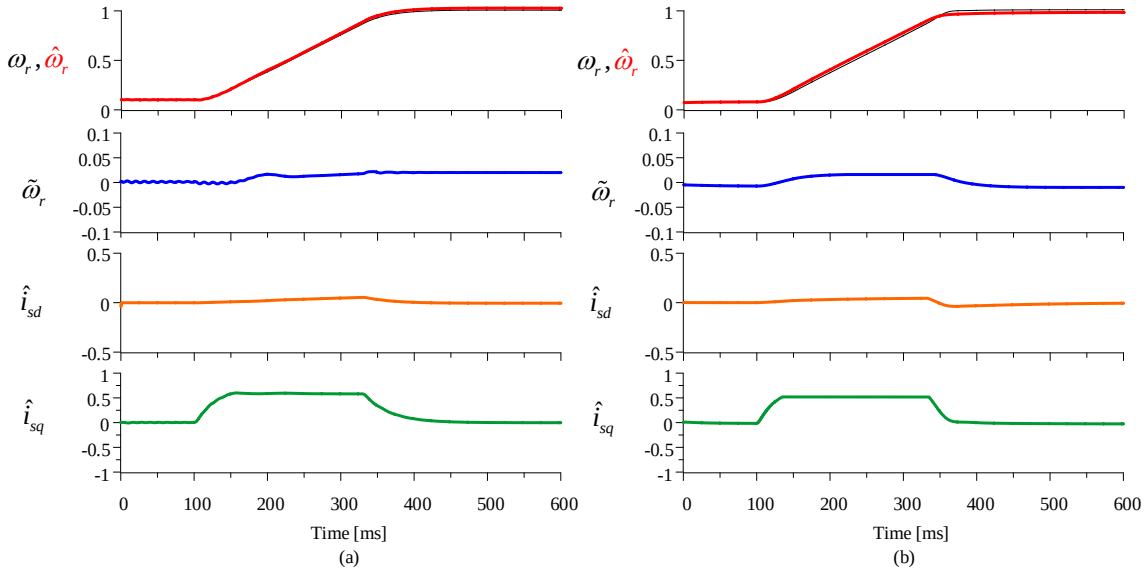

Fig. 5.3 Simulation results of three-phase IPMSM drive starting up to 1.0 p.u. (a) Adaptive observer structure (b) Non-adaptive observer structure

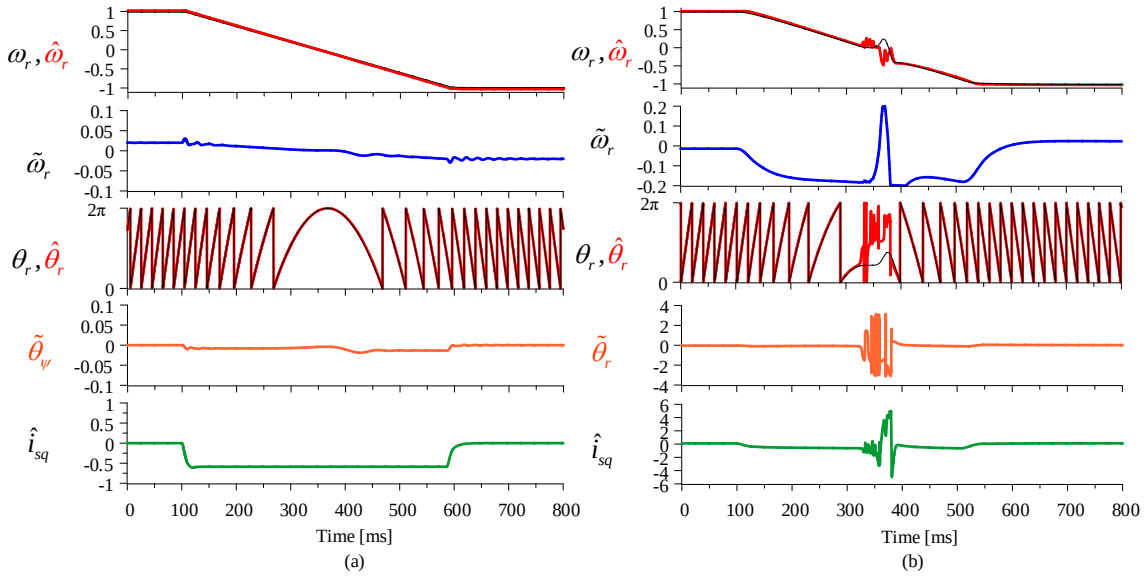

Fig. 5.4 Simulation results of three-phase IPMSM drive reversing from 1.0 p.u to -1.0 p.u. (a) Adaptive observer structure (b) Non-adaptive observer structure

Fig. 5.4 depicts the performance of three-phase IPMSM drive using adaptive observer and non-adaptive observer structure for the case of drive reversal from 1.0 p.u. and -1.0 p.u. State variables such as Measured speed ω_r, estimated speed $\hat{\omega}_r$, speed estimation error $\tilde{\omega}_r$, measured position θ_r and estimated position $\hat{\theta}_r$, position estimation error $\tilde{\theta}_r, \tilde{\theta}_\psi$, torque controlling current component $\hat{i}_{sq}$ are visible in Fig. 5.4. It can be observed from Fig. 5.4(a) that using adaptive observer structure, three-phase IPMSM drive crosses zero speed successfully and reaches to -1.0 p.u., while non-adaptive observer structure fails to provide desired result at zero crossing as shown in Fig. 5.4(b). In Fig. 5.4(a), position error calculation is made using the proposed stabilization

function given in (3.62). From the given simulation results, it can be noticed that due to lower amplitude of back EMF non-adaptive observer structure provides poor performance compared to adaptive observer structure. The dynamic performance of is close to Fig. 5.2 for same state variables.

Compared to Fig. 5.2(b), non-adaptive estimation using active flux-based observer also struggles to estimate at speed reversal but provide better performance as shown in Fig. 5.4(b). The theoretical hypothesis is confirmed using the chosen simulation results for the case of drive starting up to nominal speed and drive reversal. The effectiveness of the active flux-based observer structures and rotor flux vector-based observer structure are verified using the experimental investigations in the following sections.

5.3 Experimental results of 3-phase IPMSM drive

The performance of the sensorless control system using the adaptive observer structure and non-adaptive observer structure is evaluated in real-time operating conditions using the set of laboratory equipment. The experimental test was carried out on a 3.5kW IPMSM drive system. A voltage source converter supplies the three-phase drive system. All the nominal parameters of the three-phase IPMSM drive is provided in Appendix – A. The control system was interfaced with digital signal processor (DSP) *Sharc* ADSP21363 floating-point signal processor and Altera Cyclone 2 FPGA with sampling time of 150μs (6.6kHz). The switching frequency of the transistor was 3.3kHz. The three-phase IPMSM drive contains spatial harmonics and non-sinusoidal distribution of EMF as presented in Fig. 5.5.

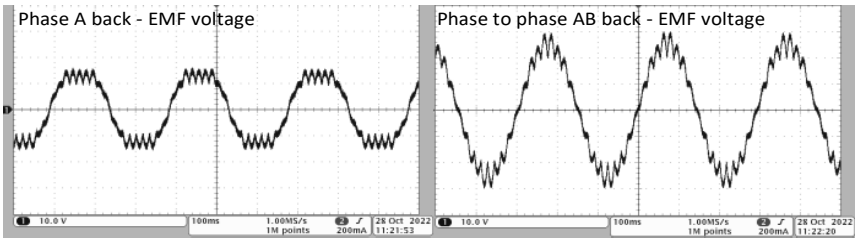

(a) (b)

Fig. 5.5 Steady state of three-phase machine (a) Phase – A back EMF (b) Phase to phase AB back EMF

The control system structure can be seen in Fig. 4.2. To measure the current in natural reference frame, LA 25-NP transducer was used. To implement observer structure in the stationary reference frame, the measured current was transformed to stationary coordinate system (α-β) using the Clarke transformation. Furthermore, the estimated state variables are transformed to rotating coordinate system to apply

classical FOC where i_{sd}^{*} = 0 applied. The depicted results are in per unit system. The nominal value of torque limit was around 1.0 p.u. but for thermal management, safety and protection reasons torque limit was adjusted to small value around 0.7 p.u. or 0.6 p.u. In addition, the computation time of the control system is 49µs without applying the code optimization. The incremental encoder of 2048 pulses per revolution (PPR) was used to measure the speed of three-phase IPMSM drive. The only purpose of using the encoder was to confirm the estimation accuracy of the observer structures.

5.3.1 Experimental results of rotor flux-based adaptive observer and non-adaptive observer using classical FOC structure

In Fig. 5.6, reversal of IPMSM drive is shown from 0.1 p.u. to -0.1 p.u. using the adaptive observer structure. During the low-speed reversal test, torque value was limited up to 0.5 p.u. The observer structure is prepared using the sinusoidal machine model. Due to machine asymmetry, small oscillations are visible at low-speed operation of the IPMSM drive. It can be observed that estimated speed and position follows that measured speed and position. Estimated current component in q-axis and speed error are also shown.

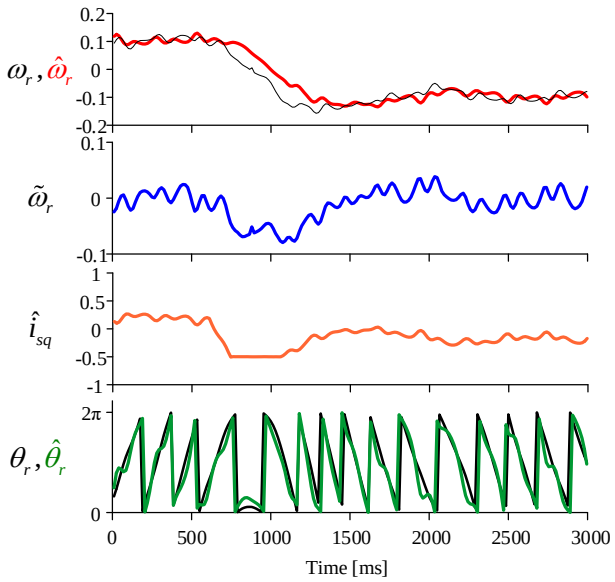

Fig. 5.6 Experimental results of 3-phase IPMSM drive reversing from 0.1 p.u to -0.1 p.u. using Adaptive observer

In Fig. 5.7, drive reversal performance is presented using the non-adaptive observer structure. Fig. 5.7(a) shows that the drive reverses from 0.1 p.u. to -0.1 p.u. and in Fig. 5.7(b) drive reverses back from -0.1 p.u. to 0.1 p.u. At zero crossing, the estimation of speed and position becomes extremely difficult for observer structure. The IPMSM

drive suffers heavily due to machine disturbances at low-speed operation. Overall, in both cases, as shown in Fig. 5.7(a) and Fig. 5.7(b) observer structure fails to provide satisfactory results at low speed even though torque reaches to maximum value of 1.0 p.u., other estimated parameters are also shown in Fig. 5.7.

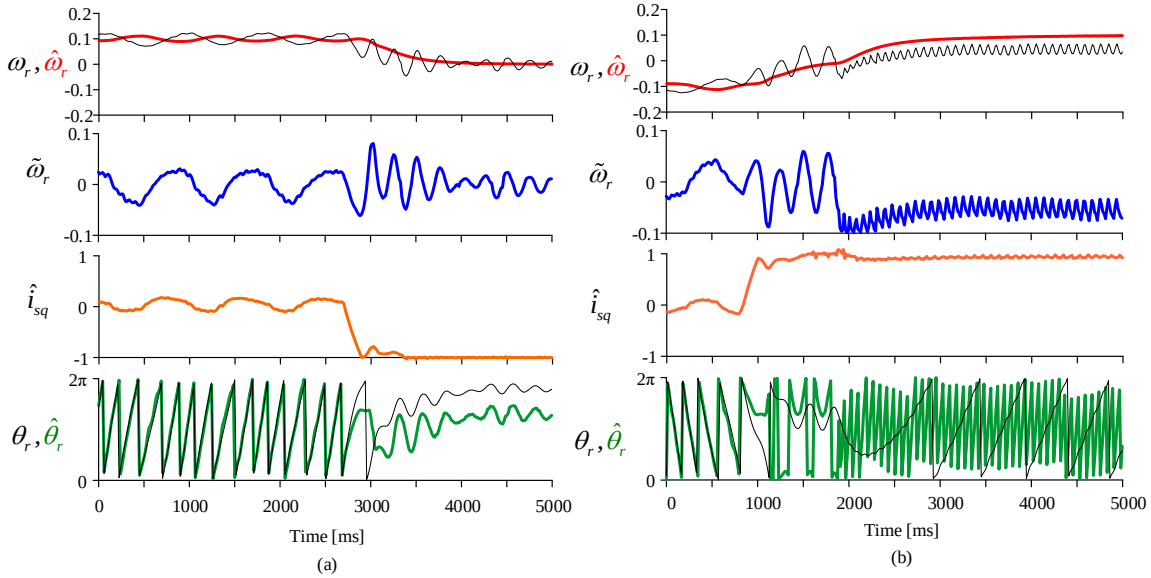

Fig. 5.7 Experimental results of 3-phase IPMSM drive reversing from 0.1 p.u to -0.1 p.u. using Non-adaptive observer

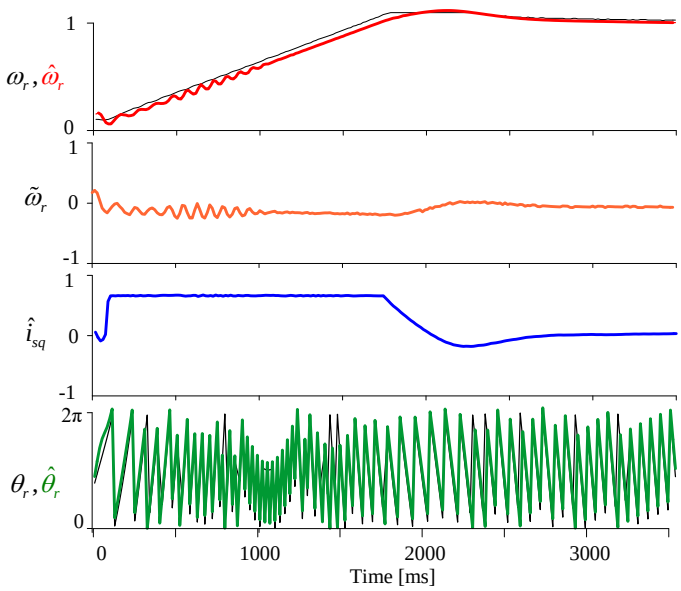

Fig. 5.8 Experimental results of 3-phase IPMSM drive starting to nominal speed using the adaptive observer

Results of the three-phase IPMSM drive starting up from 0.1 p.u to 1.0 p.u. using adaptive observer structure is presented in Fig. 5.8. Adaptive observer structure follows the reference speed command but speed estimation error during the transient state is

less than 0.05 p.u. In addition, the effects of spatial harmonics are not visible during the medium and high-speed ranges as compared to low-speed range.

Three-phase IPMSM drive reversal from 1.0 p.u to -1.0 p.u. is shown in Fig. 5.9. Three-phase IPMSM drive successfully crosses the zero-speed range using the adaptive observer structure. The calculated speed estimation error during the dynamic state is significantly less than 0.05 p.u. during drive reversal. Considering the results of IPMSM drive, the adaptive observer structure is more robust than the non-adaptive observer structure.

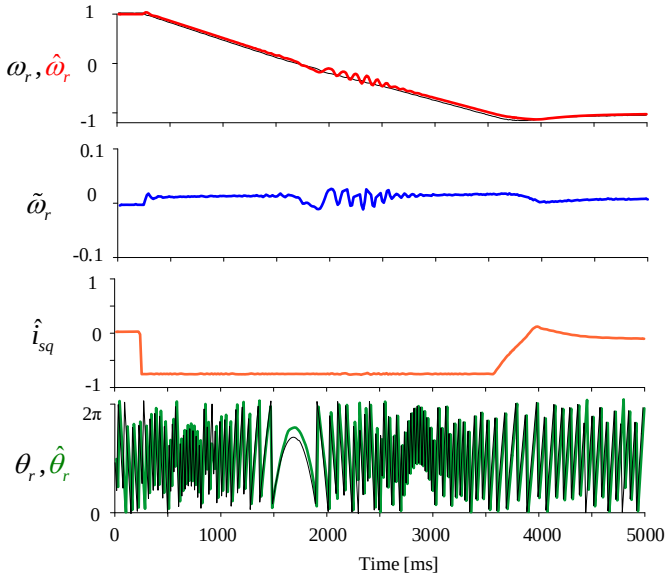

Fig. 5.9 Experimental results of 3-phase IPMSM drive reversing from 1.0 p.u to -1.0 p.u. using the adaptive observer

5.3.2 Experimental results of active flux-based adaptive observer and non-adaptive observer using classical FOC structure

In Fig. 5.10(a), the three-phase IPMSM drive successfully reverses from -0.1 p.u to 0.1 p.u. using the adaptive observer structure but in Fig. 5.10(b), the IPMSM drive struggles to reverse at zero speed using the non-adaptive observer structure. The observer structure is based on sinusoidal machine model. Due to spatial harmonics and non-sinusoidal distribution of EMF, disturbances significantly affect at the low-speed operation as shown in Fig. 5.10. Extending the control system to the damping structure presented in [144], [145] can compensate for this oscillation. However, this thesis only focuses on speed observer structure; the problem of non-sinusoidal distribution of EMF is treated as a disturbance. A low-pass filter (LPF) can be employed to minimize the disturbances.

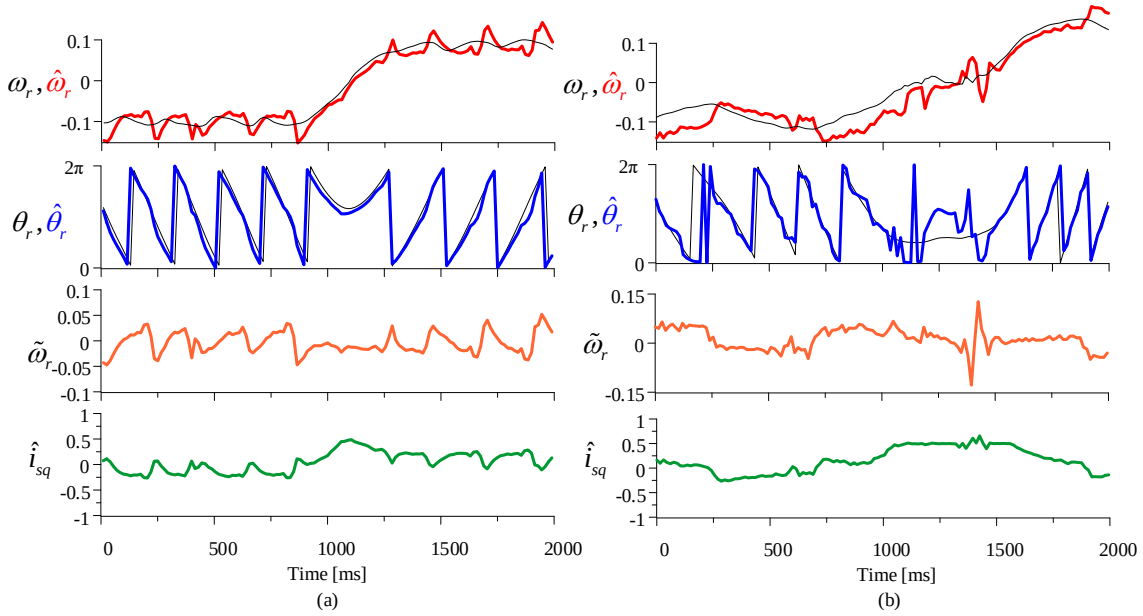

Fig. 5.10 Experimental results of 3-phase IPMSM drive reversing from -0.1 p.u to 0.1 p.u. (a) Adaptive observer (b) Non-adaptive observer

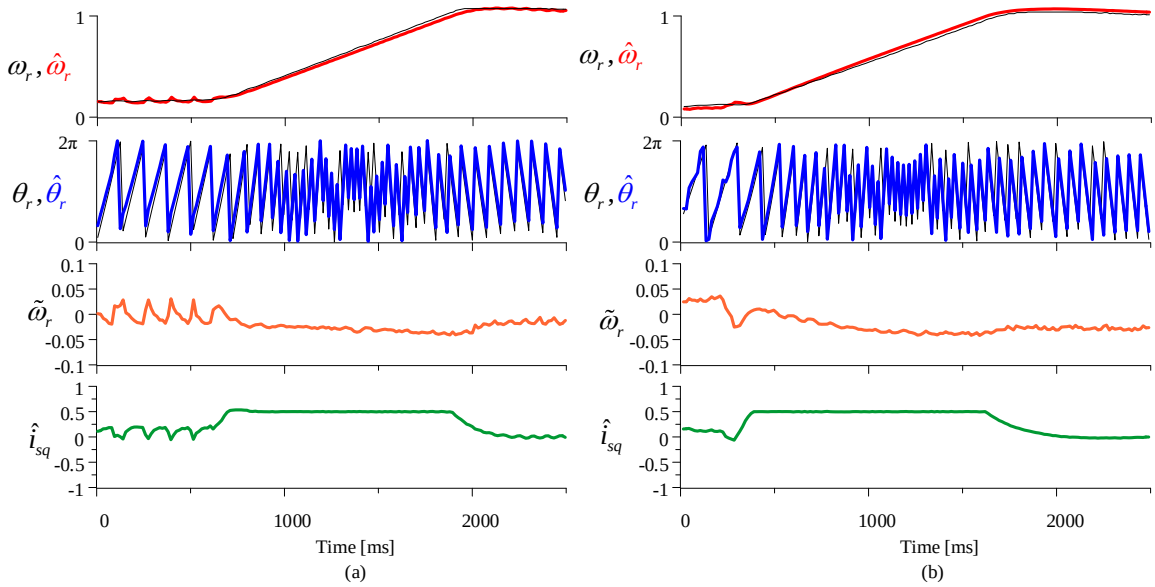

Fig. 5.11 Experimental results of 3-phase IPMSM drive starting up to 1.0 p.u. (a) Adaptive observer (b) Non-adaptive observer

In Fig. 5.11, experimental test is conducted for drive starting up from 0.1 p.u. to 1.0 p.u. It can be seen that the estimated state variables using both types of observer structures works well at medium and high speed but struggle at low speed. Error between estimated speed and measured speed was less than 0.05 p.u. for both observer structure. To minimize the mechanical stress on the machine and reduce overcurrent issues, maximum torque limit was set around 0.5 p.u. When speed changes from 0.1 p.u. to 1.0 p.u., the q-axis current increases from 0.0 p.u to 0.5 p.u. and when drive reaches to steady state q-axis current decreases to 0.0 p.u as shown in Fig. 5.11.

measured speed ω_r, estimated speed $\hat{\omega}_r$, speed estimation error $\tilde{\omega}_r$, measured position θ_r, estimated position $\hat{\theta}_r$, torque repressing current component $\hat{i}_{sq}$ are shown in Fig. 5.11.

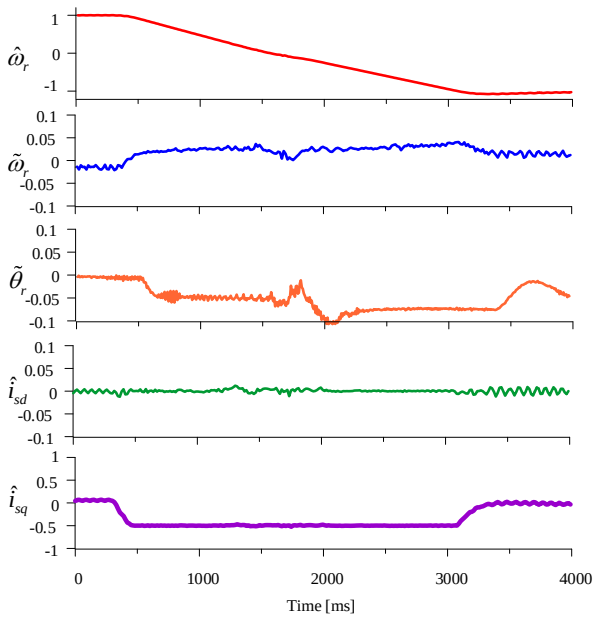

Fig. 5.12 Experimental results of 3-phase IPMSM drive reversing from 1.0 p.u to -1.0 p.u. using Adaptive observer

Fig. 5.12 presents the working of the adaptive observer structure during IPMSM reversal from 1.0 p.u. to -1.0 p.u. The results shows that control system using the adaptive observer crosses the zero-speed range without any problem and reaches to desired speed -1.0 p.u. Important parameters such as estimated speed $\hat{\omega}_r$, speed estimation error $\tilde{\omega}_r$, position estimation error $\tilde{\theta}_r$, current components in *d-q* coordinates system are shown.

Fig. 5.13(a) shows that IPMSM drive reverses from 1.0 p.u. to -1.0 p.u. and in Fig. 5.13(b) IPMSM drive reverses back from -1.0 p.u. to 1.0 p.u. In both cases, IPMSM drive struggles during the zero crossing, however, it reaches maximum value again, but at zero speed, it does not provide satisfactory results. Speed error $\tilde{\omega}_r$ and position error $\tilde{\theta}_r$ are high compared to adaptive observer. As back EMF value is extremely low, which is not enough to estimate speed; hence, the observer structures fail to estimate during the extremely low speed of IPMSM.

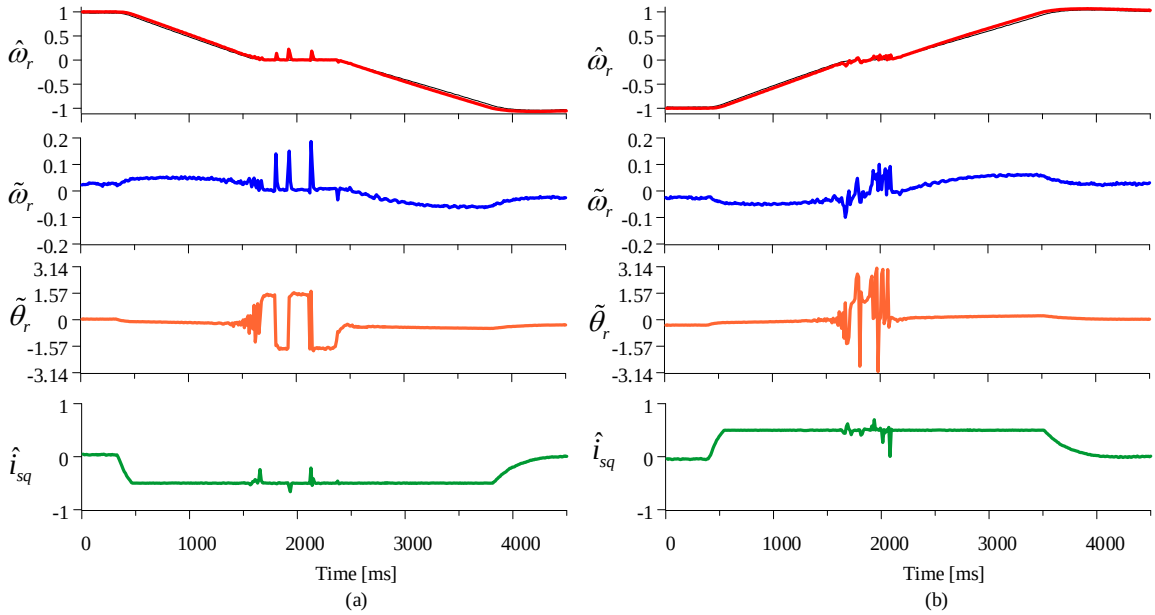

Fig. 5.13 Experimental results of 3-phase IPMSM drive reversing from 1.0 p.u to -1.0 p.u. using Non-adaptive observer

To examine observer structures performance during loading condition, rotor speed was set at 0.5 p.u. and torque limit was increased from 0.5 p.u. to 0.8 p.u as shown in Fig. 5.14.

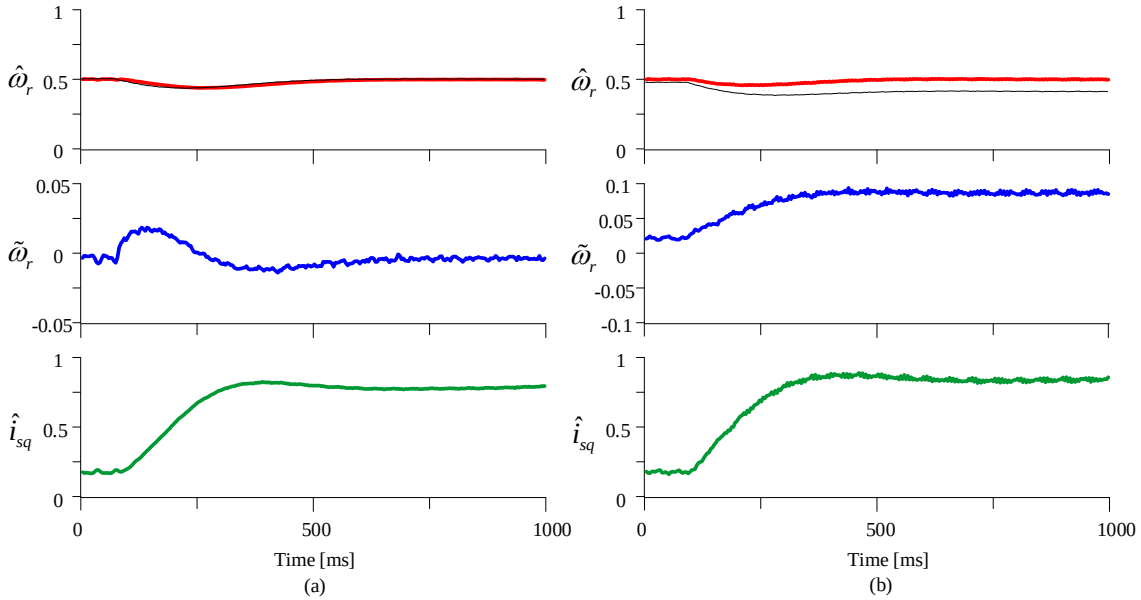

Fig. 5.14 Experimental results of 3-phase IPMSM drive when speed is 0.5 p.u. and load torque increased from 0.2 p.u. to 0.75 p.u. (a) Adaptive observer (b) Non-adaptive observer

After 0.1s applied load torque was increased from 0.2 p.u. to 0.75 p.u. Performance of both observer structure can be visualized in Fig. 5.14(a) and Fig. 5.14(b), respectively. Speed estimation error $\tilde{\omega}_r$ was less than 0.05 p.u. for adaptive observer throughout the test and while speed error was increased non-adaptive observer as

applied load was increased from 0.2 p.u. to 0.75 p.u. It can be seen that the adaptive observer structure is more reliable and provides satisfactory results than non-adaptive observer structure.

The simulation and experimental results of the adaptive and non-adaptive observer structures of three-phase IPMSM validate its effectives. Building on this, the following section provides discussion on simulation results of five-phase IPMSM.

5.4 Simulation investigation of 5-phase IPMSM drive

This section presents the simulation results of different control schemes the five-phase IPMSM drive. The simulation analysis of five-phase IPMSM drive with 3rd harmonic injection was also conducted in Microsoft Visual Studio software. It is important to mention that the 3rd harmonic injection turned on means, the control system in the second plane is turned on. Major portion of the simulation work involves solution of differential equations, reference frame transformation matrices and gain tuning of PI controller. To facilitate the implementation of simulation work in the practical DSP program during the experimental investigations, simulation work was carried out in WinSim. To confirm the theoretical hypothesis, the simulation and experimental tests are conducted using the proposed control structures for different scenarios. The nominal parameters of the five-phase IPMSM are presented in Appendix – A.

5.4.1 Simulation investigation of ($\boldsymbol{\psi}_{f(i)}$,$\mathbf{i}_{s(i)}$) vector based control structure of five-phase IPMSM drive

Simulation results of five-phase IPMSM drive starting up to nominal speed and reversing from 1.0 p.u. to -1.0 p.u. using ($\boldsymbol{\psi}_{f(i)}$,$\mathbf{i}_{s(i)}$) vector based control structure are shown in Fig. 5.15 and Fig. 5.16, respectively. To reduces the losses and enhance the drive performance, MTPA control was employed in the first plane in the proposed control structure using (4.23). As reluctance torque production is extremely small in the second plane, $x^{*}_{22(2)} = 0$ was applied. Moreover, ($\boldsymbol{\psi}_{f(i)}$,$\mathbf{i}_{s(i)}$) vector based control structure is also compared with field-oriented control scheme. For FOC structure maximum limit for torque controlling current $i_{sq(1)}$ and maximum torque limit in the multiscalar control structure was around 1.0 p.u.

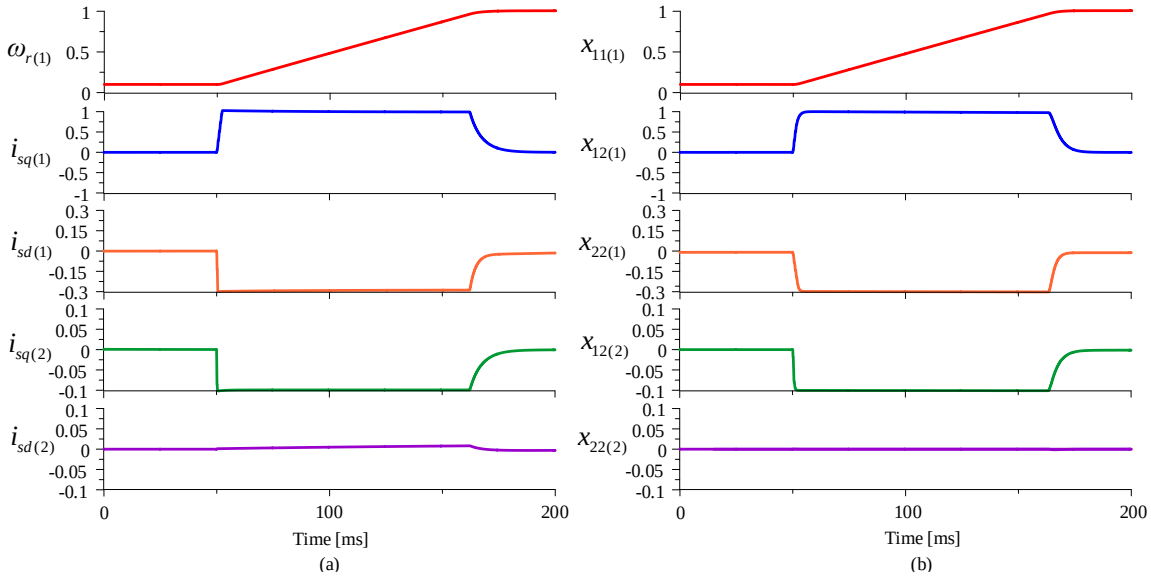

Fig. 5.15 Simulation result of five-phase IPMSM starting up to 1.0 p.u. (a) Field-oriented control (b) $(\boldsymbol{\psi}_{f(i)},\mathbf{i}_{s(i)})$ vector based control structure

In Fig. 5.15(b) and Fig. 5.16(b), multiscalar variables: rotor angular speed in first plane $x_{11(1)}$, generated torque $x_{12(1)}$, $x_{12(2)}$ and flux controlling variables $x_{22(1)}$, $x_{22(2)}$ in first plane and second plane are shown. In Fig. 5.15, when drive accelerates from 0.1 p.u., torque generated in first plane reaches to 1.0 p.u. Simultaneously, torque production in second plane was almost 10% of fundamental torque.

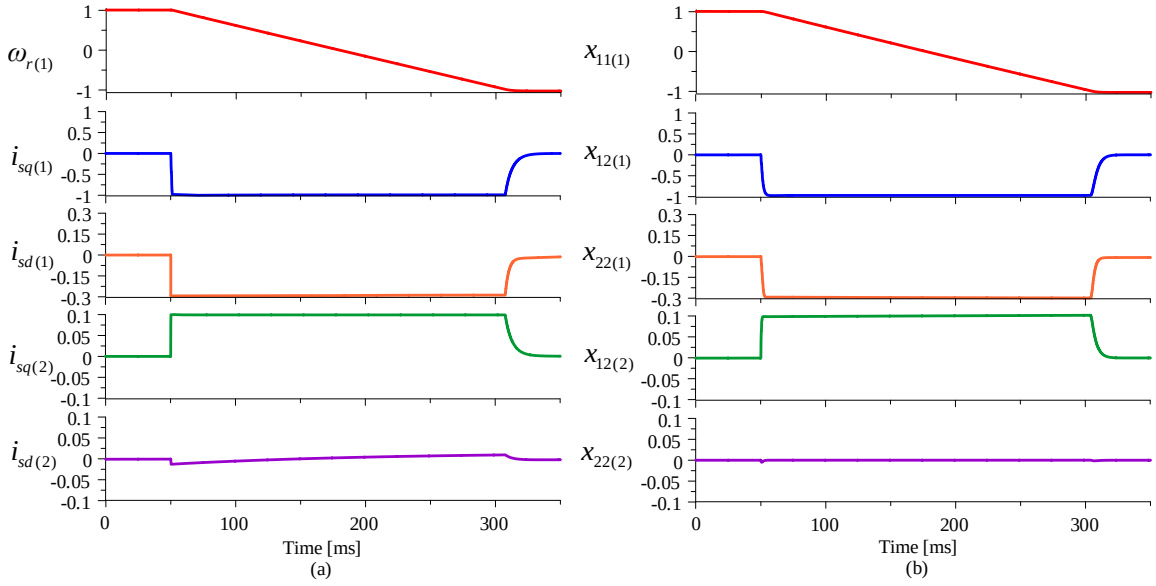

Fig. 5.16 Simulation result of five-phase IPMSM reversing from 1.0 p.u. to -1.0 p.u. (a) Field-oriented control (b) $(\boldsymbol{\psi}_{f(i)},\mathbf{i}_{s(i)})$ vector based control structure

It is important to mention that Fig. 5.23 presents Fast Fourier Transform (FFT) analysis of scrutinized five-phase IPMSM. Based on the FFT results, 3rd harmonic

component exists in the designed five-phase IPMSM. The value of 3rd harmonic component was approximately around 12% to 15% of the fundamental component.

In Fig. 5.16, when speed changes from 1.0 p.u. to -1.0 p.u., torque changes from 0.0 p.u. to -1.0 p.u. during the transient state and as drive reaches to desired speed, torque value also reduces to 0.0 p.u. At transient state, torque contribution from second plane was 0.1 p.u. In the simulation investigations, upper limit and lower limit of PI controller was set 1.0 p.u. and -1.0 p.u. respectively. Performance of the five-phase IPMSM drive using ($\boldsymbol{\psi}_{f(i)}$,$\mathbf{i}_{s(i)}$) vector based control structure and FOC provides similar dynamic response.

5.4.2 Simulation investigation of ($\boldsymbol{\psi}_{s(i)}$,$\mathbf{i}_{s(i)}$) vector based control structure - 1 and control structure – 2 of five-phase IPMSM drive

In Fig. 5.17 and Fig. 5.18, chosen simulation results are presented for control structure – 1 presented in Section 4.3.3 and control structure – 2 depicted in Section 4.3.4 in Chapter 5.

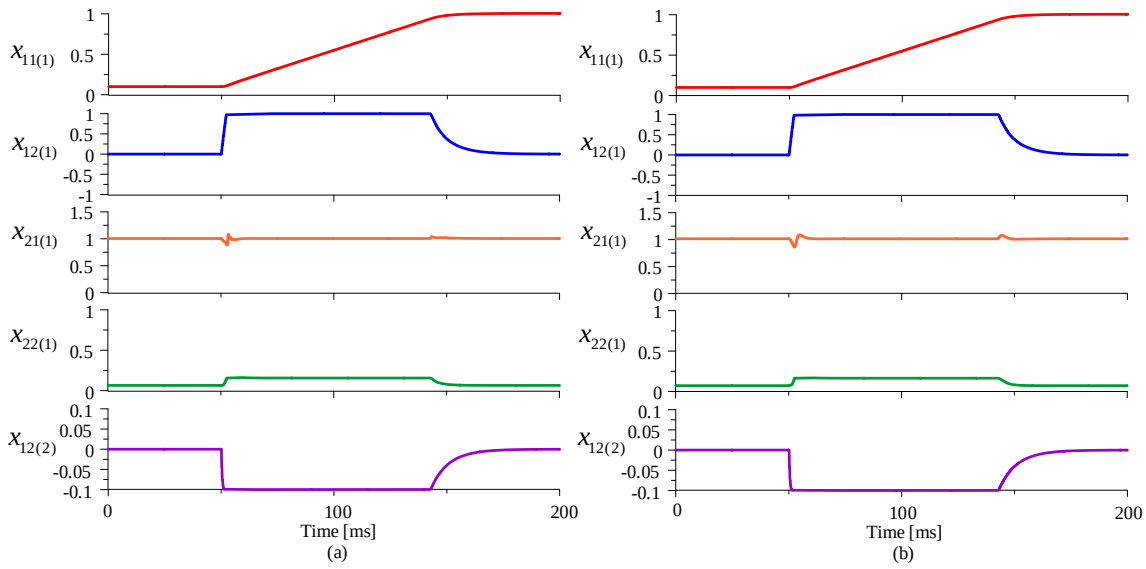

Fig. 5.17 Simulation result of five-phase IPMSM starting up to 1.0 p.u. (a) control structure - 1 (b) control structure – 2

In Fig. 5.17, five-phase IPMSM drive with 3rd harmonic injection is starting up to 1.0 p.u. The performance of control structure – 1 and control structure – 2 is shown in Fig. 5.17(a) and Fig. 5.17(b), respectively. Multiscalar variables such as rotor speed of the first plane $x_{11(1)}$, torque produced in first $x_{12(1)}$ and second plane $x_{12(2)}$, square of stator flux $x_{21(1)}$ and flux controlling variable $x_{22(1)}$ components are shown.

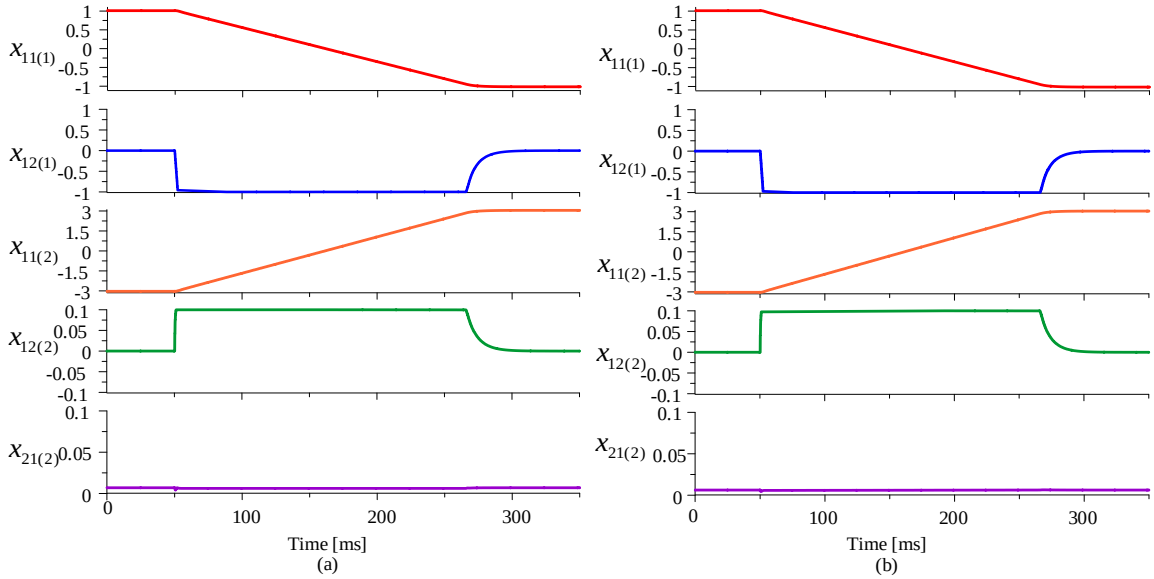

Fig. 5.18 Simulation result of five-phase IPMSM reversing from 1.0 p.u. to -1.0 p.u. (a) control structure - 1 (b) control structure - 2

The dynamic performance of reversal of five-phase IPMSM drive from 1.0 p.u. to -1.0 p.u is presented in Fig. 5.18(a) for control structure – 1 and in Fig. 5.18(b) for control structure – 2. Angular speed of first plane $x_{11(1)}$ and second plane $x_{11(2)}$, torque generated in the first plane $x_{12(1)}$ and second plane $x_{12(2)}$, Square of stator flux $x_{21(1)}$ in second plane are depicted in Fig. 5.18.

It can be observed that transient performance of both control structures presented in Fig. 5.17 and Fig. 5.18 are identical. By injecting 3rd harmonic current in second plane, motor torque generated in second plane was 10% of fundamental torque. The dynamic control of electro-mechanical subsystem is same in both control structures but the control of electro-magnetic subsystems is different as shown in Fig. 4.6 and Fig. 4.7. In the control structure – 2, to control square of stator flux only 1 controller is required each plane and the flux controlling variable is controlled internally, while in control structure – 1, 2 controllers are needed in each plane.

5.4.3 Simulation investigation of predictive control using multi-scalar variables of 1st plane and multi-scalar model-based control of 2nd plane of five-phase IPMSM

The simulation results of the predictive multiscalar-based control structure of the five-phase IPMSM as shown in Fig. 4.9 are presented here. Moreover, to provide comparative analysis, the predictive multiscalar-based control structure is compared with predictive field-oriented control structure. In Fig. 5.19 and Fig. 5.20, the chosen

simulation results are provided for two scenarios: 1) five-phase IPMSM drive starting up to nominal speed 2) drive reversal from 1.0 p.u to -1.0 p.u.

In Fig. 5.19(a) and Fig. 5.20(a), performance of predictive field-oriented control is shown where rotor speed $\omega_{r(1)}$, flux controlling current components $i_{sd(1)}$ and $i_{sd(2)}$, torque controlling current components $i_{sq(1)}$ and $i_{sq(2)}$ are shown, while Fig. 5.19(b) and Fig. 5.20(b) dynamic performance of predictive multiscalar is shown. Multiscalar variables: rotor speed $x_{11(1)}$, generated torque in first plane $x_{12(1)}$ and second plane $x_{12(2)}$, square of stator flux $x_{21(1)}$ and flux controlling variable $x_{22(1)}$ are shown.

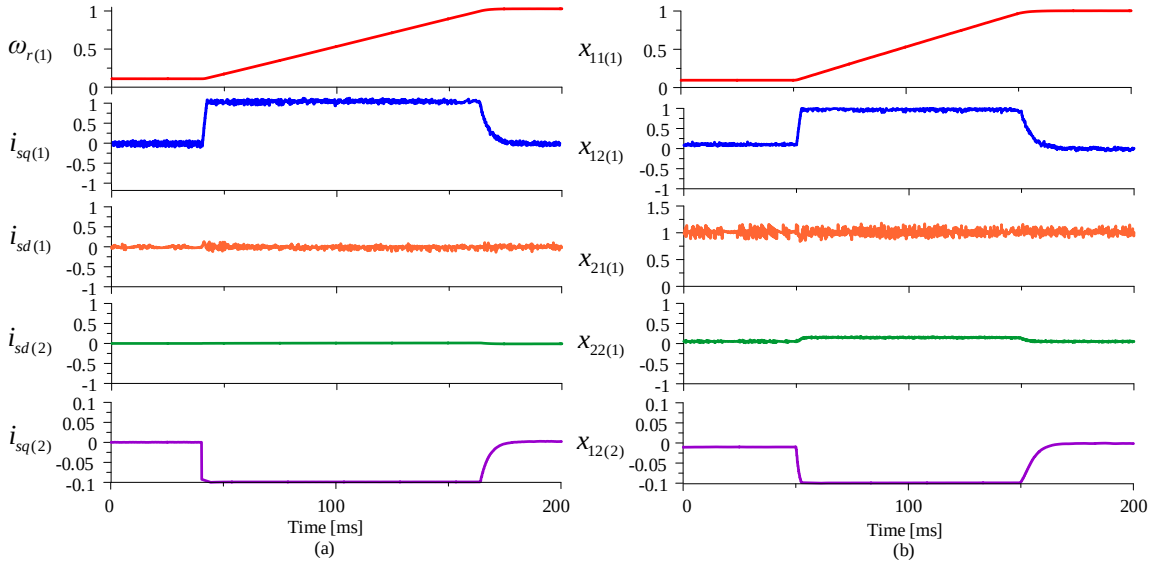

Fig. 5.19 Simulation result of five-phase IPMSM starting up to 1.0 p.u. (a) Predictive field-oriented control (b) Predictive multiscalar control

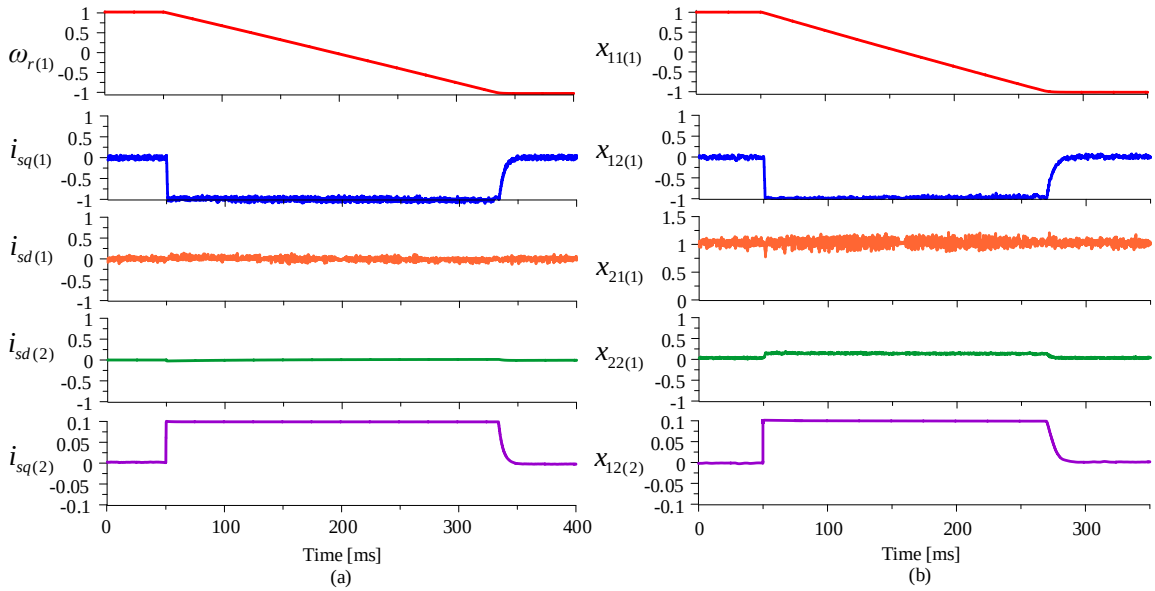

Fig. 5.20 Simulation result of five-phase IPMSM reversing from 1.0 p.u. to -1.0 p.u. (a) Predictive field-oriented control (b) Predictive multiscalar control

By injecting 3rd harmonic current with fundamental current, both control structure ensures overall torque enhancement. It can be observed at transient state that torque contributions by the first plane and second plane were 1.0 p.u. and 0.1 p.u., respectively. In addition, when drive reaches to steady state torque generation is reduced to 0.0 p.u. due to no-load condition. Simulation results shows that predictive multiscalar control schemes of five-phase IPMSM provides faster dynamic response than predictive field-oriented control for both scenarios. Predictive control provides excellent dynamic response compared to other control structure; however, it also introduces higher harmonic components which is visible in the torque response as shown in Fig. 5.19.

5.4.4 Simulation investigation of backstepping multiscalar control structure of five-phase IPMSM

In this section, simulation results of backstepping multiscalar control structure are presented for start-up and reversal tests. The backstepping mutliscalar control structure is also compared to field-oriented control for the case of drive starting up to nominal speed and reversal from 1.0 p.u. to -1.0 p.u. Simulation results of drive starting up to 1.0 p.u. using the Field-oriented control is shown in Fig. 5.21(a) and using backstepping mutliscalar control structure illustrated in Fig. 5.21(b). In Fig. 5.22(a) and Fig. 5.22(b), simulation outcome of five-phase IPMSM drive reversal from 1.0 p.u. to -1.0 p.u. is presented using the both control structures.

It can be noticed, MTPA control strategy was employed in the first plane of both control structure to obtain reluctance torque, while in the second plane $i_{sd(2)} = 0$ control was implemented because output reluctance torque value is very small. With third harmonic injection, overall output torque generation was enhanced as can be seen from Fig. 5.21 and Fig. 5.22, respectively. From the simulation results, backstepping multiscalar technique achieved similar dynamic response as field-oriented control scheme.

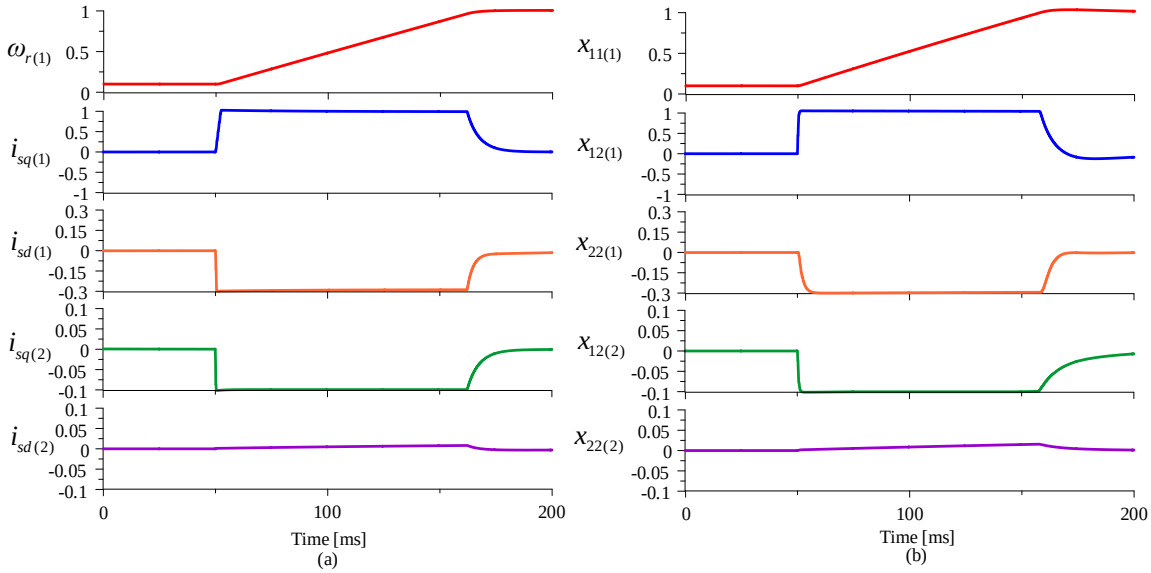

Fig. 5.21 Simulation result of five-phase IPMSM starting up to 1.0 p.u. (a) Field-oriented control (b) backstepping mutliscalar control structure

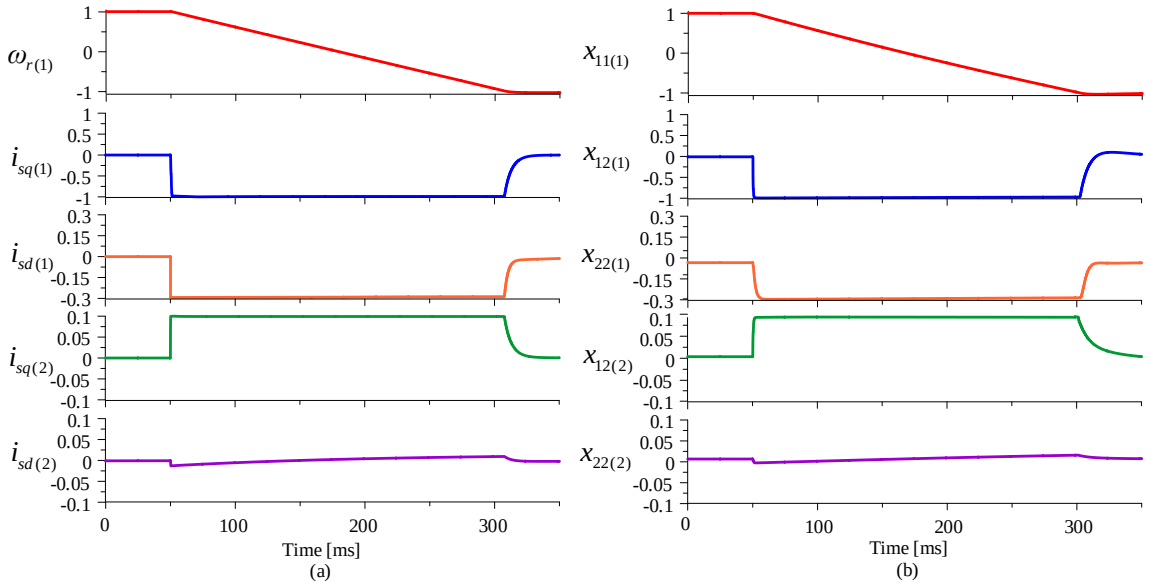

Fig. 5.22 Simulation result of five-phase IPMSM reversing from 1.0 p.u. to -1.0 p.u. (a) Field-oriented control (b) backstepping mutliscalar control structure

In the next section, experimental results of the proposed control solutions are discussed in details.

5.5 Experimental investigation of five-phase IPMSM drive

In this section, the theoretical hypothesis is validated using the experimental tests on five-phase IPMSM drive with proposed control structures in first plane and second plane utilizing 3rd harmonics for different cases. To start, a brief overview of experimental testbench is given to show the capabilities of five-phase IPMSM drive system.

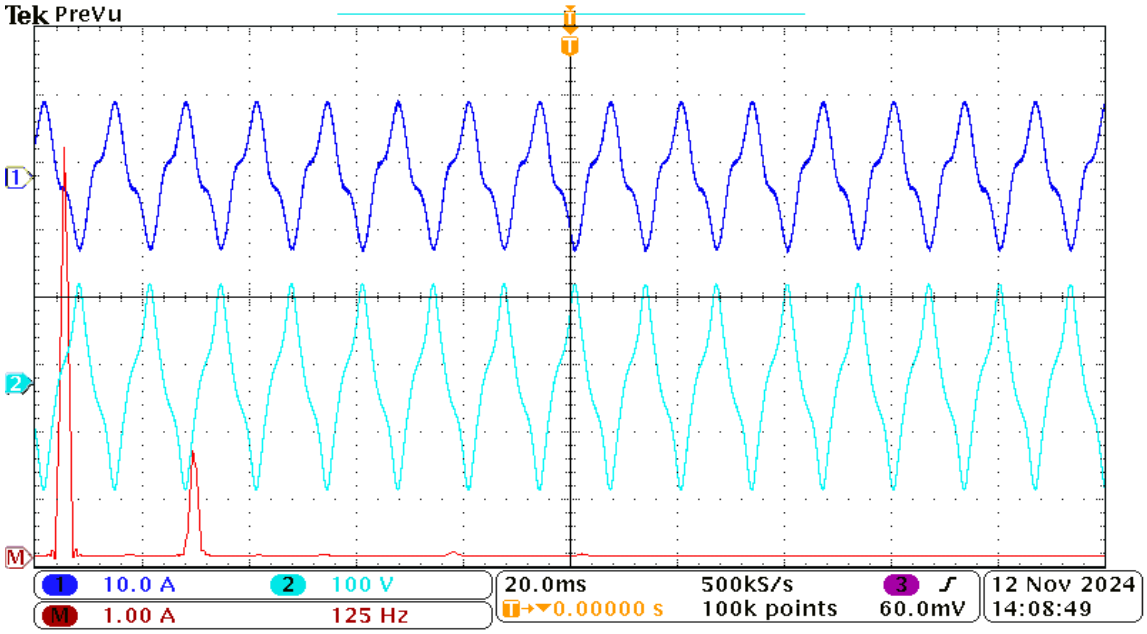

Fig. 5.23 Current waveform (Blue), Phase A back EMF (Cyan), FFT measurement (Red) of the examined five-phase IPMSM at Nominal speed

In Fig. 5.23, measurements of current waveform, phase A back EMF and FFT analysis of investigated five-phase IPMSM is depicted. In this test, five-phase IPMSM was mechanically coupled with three-phase induction machine (load). The load machine was operating at rated condition during this test. It can be observed from the measured current waveform and FFT curve that the component of 3rd harmonic exists in the phase current in five-phase IPMSM. The amplitude of third harmonic component was around 15% of the fundamental component. The uncontrolled presence of the 3rd harmonic component in the phase current shape is not inherently disadvantageous but indicates that the magnetic circuit of the five-phase IPMSM is not being utilized to its full potential. To utilize the 3rd harmonic component to enhance output torque level, control structure in the second vector plane requires to implement. Fig. 5.23 ensures that the designed five-phase IPMSM allows to inject 3rd harmonic currents to enhance the output torque generation.

In order to examine the behavior of the proposed control solution in real-time operating conditions, the presented control system was precisely verified by the use of set of laboratory equipment. The laboratory set employed 5.5kW five-phase IPMSM drive system supplied by voltage source converter (VSC). The experimental testbench of the five-phase IPMSM drive can be seen in Fig. 5.24. Parameters of the five-phase drive systems are given in Appendix – A. The signal processing unit plays a crucial in

the overall implementation of the drive system. DSP sharc ADSP21363 floating-point signal processor and Alter Cyclone 2 FPGA are used in the interface for control system implementation. The experimental setup is constrained by a strict execution time limit of 150μs. In this case, code optimization and time-saving compromises become crucial. Computation and signal processing unit are split between two subsystems.

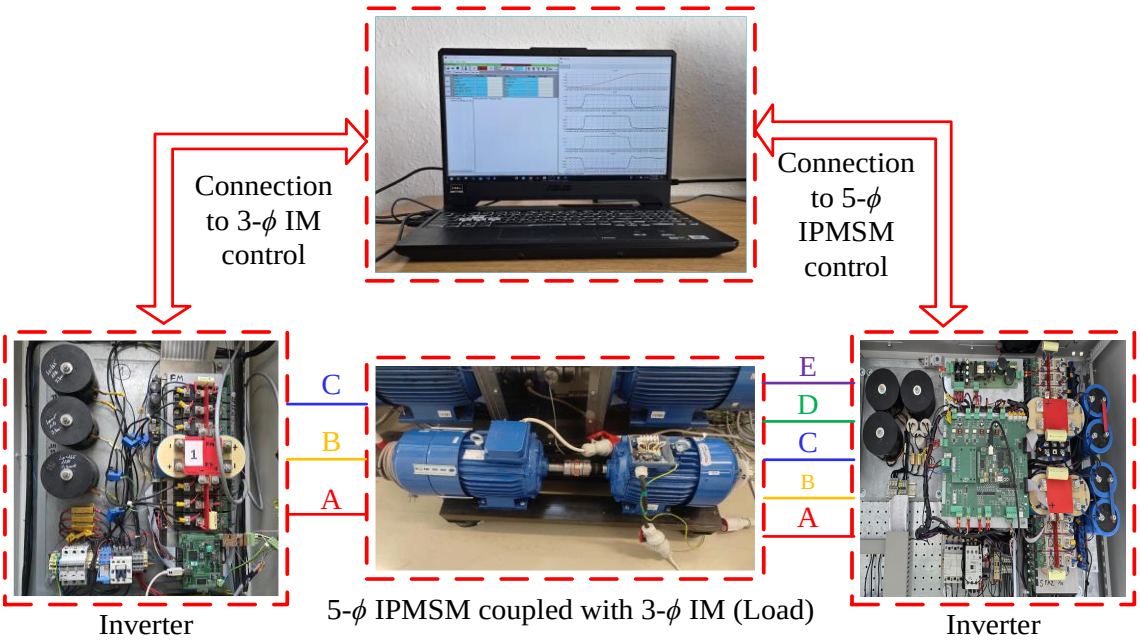

Fig. 5.24 Experimental testbench of five-phase IPMSM drive

The Alter Cyclone 2 FPGA handles communication between the computer console, memory and Analog to Digital Converter (ADC), while also controlling the transistor gate unit and relays. Additionally, the FPGA supplies the clock and triggers for DSP interrupt routine, in which all calculations are executed. The connection between DSP sharc ADSP21363 and FPGA is made using address and data bus, facilitating data exchange between the two integrated circuits.

In the next task, computation of observer structure for first plane and second plane are carried out using the different control solutions, chosen by the operator. Subsequently, the required space vector modulation (SVM) calculations are carried out to determine the switching times for the required voltages. In time period of 150μs, the calculation must be completed. The switching frequency of the transistor was 3.3kHz. Current measurement was done using LA 25-NP current transducers and later on transformed to stationary reference frame (α-β) using the Clarke transformation. The angular speed of the machine was measured using the incremental encoder 2048 PPR.

The only purpose of using the encoder was to verify the estimation accuracy of the observer structure

5.5.1 Experimental results of control system based on the $\psi_{f(i)}$,$i_{s(i)}$ vectors

In Fig. 5.25 and Fig. 5.26, the performance of the multiphase IPMSM drive is depicted for the case of drive starting up to 1.0 p.u. and reversing from -1.0 p.u. to 1.0 p.u., respectively. To apply speed command, ramp time of 260 ms was introduced to reduce torque pulsation and obtain smooth dynamic response transient performance of the five-phase IPMSM drive.

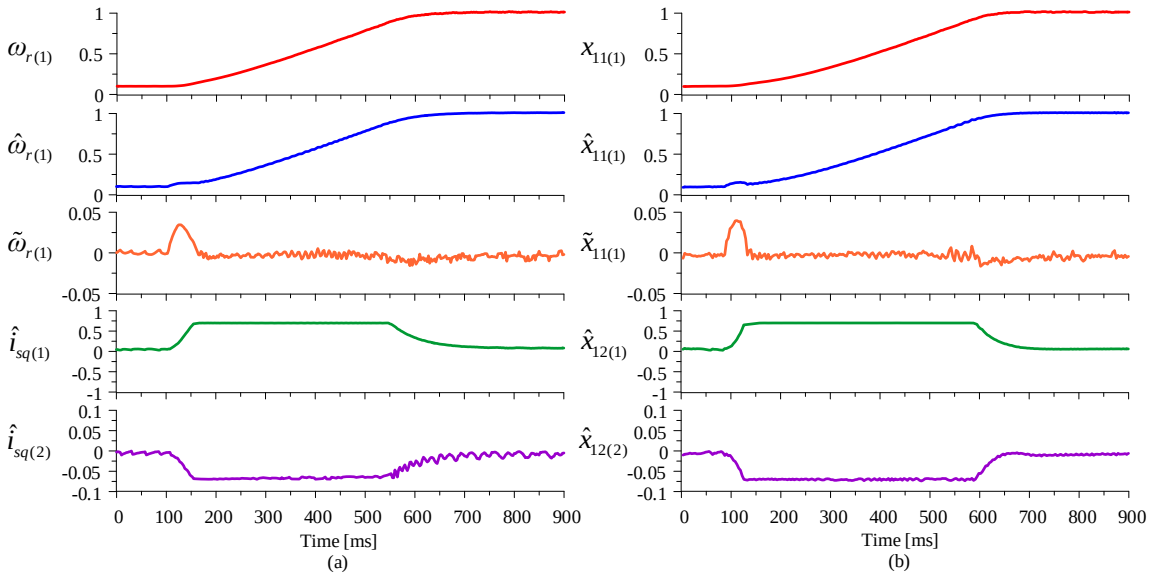

Fig. 5.25 Experimental of five-phase IPMSM drive starting up to 1.0 p.u. (a) FOC structure (b) control system based on the $\psi_{f(i)}$,$i_{s(i)}$ vectors

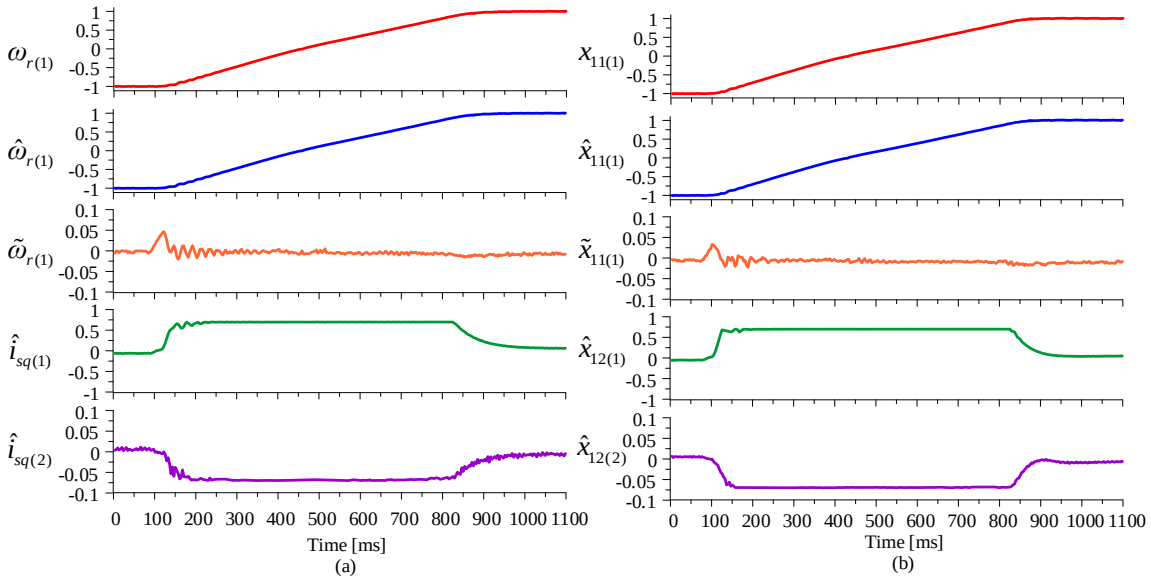

Fig. 5.26 Experimental results of five-phase IPMSM reversing from -1.0 p.u. to 1.0 p.u (a) FOC structure (b) control system based on the $\psi_{f(i)}$,$i_{s(i)}$ vectors

In Fig. 5.25(a) and Fig. 5.25(b), the multiphase IPMSM drive starting up to nominal speed using the FOC structure and control system based on the $\boldsymbol{\psi}_{\mathbf{f}(i)}$,$\mathbf{i}_{\mathbf{s}(i)}$ vectors. Measured rotor speed $\omega_{r(1)} \sim x_{11(1)}$, estimated speed $\hat{\omega}_{r(1)} \sim \hat{x}_{11(1)}$, speed estimation error $\tilde{\omega}_{r(1)} \sim \tilde{x}_{11(1)}$, generated torque in the fundamental plane $\hat{i}_{sq(1)} \sim \hat{x}_{12(1)}$ and in the second plane $\hat{i}_{sq(2)} \sim \hat{x}_{12(2)}$ are show. When the reference speed of the machine was changed from 0.1 p.u. to 1.0 p.u., electromagnetic torque was generated and increased up to the defined limit around 0.7 p.u. for the first plane and 0.07 p.u. for the second plane. When the machine speed reaches to 1.0 p.u., torque reducues to zero value as no-load was applied. During the transient state, the error between the measured and estimated speeds was less than 0.05 p.u. It can be observed that torque contribution from second plane was almost 10% of the fundamental plane.

Fig. 5.26(a) presents the response of FOC structure variables in rotating coordinates $(d\text{-}q)_{(i)}$ and Fig. 5.26(b) shows the response of $\boldsymbol{\psi}_{\mathbf{f}(i)}$,$\mathbf{i}_{\mathbf{s}(i)}$ vectors based variables in stationary coordinates $(\alpha\text{-}\beta)_{(i)}$ for the case of drive reversal from -1.0 p.u. to 1.0 p.u. for both sensorless control structure. At no-load, the IPMSM drive reverses from -1.0 p.u. to 1.0 p.u. during the transient state, electromagnetic torque increases up to the defined upper limit in the controllers for the first plane and second plane, and as drive completes the reversal, the generated torque decreases to zero. The speed estimation error was less than 0.05 p.u. The torque generated in the second plane was 10% of the first plane during the transient state.

The maneuver corresponds to drive staring up to nominal speed and drive reversal from -1.0 p.u. to 1.0 p.u. using the $\boldsymbol{\psi}_{\mathbf{f}(i)}$,$\mathbf{i}_{\mathbf{s}(i)}$ vectors based control system is identical to sensorless FOC structure. The $\boldsymbol{\psi}_{\mathbf{f}(i)}$,$\mathbf{i}_{\mathbf{s}(i)}$ vectors based control system eliminates the requirement of variables transformation to rotating coordinates for control structure implementation. In addition, the $\boldsymbol{\psi}_{\mathbf{f}(i)}$,$\mathbf{i}_{\mathbf{s}(i)}$ vectors based control scheme ensures the torque enhancement by injecting 3rd harmonics in five-phase IPMSM drive and also provides proper decoupling between the mechanical and electromagnetic subsystems.

In the second scenario, $\boldsymbol{\psi}_{\mathbf{f}(i)}$,$\mathbf{i}_{\mathbf{s}(i)}$ vectors based control system of the five-phase IPMSM drive was tested against the load torque injection at medium speed and nominal speed. In Fig. 5.27 and Fig. 5.28, the tracking response of the variables based on $\boldsymbol{\psi}_{\mathbf{f}(i)}$,$\mathbf{i}_{\mathbf{s}(i)}$ vectors are shown for the load torque injection. In Fig. 5.27(a), the IPMSM drive was running at steady state around 0.5 p.u. with applied load at 0.1 p.u. and after 0.65s, the

applied load torque was changed from 0.1 p.u. to 0.91 p.u. When sudden load torque change T_L is applied to the IPMSM drive, the $\boldsymbol{\psi}_{\mathbf{f}(i)}$,$\mathbf{i}_{\mathbf{s}(i)}$ vectors based control system provides fast and adequate response, as can be seen in Fig. 5.27(a).

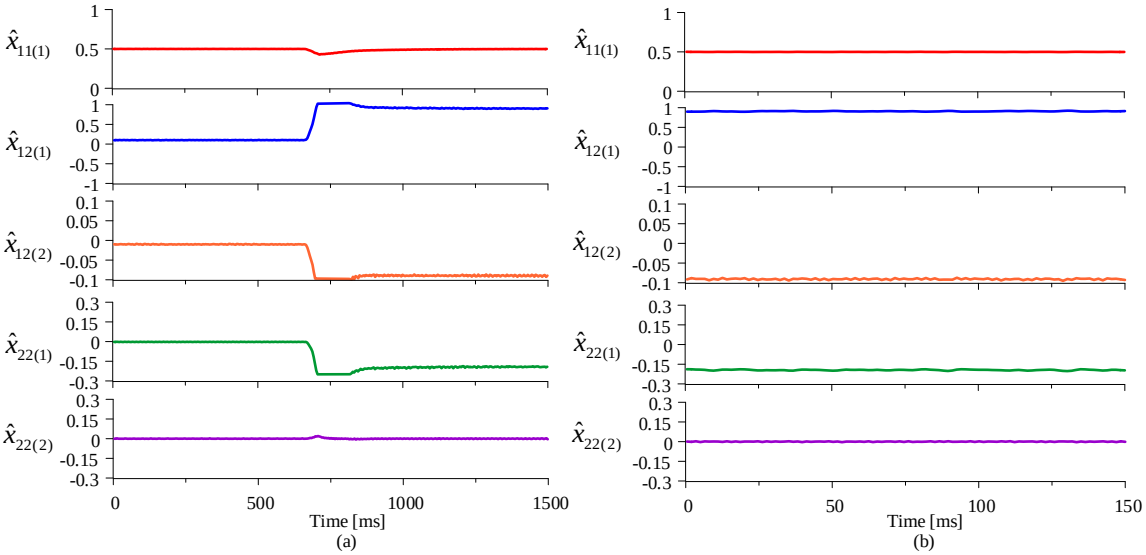

Fig. 5.27 Experimental results of five-phase IPMSM drive using $\boldsymbol{\psi}_{\mathbf{f}(i)}$,$\mathbf{i}_{\mathbf{s}(i)}$ vectors based control system (a) Load torque was changed from 0.1 p.u. to 0.91 p.u. after 0.65s (b) steady state is presented for 150ms

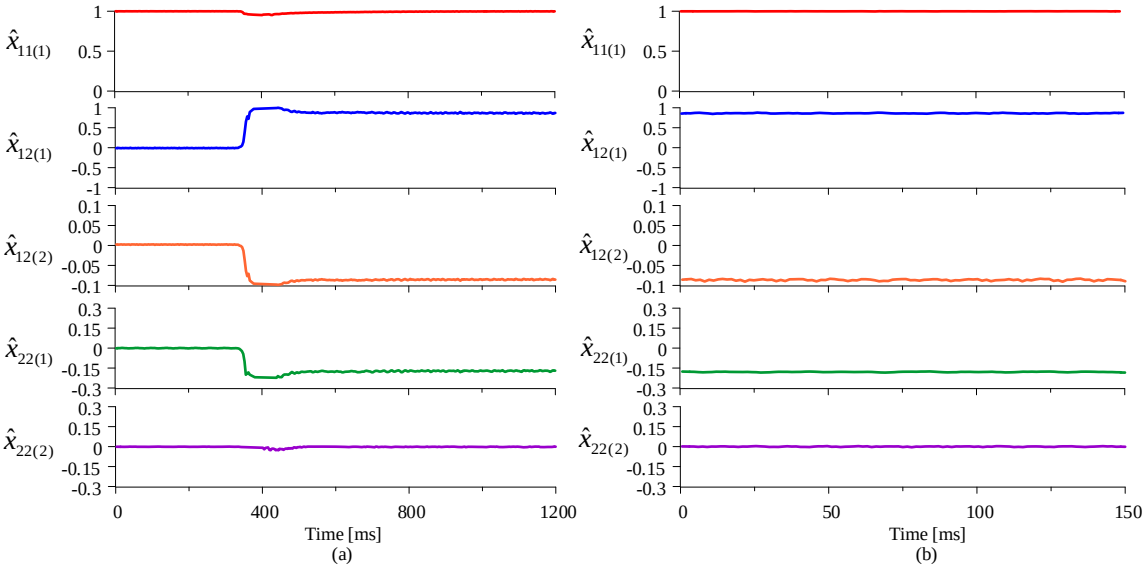

Fig. 5.28 Experimental results of five-phase IPMSM drive using $\boldsymbol{\psi}_{\mathbf{f}(i)}$,$\mathbf{i}_{\mathbf{s}(i)}$ vectors based control system (a) Load torque was applied after 0.36s (b) steady state is presented for 150ms

The electromagnetic torque increases from 0.1 p.u. to 0.91 p.u. for the first plane $\hat{x}_{12(1)}$ and 0.01 p.u. to 0.091 p.u. for the second plane $\hat{x}_{12(2)}$. In the first plane, the benefit of the reluctant torque $\hat{x}_{22(1)}$ was utilized to enhance the drive performance, however in the second plane due small value of reluctance torque $x^*_{22(2)} = 0$ was set. In Fig. 5.27(b),

steady state operating performance of the same variables is shown for 150ms. At steady state, the drive runs at desired speed and at applied load torque without any issue.

In Fig. 5.28(a), the drive was running at 1.0 p.u. without load. After 0.36s, the applied load torque was increased increases from 0.0 p.u. to 0.87 p.u. As the sudden load was applied, speed undershoot less than 4% for a very short duration can be seen and again rotor speed quickly settled at desired speed at 1.0 p.u. As the load was connected after 0.36s, the torque generation in the first plane $\hat{x}_{12(1)}$, in the second plane $\hat{x}_{12(2)}$ and reluctance torque $\hat{x}_{22(1)}$ in the first plane increased as shown in Fig. 5.28(a). In Fig. 5.28(b), the same machine variables are represented for 150ms period. It is visible that at a dynamic and steady state, the $\boldsymbol{\psi}_{\mathbf{f}(i)}$,$\mathbf{i}_{\mathbf{s}(i)}$ vectors based control system responds appropriately in the case of load torque injection at medium speed and high speed.

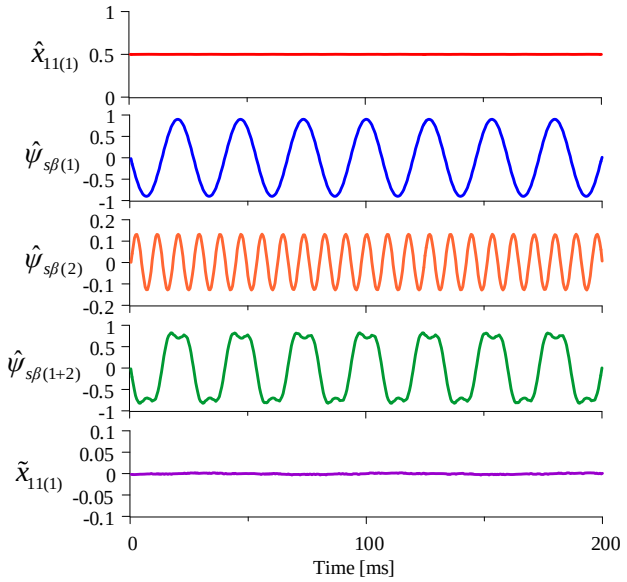

Fig. 5.29 Estimated stator flux distribution of $\hat{\psi}_{s\beta(i)}$ for first plane and second plane in stationary reference frame using $\boldsymbol{\psi}_{\mathbf{f}(i)}$,$\mathbf{i}_{\mathbf{s}(i)}$ vectors based control system

In Fig. 5.29, stator flux distribution using $\boldsymbol{\psi}_{\mathbf{f}(i)}$,$\mathbf{i}_{\mathbf{s}(i)}$ vectors based control system for first plane and second plane are depicted. The following variables are illustrated: estimated rotor speed $\hat{x}_{11(1)}$, calculated speed estimation error $\tilde{x}_{11(1)}$, estimated stator flux components in the first plane $\hat{\psi}_{s\beta(1)}$, second plane $\hat{\psi}_{s\beta(2)}$ and total flux distribution $\hat{\psi}_{s\beta(1+2)}$. In $\boldsymbol{\psi}_{\mathbf{f}(i)}$,$\mathbf{i}_{\mathbf{s}(i)}$ vectors based control system, stator flux level of the machine was maintained at permanent magnet flux level of the machine. Fundamental component with 3rd harmonic injection results in quasi-trapezoidal stator flux distribution $\hat{\psi}_{s\beta(1+2)}$

as shown in Fig. 5.29. Peak value of stator flux components $\hat{\psi}_{s\beta(1)}$, $\hat{\psi}_{s\beta(2)}$ and $\hat{\psi}_{s\beta(1+2)}$ were around 0.8841 p.u., 0.1326 p.u. and 0.77 p.u., respectively.

In the next scenario, the IPMSM drive performance was examined for low speed reversal and standstill test using the $\boldsymbol{\psi}_{\mathbf{f}(i)}$,$\mathbf{i}_{\mathbf{s}(i)}$ vectors based control structure. In Fig. 5.30(a), the multiphase drive was reversed from -0.1 p.u. to 0.1 p.u. at no load condition. Machine parameters such as measured speed $x_{11(1)}$, estimated speed in the first plane $\hat{x}_{11(1)}$ and second plane $\hat{x}_{11(2)}$, generated electromagnetic torque in fundamental plane $\hat{x}_{12(1)}$and second plane $\hat{x}_{12(2)}$ are shown. When fundamental speed $\hat{x}_{11(1)}$ reverses from -0.1 to 0.1 p.u., speed in second plane $\hat{x}_{11(2)}$ reverse from 0.3 p.u. to -0.3 p.u. as shown in Fig. 5.30(a). The calculated speed estimation error was under 0.05 p.u. at dynamic state, electromagnetic torque rises up to 0.7 p.u. and 0.07 p.u. for fundamental plane $\hat{x}_{12(1)}$ and second plane $\hat{x}_{12(2)}$, respectively. When machine reaches 0.1 p.u. torque quantities reduce zero value as no-load was applied for this test. At low-speed operation, the effect of voltage drop due to stator resistance and the presence of nonlinearities in the drive system components affects the drive operation significantly.

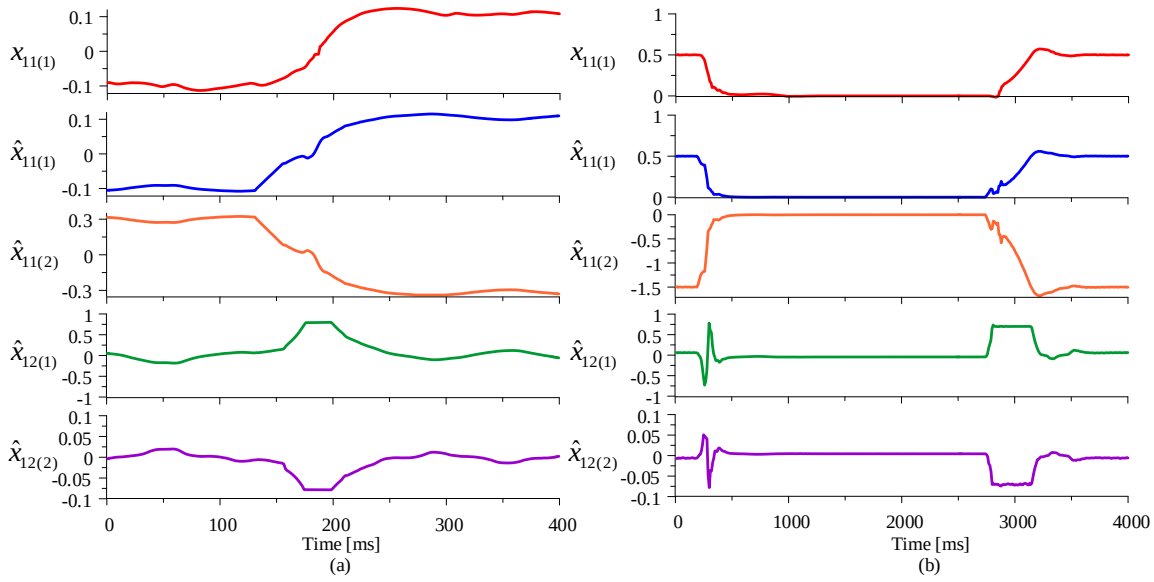

Fig. 5.30 Experimental results of five-phase IPMSM drive using $\boldsymbol{\psi}_{\mathbf{f}(i)}$,$\mathbf{i}_{\mathbf{s}(i)}$ vectors based control system (a) machine reversing from -0.1 p.u. to 0.1 p.u. (b) Standstill test

In Fig. 5.30(b), the $\boldsymbol{\psi}_{\mathbf{f}(i)}$,$\mathbf{i}_{\mathbf{s}(i)}$ vectors based control strategy was tested for the case of standstill test. The five-phase IPMSM drive was running at medium speed $\hat{x}_{11(1)}$ around 0.5 p.u. After 0.25s, speed of the IPMSM drive was changed from 0.5 p.u. to 0.0 p.u. The rotor of the machine was held at 0.0 p.u. for almost 2.4s and after 2.65s, rotor speed was changed back to 0.5 p.u. as shown in Fig. 5.30(b). Speed of the second plane $\hat{x}_{11(2)}$

changes from -1.5 p.u. to 0.0 p.u. and again 0.0 p.u. to -1.5 p.u. for this test. The control structure using $\boldsymbol{\psi}_{\mathbf{f}(i)}$,$\mathbf{i}_{\mathbf{s}(i)}$ vectors does not lose synchronism at zero speed and follow the reference command. The torque variables of each plane are also shown in Fig. 5.30(b).

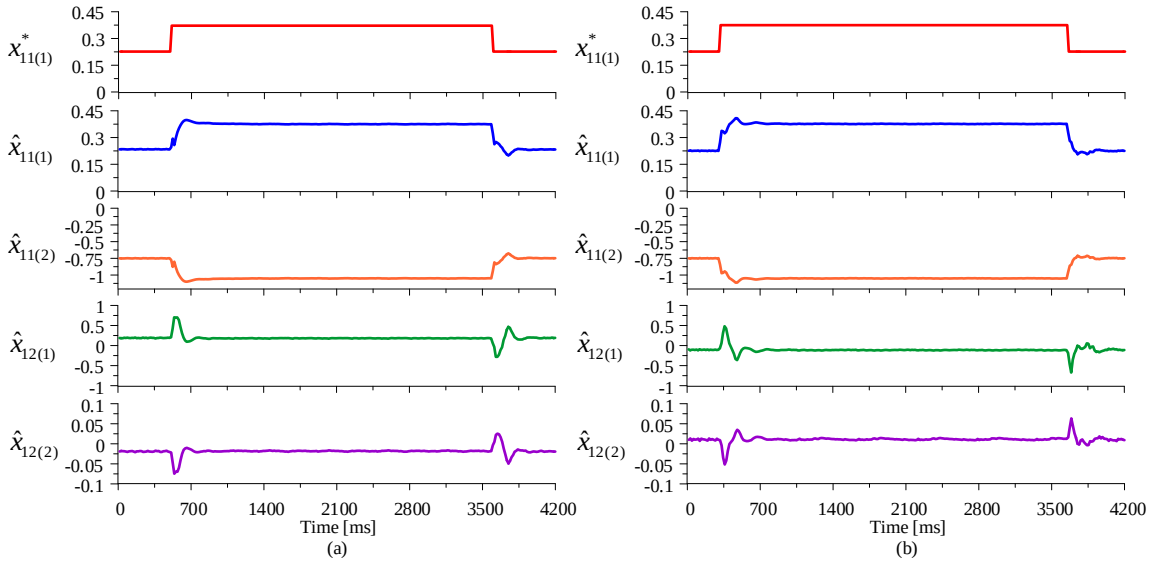

Fig. 5.31 Experimental results of five-phase IPMSM drive using $\boldsymbol{\psi}_{\mathbf{f}(i)}$,$\mathbf{i}_{\mathbf{s}(i)}$ vectors based control system (a) Motoring mode at T_L = 0.2 p.u. (b) Regenerative mode at T_L = -0.1 p.u.

In Fig. 5.31, the performance of $\boldsymbol{\psi}_{\mathbf{f}(i)}$,$\mathbf{i}_{\mathbf{s}(i)}$ vectors based control strategy is presented for motoring mode and regenerative operations. In Fig. 5.31, reference speed step change $x^*_{11(1)}$, estimated speed for each plane $\hat{x}_{11(1)}$ and $\hat{x}_{11(2)}$, generated torque in each plane $\hat{x}_{12(1)}$ and $\hat{x}_{12(2)}$ are depicted. In Fig. 5.31, the reference speed $x^*_{11(1)}$ was changed from 0.25 p.u. to 0.35 p.u. and again switch back from 0.35 p.u. to 0.25 p.u. During motoring mode, the applied load was 0.2 p.u. and for the regenerative test load torque was -0.1 p.u. as can be confirmed in Fig. 5.31(a) and Fig. 5.31(b). For motoring mode and regenerative mode, the tracking response of electromagnetic torque variables for the fundamental plane and second plane was opposite in sign. The control structure provides satisfactory results for both operations modes as can be seen in Fig. 5.31.

In the next scenario, to verify the torque enhancement in the multiphase IPMSM drive, third harmonic current injection was turned on and turned off as shown in Fig. 5.32 and Fig. 5.33. Estimated speed $\hat{x}_{11(1)}$, fundamental current $\hat{i}_{s\alpha(1)}$, third harmonic current $\hat{i}_{s\alpha(2)}$and total current $\hat{i}_{s\alpha(1+2)}$ and torque generated in second plane $\hat{x}_{12(2)}$ are presented. In Fig. 5.32(a), the IPMSM drive was running at 0.7 p.u. with applied load of 0.3 p.u. After 0.14s, third harmonic injection was turned on. It can be noticed that, as third harmonic was injected torque contribution from second plane increases from

0.0 p.u. to 0.03 p.u. and total current waveshape changes from sinusoidal to quasi-trapezoidal wave as shown in Fig. 5.32(a). In addition, steady state results of third harmonic injection were presented in Fig. 5.32(b) for same state variables.

In Fig. 5.33(a), after 0.17s third harmonic injection was turned off. As third harmonic current was turned off, current and torque contribution in the second plane reduced to zero. The shape of total current changes from quasi-trapezoidal to sinusoidal as shown in Fig. 5.33(a). The performance of the drive during the steady state when third harmonic was turned off is presented in Fig. 5.33(b).

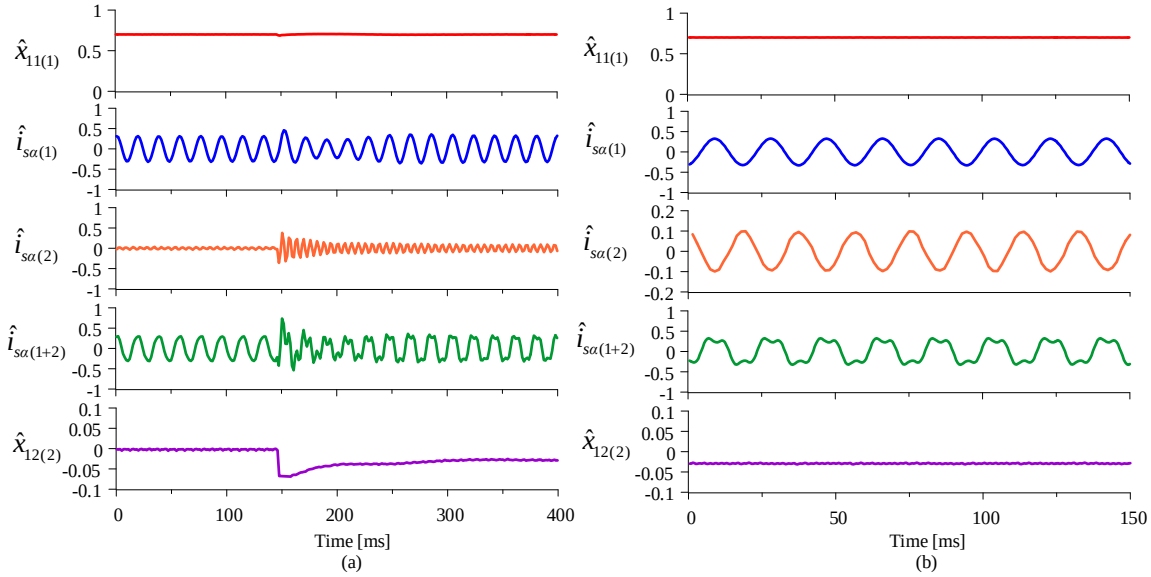

Fig. 5.32 Experimental results of loaded five-phase IPMSM (a) after 0.14s 3rd harmonic injection was turned on (b) steady state

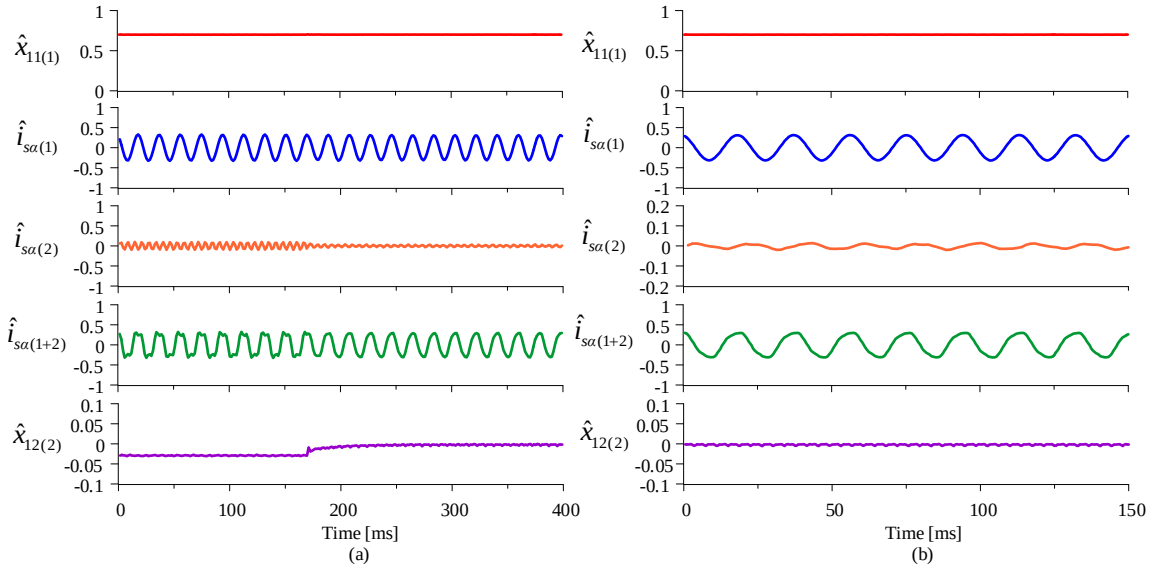

Fig. 5.33 Experimental results of loaded five-phase IPMSM (a) after 0.17s 3rd harmonic injection was turned off (b) steady state

In the next scenario, to examine robustness of the $\boldsymbol{\psi}_{\mathbf{f}(i)}$,$\mathbf{i}_{\mathbf{s}(i)}$ vectors based control system uncertainty tests were conducted on five-phase IPMSM drive by varying the machine parameters as shown Fig. 5.34 and Fig. 5.35. To conduct uncertainty test, machine was rotating at steady state around 0.5 p.u. with applied load around 0.53 p.u. In Fig. 5.34(a) and Fig. 5.34(b) inductance of the first plane $L_{q(1)}$ and second plane $L_{q(2)}$ was varied in 3 stages. In the first plane $L_{q(1)}$ was $0.5L_{qn(1)}$ for up to 1.2s, after 1.2s $L_{q(1)}$ = $L_{qn(1)}$ for up to 4s, and after almost 4s $L_{q(1)} = 2L_{qn(1)}$ as shown in Fig. 5.34(a). Similarly, in second plane $L_{q(2)}$ was $0.5L_{qn(2)}$ for up to 1.1s, after 1.1s $L_{q(2)} = L_{qn(2)}$ for up to 4.65s, and after 4.65s $L_{q(2)}$ was $2L_{qn(2)}$ as presented in Fig. 5.34(b). It can be observed from Fig. 5.34(a), as inductance value of the first plane $L_{q(1)}$ increased above nominal value control system losses the stability. Speed estimation error is also more than the permissible limit and ripple in output torque also increases. In addition, it can be noticed from Fig. 5.34(b), that the control system remains the stable against the variation of inductances in the second plane $L_{q(2)}$.

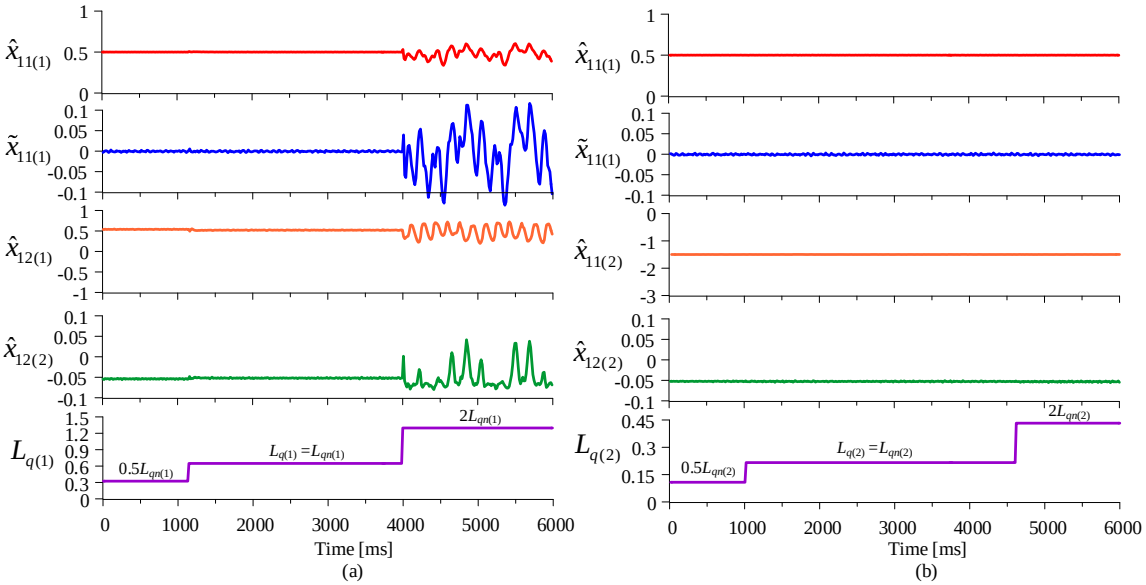

Fig. 5.34 Experimental test of five-phase IPMSM for different value of inductances (a) $L_{q(1)}$ (b) $L_{q(2)}$

Fig. 5.35 presents the variation of stator resistance to verify the robustness of the control system. Machine parameters such as rotor speed in the first plane $\hat{x}_{11(1)}$ and second plane $\hat{x}_{11(2)}$, speed estimation error $\tilde{x}_{11(1)}$, torque in second plane $\hat{x}_{12(2)}$ are shown. Rotor speed was set at 0.5 p.u., speed estimation errors was less than 0.05 p.u., and torque contribution by second plane was 0.053 p.u. Stator resistance R_s was $0.5R_{sn}$ up to 1.4s, after that R_s was equal to R_{sn} up to 5.7s and beyond that R_s was $1.5R_{sn}$. With

the variation in stator resistance control system remains stable and has been proven to be robust.

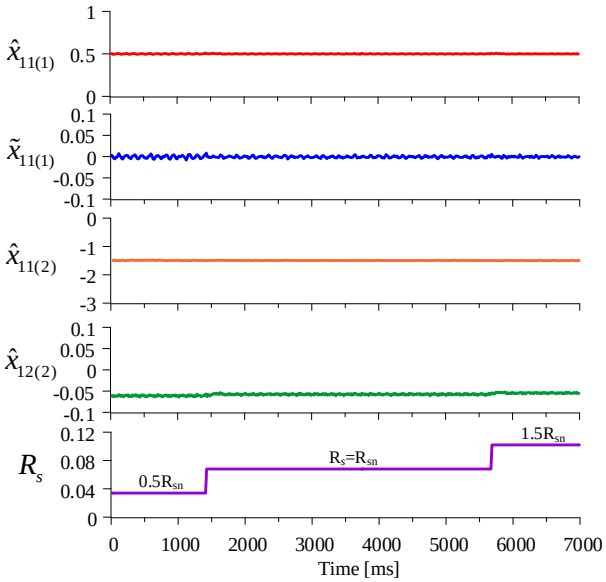

Fig. 5.35 Experimental test of five-phase IPMSM for different value of stator resistance R_s

In the next scenario, five-phase IPMSM drive was operated from 0.1 p.u. to 2.0 p.u. in the field weakening region using the $\boldsymbol{\psi}_{\mathbf{f}(i)}$,$\mathbf{i}_{\mathbf{s}(i)}$ vectors based control system as Fig. 5.36(b). It is important to mention that in this test, drive operates in the constant power region. To compare the dynamic performance of $\boldsymbol{\psi}_{\mathbf{f}(i)}$,$\mathbf{i}_{\mathbf{s}(i)}$ vectors based control system, the performance of FOC structure is also presented in Fig. 5.36(a). Measured speed $\omega_{r(1)} \sim x_{11(1)}$, estimated speed $\hat{\omega}_{r(1)} \sim \hat{x}_{11(1)}$, speed estimation error $\tilde{\omega}_{r(1)} \sim \tilde{x}_{11(1)}$, electromagnetic torque $\hat{i}_{sq(1)} \sim \hat{x}_{12(1)}$ and reluctance torque $\hat{i}_{sd(1)} \sim \hat{x}_{22(1)}$ in the first plane are shown in Fig. 5.36. During this test, third harmonic injection was turned off as drive was operating above the base speed region. Fig. 5.36 shows that as drive starts to accelerates from 0.1 p.u., generated electromagnetic torque reaches to defined upper limit 1.0 p.u. and reluctance torque reaches to 0.22 p.u. When drive operates beyond the base speed 1.0 p.u., field of permanent magnet weaken by the negative ($\hat{i}_{sd(1)} \sim \hat{x}_{22(1)}$) and electromagnetic torque $\hat{i}_{sq(1)} \sim \hat{x}_{12(1)}$ also reduces to operate the drive in constant power region. During this operation, the calculated speed error between the measured and estimated speed was less than 0.05 p.u. in both control structures. It can be observed from the given results that $\boldsymbol{\psi}_{\mathbf{f}(i)}$,$\mathbf{i}_{\mathbf{s}(i)}$ vector based control system provides fast and adequate dynamic response for field weakening region. The dynamic performance of $\boldsymbol{\psi}_{\mathbf{f}(i)}$,$\mathbf{i}_{\mathbf{s}(i)}$ vector based control system matches with the well-established control structure such as FOC.

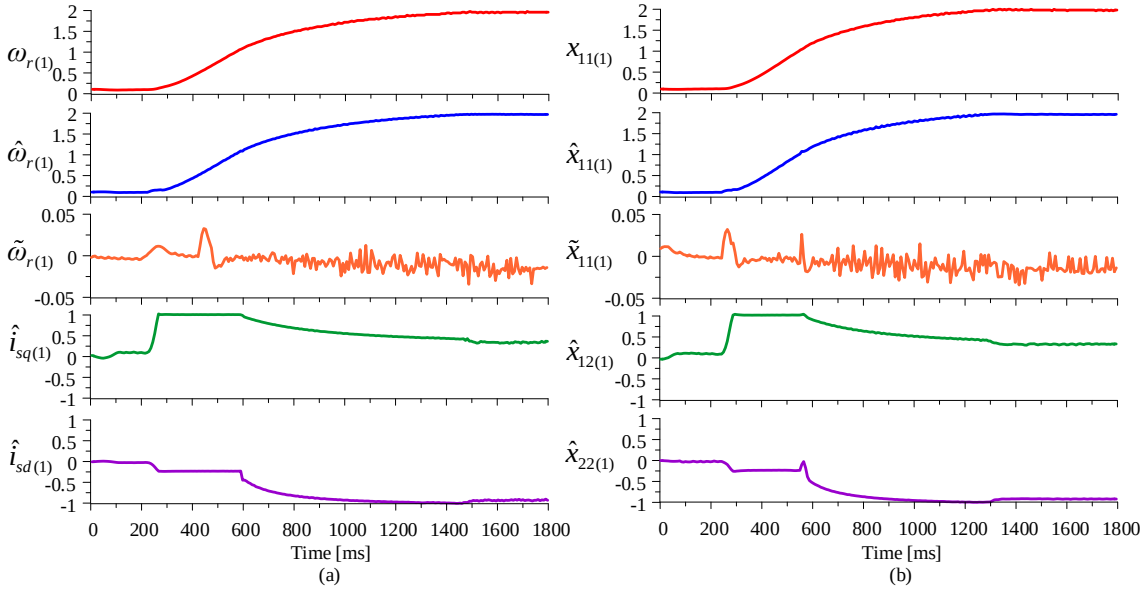

Fig. 5.36 Field weaking operation of five-phase IPMSM (a) FOC structure (b) control system based on the $\boldsymbol{\psi}_{\mathbf{f}(i)}$,$\mathbf{i}_{\mathbf{s}(i)}$ vectors

Fig. 5.37 shows the field weakening operation when drive is accelerating from 0.1 p.u. to 1.8 p.u. using the proposed $\boldsymbol{\psi}_{\mathbf{f}(i)}$,$\mathbf{i}_{\mathbf{s}(i)}$ vector based control system. Measured speed $x_{11(1)}$, estimated speed $\hat{x}_{11(1)}$, calculated speed estimation error $\tilde{x}_{11(1)}$, stator flux component in the α-coordinate $\hat{\psi}_{s\alpha(1)}$, and amplitude of stator flux $|\hat{\psi}_{s(1)}|$ are shown.

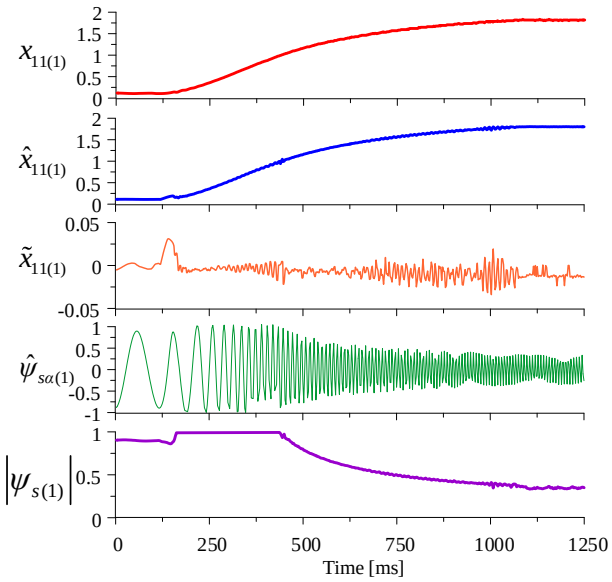

Fig. 5.37 Field weaking operation of five-phase IPMSM using proposed control system based on the $\boldsymbol{\psi}_{\mathbf{f}(i)}$,$\mathbf{i}_{\mathbf{s}(i)}$ vectors

All variables presented in Fig. 5.37 are from the fundamental plane, as third harmonic injection was turned off during this experimental test. It can be observed from Fig. 5.37 that as speed crosses 1.0 p.u., flux amplitude of the machine starts to decreases

as drive operates in the field weakening region. Speed estimation error was less than 0.05 p.u. during this test.

One of the key benefits of a multiphase machine is its ability to keep operating even when a fault occurs in one or two phases. The fault-tolerance performance of $\boldsymbol{\psi}_{\mathbf{f}(i)},\mathbf{i}_{\mathbf{s}(i)}$ vector based control system is shown in Fig. 5.38. To create open phase faults manually switched circuit breaker was employed. In Fig. 5.38(a), drive was running at steady state around 0.3 p.u. with no-load condition and without injection of third harmonics. After 0.28s, phase A was deactivated by manually switched circuit breaker. As phase A was removed, inverter output current increases and oscillations in estimated rotor speed can be visualized in Fig. 5.38(a).

In Fig. 5.38(b), five-phase IPMSM drive was operating around 0.3 p.u. at no-load and with third harmonics injection. Due to third harmonic injection, current waveshape deformed to quasi-trapezoidal waveshape. After 0.21s, phase A and phase C both were deactivated. Drive continues to rotate in the event of 2 phase deactivation. Current in healthy phases increases and small oscillation can be seen in Fig. 5.38(b).

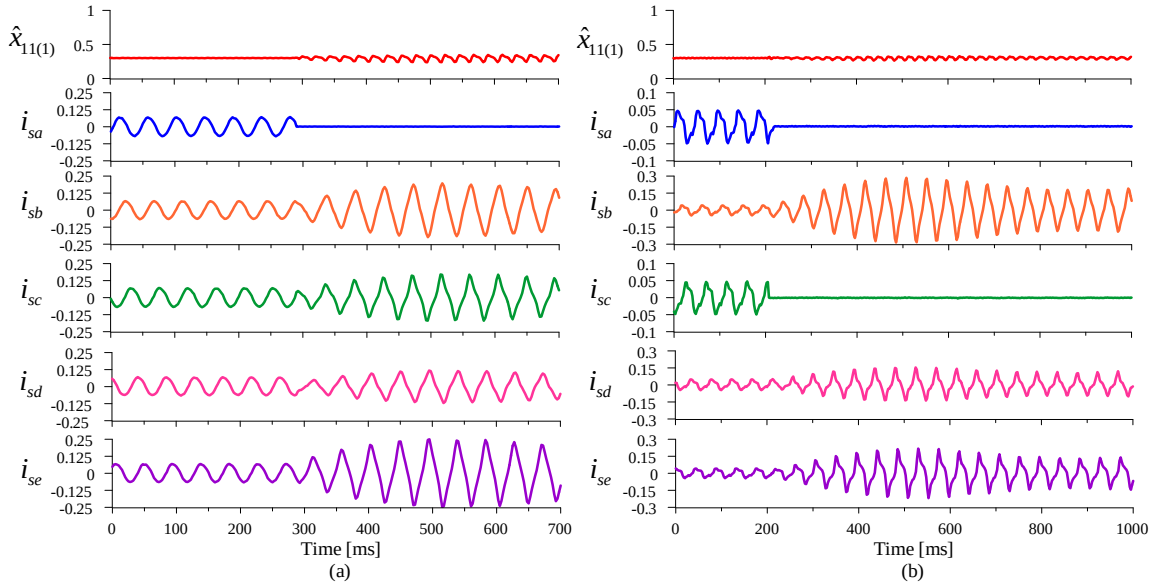

Fig. 5.38 Fault-tolerance test on five-phase IPMSM using control system based on the $\boldsymbol{\psi}_{\mathbf{f}(i)},\mathbf{i}_{\mathbf{s}(i)}$ vectors (a) phase A deactivated (b) phase A and C deactivated

5.5.2 Experimental results of $\boldsymbol{\psi}_{\mathbf{s}(i)},\mathbf{i}_{\mathbf{s}(i)}$ vectors based control systems

The tracking response of state variables of the five-phase systems using $\boldsymbol{\psi}_{\mathbf{s}(i)},\mathbf{i}_{\mathbf{s}(i)}$ vectors based control system are presented here for different cases. The $\boldsymbol{\psi}_{\mathbf{s}(i)},\mathbf{i}_{\mathbf{s}(i)}$ vectors based control structure – 1 is also compared with $\boldsymbol{\psi}_{\mathbf{s}(i)},\mathbf{i}_{\mathbf{s}(i)}$ vectors based control structure-2 for the case of drive start up to nominal speed and reversing from 1.0 p.u.

to -1.0 p.u. It is important to realize that $\boldsymbol{\psi}_{s(i)}$,$\mathbf{i}_{s(i)}$ vectors based control structure-1 requires additional PI controller to control electromagnetic subsystems as shown in Fig. 4.6, while $\boldsymbol{\psi}_{s(i)}$,$\mathbf{i}_{s(i)}$ vectors based control structure-2 ensures the direct control of flux controlling variable which eliminates the requirement of 1 controller in electromagnetic subsystem in each plane as shown in Fig. 4.7. In Fig. 5.39 and Fig. 5.40, the dynamic performance of drive accelerating from 0.1 p.u. to nominal speed and reversing from 1.0 p.u. to -1.0 p.u. using the $\boldsymbol{\psi}_{s(i)}$,$\mathbf{i}_{s(i)}$ vectors based control structure-1 and control structure-2 are presented. It is important to mention that small ramp time of 260 ms was added to the speed command during these tests.

Five-phase IPMSM drive running to rated speed is shown in Fig. 5.39(a) using the control structure – 1 and in Fig. 5.39(b) using the control structure-2. Estimated parameters are used in both control structure. Variables in the first plane $(\alpha\text{-}\beta)_{(1)}$ represented using the index (1) and variables in the second planes are expressed using the index (2). In Fig. 5.39(a) and Fig. 5.39(b), variables such as machine speed $\hat{x}_{11(1)}$, square of stator flux $\hat{x}_{21(1)}$, flux controlling variable $\hat{x}_{22(1)}$ in first plane, and generated electromagnetic torque in the first plane $\hat{x}_{12(1)}$ and second plane $\hat{x}_{12(2)}$ are depicted.

The reference command of the stator flux was 1.0225 p.u. and 0.0225 p.u. for the first plane and second plane, respectively. From FFT analysis presented in Fig. 5.23, torque contribution in the second plane was considered around 10% of the fundamental torque. From Fig. 5.39 (a) and (b), it can be observed that torque generation in the second plane was around 0.07 p.u. of first plane as shown. Square of stator flux kept constant during the steady state and dynamic state. To keep stator flux constant, requirement of flux controlling variable $\hat{x}_{22(1)}$ was increased from 0.08 p.u. to 0.15 p.u.

In the next case, the drive reversal from 1.0 p.u. to -1.0 is shown using the control structure-1 and control structure-2 in Fig. 5.40(a) and Fig. 5.40(b), respectively. Measured speed $x_{11(1)}$, estimated speed $\hat{x}_{11(1)}$, error between the measured speed and estimated speed $\tilde{x}_{11(1)}$, torque generation in the first plane $\hat{x}_{12(1)}$ and second plane $\hat{x}_{12(2)}$ are shown. Speed estimation error $\tilde{x}_{11(1)}$ was less than 0.05 p.u. in both control structures. During the drive reversal, torque generation due to third harmonic injection increased up to 0.07 p.u. in the second plane which is the 10% of the fundamental torque generation.

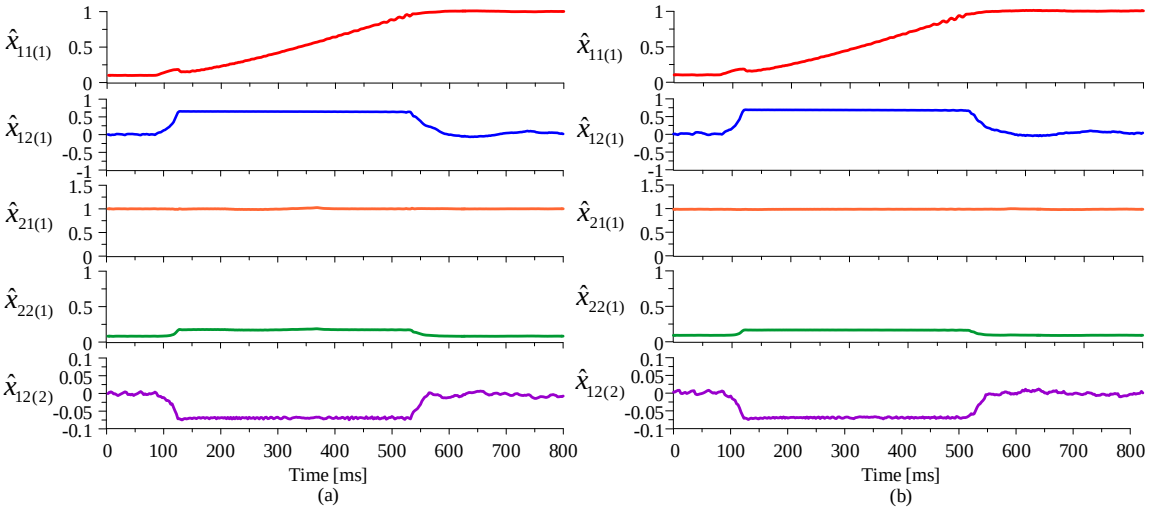

Fig. 5.39 Experimental results of five-phase IPMSM drive starting up to 1.0 p.u. (a) $\boldsymbol{\psi}_{s(i)}$,$\mathbf{i}_{s(i)}$ vectors based control structure – 1 (b) $\boldsymbol{\psi}_{s(i)}$,$\mathbf{i}_{s(i)}$ vectors based control structure – 2

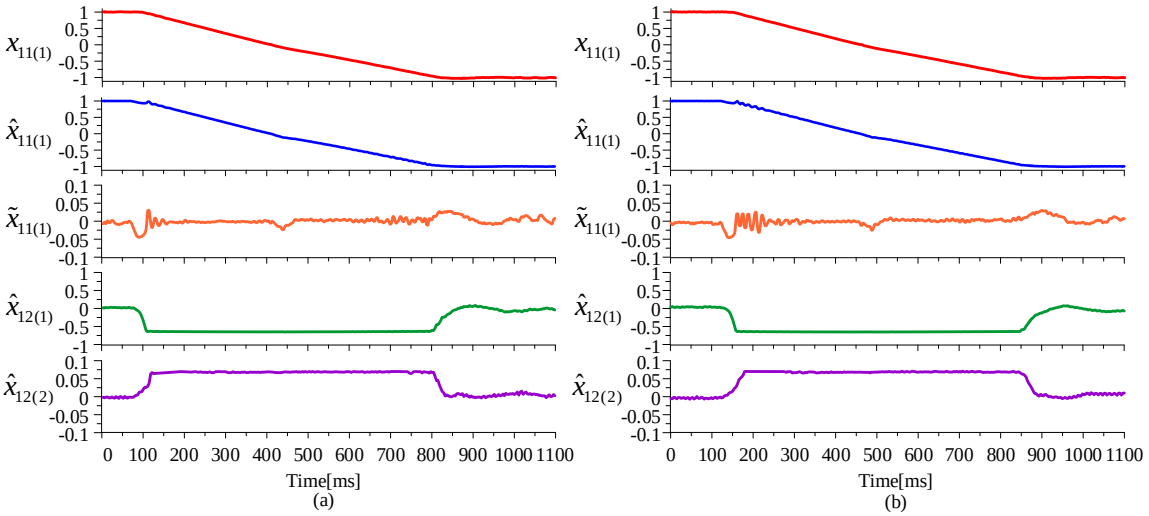

Fig. 5.40 Experimental results of five-phase IPMSM drive reversing from 1.0 p.u. to -1.0 p.u. (a) $\boldsymbol{\psi}_{s(i)}$,$\mathbf{i}_{s(i)}$ vectors based control structure – 1 (b) $\boldsymbol{\psi}_{s(i)}$,$\mathbf{i}_{s(i)}$ vectors based control structure – 2

From Fig. 5.39 and Fig. 5.40, it can be visualized that the output performance of control structure-2 is almost the same as control structure-1. The $\boldsymbol{\psi}_{s(i)}$,$\mathbf{i}_{s(i)}$ vectors based control structure-2 is simple and also reduces the overall control efforts as flux controller is not required as shown in Fig. 4.7., while in the $\boldsymbol{\psi}_{s(i)}$,$\mathbf{i}_{s(i)}$ vectors based control structure – 1 flux controller is necessary presented in Fig. 4.6.

FOC structure variables are compared with the variables of $\boldsymbol{\psi}_{s(i)}$,$\mathbf{i}_{s(i)}$ vectors based control structure-2 in Fig. 5.41. Fig. 5.41(a) shows the speed change from 0.1 p.u. to 1.0 p.u. The electromagnetic torque components $\hat{x}_{12(1)}$, $\hat{x}_{12(2)}$ of $\boldsymbol{\psi}_{s(i)}$,$\mathbf{i}_{s(i)}$ vectors based control structure-2 and FOC system $\hat{i}_{sq(1)}$, $\hat{i}_{sq(2)}$ are shown. When the reference speed $x^*_{11(1)}$ is changed from 0.1 p.u. to 1.0 p.u., machine accelerates and electromagnetic

torque quantities increases up to applied limit 0.7 p.u. and 0.07 p.u. for fundamental plane and second plane, respectively and as machine reaches to 1.0 p.u. torque generation reduces to 0.0 p.u. due to load condition. Steady state results of five-phase IPMSM drive is presented in Fig. 5.41(b). In Fig. 5.41(b), drive was running at 1.0 p.u. and square of stator flux $x^{*}_{21(1)}$ was set 1.0225 p.u. for the first plane. The flux level is maintained as per command value, when flux controlling variable $\hat{x}_{22(1)}$ is positive and closed to 0.08 p.u. during the steady state condition. Similarly, flux controlling component $\hat{i}_{sd(1)}$ of FOC system behave the same as flux controlling variable $\hat{x}_{22(1)}$ of $\boldsymbol{\psi}_{s(i)}$,$\mathbf{i}_{s(i)}$ vectors based control structure-2.

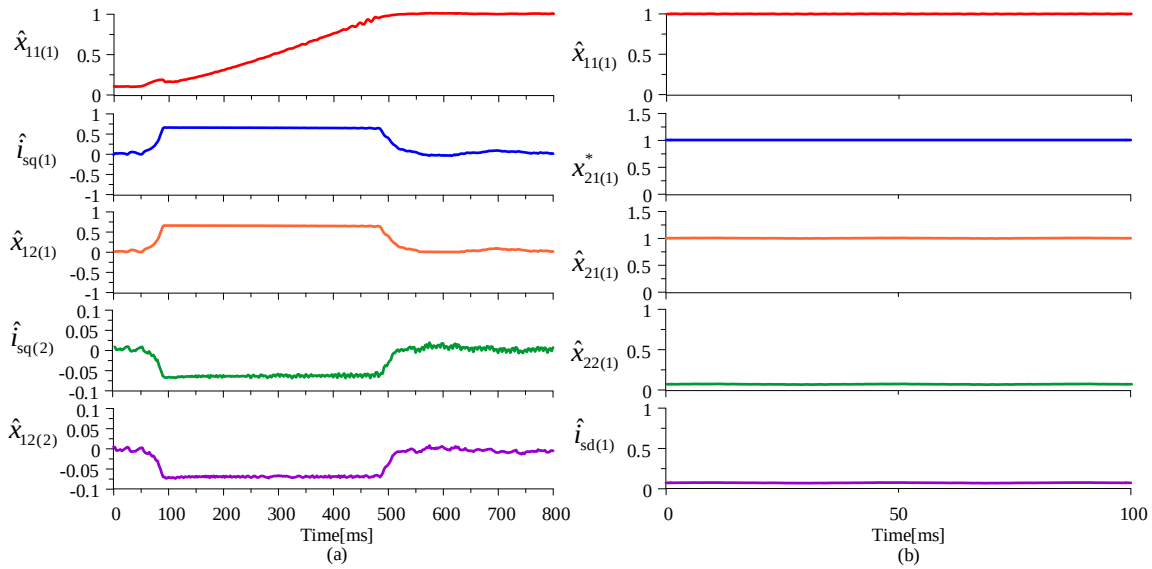

Fig. 5.41 Experimental results of $\boldsymbol{\psi}_{s(i)}$,$\mathbf{i}_{s(i)}$ vectors based control structure – 2 compared FOC structure variables (a) drive starting up to 1.0 p.u. (b) steady state

In Fig. 5.42 and Fig. 5.43 $\boldsymbol{\psi}_{s(i)}$,$\mathbf{i}_{s(i)}$ vectors based control structure-2 was examined for the case of sudden load injection and load removal at low speed and medium speed, respectively. The five-phase IPMSM was loaded with three-phase induction machine. Both machines were coupled mechanically as shown in Fig. 5.24. Important variables are shown such as measured speed $x_{11(1)}$, estimated speed $\hat{x}_{11(1)}$, speed estimation error $\tilde{x}_{11(1)}$, and torque production in each plane $\hat{x}_{12(1)}$, $\hat{x}_{12(2)}$.

In Fig. 5.42(a), drive was running at steady state around 0.15 p.u. without load. After 0.12s, the load torque was changed to 0.45 p.u. With applied load, torque production in first plane $\hat{x}_{12(1)}$ and second plane $\hat{x}_{12(1)}$ increases up to 0.25 and 0.045 p.u., respectively. Similarly, in Fig. 5.42(b). In Fig. 5.43(a), speed of five phase IPMSM was set at 0.5 p.u. and after 0.24s the load torque was changed from 0.2 p.u. to 0.74 p.u.

as shown. In Fig. 5.43(b), applied load was pulled out from 0.74 p.u. to 0.0 p.u. after 0.19s. During both tests, calculate speed estimation error was almost close to zero. The $\boldsymbol{\psi}_{s(i)}$,$\mathbf{i}_{s(i)}$ vectors based control structure-2 provides satisfactory performance for both cases: load torque injection and load torque removal.

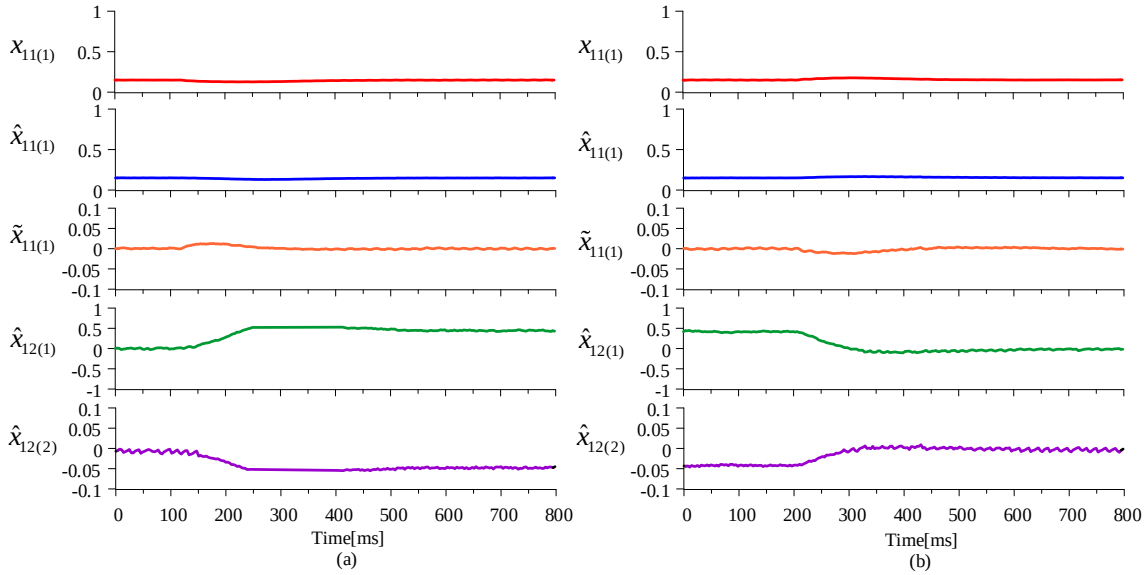

Fig. 5.42 Experimental result of loaded five-phase IPMSM using $\boldsymbol{\psi}_{s(i)}$,$\mathbf{i}_{s(i)}$ vectors based control structure – 2 (a) after 0.12s load torque was changed from 0.0 p.u. to 0.45 p.u. (b) after 0.2s load torque was changed from 0.45 p.u. to 0.0 p.u.

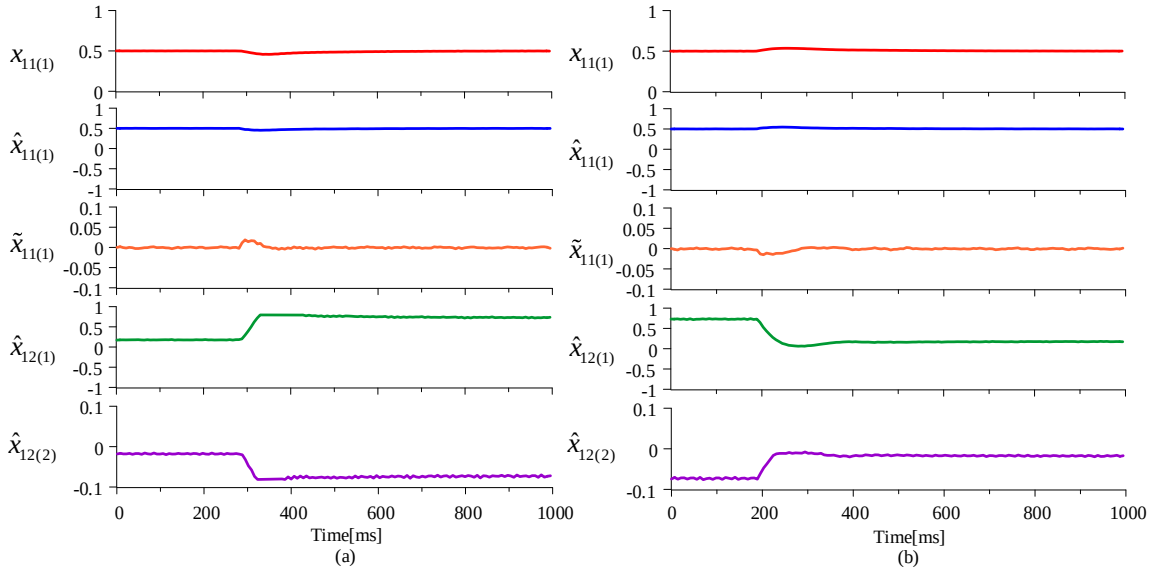

Fig. 5.43 Experimental result of loaded five-phase IPMSM using $\boldsymbol{\psi}_{s(i)}$,$\mathbf{i}_{s(i)}$ vectors based control structure – 2 (a) after 0.24s load torque was changed from 0.2 p.u. to 0.74 p.u. (b) after 0.19s the load torque was removed from 0.74 p.u. to 0.0 p.u.

In Fig. 5.44(a), rotor speed $\hat{x}_{11(1)}$ was set at 0.25 p.u. with an applied load around 0.4 p.u. and after 0.16s third harmonic injection was turned on. When third harmonic injection was turned on torque generation $\hat{x}_{12(2)}$ in second plane increases from zero to

0.04 p.u. which is 10% of the fundamental torque. Total current of the first plane and second plane $\hat{i}_{s\alpha(1+2)}$, fundamental current $\hat{i}_{s\alpha(1)}$, and injected third harmonic current $\hat{i}_{s\alpha(2)}$are shown. In Fig. 5.44(b), steady state behavior with third harmonic injection in IPMSM drive is presented. It can be noticed that the current waveshape changes from sinusoidal to quasispheroidal wave with third harmonics injection.

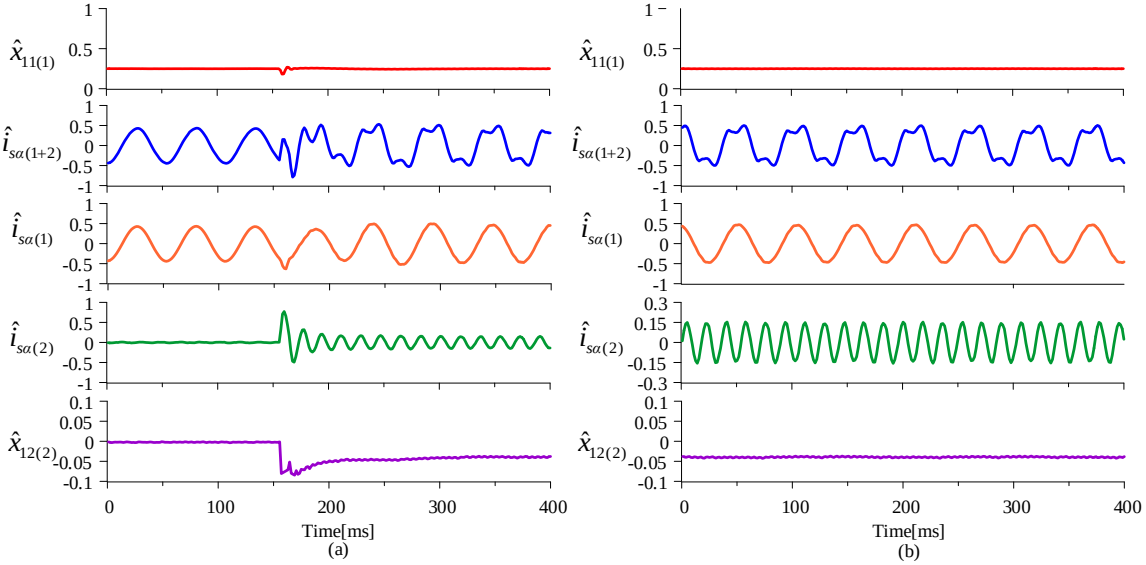

Fig. 5.44 Experimental result of loaded five-phase IPMSM using $\boldsymbol{\psi}_{s(i)}$,$\mathbf{i}_{s(i)}$ vectors based control structure – 2 (a) after 0.16s 3rd harmonic injection was turned on (b) steady state

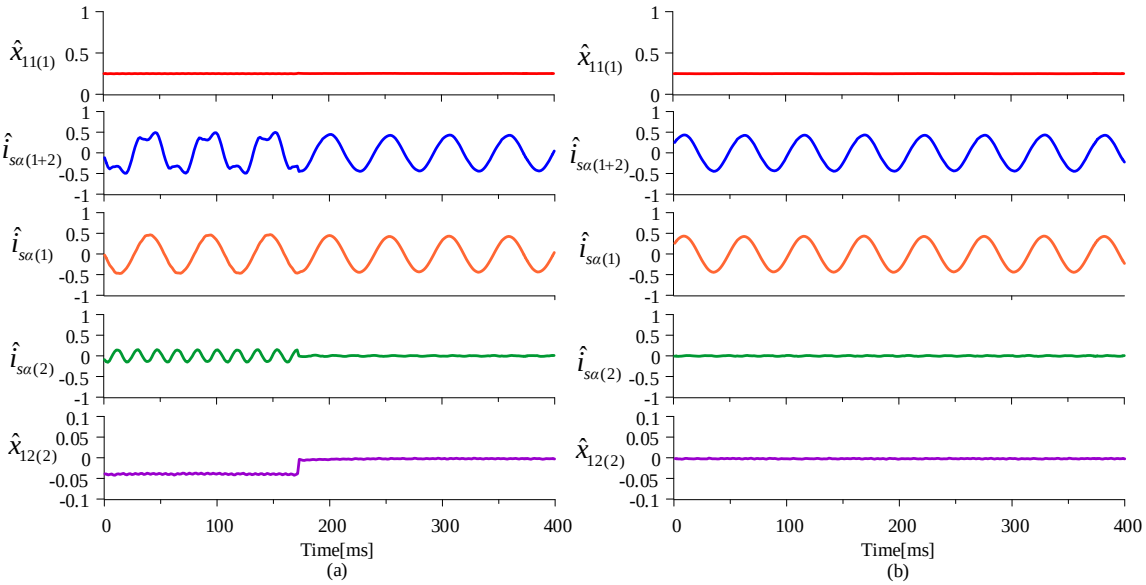

Fig. 5.45 Experimental result of loaded five-phase IPMSM using $\boldsymbol{\psi}_{s(i)}$,$\mathbf{i}_{s(i)}$ vectors based control structure – 2 (a) after 0.17s 3rd harmonic injection was turned off (b) steady state

In Fig. 5.45(a), third harmonic injection was turned off after 0.17s. The value of current torque in second plane reduces to zero and only fundamental current is supplied to five-phase IPMSM. The shaper of total current changes from quasi-trapezoidal to

sinusoidal. Fig. 5.45(b), shows the performance of the drive during the steady state when third harmonic was off.

Fig. 5.46 shows the performance of the five-phase IPMSM drive when 3rd harmonic injection was turned off. The same variables shown in Fig. 5.45 are depicted in Fig. 5.46. During this test, drive was running around 0.7 p.u. and applied load torque was around 0.37 p.u. Torque limit in the first plane was reduced from 0.7 p.u. to 0.4 p.u. to check the performance of the drive during the break test. It can be noticed from Fig. 5.46, as 3rd harmonic injection was turned off after 80 ms slight reduction in estimated speed curve is visible from 0.7 p.u. to 0.66 p.u. It can be understood from Fig. 5.46 that injection of 3rd harmonics improves the dynamic performance of five-phase IPMSM drive.

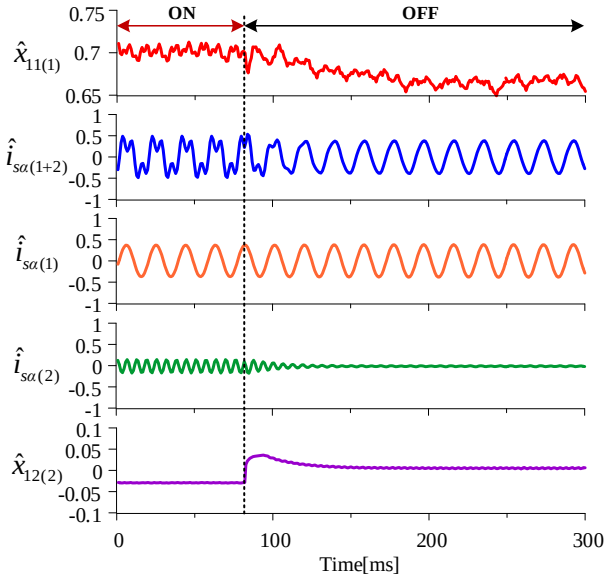

Fig. 5.46 Experimental result of loaded five-phase IPMSM using $\boldsymbol{\psi}_{s(i)}$,$\mathbf{i}_{s(i)}$ vectors based control structure – 2 for the case of 3rd harmonic injection off at speed around 0.7 p.u.

Fig. 5.47 shows the performance of drive for the similar case as presented in Fig. 5.46. In Fig. 5.47, state variables such as estimated speed $\hat{x}_{11(1)}$, torque components in the first plane $\hat{x}_{12(1)}$ and second plane $\hat{x}_{12(1)}$, total torque $\hat{x}_{12(1+2)}$ and applied load torque T_L measured using the torque meter. In this test, five-phase IPMSM drive was running around 0.5 p.u with load around 0.5 p.u. (17.5 Nm). At 100 ms, 3rd harmonic injection was turned off and drive was running with fundamental supply. As 3rd harmonic injection was cut off, speed curve reduced from 0.5 p.u. to 0.43 p.u., torque generation in the second plane reduces to 0.0 p.u., total electromagnetics produced by the machine also reduces from 0.55 p.u. to 0.45 p.u., applied load torque also reduced from 17.5 Nm

to 15.75 Nm. The torque meter used in the experimental stand is manufactured by messtechnik and it capable to measure torque up to 50 Nm. To measure the load torque of IPMSM drive, torque meter model DRBK-50-n was used.

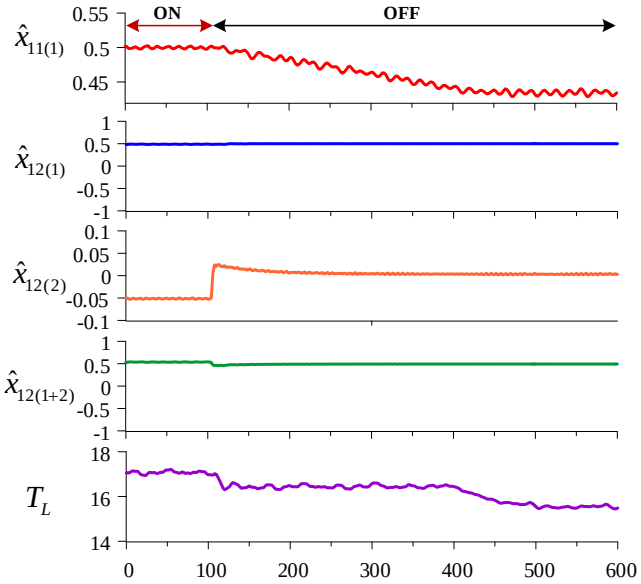

Fig. 5.47 Experimental result of loaded five-phase IPMSM using $\boldsymbol{\psi}_{s(i)}$,$\mathbf{i}_{s(i)}$ vectors based control structure – 2 for the case of 3rd harmonic injection off at speed around 0.5 p.u.

To verify the drive performance at low speed and zero speed, speed reversal test from 0.1 p.u. to -0.1 p.u. and standstill test were conducted on five-phase IPMSM drive using $\boldsymbol{\psi}_{s(i)}$,$\mathbf{i}_{s(i)}$ vectors based control structure-2 as presented in Fig. 5.48. Estimated speed in the first plane $\hat{x}_{11(1)}$ and second plane $\hat{x}_{11(2)}$, square of flux $\hat{x}_{21(1)}$, torque generation first plane $\hat{x}_{12(1)}$ and second plane $\hat{x}_{12(2)}$ are presented in Fig. 5.48. In Fig. 5.48(a), when drive reverses from 0.1 p.u. to -0.1 p.u., electromagnetic torque increases up to the defined limit in each plane during the transient state and reduces to zero as drive completes the reversal and reaches to steady state at -0.1 p.u.

In Fig. 5.48(b), five-phase IPMSM drive performance is shown under the standstill test. To conduct this test, drive was running at 0.15 p.u. with no-load condition. After 0.4s, reference speed was changed to 0.0 p.u. and after 4.3s reference speed changed back to 0.15 p.u. From Fig. 5.48(b), It can be observed that rotor kept at zero speed for almost 3.9s and after that it returns back to the defined reference speed. Speed of second plane changes after 0.4s from -0.45 p.u. to 0.0 p.u. and after 4.3s speed changes from 0.0 p.u. to -0.45 p.u. square of stator flux is maintained at desired level in the both cases: drive reversal and standstill test as shown in Fig. 5.48(a) and (b).

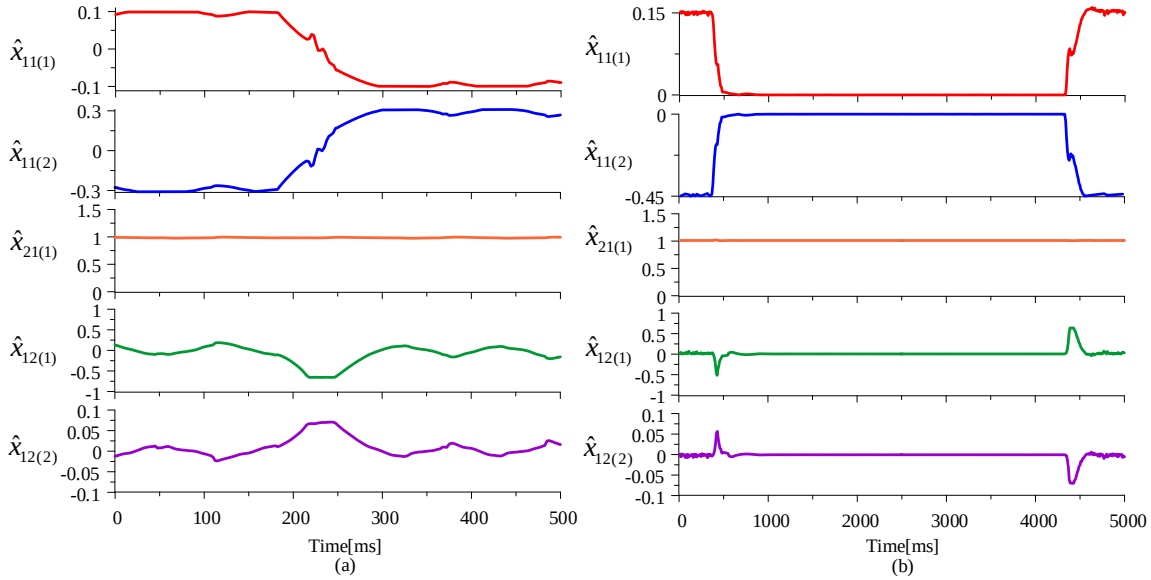

Fig. 5.48 Experimental result of five-phase IPMSM using $\boldsymbol{\psi}_{s(i)}$,$\mathbf{i}_{s(i)}$ vectors based control structure – 2 (a) machine reversing from 0.1 p.u. to -0.1 p.u. (b) standstill test

In Fig. 5.49, the five-phase IPMSM drive is operating in motoring mode and regenerating mode. Step change in reference speed $x^*_{11(1)}$, estimated speed $\hat{x}_{11(1)}$, $\hat{x}_{11(2)}$ and electromagnetic torque $\hat{x}_{12(1)}$, $\hat{x}_{12(2)}$ in first plane and second plane are illustrated in Fig. 5.49. In Fig. 5.49(a), the drive performance is presented under the motoring mode. Reference speed was changed from 0.15 p.u. to 0.25 p.u. after 0.3s and again changed to 0.15 p.u. after 3.15s. Applied load torque was 0.2 p.u. for the motoring mode. In Fig. 5.49(b), regenerating mode of operation of five-phase IPMSM drive is presented. In this test, applied load torque was -0.2 p.u. and reference speed was changed from 0.1 p.u. to 0.2 p.u. after 0.5s and again speed was switched back to 0.1 p.u. after 3.3s.

To examine the robustness of the $\boldsymbol{\psi}_{s(i)}$,$\mathbf{i}_{s(i)}$ vectors based control system-2 uncertainty tests were conducted on five-phase IPMSM drive as shown in Fig. 5.50 and Fig. 5.51. For this test, angular speed of the first plane was set around 0.7 p.u., the speed of second plane was around 2.1 p.u., applied load torque was around 0.57 p.u. In Fig. 5.50(a) and (b), uncertainty test carried out by varying inductance in each plane. In Fig. 5.50(a), it can be observed that initially $L_{q(1)}$ was 50% of $L_{qn(1)}$, and after 3.2s $L_{q(1)}$ was equal to $L_{qn(1)}$, and again after 6.9s $L_{q(1)}$ was 150% of $L_{qn(1)}$. Similarly in Fig. 5.50(b), $L_{q(2)}$ was 0.7 time of $L_{qn(2)}$, and after 3.2s $L_{q(2)} = L_{qn(2)}$, and again after 6.2s $L_{q(2)}$ was 1.7 time of $L_{qn(2)}$. In Fig. 5.50(a), system loses stability when inductance of the first plane

value is changed to $L_{q(1)}$ =1.5$L_{qn(1)}$. While in Fig. 5.50(b), system remains stable for all the cases of inductance variation $L_{q(2)}$ in the second plane.

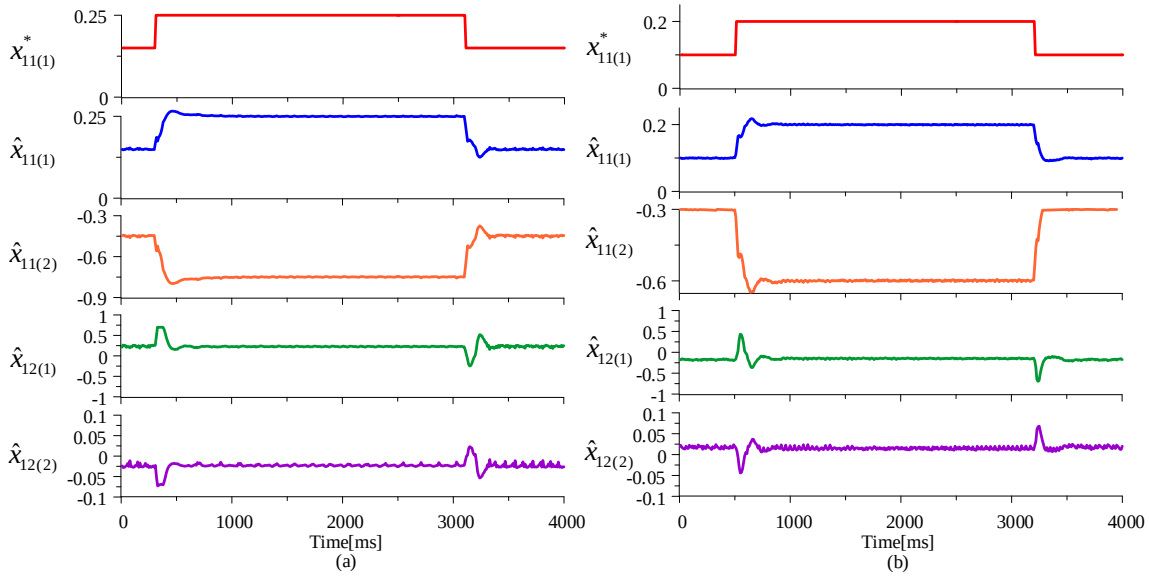

Fig. 5.49 Experimental result of loaded five-phase IPMSM using $\boldsymbol{\psi}_{s(i)}$,$\mathbf{i}_{s(i)}$ vectors based control structure – 2 (a) Motoring mode (b) Regenerating mode

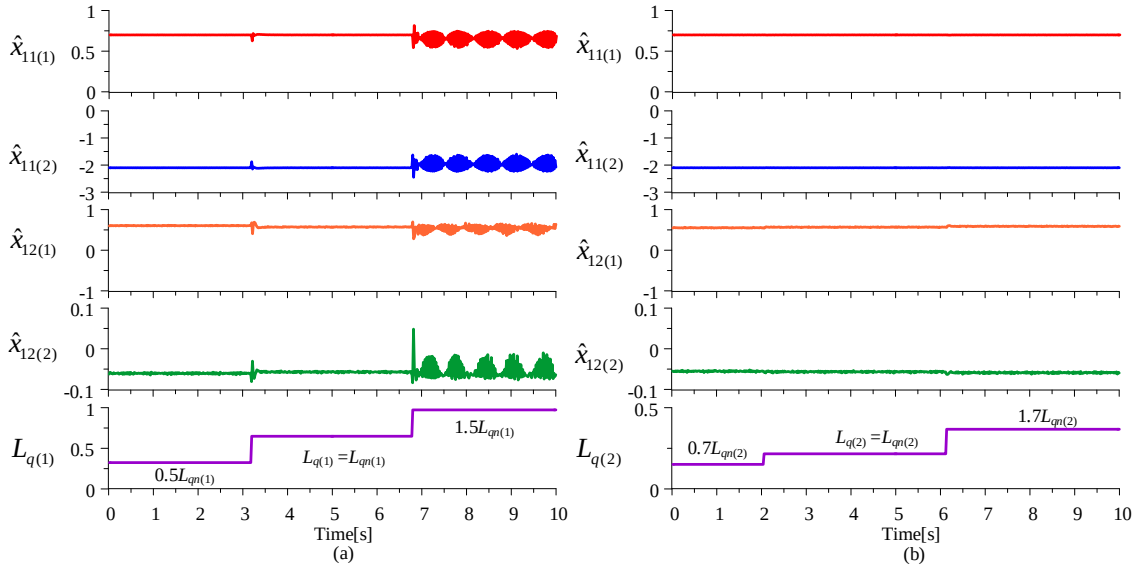

Fig. 5.50 Experimental result of loaded five-phase IPMSM using $\boldsymbol{\psi}_{s(i)}$,$\mathbf{i}_{s(i)}$ vectors based control structure – 2 for different value of inductance (a) $L_{q(1)}$ (b) $L_{q(2)}$

In Fig. 5.51, nominal value of stator resistance was changed to carry out the uncertainty on the five-phase IPMSM drive. Initially, Resistance was 0.5R_{sn}, and after 4.4s R_s = R_{sn}, and again after 7.5s R_s was switched to 1.5R_{sn}. From Fig. 5.51, $\boldsymbol{\psi}_{s(i)}$,$\mathbf{i}_{s(i)}$ vectors based control system-2 does not loose stability while varying the resistance in three different cases.

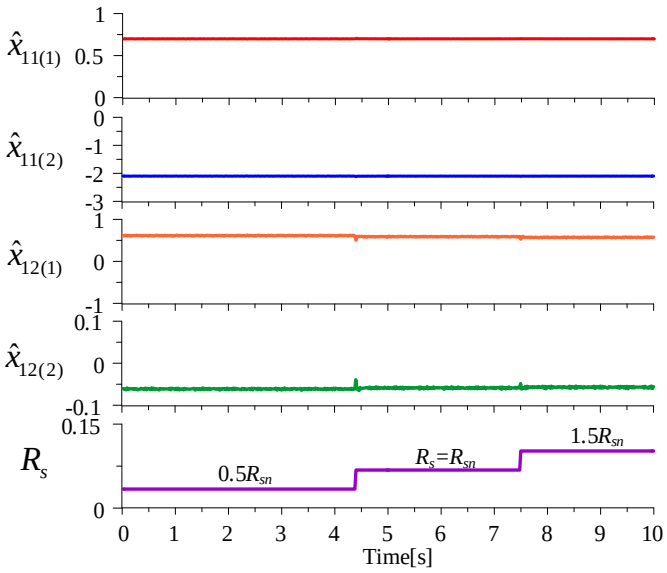

Fig. 5.51 Experimental result of loaded five-phase IPMSM using $\boldsymbol{\psi}_{s(i)}$,$\mathbf{i}_{s(i)}$ vectors based control structure – 2 for different value of resistance

The fault tolerant performance of five-phase IPMSM drive is analyzed using the $\boldsymbol{\psi}_{s(i)}$,$\mathbf{i}_{s(i)}$ vectors based control system-2 as presented in Fig. 5.52. The open phase faults were created using the manually switched circuit breaker. Fig. 5.52 (a) and Fig. 5.52 (b), IPMSM drive was running at steady state around 0.5 p.u. and indicates the current vector components phase A (dark blue), phase C (light blue), and phase E (pink) in natural reference frame measured using an oscilloscope. The current waveform is shown as quasi-trapezoidal due to third harmonic injection. In Fig. 5.52 (a), phase A was deactivated and in Fig. 5.52 (b), phase A and phase C both were deactivated. By deactivating one phase and two-phase, five-phase IPMSM drive continues to rotate.

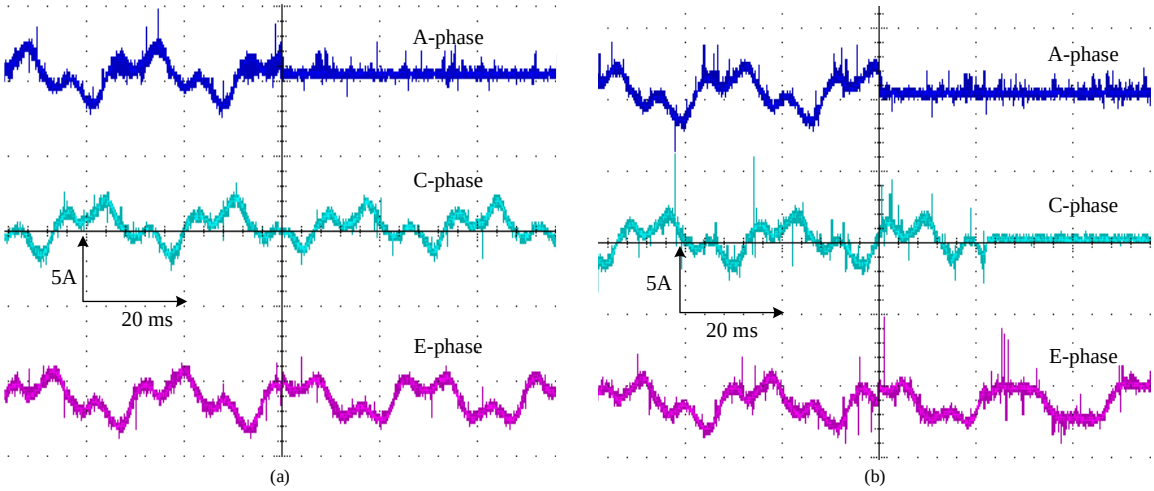

Fig. 5.52 Fault-tolerance test on five-phase IPMSM using $\boldsymbol{\psi}_{s(i)}$,$\mathbf{i}_{s(i)}$ vectors based control structure – 2 (a) phase A was deactivated (b) phase A and C were deactivated

Stator flux reference for the first plane was set around $x^*_{21(1)}$ = 1.0225 p.u. for the first plane, however using this approach flux controlling variable value at steady state was around 0.08 p.u. and during the transient state the flux controlling variable increases up to 0.15 p.u. to maintain the stator flux at defined level as shown in Fig. 5.39. Fig. 5.53 shows the five-phase IPMSM drive performance for two cases: drive start up to nominal speed and drive reversal from 1.0 p.u. to -1.0 p.u. using the $\boldsymbol{\psi}_{s(i)}$,$\mathbf{i}_{s(i)}$ vectors based control system-2 for optimal stator flux reference $x^*_{21(1)}$. The value of optimal stator flux reference $x^*_{21(1)}$ is calculated using the (5.1). The value of $x_{22(1)}$ is substituted using (4.23)

$$x^*_{21(1)} = \left(L_{d(1)}x_{22(1)} + \psi_{f(1)}\right)^2 + \left(L_{q(1)}x_{12(i)} / \left|\psi_{s(i)}\right|\right)^2 \tag{5.1}$$

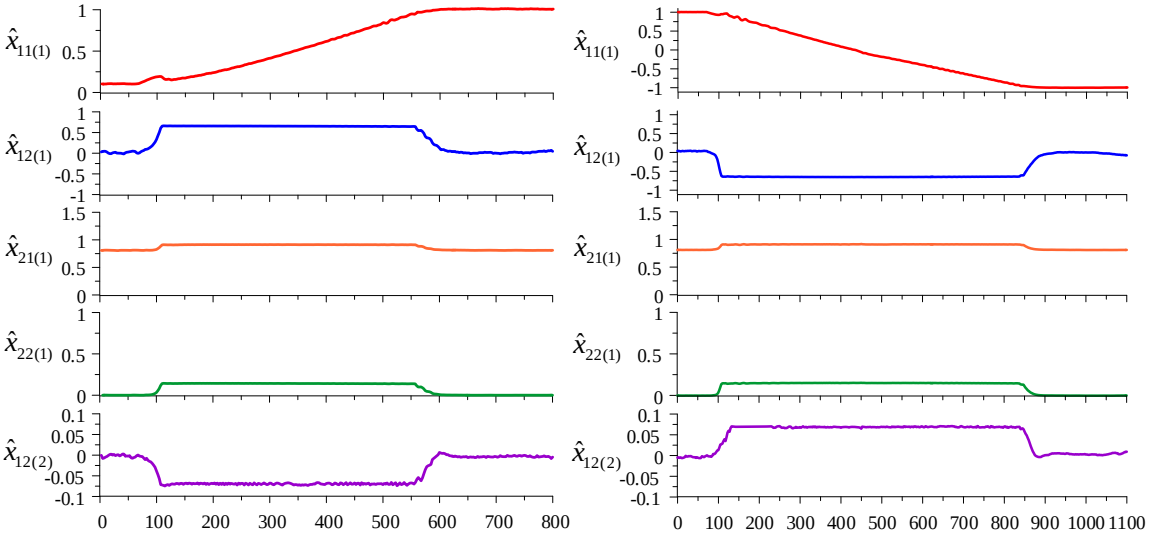

Fig. 5.53 Optimal stator flux based performance of five-phase IPMSM using $\boldsymbol{\psi}_{s(i)}$,$\mathbf{i}_{s(i)}$ vectors based control structure – 2 (a) starting up to 1.0 p.u. (b) reversing from 1.0 p.u. to -1.0 p.u.

By using stator flux reference defined in (5.1), at steady state square of stator flux components remains equal to square of permanent magnet flux which results in better dynamic control of flux controlling variable $\hat{x}_{22(1)}$. During the transient condition, flux controlling variable increases up to 0.15 p.u. and as drive reaches to steady state, flux controlling variable reduces to zero value. Estimated speed $\hat{x}_{11(1)}$, torque generation $\hat{x}_{12(1)}$, $\hat{x}_{12(2)}$ in each plane, square of stator flux $\hat{x}_{21(1)}$ and flux controlling variable $\hat{x}_{22(1)}$ in first plane are shown. Fig. 5.53(a) shows drive acceleration from 0.1 p.u. to 1.0 p.u. and in Fig. 5.53(b) presents drive reversal from 1.0 p.u. to -1.0 p.u. Electromagnetic torque components in the first plane and second plane increases up to the defined limit 0.7 p.u. and 0.07 p.u., respectively. From given results in Fig. 5.53, it can be confirmed

that by using (5.1), square of stator flux was equal to square of permanent flux components at steady state and at dynamic state it was increased up to 0.95 p.u. Simultaneously, at steady state flux controlling variable contribution is not required and flux controlling variable contribution at dynamic state was around 0.15 p.u.

5.5.3 Experimental results of sensorless predictive multiscalar-based control

The first scenario is presented in Fig. 5.54, machine is starting up to 1.0 p.u. at no-load. In Fig. 5.54, measured speed $x_{11(1)}$, estimated speed $\hat{x}_{11(1)}$, speed estimation error $\tilde{x}_{11(1)}$, generated torque in the fundamental plane $\hat{x}_{12(1)}$ and in the secondary plane $\hat{x}_{12(2)}$ are depicted. In Fig. 5.54(a), predictive FOC structure and in Fig. 5.54(b), predictive multiscalar based control structure is presented. The calculated speed estimation error was below 0.05 p.u. In Fig. 5.54, during the transient state, torque reaches to maximum limit around 0.7 for the first plane and 0.07 for the second plane and minimizes to zero when the motor reaches a steady state. The torque provided by the first plane and second planes during the dynamic state in both control structure is almost the same as simulation results, confirming the theoretical hypothesis.

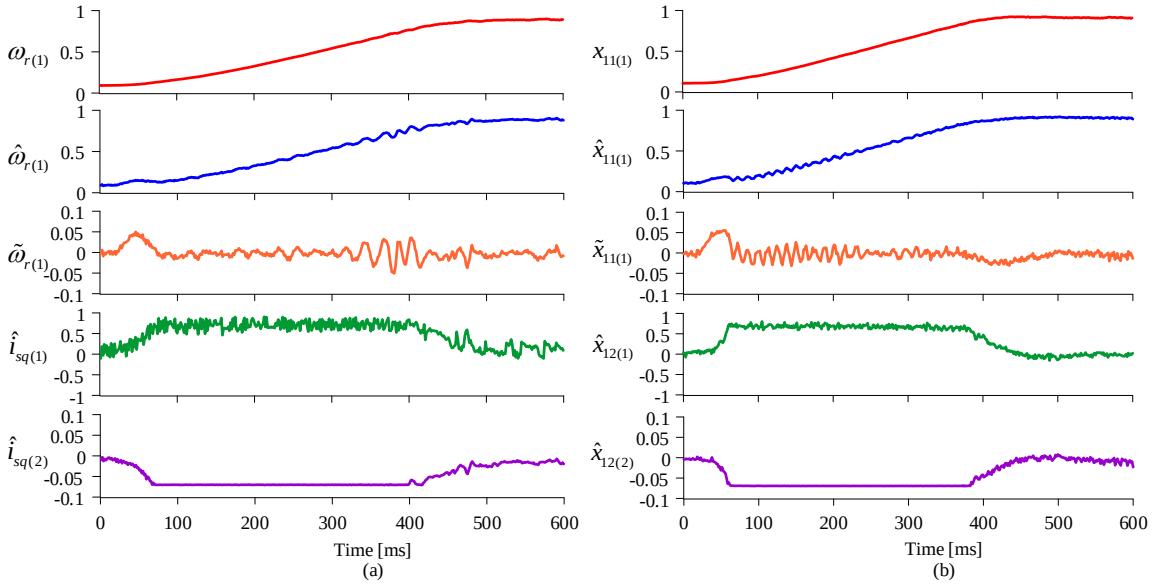

Fig. 5.54 Experimental result of five-phase IPMSM drive starting up to nominal speed (a) classical predictive FOC based structure (b) predictive multiscalar based scheme

In Fig. 5.55, the five-phase IPMSM drive reverses from -1.0 p.u. to 1.0 p.u. at no-load using the estimated rotor speed. Fig. 5.55(a) shows the performance of the classical control scheme and Fig. 5.55(b), depicts the performance of predictive multiscalar based control scheme. The maneuver corresponds to speed reversal using the predictive multiscalar based control introduces less disturbances than the classical PTC. During

the dynamic state, the torque generated in the second plane by third harmonic current injection is almost 10% of the fundamental torque. Moreover, without using the weighting factor, multiscalar based predictive control provides a better dynamic response than the classical control scheme.

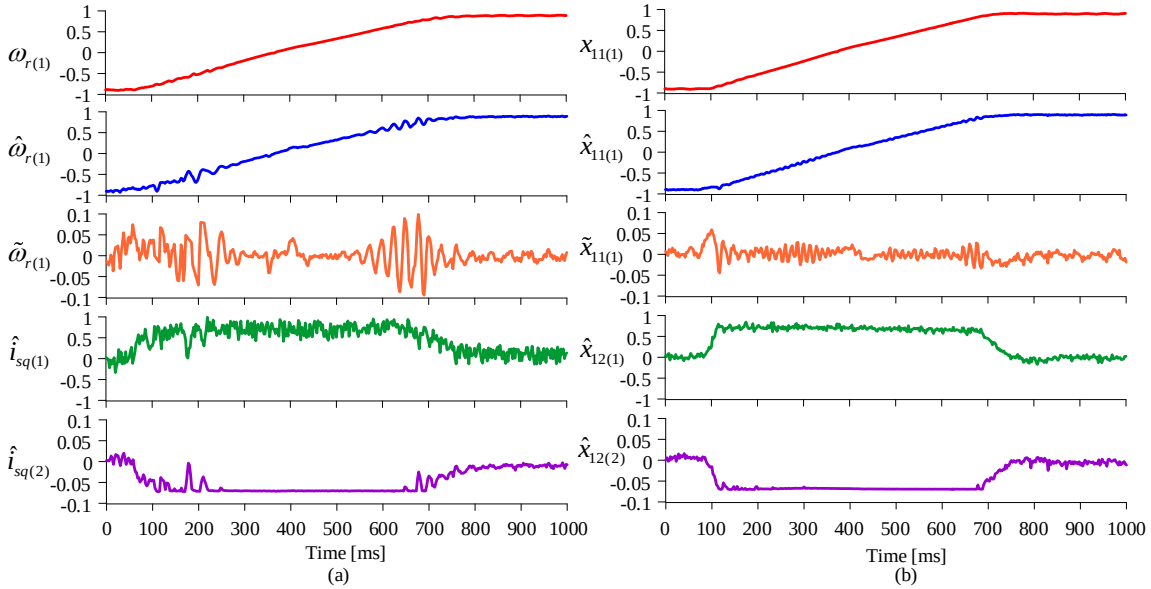

Fig. 5.55 Experimental result of five-phase IPMSM drive reversing from -1.0 p.u. to 1.0 p.u. (a) classical predictive FOC based structure (b) predictive multiscalar based scheme

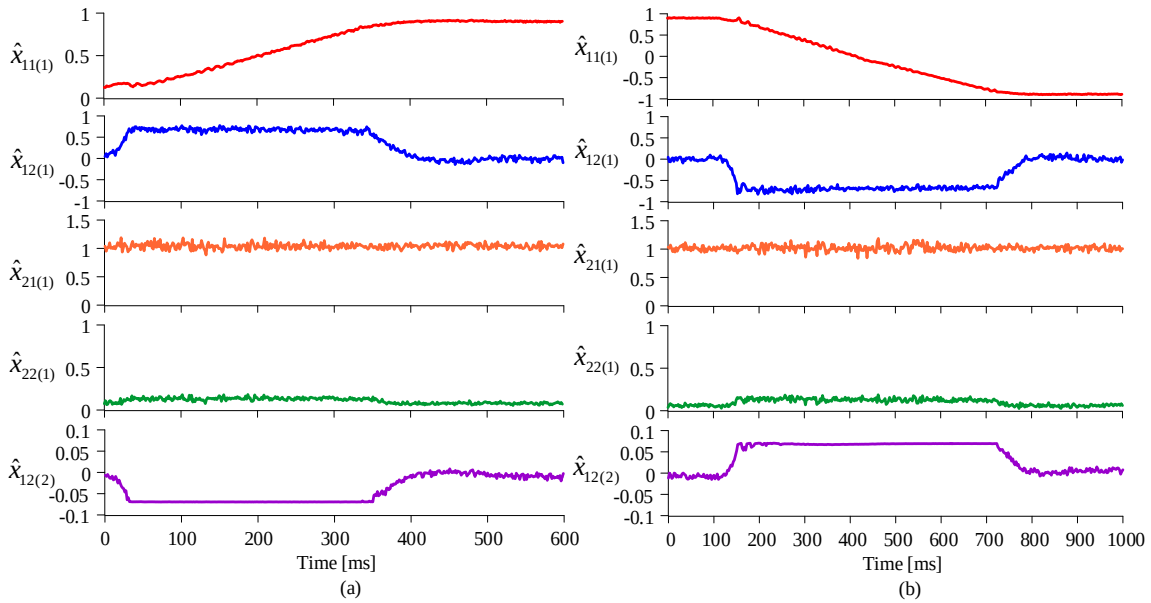

Fig. 5.56 Experimental result of five-phase IPMSM drive (a) starting up to nominal speed b) reversing from 1.0 p.u. to -1.0 p.u. using predictive multiscalar based scheme

In Fig. 5.56(a), five-phase IPMSM drive is starting up to nominal speed and in Fig. 5.56(b) five-phase IPMSM drive is reversing from 1.0 p.u. to -1.0 p.u. using the predictive multiscalar based control. Multiscalar variables: estimated speed $\hat{x}_{11(1)}$, square of stator flux $\hat{x}_{21(1)}$, flux controlling variable $\hat{x}_{22(1)}$ of the first plane and generated

electromagnetic torque in first plane $\hat{x}_{12(1)}$ and second plane $\hat{x}_{12(2)}$ are illustrated in Fig. 5.56. In this control scheme, the square of stator flux is kept constant at defined value $x^*_{21(1)}$ = 1.0225 p.u. for the first plane and $x^*_{21(2)}$ = 0.0225 p.u. for the second plane. To maintain a constant value of stator flux level in five-phase IPMSM for the first plane, the flux controlling variable has to be positive, which can be seen for both cases: machine starting up to nominal speed and reversing from 1.0 p.u. to -1.0 p.u. From Fig. 5.56, to keep the flux level constant $\hat{x}_{21(1)}$, the demand of flux controlling variable $\hat{x}_{22(1)}$ is less during the steady-state conditions, but during dynamic conditions, the requirement of flux controlling variable increases. In Fig. 5.56, torque contribution of each plane is also shown for both cases.

In the next scenario, the rotor speed was set at 0.5 p.u. and applied load torque was 0.1 p.u. After 0.13s, load torque was increased to 0.6 p.u. To conduct the test, torque variables was limited to 0.7 p.u. and to 0.07 p.u., respectively. In Fig. 5.57, estimated rotor speed in first plane $\hat{x}_{11(1)}$ and second plane $\hat{x}_{11(2)}$, torque variables of both plane $\hat{x}_{12(1)}$, $\hat{x}_{12(2)}$, and flux controlling variable $\hat{x}_{22(1)}$ of first plane are displayed. Fig. 5.57(a), presents when applied load was changed from 0.1 p.u. to 0.6 p.u., the demand of flux controlling variable also increased to maintain constant level of stator flux. In Fig. 5.57(b), steady state performance of the five-phase IPMSM drive is presented for the same working points about time period of 150 ms. It can be noticed that at steady state, estimated speed of first plane was maintained at 0.5 p.u. and estimated speed of the second plane was maintained at -1.5 p.u. Moreover, generated electromagnetic torque in first plane and second plane were around 0.6 p.u. and 0.06 p.u., respectively. Demand of flux controlling variable also increased from 0.08 p.u. to 0.15 p.u. to keep the stator flux at desired level.

Fig. 5.58 shows the dynamic and steady-state performance of the five-phase IPMSM when the load is reduced. In Fig. 5.58 (a), the rotor was rotating at a reference speed of 0.5 p.u. for the first plane and 0.6 p.u. load was connected. After 0.1s, load was reduced to 0.1 p.u. Due to sudden reduction in load, speed increases for a very small time and again reaches the reference speed, and the torque value settles at the desired value. The requirement of flux controlling variables to maintain stator flux level also reduced as the applied load is reduced. Steady-state performance for the same working points is visible in Fig. 5.58(b) for the small time period of 150 ms. As shown

in Fig. 5.58(b), estimated speed was maintained at defined value, electromagnetic torque supplied by five-phase IPMSM for fundamental plane $\hat{x}_{12(1)}$ was around 0.1 p.u. and for second plane $\hat{x}_{12(2)}$ was around 0.01 p.u. Flux controlling variable $\hat{x}_{22(2)}$ demand was reduced up to 0.08 p.u. in steady state. From Fig. 5.57 and Fig. 5.58, predictive multiscalar-based control solution remains stable and provides fast dynamic response in the case of load injection and load removal.

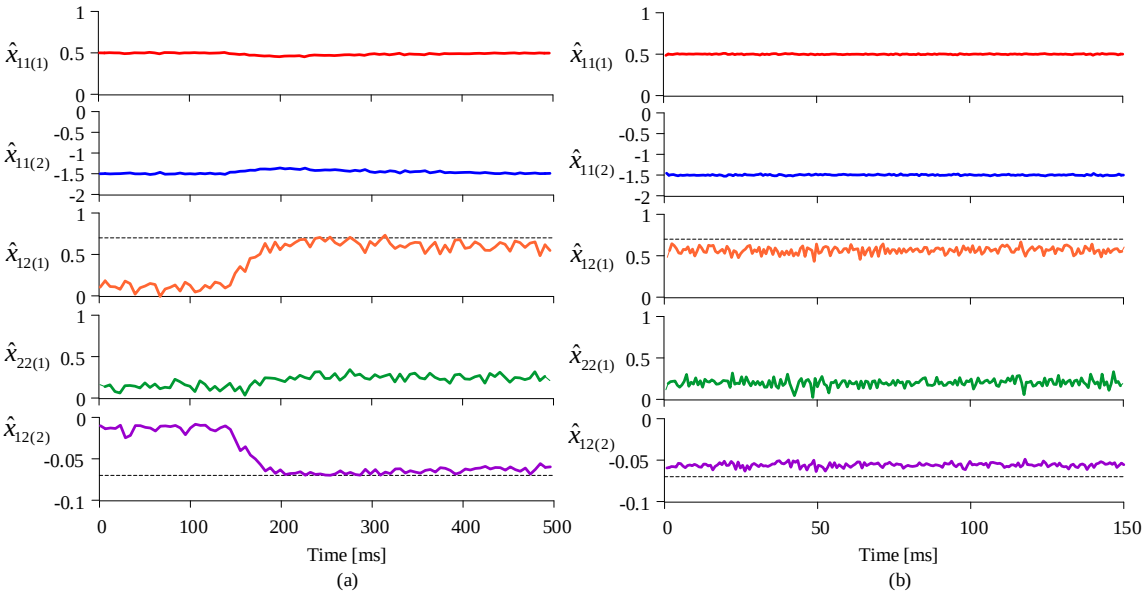

Fig. 5.57 Experimental result of five-phase IPMSM drive (a) after 0.13s load torque T_L was changed from 0.1 p.u. to 0.6 p.u. b) steady state is presented for 150 ms period

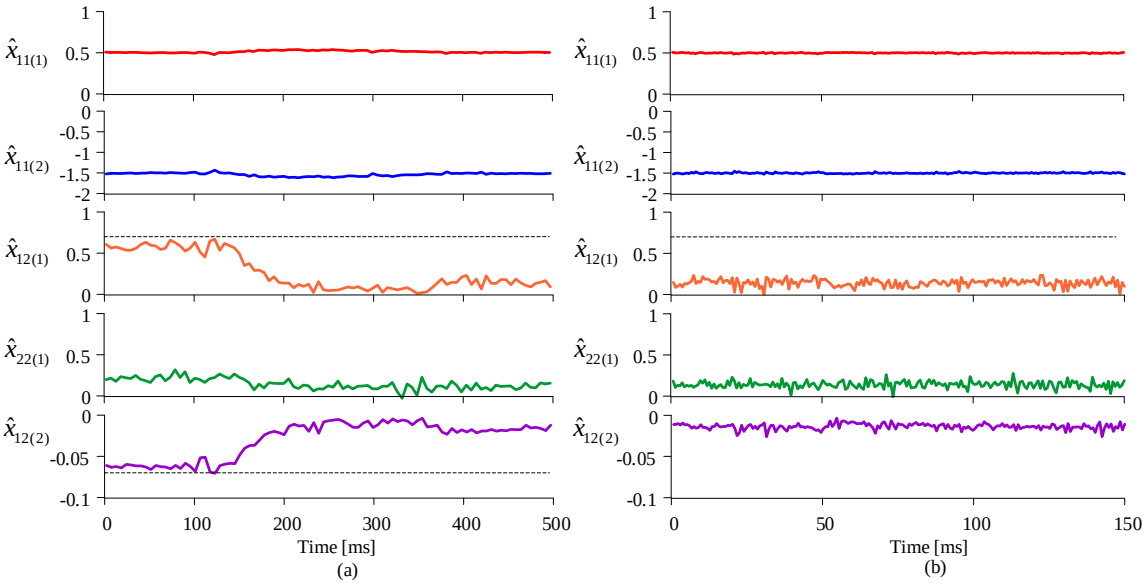

Fig. 5.58 Experimental result of five-phase IPMSM drive (a) after 0.1s load torque T_L was changed from 0.6 p.u. to 0.1 p.u. b) steady state is presented for 150 ms period

In the next scenario, five-phase IPMSM drive was investigated for low-speed reversal test and standstill test. In Fig. 5.59(a), IPMSM drive reverses under load torque

T_L = -0.2 p.u. Performance of predictive multiscalar-based control provides excellent dynamic response at low-speed reversal. Fundamental speed reverses $\hat{x}_{11(1)}$ from 0.1 to -0.1 p.u. and speed of second plane $\hat{x}_{11(2)}$ reverses from -0.3 p.u. to 0.3 p.u. Flux level $\hat{x}_{21(1)}$ is maintained at constant at 1.0225 p.u. for the first plane. During the transient state, the supplied electromagnetic torque changes from -0.2 p.u. and 0.02 p.u. to maximum allowable limit -0.7 p.u. and 0.07 p.u., respectively, and when the reversal is completed to -0.1 p.u., the torque value again approaches -0.2 p.u. and 0.02 p.u. In Fig. 5.59(b), standstill test on five-phase IPMSM drive is presented. The IPMSM drive was running at steady state around 0.3 p.u. and after 450ms, reference speed command was changed to 0.0 p.u. The drive successfully operates at zero speed and the rotor of the five-phase IPMSM was held at zero speed for almost 1.9s. After 2.3s drive returned to desired speed command around 0.3 p.u. in the first plane as shown. The proposed control solution of five-phase IPMSM ensures that drive remains stable during zero speed reference and does not loose synchronism.

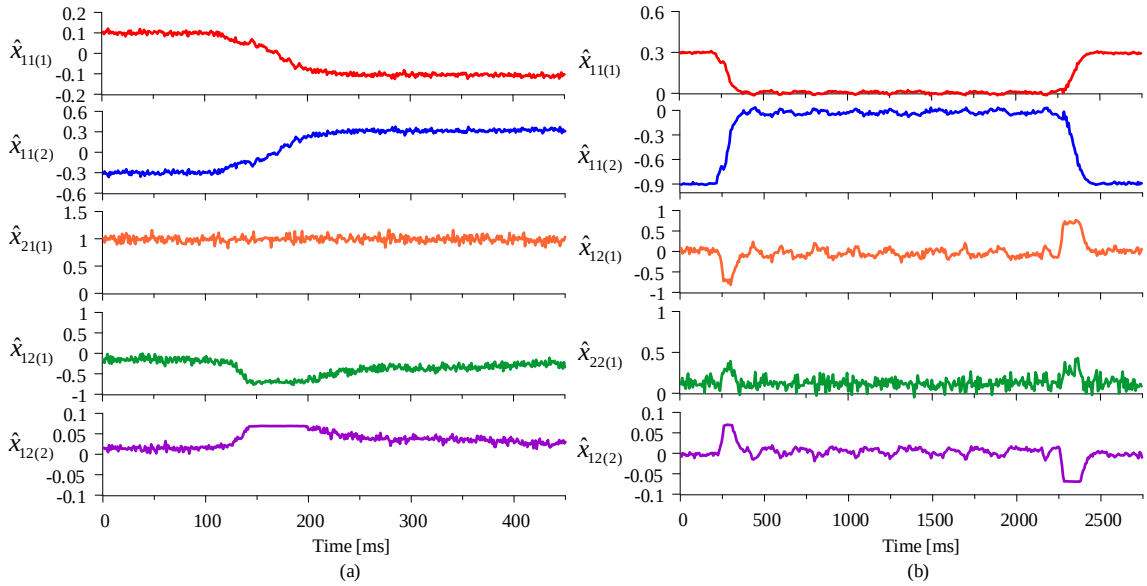

Fig. 5.59 Experimental result of five-phase IPMSM drive (a) drive reversing from 1.0 p.u. to -1.0 p.u. (b) standstill test

In the next scenario, the test of robustness was carried out using the predictive multiscalar control structure of five-phase IPMSM drive. In Fig. 5.60 and Fig. 5.61, the nominal value of inductances in each plane and stator resistance was changed in 3 different scenarios. The reference speed of the rotor was set at 0.5 p.u. and the value of load torque T_L = 0.45 p.u. In Fig. 5.55(a), $L_{q(1)}$ was $0.5L_{qn(1)}$ and after 1.7s $L_{q(1)}$ was equal to $L_{qn(1)}$ and after 5.7s $L_{q(1)}$ = 1.5 $L_{qn(1)}$. In Fig. 5.55(b), the same working points

are implemented for various value of the second plane's inductance $L_{q(2)}$. In Fig. 5.60(b), the control system is robust and maintains the system's stability on changes in the value of inductance $L_{q(2)}$: however, when the value of inductance of the first plane changes to $1.5L_{qn(1)}$, the stability of the system reduces. Similarly, in Fig. 5.61 the value of resistance is altered in three stages: $R_s = 0.5R_{sn}$, $R_s = R_{sn}$ and $R_s = 1.5R_{sn}$. The control system proves to robust and stable against the changes of different resistance values as shown in Fig. 5.61.

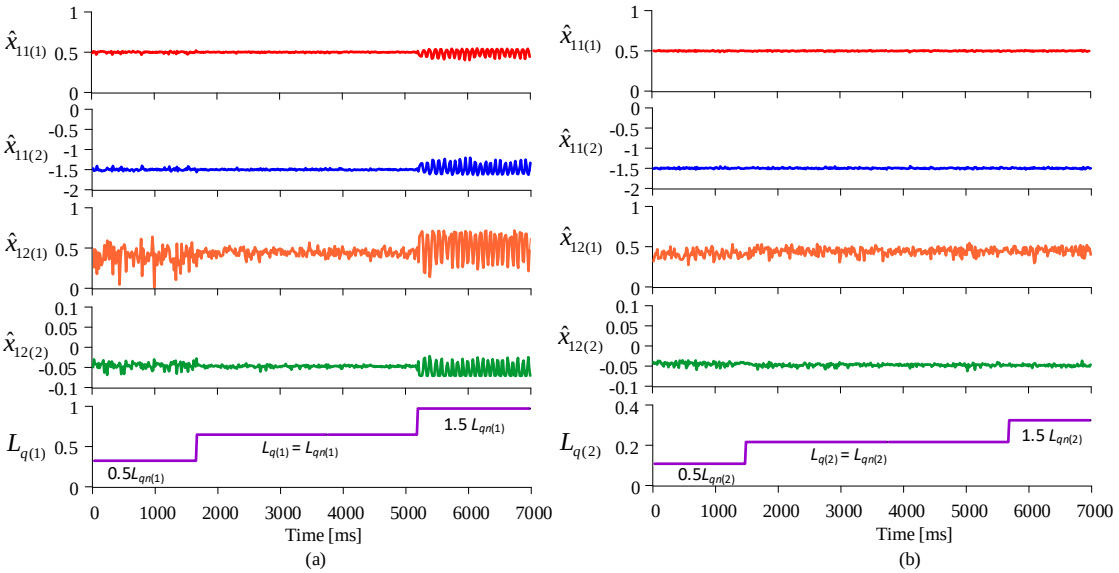

Fig. 5.60 Experimental result of five-phase IPMSM drive for different value of inductances (a) $L_{q(1)}$ (b) $L_{q(2)}$

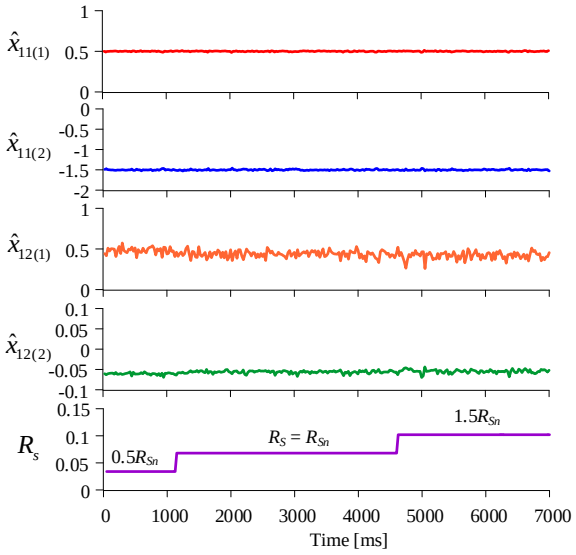

Fig. 5.61 Experimental result of five-phase IPMSM drive for different value of resistance

5.5.4 Experimental results of backstepping mutliscalar control structure

Fig. 5.62 and Fig. 5.63 shows two sets of plots where IPMSM drive is starting up to nominal speed and reversing from -1.0 p.u. to 1.0 p.u., respectively. Different

variables such as measured angular speed $x_{11(1)}$, estimated speed $\hat{x}_{11(1)}$, error between the measured and estimated speed $\tilde{x}_{11(1)}$, electromagnetic torque generation in first plane $\hat{x}_{12(1)}$ and second plane $\hat{x}_{12(2)}$ are illustrated.

The time domain response of five-phase IPMSM drive over a time period of about 900 ms is shown using FOC structure in Fig. 5.62(a) and by backstepping mutliscalar control structure in Fig. 5.62(b). From Fig. 5.62(b), it is possible to enhance toque generation by third harmonic injection using the backstepping mutliscalar control structure. As drive accelerates from 0.1 p.u. to 1.0 p.u., torque production in each plane rises from zero to 0.7 p.u. and 0.07 p.u., respectively. In this test, speed estimation error was less than 0.05 p.u. for both control structures. From the given experimental results, it can be noticed that Fig. 5.62(b) appears slightly more damped with less oscillation and the system variables settle quicker.

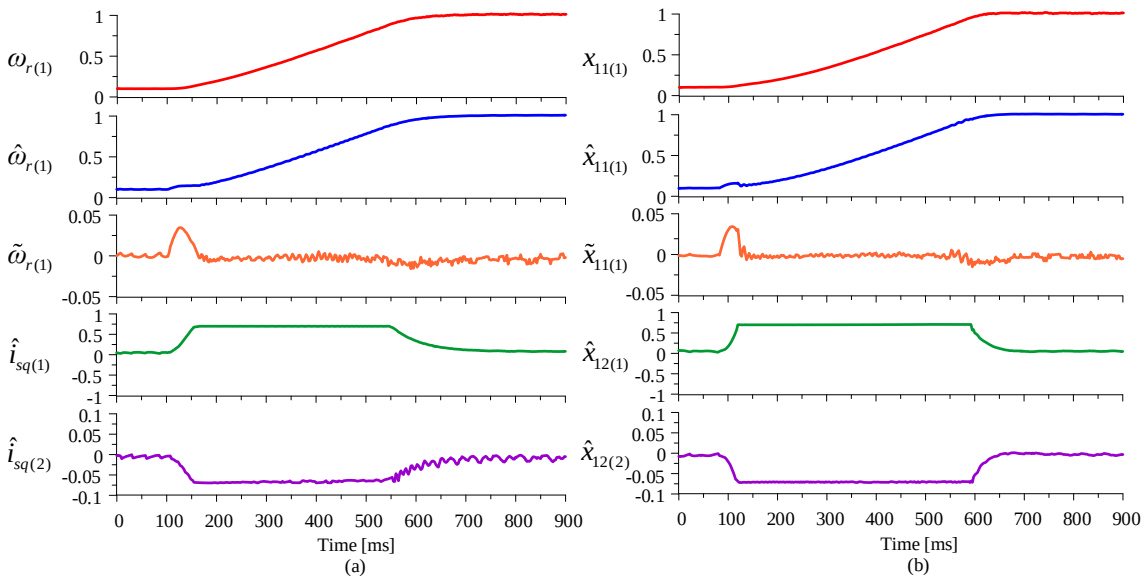

Fig. 5.62 Experimental results of five-phase IPMSM drive starting up to 1.0 p.u. (a) FOC structure (b) backstepping mutliscalar control structure

Fig. 5.63 presents time-domain plots of drive reversing from -1.0 p.u. to 1.0 p.u. over a duration of 1100ms. Fig. 5.63(a) and (b), provides comparative analysis between the drive system behavior under different control strategies. Similar to Fig. 5.62(b), torque enhancement using the backstepping based control structure can be seen in Fig. 5.63(b). Moreover, compared to Fig. 5.63(a), Fig. 5.63(b) shows smooth responses and less disturbances in the output response. Backstepping mutliscalar control structure approach provides excellent dynamic performance in both cases: drive starting up to nominal speed and drive reversing from 1.0 p.u. to -1.0 p.u.

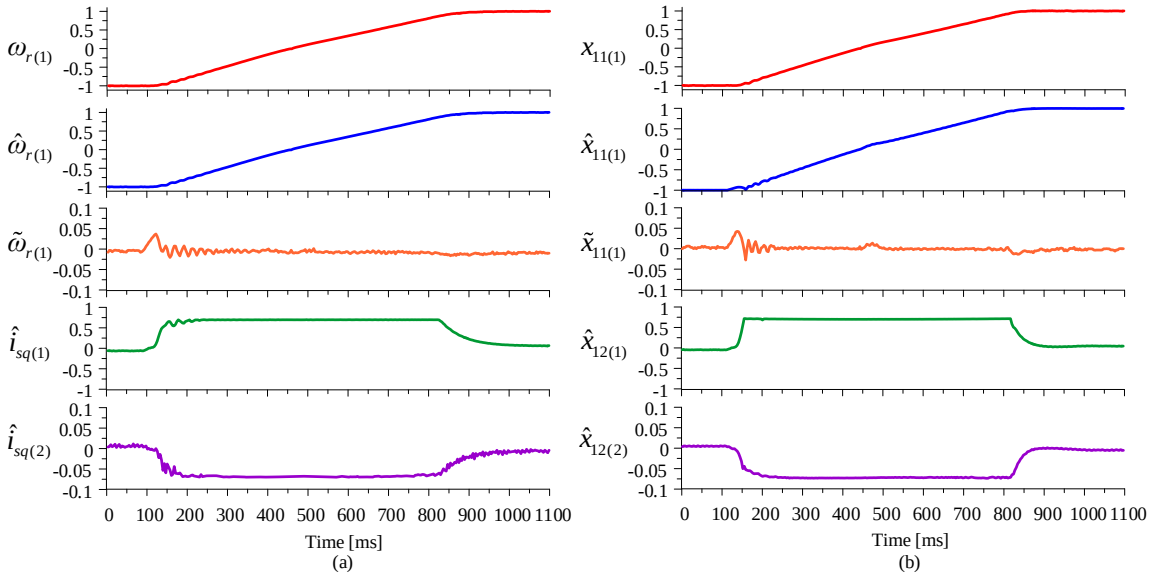

Fig. 5.63 Experimental results of five-phase IPMSM reversing from 1.0 p.u. to -1.0 p.u. (a) FOC structure (b) backstepping mutliscalar control structure

In the next case, backstepping control of five-phase IPMSM drive was tested against the load torque injection in Fig. 5.64 and removal in Fig. 5.65, respectively. Estimated angular speed of the machine $\hat{x}_{11(1)}$, electromagnetic torque generation in each plane $\hat{x}_{12(1)}$,$\hat{x}_{12(2)}$, and reluctance torque $\hat{x}_{22(1)}$ in first plane and calculated speed estimation error $\tilde{x}_{11(1)}$ are visible in the given plots.

In Fig. 5.64(a), five-phase IPMSM drive was running at steady state around 0.5 p.u with no-load. After 0.45s load torque T_L was injected up to 0.86 p.u. With injection of load torque T_L, electromagnetic torque generation increases in each plane up to the defined limit in the controller. In the first plane, electromagnetic generation $\hat{x}_{12(1)}$ increases up to 0.7 p.u. and in the second plane, torque contribution $\hat{x}_{12(2)}$ is up to 0.07 p.u. which is the 10% of the fundamental torque. The contribution of reluctance torque in the first plane is also presented. The speed estimation error was significantly less through the test. In Fig. 5.64(b), steady state performance of the five-phase IPMSM drive with the same operating points are presented for the time period of 150 ms.

In Fig. 5.65(a), the drive performance was investigated for load ejection. Drive was running at 0.5 p.u. with applied load around 0.86 p.u. After 0.48s, load torque was removed from 0.86 p.u. to 0.12 p.u. During the transient state, small overshoot is visible in the speed curve, but drive quickly settle at 0.5 p.u. with the given load condition of 0.12 p.u. The contribution of torque in each plane also changes to required level. For

the time period of 150 ms, stable drive performance is shown in the same operating points in Fig. 5.65(b).

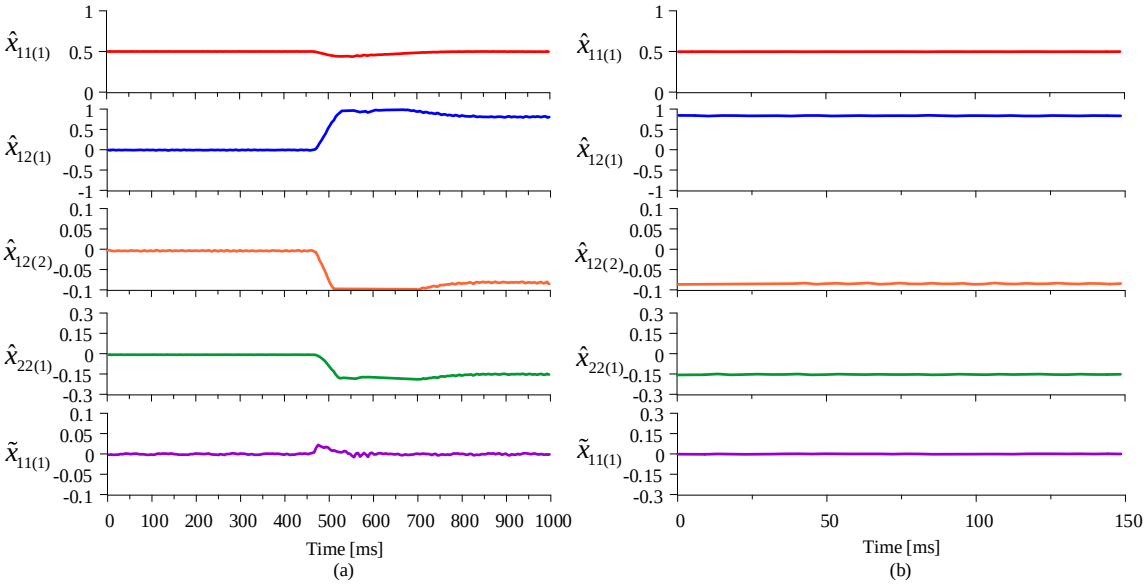

Fig. 5.64 Experimental result of backstepping mutliscalar control structure of five-phase IPMSM (a) after 0.45s load torque was changed to 0.86 p.u. (b) steady state

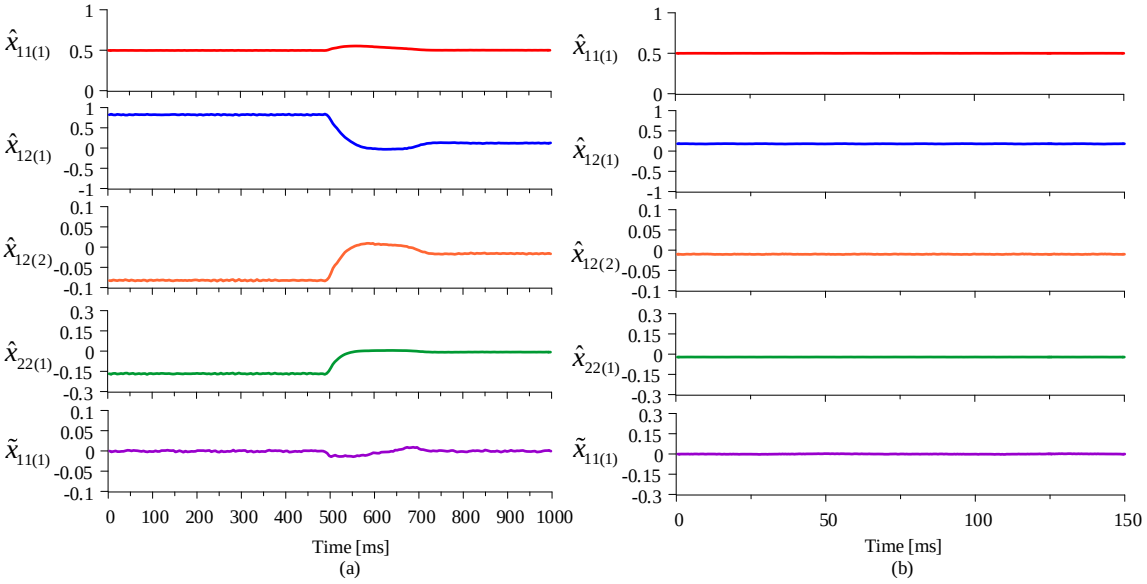

Fig. 5.65 Experimental result of backstepping mutliscalar control structure of five-phase IPMSM (a) after 0.48s load torque was removed from 0.86 p.u. to 0.15 p.u.(b) steady state

In the next scenario, performance of the drive was verified by turning on and off 3rd harmonic injection as depicted in Fig. 5.66 and Fig. 5.67. In the given experimental results, estimated speed $\hat{x}_{11(1)}$, fundamental current $\hat{i}_{s\alpha(1)}$, third harmonic current $\hat{i}_{s\alpha(2)}$, total current $\hat{i}_{s\alpha(1+2)}$, and torque generation in the second plane $\hat{x}_{12(2)}$ are shown. In Fig. 5.66(a), drive was running at 0.4 p.u. with fundamental supply only. The applied load was around 0.5 p.u. After 0.15s, 3rd harmonic current was injected into the five-phase

IPMSM drive. As 3rd harmonic current was injected, the waveshape of total current changed from sinusoidal to quasi-trapezoidal wave. In addition, torque contribution from second plane increased from zero to 0.05 p.u. In Fig. 5.66(b), steady state operation of the drive is illustrated with same operating points.

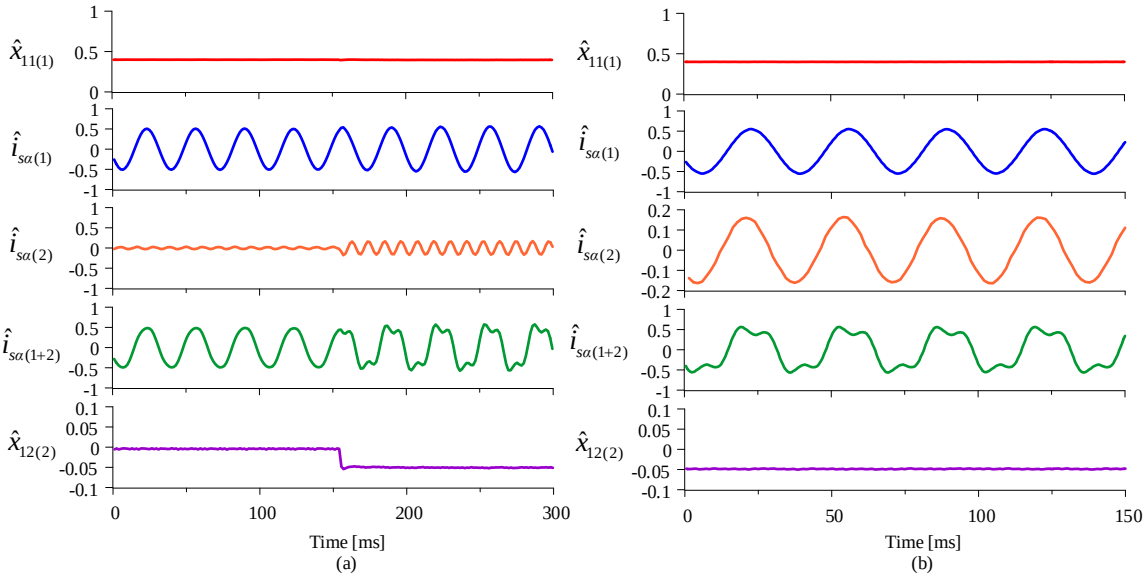

Fig. 5.66 Experimental result of backstepping mutliscalar control structure of five-phase IPMSM (a) after 0.15s 3rd harmonic injection was turned on (b) steady state

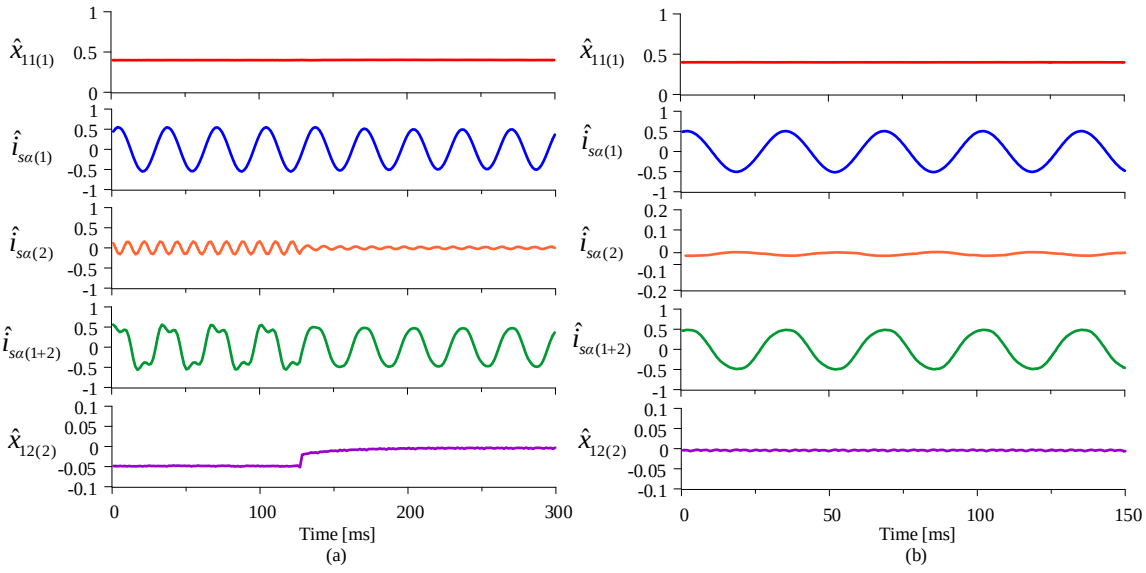

Fig. 5.67 Experimental result of backstepping mutliscalar control structure of five-phase IPMSM (a) after 0.12s 3rd harmonic injection was turned off (b) steady state

Fig. 5.67(a) shows that after 0.12s, 3rd harmonic injection was turned off. As 3rd harmonic injection was turned off, current waveshape becomes sinusoidal from quasi-trapezoidal. Due to purely sinusoidal supply, torque generation in second plane reduces to zero. Fig. 5.67(b), steady state of the drive is visible for 150 ms time period. As

shown in Fig. 5.66 and Fig. 5.67, that 3rd harmonic current injection leads to enhancement of electromagnetic torque up to 10% of the fundamental torque.

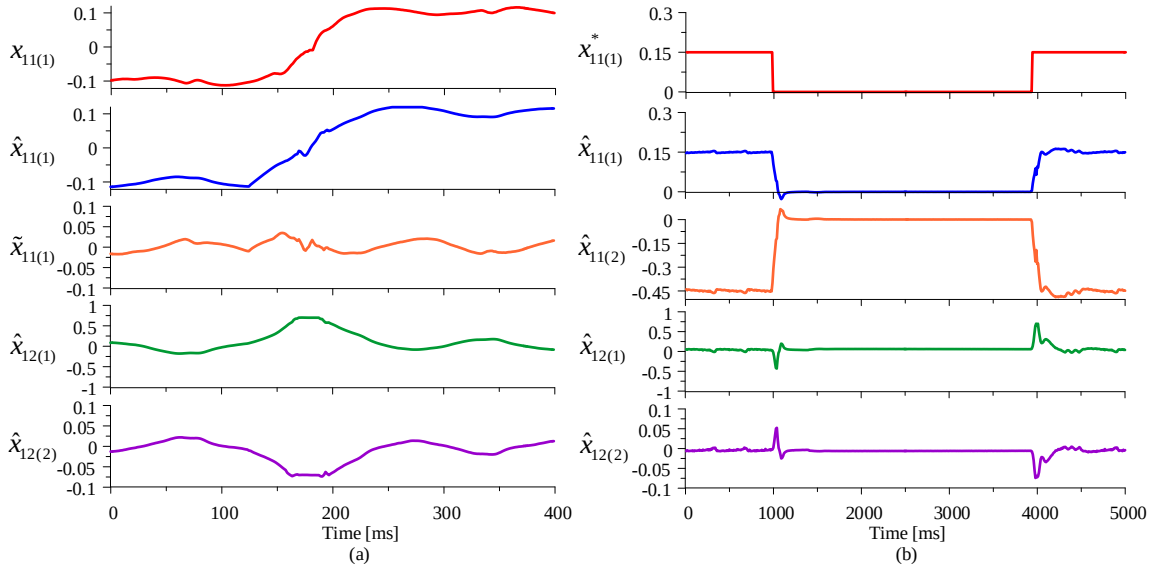

Fig. 5.68 Experimental result of backstepping mutliscalar control structure of five-phase IPMSM (a) drive reversal from -0.1 p.u. to 0.1 p.u. (b) standstill test

In Fig. 5.68(a), backstepping mutliscalar control structure was examined for low speed reversal from -0.1 p.u. to 0.1 p.u. Different variables: measured speed $x_{11(1)}$, estimated speed $\hat{x}_{11(1)}$, calculated speed estimation error $\tilde{x}_{11(1)}$ and electromagnetic torque $\hat{x}_{12(1)}$, $\hat{x}_{12(1)}$ in each plane are shown. At low speed reversal test, the effect of voltage drop due to stator resistance and nonlinerities of the inverter plays a signficant role hence oscillaion are visibile in the speed response curve. At low speed test, speed estimation error was less than 0.05 p.u.

Fig. 5.68(b), shows that standstill of the five-phase IPMSM drive by backstepping mutliscalar control structure. In Fig. 5.68(b), presents the behavior of step change in reference speed $x^*_{11(1)}$, estimated speed in first plane $\hat{x}_{11(1)}$ and second plane $\hat{x}_{11(2)}$, torque production in first plane $\hat{x}_{12(1)}$ and second plane $\hat{x}_{12(1)}$. In this test, drive was running around 0.15 p.u., after 1s reference speed $x^*_{11(1)}$ was changed from 0.15 p.u. to 0.0 p.u. At zero speed, rotor was held stationary for nearly 3s and after 4s rotor speed was changed back to 0.15 p.u. Electrical machine does not loose synchronism at zero speed by using the backstepping technique, in addition the control system provides adequate and reliable control at zero speed also.

In Fig. 5.69, the experimental results of motoring test and regenerating test are given over a time period of 4200 ms. Experimental results contain the information of reference speed $x^*_{11(1)}$, estimated speed in first plane $\hat{x}_{11(1)}$ and second plane $\hat{x}_{11(2)}$, production of electromagnetic torque $\hat{x}_{12(1)}$,$\hat{x}_{12(2)}$ in each plane. First, motoring test on five-phase IPMSM drive is explained, followed by the regenerating test.

In Fig. 5.69(a), drive was running at 0.25 p.u. with applied load was around 0.2 p.u. Around 0.5s, reference speed was altered from 0.25 p.u. to 0.35 p.u. for up to 3.3s and after 3.3s reference speed was returned back to 0.25 p.u. Thorough out the test, torque contribution from first plane and second plane was obtained at desired value. It can be noticed that produced electromagnetic torque in first plane was around 0.2 p.u. and in second plane was around -0.02 p.u.

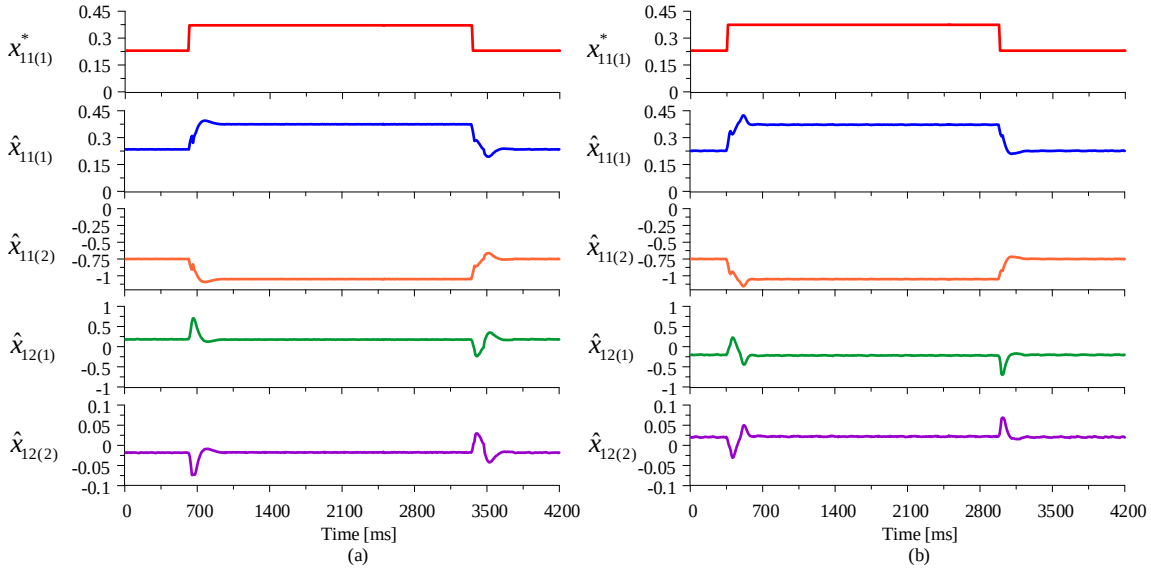

Fig. 5.69 Experimental result of backstepping mutliscalar control structure of five-phase IPMSM (a) mototring test (b) regenrating test

In Fig. 5.69(b), experimental test is shown for regenerating test with similar operating points of motoring test. It can be observed as current direction reverse in this test, produced electromagnetic torque is negative. The electromagnetic toque value is -0.2 p.u. in the first plane and 0.02 p.u. in the second plane. In both tests, it is visible that speed of the second pane changed from -0.75 p.u. to -1.05 p.u. and again back to -0.75 p.u. after some interval of time. Backstepping mutliscalar control structure ensures efficient and rapid dynamic control of five-phase IPMSM drive in both cases: motoring mode and regenerating mode. In the next scenario, drive performance is evaluated for

different value of inductances in each plane and stator resistant to ensure robustness of the given control structure.

In Fig. 5.70, drive was running at 0.5 p.u. with applied load around 0.5 p.u. and inductance value of the first plane $L_{q(1)}$ and second plane $L_{q(2)}$ was modified across three distinct cases. In Fig. 5.70(a), initially inductance value of the first plane was around $0.5L_{qn(1)}$ and after 1.3s $L_{q(1)}$ was equal to $L_{qn(1)}$ and in the case $L_{q(1)}$ was twice than the nominal value of inductance. In the similar manner, inductance in the second plane was also altered: initially the value of $L_{q(2)}$ was half of the nominal value of inductance in the second plane, after 1s $L_{q(2)} = L_{qn(2)}$, and in the last stage $L_{q(2)} = 2L_{qn(2)}$.

Based on the given experimental results in Fig. 5.70(a), the control system loses stability when inductance of first plane changed to twice the nominal value of inductance. Speed estimation error was significantly higher when inductance value was doubled. In Fig. 5.70(b), control system maintains stability and remains stable across all 3 scenarios. Speed estimation error was extremely small in the second plane in all 3 scenarios.

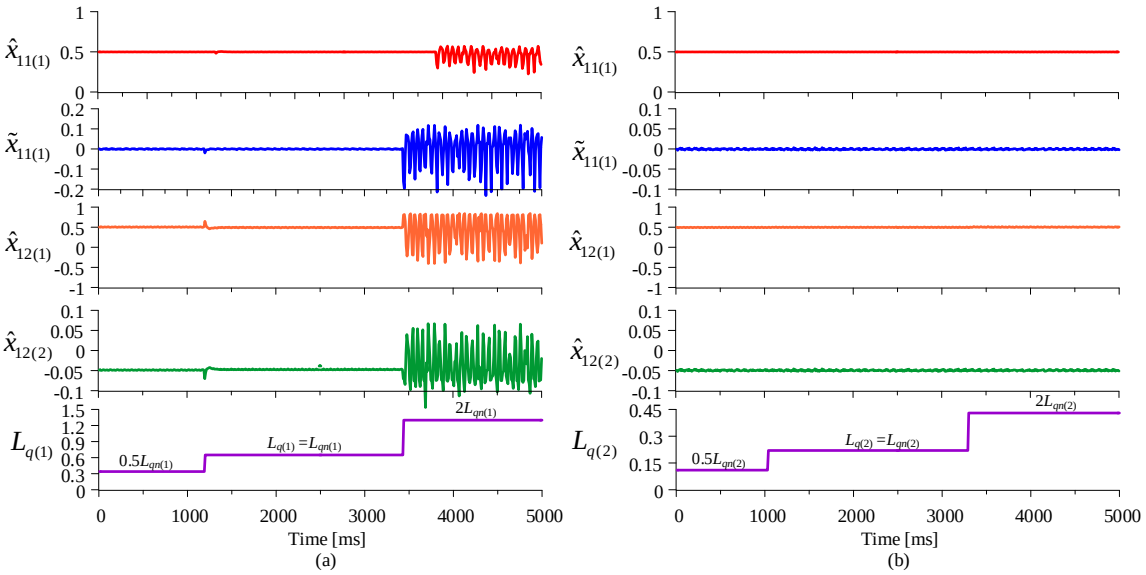

Fig. 5.70 Experimental result of backstepping mutliscalar control structure of five-phase IPMSM for different value of inductanes (a) $L_{q(1)}$ (b) $L_{q(2)}$

In Fig. 5.71, stator resistance was varied in 3 different cases to conduct uncertainty test on five-phase IPMSM drive. In this test, drive was running at 0.5 p.u. with applied load around 0.5 p.u. Stator resistance was half of R_{sn} up to 0.8s, after 0.8s R_s was equal to R_{sn} and after 0.33s R_s=1.5R_{sn}. From given result, it can be observed that speed estimation error was significantly less almost close to zero. By varying the value of

stator resistance in all scenarios, the control system is proved to be robust and remains stable.

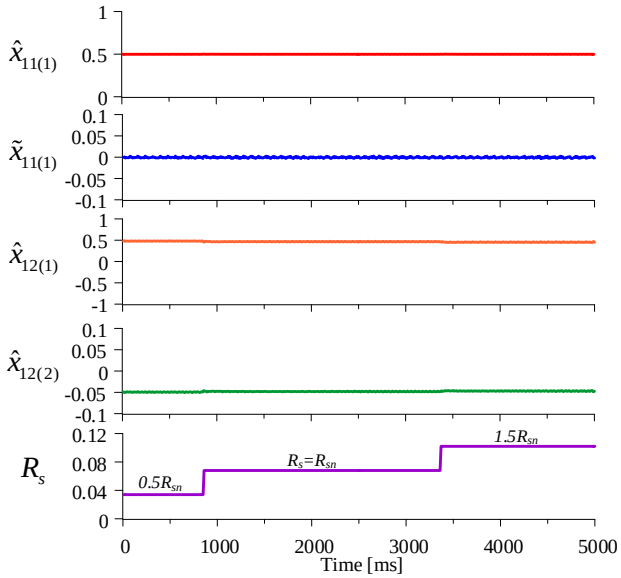

Fig. 5.71 Experimental result of backstepping mutliscalar control structure of five-phase IPMSM for different value of inductance (a) $L_{q(1)}$ (b) $L_{q(2)}$

To examine drive performance above the based speed, field weakening test was implemented on five-phase IPMSM drive using backstepping mutliscalar control structure as shown in Fig. 5.72(b). To conduct comparative analysis, field weakening performance using FOC structure is also presented in Fig. 5.72(a). In Fig. 5.72, important variables of the drives such as: measured speed $\omega_{r(1)} \sim x_{11(1)}$,, estimated speed $\widehat{\omega}_{r(1)} \sim \hat{x}_{11(1)}$, calculated error between the measured speed and estimated speed $\widetilde{\omega}_{r(1)} \sim \tilde{x}_{11(1)}$, electromagnetic torque component $\hat{i}_{sq(1)} \sim \hat{x}_{12(1)}$, reluctance torque component $\hat{i}_{sd(1)} \sim \hat{x}_{22(1)}$ in first plane are presented. Field weakening test was conducted using fundamental plane variables, third harmonic injection was off during this test.

From the experimental results presented in Fig. 5.72, it is visualized that the drive is accelerating from 0.1 p.u. to 2.0 p.u. using both control structures. It can be observed that as drive accelerates from 0.1 p.u. to 1.0 p.u., electromagnetic torque $\hat{i}_{sq(1)} \sim \hat{x}_{12(1)}$ increased up to maximum permissible limit 1.0 p.u. and as speed crosses the base speed, electromagnetic torque reduces and to decreases the permanent magnet flux linkage reluctance torque $\hat{i}_{sd(1)} \sim \hat{x}_{22(1)}$ decreases further. In the field weakening region, drive operates in constant power region following applied voltage and current limit. For both control structure, speed estimation error $\widetilde{\omega}_{r(1)} \sim \tilde{x}_{11(1)}$ was less than 0.05 p.u. as can be seen from Fig. 5.72.

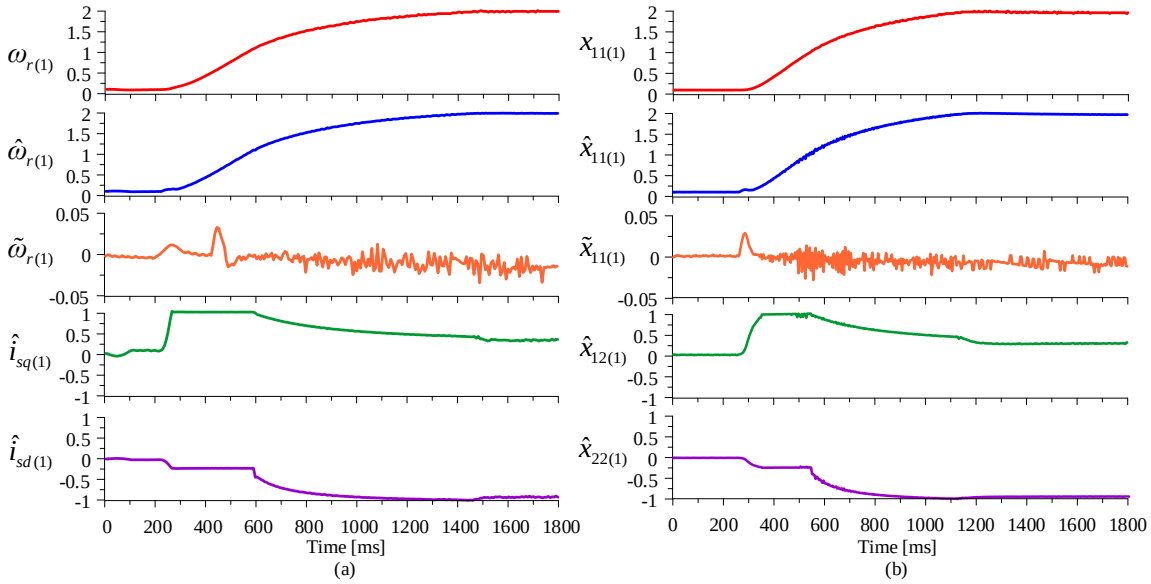

Fig. 5.72 Field weaking operation of five-phase IPMSM (a) FOC structure (b) backstepping mutliscalar control structure

In the next scenario, fault tolerant performance of the drive was examined by backstepping mutliscalar control structure as presented in Fig. 5.73. For this test, drive was running at steady state around 0.35 p.u. with no-load condition. This test was conducted using two cases: in the first case Phase C was disconnected and in the second case phase A and C were cutoff by manually switched circuit breaker.

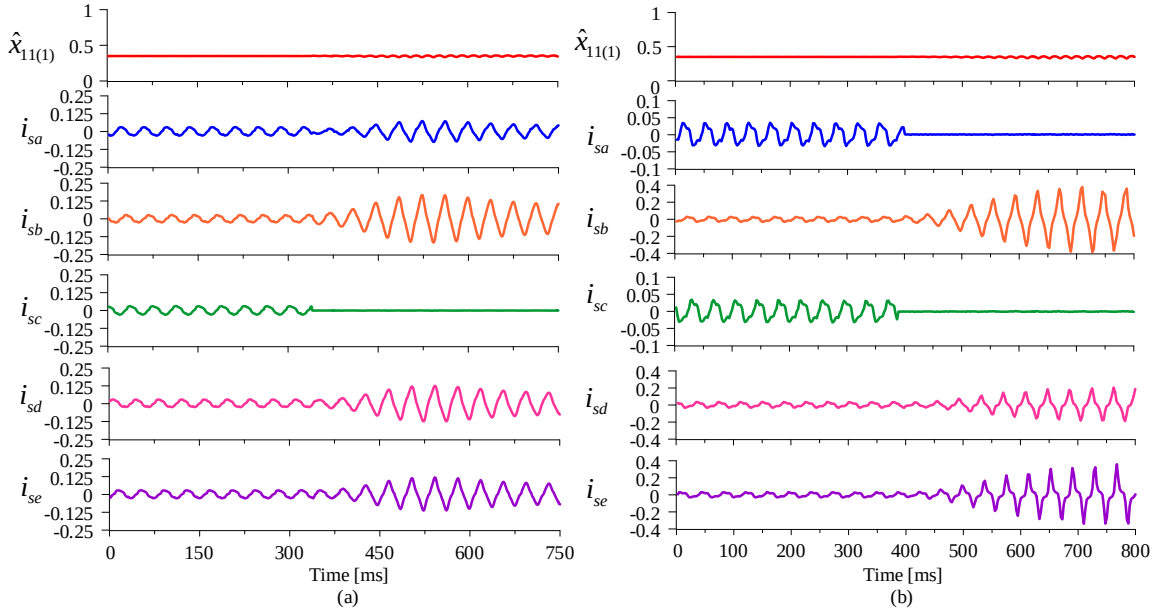

Fig. 5.73 Experimental results of backstepping mutliscalar control structure of five-phase IPMSM (a) phase A was deactivated (b) phase A and C were deactivated

From Fig. 5.73(a), it can be observed that after 0.32s phase C was disconnected. Third harmonic injection was turned off in the first case. As phase C was disconnected, current amplitude in other phases increased. Oscillation in speed response is also visible

after phase C outage. Similarly, Fig. 5.73(b), after 0.39s both phases A and C were disconnected. In the second case, third harmonic injection was on throughout the test. It can be noticed that backstepping control structure provides adequate control during outage of up to two phases. In Table 5.1, differences and similarities between existing control solutions and proposed control solutions are provided for chosen properties.

Table 5.1 Comparison of selected properties of the proposed control structures

Property	**Field-oriented control**	**($\psi_{f(i)}$,$\mathbf{i}_{s(i)}$) vector based control**	**($\psi_{s(i)}$,$\mathbf{i}_{s(i)}$) vector based control - 1**	**($\psi_{s(i)}$,$\mathbf{i}_{s(i)}$) vector based control - 2**	**Predictive FOC control**	**Predictive multi-scalar control**	**Back-stepping multi-scalar control**
No. PI controllers (1st + 2nd planes)	5	5	7	5	3	5	0
Decoupled control law	No	Yes	Yes	Yes	No	Yes	Yes
Complexity in gain tuning	Medium	Medium	High	Medium	Easy	Easy	Medium
Tracking error of the rotor speed at dynamic state (p.u.)	≤ 0.05 p.u.	≤ 0.05 p.u.	≤ 0.05 p.u.	≤ 0.05 p.u.	≤ 0.05 p.u.	≤ 0.05 p.u.	≤ 0.05 p.u.
Park transformation requirement	Yes	No	No	No	Yes	No	No
Oscillation of state variable at dynamic state	Medium	Small	Medium	Small	Medium	Small	Small
Steady state error of rotor speed (p.u.)	< 0.002	< 0.002	< 0.002	< 0.002	< 0.007	< 0.005	< 0.0015

This research studies makes significant contributions to the progress of advanced control structures for five-phase IPMSM drive system by demonstrating comprehensive comparison using simulation and experimental results. Using multiscalar transformation, proposed control structure are developed using $\boldsymbol{\psi}_{f(i)},\mathbf{i}_{s(i)}$ vectors and $\boldsymbol{\psi}_{s(i)},\mathbf{i}_{s(i)}$ vectors.Firstly, $\boldsymbol{\psi}_{f(i)},\mathbf{i}_{s(i)}$ vectors based control structure is proposed for five-phase IPMSM drive. Compared to classical FOC structure, $\boldsymbol{\psi}_{f(i)},\mathbf{i}_{s(i)}$ vectors based control structure provides excellent dynamic control in the second plane as shown in Fig. 5.25(b). Torque controlled in the second plane is smoother and better controlled in the proposed control solution. Both control structures required total five controllers. Proposed control solution can be applied directly in the stationary coordinate system compared to classical FOC structure.

In the following, $\boldsymbol{\psi}_{s(i)},\mathbf{i}_{s(i)}$ vectors based control structures are proposed for five-phase IPMSM drive. Compared to $\boldsymbol{\psi}_{s(i)},\mathbf{i}_{s(i)}$ vectors based control structure – 1, $\boldsymbol{\psi}_{s(i)},\mathbf{i}_{s(i)}$ vectors based control structure – 2 allows direct control of flux controlling variable in

each plane which reduced 1 PI controller in electromagnetic subsystem in each plane. The reduction of PI controller simplifies overall control structure. In addition, proposed stator flux reference defined in (5.1) enables improved dynamic control of flux controlling variables. $\boldsymbol{\psi}_{s(i)}, \mathbf{i}_{s(i)}$ vectors based control structure – 1 requires total 7 controllers while $\boldsymbol{\psi}_{s(i)}, \mathbf{i}_{s(i)}$ vectors based control structure – 2 requires total 5 controllers only.

Furthermore, this doctoral thesis cover proposition of advanced control structure utilizing predictive multiscalar control for the first plane and model based multiscalar control for the second plane. To conduct comparative analysis, proposed predictive control structure was compared with predictive FOC structure. Proposed control structure provides better dynamic control than classical predictive FOC control for both cases drive stating to nominal speed and drive reversal from -1.0 p.u. from 1.0 p.u.

Finally, backstepping multiscalar control structure is proposed in this thesis. Backstepping multiscalar control structure provides excellent performance during the transient and steady state. Backstepping multiscalar control structure also compared with classical FOC structure for different cases: drive startup, drive reversal and field weakening test. Backstepping multiscalar control structure ensure improved dynamic control in second plane compared to classical FOC structure as shown in Fig. 5.62 Fig. 5.63.

This chapter has provided detailed discussion of proposed control solutions of five-phase IPMSM drive. With these insights in place, the next and final chapter will provide comprehensive conclusion and exploring potential future research direction.

CHAPTER 6: CONCLUSION AND FUTURE WORK

This doctoral thesis covers the development of two control strategies: 1) $\boldsymbol{\psi}_{f(i)}, \mathbf{i}_{s(i)}$ vectors and 2) $\boldsymbol{\psi}_{s(i)}, \mathbf{i}_{s(i)}$ vectors of five-phase interior permanent magnet synchronous motor drive. The proposed control solutions of five-phase IPMSM ensures the injection of 3rd harmonic to utilize magnetic circuit in preferred way.

In the first step, mathematical model of the three-phase IPMSM and five-phase IPMSM are discussed in rotating coordinate system as well as in stationary coordinates system. In the following, adaptive observer structures with enhanced stabilization functions and non-adaptive observer structure are presented for three-phase IPMSM. The observer structures are prepared using the two approaches: 1) active-flux concept-based observer structure and 2) rotor flux vector-based observer structure. Stability analysis of the observer structures conducted by linearizing observer error model to equilibrium points in rotating reference frame. To conduct the comparative analysis, adaptive observer structures are compared to non-adaptive EEMF observer structure.

In the adaptive observer structure, based on the defined errors in the system adaptive law is prepared to estimate the value of rotor angular speed. In the case of non-adaptive observer structure, speed estimation process was conducted using the dependencies of EEMF and flux. Based on the calculated estimation errors, stabilizing functions are developed for observer structure implementation. Additional stabilizing functions are proposed to improve estimation accuracy and robustness of the observer structure. The final form of the stabilizing functions are prepared using the Lyapunov stability theorem.

When drive operates under 10% of nominal speed, the problems of non-sinusoidal distribution of EMF and slot harmonics are visible. Compared to non-adaptive observer structure, adaptive observer structure provides satisfactory performance at different speed range. Non-adaptive observer structure struggles to cross zero speed during the drive reversal. No signal injection is required to estimated speed and position at low speed in the adaptive observer structure. Both observer structures are tested in simulation as well as in the experimental stand to confirm the behavior of three-phase drive system at different speed range.

From the FFT analysis presented in Chapter – 5, it can be visualized that 3rd harmonic component exist in the designed five-phase IPMSM. The presence of 3rd harmonic component in phase current plot is uncontrolled which is disadvantage as magnetic circuit of the five-phase IPMSM is not being effectively utilized. To utilize the magnetic circuit properly, the control approach of five-phase IPMSM relies on coexistence of two machines in one single physical motor, hence it is possible to inject 3rd harmonic current with fundamental current to enhance output torque generation. To inject 3rd harmonic in the five-phase IPMSM drive, independent control in the 2nd vector plane is employed which allows independent voltage generation, estimating system's parameters and control implementation. The 2nd vector plane work with three times higher frequency compared to 1st plane.

To implement sesnsorless control of multiphase IPMSM, adaptive observer structure using the active-flux concept was designed specifically for the fundamental plane and third harmonic plane. Design procedure of the observer structures for fundamental plane and second plane in five-phase machine remains the same as traditional three-phase machine. The Lyapunov stability theorem was used to designed the final form of the stabilizing functions. By linearizing the observer structure near to equilibrium points, tuning gains are identified for each plane by performing stability analysis of the observer structure.

The main contributions of the doctoral thesis are:

- Control structure with multiscalar variables using the ($\boldsymbol{\psi}_{f(i)}$,$\mathbf{i}_{s(i)}$) vectors.
- Control structure with multiscalar variables using the ($\boldsymbol{\psi}_{s(i)}$,$\mathbf{i}_{s(i)}$) vectors.
- Predictive control of five-phase IPMSM.
- Backstepping control of five-phase IPMSM.

The proposed control solutions in the thesis are also compared with traditional field-oriented control structure to conduct the comparative analysis.

To confirm the theoretical hypothesis, proposed control of five-phase IPMSM first examined using the simulation tests on WinSim. Presented FFT analysis in Chapter 5 confirmed that it is possible to inject 3rd harmonic current to increase the output value of torque. The simulation results have verified that the proposed control structure in this thesis allows third harmonic injection to enhance the torque generation up to 10% of

fundamental torque, which offered opportunities for hand-on implementation of the five-phase IPMSM drive. Simulation results of five-phase IPMSM drive are provided for two scenarios: drive starting up to nominal speed and drive reversal.

The proposed control structures were validated in real time by the experimental tests on 5.5kW five-phase IPMSM drive systems.

The ($\boldsymbol{\psi}_{\mathbf{f}(i)}$,$\mathbf{i}_{\mathbf{s}(i)}$) vector based control system of five-phase IPMSM allows injection of 3rd harmonic to increase output torque. In this control structure, multiscalar variables are prepared using vector and scalar product of permanent magnet components $\boldsymbol{\psi}_{\mathbf{f}(i)}$, stator current components $\mathbf{i}_{\mathbf{s}(i)}$ in stationary coordinate system. The multiscalar model of the control system is constructed from established multiscalar variables. To linearized the nonlinear model, signals $m_{1(i)}$ and $m_{2(i)}$ are computed using the PI controllers and provided as state feedback. The reference voltage components in stationary reference frame can be computed using the control signals $u_{1(i)}$ and $u_{2(i)}$ after the completing the decoupling process.

Experimental results validate the performance of the ($\boldsymbol{\psi}_{\mathbf{f}(i)}$,$\mathbf{i}_{\mathbf{s}(i)}$) vector based control solution. The ($\boldsymbol{\psi}_{\mathbf{f}(i)}$,$\mathbf{i}_{\mathbf{s}(i)}$) vector based control solution and FOC structure are both suitable solution for the control of five-phase IPMSM drive. In the ($\boldsymbol{\psi}_{\mathbf{f}(i)}$,$\mathbf{i}_{\mathbf{s}(i)}$) vector based control solution eliminates the variable transformation to rotating coordinates for the control structure implementation. Independent control of electro-mechanical subsystem and electro-magnetic subsystem is also obtained using the proposed control solution.

This doctoral thesis presents ($\boldsymbol{\psi}_{\mathbf{s}(i)}$,$\mathbf{i}_{\mathbf{s}(i)}$) vector based control solutions for five-phase IPMSM. Two approaches are proposed using the stator flux vector $\boldsymbol{\psi}_{\mathbf{s}(i)}$ and stator current vector $\mathbf{i}_{\mathbf{s}(i)}$. In the ($\boldsymbol{\psi}_{\mathbf{s}(i)}$,$\mathbf{i}_{\mathbf{s}(i)}$) vector based control system – 1, control signals $u_{1(i)}$ and $u_{2(i)}$ are obtained from differential equation of $x_{12(i)}$ and $x_{22(i)}$, respectively, while in ($\boldsymbol{\psi}_{\mathbf{s}(i)}$,$\mathbf{i}_{\mathbf{s}(i)}$) vector based control system – 2, control signals $u_{1(i)}$ and $u_{2(i)}$ are computed from differential equation $x_{12(i)}$ and $x_{21(i)}$, respectively. For control system – 1, implementation total 7 controllers are required 4 in the first plane and 3 in the second plane, while to apply control structure – 2 total 5 PI controller are required 3 in the first plane and 2 in second plane.

In comparison, the control of electro-mechanical subsystems remains same in both control system, but the control of electro-magnetic subsystems is simpler in control

system – 2. In control system – 2, it is possible to control the flux controlling variable directly from $x_{21(i)}$ controller in each plane. In control system – 2, optimal stator flux $x^{*}_{21(1)}$ reference-based performance of the five-phase IPMSM drive is presented for the case of drive starting up to nominal speed and drive reversal. Using the optimal stator flux $x^{*}_{21(1)}$, flux amplitude is controlled in the desired way. At steady state, stator flux equals to permanent magnet flux level and during dynamic state stator flux increases up to 0.95 p.u. Five-phase IPMSM drive performance using the ($\boldsymbol{\psi}_{s(i)}$,$\mathbf{i}_{s(i)}$) vector based control systems for different scenarios are presented in the doctoral thesis.

First research hypothesis of the doctoral work is successfully completed by proposition of control structures with multiscalar transformation using the ($\boldsymbol{\psi}_{f(i)}$,$\mathbf{i}_{s(i)}$) vectors and the ($\boldsymbol{\psi}_{s(i)}$,$\mathbf{i}_{s(i)}$) vectors in stationary reference frame of five-phase IPMSM presented in Chapter 5. First research hypothesis is validated using the simulation and experimental tests on five-phase IPMSM.

To achieve second research hypothesis, doctoral work presents predictive control of five-phase IPMSM. Fundamental components are in the first plane and controlled by the predictive control using multiscalar variables. Third harmonic components are in the second plane and controlled by PI based multiscalar control scheme. The proposed control structure is in stationary reference frame $(\alpha\text{-}\beta)_{(i)}$. The proposed predictive control structure is compared with classical predictive torque control for first plane and FOC structure for second plane in the rotating coordinate system $(d\text{-}q)_{(i)}$ for drive accelerating to nominal speed and reversal.

The performance of predictive control structure is more adequate, and the introduced distortion is less in the generated torque compared to the classical control structure. In addition, the use of weighting factor to apply predictive control is eliminated without the degrading the performance of the control structure. Both the simulation and experimental results validate the stable performance of the drive using predictive multiscalar control solution even if the parameters of the five-phase IPMSM are different from their nominal values.

Finally, for five-phase IPMSM drive backstepping control approach incorporating with multiscalar variables is discussed in this thesis. Backstepping multiscalar control structure is validated using the simulation and experimental results. In the experimental results drive performance is shown for various cases using backstepping multiscalar

control: drive start up to nominal speed and reversal, low speed reversal, load injection and load removal, third harmonic injection on and off, low speed drive reversal and standstill test, uncertainty parameters test, MTPA with field weakening test and fault tolerance test. For chosen cases, the proposed backstepping control approach is compared with FOC structure of five-phase IPMSM. Backstepping multiscalar control provides satisfactory performance of the five-phase IPMSM drive under different speed of operation.

This doctoral thesis fulfills the second research hypothesis by proposing the control structures of five-phase IPMSM using the multiscalar transformation through classical PI, predictive and backstepping controllers. The proposed control structures of five-phase IPMSM using PI, predictive and backstepping controllers ensures independent control of the electromechanical and electromagnetic subsystems variables for each plane, even in the presence of third harmonic injection as promised in second research hypothesis.

Finally, proposed control system structure using the ($\boldsymbol{\psi}_{\mathbf{f}(i)}$,$\mathbf{i}_{\mathbf{s}(i)}$) vectors and the ($\boldsymbol{\psi}_{\mathbf{s}(i)}$,$\mathbf{i}_{\mathbf{s}(i)}$) vectors in stationary coordinate system allows utilization of 3rd harmonic injection to enhance the output torque value which completes the final research hypothesis of the doctoral thesis

All three aims presented in Chapter 1 have been successfully achieved in this doctoral thesis. It is presumed that this doctor work can be utilized for the further estimation-based drive implementations.

The implementation of a high performance multiphase IPMSM drive is an active area of research. The doctoral work presented in this thesis identify some issues for the consideration of future work and to be investigated further. Apply different observer structures with improved stabilization functions to enhance estimation of system parameters to improve sensorless control properties of multiphase machine. Implement artificial intelligence-based control techniques to replace PI controller.

To improve robustness of the system, neural network-based estimator can be employed to estimate the system parameters. Drive performance can be further investigated to improve the effective operation during the open phase faults.

BIBLIOGRAPHY

[1] Dominik B, Reinhard N, Wolfgang M, and Hans-Georg H, "Comparison of Electrical Machine Types in Hybrid Drive Trains: Induction Machine vs. Permanent Magnet Synchronous Machine," in *2008 International Conference on Electrical Machines*, I E E E, 2008.

[2] K. A. Gore and R. T. Ugale, "Design and Comparative Analysis of PMSM, BLDC, SynRM, and PMAssi-SynRM Motors for Two-Wheeler Electric Vehicle Application," in *2022 IEEE Conference on Interdisciplinary Approaches in Technology and Management for Social Innovation, IATMSI 2022*, Institute of Electrical and Electronics Engineers Inc., 2022. doi: 10.1109/IATMSI56455.2022.10119363.

[3] S. S. Rauth and B. Samanta, "Comparative Analysis of IM/BLDC/PMSM Drives for Electric Vehicle Traction Applications Using ANN-Based FOC," in *2020 IEEE 17th India Council International Conference, INDICON 2020*, Institute of Electrical and Electronics Engineers Inc., Dec. 2020. doi: 10.1109/INDICON49873.2020.9342237.

[4] Thomas F, Matthias F, and Kay H, "Comparison and design of different electrical machine types regarding their applicability in hybrid electrical vehicles.," in *2008 INTERNATIONAL CONFERENCE ON ELECTRICAL MACHINES*, I E E E, 2008.

[5] Sakunthala S, R.Kiranmayi, and Nagaraju P, "A Study on Industrial Motor Drives Comparison and Applications of PMSM and BLDC Motor Drives," in *ICECDS : 2017 International Conference on Energy, Communication, Data Analytics and Soft Computing : 1-2 August 2017, Chennai, India*, Institute of Electrical and Electronics Engineers, 2018.

[6] Y. Wang, Y. Huang, M. Zhao, and M. Lu, "A Novel Halbach Design for Hybrid Rotor and Performance Optimization in PMSM," in *2023 26th International Conference on Electrical Machines and Systems, ICEMS 2023*, Institute of Electrical and Electronics Engineers Inc., 2023, pp. 2492–2497. doi: 10.1109/ICEMS59686.2023.10344673.

[7] Namitha M, Ushakumari S, and Mini V.P, "Performance comparison between different rotor configurations of PMSM for EV application," in *2020 IEEE REGION 10 CONFERENCE (TENCON)*, IEEE, 2020.

[8] G. Wang, G. Zhang, and D. Xu, *Position Sensorless Control Techniques for Permanent Magnet Synchronous Machine Drives*. Springer Nature Singapore, 2020.

[9] R. (Ramu) Krishnan, *Permanent magnet synchronous and brushless DC motor drives*. CRC Press/Taylor & Francis, 2010.

[10] B. N. Chaudhari and B. G. Fernandes, "SYNCHRONOUS MOTOR USING FERRITE MAGNETS FOR GENERAL PURPOSE ENERGY EFFICIENT DRIVE," in *IEEE TENCON*, 1999.

[11] E. Richter, T. Miller, and T. W. Neumann, "THE FERRITE PERMANENT MAGNET AC MOTOR-A TECHNICAL AND ECONOMICAL ASSESSMENT," 1984.

[12] M. A. Rahman and G. R. Slemon, "PROMISING APPLICATIONS OF NEODYi' lIUIl BORON IRON MAGNETS IN ELECTRICAL MACHINES (I n v i t e d)," 1985.

[13] Sul S, Kwon Y, and Lee Y, "Sensorless Control of IPMSM for Last 10 Years and Next 5 Years," *CES TRANSACTIONS ON ELECTRICAL MACHINES AND SYSTEMS*, vol. 1, no. 2, 2017.

[14] Xu D, Wang B, Zhang G, Wang G, and Yu Y, "A Review of Sensorless Control Methods for AC Motor Drives," *CES TRANSACTIONS ON ELECTRICAL MACHINES AND SYSTEMS*, vol. 2, no. 1, 2018.

[15] S. K. Sul and S. Kim, "Sensorless control of IPMSM: Past, present, and future," *IEEJ Journal of Industry Applications*, vol. 1, no. 1, pp. 15–23, 2012, doi: 10.1541/ieejjia.1.15.

[16] G. Wang, M. Valla, and J. Solsona, "Position sensorless permanent magnet synchronous machine drives - A review," *IEEE Transactions on Industrial Electronics*, vol. 67, no. 7, pp. 5830–5842, Jul. 2020, doi: 10.1109/TIE.2019.2955409.

[17] Y. Li, H. Hu, and P. Shi, "A Review of Position Sensorless Compound Control for PMSM Drives," Feb. 01, 2023, *MDPI*. doi: 10.3390/wevj14020034.

[18] G. Zhang, G. Wang, and D. Xu, "Saliency-Based Position Sensorless Control Methods for PMSM Drives-a Review," 2017.

[19] O. Benjak and and D. Gerling, *Review of position estimation methods for ipmsm drives without a position sensor part ii: Adaptive methods*. in Electrical Machines (ICEM), 2010 XIX International Conference on, 2010.
[20] S. Bolognani, R. Oboe, M. Zigliotto, S. Bolognani, and M. Zigliotto, "Sensorless Full-Digital PMSM Drive With EKF Estimation of Speed and Rotor Position," 1999.
[21] A. Consoli, G. Scarcella, and A. Testa, "Industry Application of Zero-Speed Sensorless Control Techniques for PM Synchronous Motors."
[22] H. Kim, J. Son, and J. Lee, "A high-speed sliding-mode observer for the sensorless speed control of a PMSM," *IEEE Transactions on Industrial Electronics*, vol. 58, no. 9, pp. 4069–4077, Sep. 2011, doi: 10.1109/TIE.2010.2098357.
[23] H. Chaoui and P. Sicard, "Adaptive fuzzy logic control of permanent magnet synchronous machines with nonlinear friction," *IEEE Transactions on Industrial Electronics*, vol. 59, no. 2, pp. 1123–1133, Feb. 2012, doi: 10.1109/TIE.2011.2148678.
[24] Urbański K, "Position Estimation at Zero Speed for PMSM Using Probabilistic Neural Network," in *2015 IEEE 2nd International Conference on Cybernetics (CYBCONF)*, IEEE, 2015, pp. 427–432. doi: 10.1109/CYBConf.2015.7175972.
[25] P. L. Jansen and R. D. Lorenz, "Transducerless Position and Velocity Estimation in Induction and Salient AC Machines," in *IEEE TRANSACTIONS ON INDUSTRY APPLICATIONS*, 1995.
[26] M. Schroedl, "Sensorless Control of AC Machines at Low Speed and Standstill Based on the 'INFORM''' Method,'" in *IAS '96. Conference Record of the 1996 IEEE Industry Applications Conference Thirty-First IAS Annual Meeting, San Diego, CA, USA*, 1996, pp. 270–277. doi: 10.1109/IAS.1996.557028.
[27] J. Holtz and J. Juliet, "Sensorless acquisition of the rotor position angle of induction motors with arbitrary stator windings," *IEEE Trans Ind Appl*, vol. 41, no. 6, pp. 1675–1682, Nov. 2005, doi: 10.1109/TIA.2005.858245.
[28] S. Bolognani, S. Calligaro, R. Petrella, and and M. Tursini, "Sensorless control of ipm motors in the low-speed range and at standstill by hf injection and dft processing," *IEEE Trans Ind Appl*, vol. 47, pp. 96–104, 2011.
[29] M. Linke, S. Member, R. Kennel, S. Member, and J. Holtz, "Sensorless position control of Permanent Magnet Synchronous Machines without Limitation at Zero Speed." [Online]. Available: http://www.emad.uni-wuppertal.de
[30] L. A. S. Ribeiro', M. W. Degne, F. Briz3, and R. D. Lorenz4, "Comparison of Carrier Signal Voltage and Current Injection for the Estimation of Flux Angle or Rotor Position."
[31] M. J. Corley and R. D. Lorenz, "Rotor Position and Velocity Estimation for a Salient-Pole Permanent Magnet Synchronous Machine at Standstill and High Speeds."
[32] D. Raca, P. Garcia, D. Reigosa, F. Briz, and and R. Lorenz, *Carrier-signal selection for sensorless control of pm synchronous machines at zero and very low speeds*, vol. 44. 2010.
[33] J.-I. Ha and S.-K. Sul, "Sensorless Field-Orientation Control of an Induction Machine by High-Frequency Signal Injection."
[34] J. M. Liu and Z. Q. Zhu, "Novel sensorless control strategy with injection of high-frequency pulsating carrier signal into stationary reference frame," *IEEE Trans Ind Appl*, vol. 50, no. 4, pp. 2574–2583, 2014, doi: 10.1109/TIA.2013.2293000.
[35] J. H. Jang, S. K. Sul, J. I. Ha, K. Ide, and M. Sawamura, "Sensorless Drive of Surface-Mounted Permanent-Magnet Motor by High-Frequency Signal Injection Based on Magnetic Saliency," *IEEE Trans Ind Appl*, vol. 39, no. 4, pp. 1031–1039, Jul. 2003, doi: 10.1109/TIA.2003.813734.
[36] M. Linke, S. Member, R. Kennel, S. Member, and J. Holtz, "Sensorless Speed and Position Control of Synchronous Machines using Alternating Carrier Injection." [Online]. Available: http://www.emad.uni-wuppertal.de
[37] A. Yamazaki and and K. Ide, *Application trend of saliency-based sensorless drives*. 2014.
[38] Y. D. Yoon, S. K. Sul, S. Morimoto, and K. Ide, "High-bandwidth sensorless algorithm for AC machines based on square-wave-type voltage injection," *IEEE Trans Ind Appl*, vol. 47, no. 3, pp. 1361–1370, May 2011, doi: 10.1109/TIA.2011.2126552.
[39] Y. D. Yoon and S. K. Sul, "Sensorless Control for Induction Machines Based on Square-Wave Voltage Injection," *IEEE Trans Power Electron*, vol. 29, no. 7, pp. 3637–3645, Jul. 2014, doi: 10.1109/TPEL.2013.2278103.

[40] R. Leidhold and P. Mutschler, “Improved Method for Higher Dynamics in Sensorless Position Detection.”
[41] F. Blaschke, “The Principle of Field Orientation as Applied to the NEW Transvector Closed-Loop System for Rotating-Field Machines.”
[42] E. Robeischl and M. Schroedl, “Optimized INFORM measurement sequence for sensorless PM synchronous motor drives with respect to minimum current distortion,” *IEEE Trans Ind Appl*, vol. 40, no. 2, pp. 591–598, Mar. 2004, doi: 10.1109/TIA.2004.824510.
[43] S. Ogasawara and H. Akagi, “An Approach to Real-Time Position Estimation at Zero and Low Speed for a P M Motor Based on Saliency.”
[44] D. Paulus, P. Landsmann, and and R. Kennel, *“Sensorless field- oriented control for permanent magnet synchronous machines with an arbitrary injection scheme and direct angle calculation*. in Proc. IEEE SLED Sympos., 2011.
[45] R. Raute *et al., A review of sensorless control in induction machines using hf injection, test vectors and pwm harmonics*. in Proc. IEEE SLED Sympos, 2011.
[46] Y. Hua, M. Sumner, G. Asher, Q. Gao, and K. Saleh, “Improved sensorless control of a permanent magnet machine using fundamental pulse width modulation excitation,” *IET Electr Power Appl*, vol. 5, no. 4, pp. 359–370, 2011, doi: 10.1049/iet-epa.2010.0108.
[47] P. L. Dirk Paulus and and R. Kennel, *“Arbitrary injection for permanent magnet synchronous machine with multiple saliencies,.”* in Proc. IEEE ECCE Conf., 2013.
[48] Y. Lee and S. K. Sul, “Model-Based Sensorless Control of an IPMSM with Enhanced Robustness Against Load Disturbances Based on Position and Speed Estimator Using a Speed Error,” in *IEEE Transactions on Industry Applications*, Institute of Electrical and Electronics Engineers Inc., Mar. 2018, pp. 1448–1459. doi: 10.1109/TIA.2017.2777390.
[49] T. C. Lin, Z. Q. Zhu, and J. M. Liu, “Improved Rotor Position Estimation in Sensorless-Controlled Permanent-Magnet Synchronous Machines Having Asymmetric-EMF with Harmonic Compensation,” *IEEE Transactions on Industrial Electronics*, vol. 62, no. 10, pp. 6131–6139, Oct. 2015, doi: 10.1109/TIE.2015.2426671.
[50] K. W. Lee and J. I. Ha, “Evaluation of back-EMF estimators for sensorless control of permanent magnet synchronous motors,” *Journal of Power Electronics*, vol. 12, no. 4, pp. 605–614, 2012, doi: 10.6113/jpe.2012.12.4.604.
[51] K. Urbanski, “A new sensorless speed control structure for PMSM using reference model,” *Bulletin of the Polish Academy of Sciences: Technical Sciences*, vol. 65, no. 4, pp. 489–496, Aug. 2017, doi: 10.1515/bpasts-2017-0054.
[52] K. Urbański and K. Zawirski, “Adaptive observer of rotor speed and position for PMSM sensorless control system,” *COMPEL - The International Journal for Computation and Mathematics in Electrical and Electronic Engineering*, vol. 23, no. 4, pp. 1129–1145, 2004, doi: 10.1108/03321640410510848.
[53] S. Bolognani, L. Tubiana, and M. Zigliotto, “Extended Kalman filter tuning in sensorless PMSM drives,” *IEEE Trans Ind Appl*, vol. 39, no. 6, pp. 1741–1747, Nov. 2003, doi: 10.1109/TIA.2003.818991.
[54] Z. Chen, M. Tomita, S. Doki, and S. Okuma, “An extended electromotive force model for sensorless control of interior permanent-magnet synchronous motors,” *IEEE Transactions on Industrial Electronics*, vol. 50, no. 2, pp. 288–295, Apr. 2003, doi: 10.1109/TIE.2003.809391.
[55] G. Wang, T. Li, G. Zhang, X. Gui, and D. Xu, “Position estimation error reduction using recursive-least-square adaptive filter for model-based sensorless interior permanent-magnet synchronous motor drives,” *IEEE Transactions on Industrial Electronics*, vol. 61, no. 9, pp. 5115–5125, 2014, doi: 10.1109/TIE.2013.2264791.
[56] I. Boldea, M. C. Paicu, and G. D. Andreescu, “Active flux concept for motion-sensorless unified AC drives,” *IEEE Trans Power Electron*, vol. 23, no. 5, pp. 2612–2618, 2008, doi: 10.1109/TPEL.2008.2002394.
[57] I. Boldea, M. C. Paicu, G. D. Andreescu, and F. Blaabjerg, “‘Active Flux’ DTFC-SVM sensorless control of IPMSM,” *IEEE Transactions on Energy Conversion*, vol. 24, no. 2, pp. 314–322, 2009, doi: 10.1109/TEC.2009.2016137.
[58] Y. Zhao, Z. Zhang, W. Qiao, and L. Wu, “An Extended Flux Model-Based Rotor Position Estimator for Sensorless Control of Salient-Pole Permanent-Magnet Synchronous Machines,”

IEEE Trans Power Electron, vol. 30, no. 8, pp. 4412–4422, 2015, doi: 10.1109/TPEL.2014.2358621.

[59] Y. Li, Z. Q. Zhu, D. Howe, and C. M. Bingham, "Improved Rotor Position Estimation in Extended Back-EMF Based Sensorless PM Brushless AC Drives with Magnetic Saliency."

[60] M. Naidu', "ROTOR POSITION ESTIMATION SCHEME OF A PERMANENT MAGNET SYNCHRONOUS MACHINE FOR HIGH PERFORMANCE VARIABLE SPEED DRIVE."

[61] M. A. Hoque and M. A. Rahman, "SPEED AND POSITION SENSORLESS PERMANENT MAGNET SYNCHRONOUS MOTOR DRIVES."

[62] K. Urbanski, "Determining the observer parameters for back EMF estimation for selected types of electrical motors," *Bulletin of the Polish Academy of Sciences: Technical Sciences*, vol. 65, no. 4, pp. 439–447, Aug. 2017, doi: 10.1515/bpasts-2017-0049.

[63] M. Rashed, P. F. A. MacConnell, A. F. Stronach, and P. Acarnley, "Sensorless indirect-rotor-field-orientation speed control of a permanent-magnet synchronous motor with stator-resistance estimation," *IEEE Transactions on Industrial Electronics*, vol. 54, no. 3, pp. 1664–1675, Jun. 2007, doi: 10.1109/TIE.2007.895136.

[64] J. Bbcker and C. Kroger, "Control of Permanent Magnet Synchronous Motor with Dual-Mode Position Estimation."

[65] T.-S. Low, T.-H. Lee, and K.-T. Chang, "A Nonlinear Speed Observer for Permanent-Magnet Synchronous Motors," 1993.

[66] N. Ertugrul and P. P. Acarnley, "A New Algorithm for Sensorless Operation of Permanent Magnet Motors," *IEEE Trans. Ind. Appl.*, vol. 30, no. 1, pp. 126–133, 1994.

[67] L. A. Jones and J. H. Lang, "A State Observer for the Permanent-Magnet Synchronous Motor," 1989.

[68] J. W. Finch and D. Giaouris, "Controlled AC electrical drives," Feb. 2008. doi: 10.1109/TIE.2007.911209.

[69] P. P. Acarnley and J. F. Watson, "Review of position-sensorless operation of brushless permanent-magnet machines," Apr. 2006. doi: 10.1109/TIE.2006.870868.

[70] J. A. Solsona, "Disturbance and Nonlinear Luenberger Observers for Estimating Mechanical Variables in Permanent Magnet Synchronous Motors Under Mechanical Parameters Uncertainties."

[71] J. Solsona, I. Valla, and C. Muravchik, "A Nonlinear Reduced Order Observer for Permanent Magnet Synchronous Motors," 1996.

[72] Z. Qiao, T. Shi, Y. Wang, Y. Yan, C. Xia, and X. He, "New sliding-mode observer for position sensorless control of permanent-magnet synchronous motor," *IEEE Transactions on Industrial Electronics*, vol. 60, no. 2, pp. 710–719, 2013, doi: 10.1109/TIE.2012.2206359.

[73] D. Bao, X. Pan, Y. Wang, X. Wang, and K. Li, "Adaptive Synchronous-Frequency Tracking-Mode Observer for the Sensorless Control of a Surface PMSM," *IEEE Trans Ind Appl*, vol. 54, no. 6, pp. 6460–6471, Nov. 2018, doi: 10.1109/TIA.2018.2851510.

[74] H. Kim, J. Son, and J. Lee, "A high-speed sliding-mode observer for the sensorless speed control of a PMSM," *IEEE Transactions on Industrial Electronics*, vol. 58, no. 9, pp. 4069–4077, Sep. 2011, doi: 10.1109/TIE.2010.2098357.

[75] L. Sun, X. Zhang, L. Sun, and K. Zhao, "Nonlinear speed control for PMSM system using sliding-mode control and disturbance compensation techniques," *IEEE Trans Power Electron*, vol. 28, no. 3, pp. 1358–1365, 2013, doi: 10.1109/TPEL.2012.2206610.

[76] Y. Feng, X. Yu, and F. Han, "High-order terminal sliding-mode observer for parameter estimation of a permanent-magnet synchronous motor," *IEEE Transactions on Industrial Electronics*, vol. 60, no. 10, pp. 4272–4280, 2013, doi: 10.1109/TIE.2012.2213561.

[77] R. Dhaouadi, N. Mohan, and L. Norum, "Design and Implementation of an Extended Kalman Filter for the State Estimation of a Permanent Magnet Synchronous Motor," *IEEE Trans Power Electron*, vol. 6, no. 3, pp. 491–497, 1991.

[78] M. Morawiec, "The adaptive backstepping control of permanent magnet synchronous motor supplied by current source inverter," *IEEE Trans Industr Inform*, vol. 9, no. 2, pp. 1047–1055, May 2013, doi: 10.1109/TII.2012.2223478.

[79] M. Moradian, J. Soltani, A. Najjar-Khodabakhsh, and G. R. Arab Markadeh, "Adaptive Torque and Flux Control of Sensorless IPMSM Drive in the Stator Flux Field Oriented Reference Frame,"

IEEE Trans Industr Inform, vol. 15, no. 1, pp. 205–212, Jan. 2019, doi: 10.1109/TII.2018.2808521.

[80] A. T. Woldegiorgis, X. Ge, H. Wang, and M. Hassan, "A New Frequency Adaptive Second-Order Disturbance Observer for Sensorless Vector Control of Interior Permanent Magnet Synchronous Motor," *IEEE Transactions on Industrial Electronics*, vol. 68, no. 12, pp. 11847–11857, Dec. 2021, doi: 10.1109/TIE.2020.3047065.

[81] S. M. Gadoue, D. Giaouris, and J. W. Finch, "MRAS sensorless vector control of an induction motor using new sliding-mode and fuzzy-logic adaptation mechanisms," *IEEE Transactions on Energy Conversion*, vol. 25, no. 2, pp. 394–402, Jun. 2010, doi: 10.1109/TEC.2009.2036445.

[82] A. Akrad, M. Hilairet, and D. Diallo, "A sensorless PMSM drive using a two stage extended Kalman estimator."

[83] P. Vas, *Sensorless Vector and Direct Torque Control*. Oxford University Press, 1998.

[84] S. Paramasivam, S. Vijayan, M. Vasudevan, R. Arumugam, and R. Krishnan, "Real-time verification of AI based rotor position estimation techniques for a 6/4 pole switched reluctance motor drive," *IEEE Trans Magn*, vol. 43, no. 7, pp. 3209–3222, Jul. 2007, doi: 10.1109/TMAG.2006.888811.

[85] P. Vas, A. F. Stronach, C. Mimare, and M. Neuroth, "APPLICATION OF CONVENTIONAL AND AI-BASED TECHNIQUES IN SENSORLESS HIGH-PERFORMANCE TORQUE-CONTROLLED INDUCTION MOTOR DRIVES."

[86] K. Urbanski and D. Janiszewski, "Position estimation at zero speed for PMSMs using artificial neural networks," *Energies (Basel)*, vol. 14, no. 23, Dec. 2021, doi: 10.3390/en14238134.

[87] T. Pajchrowski, K. Urbański, and K. Zawirski, "Artificial neural network based robust speed control of permanent magnet synchronous motors," *COMPEL - The International Journal for Computation and Mathematics in Electrical and Electronic Engineering*, vol. 25, no. 1, pp. 220–234, 2006, doi: 10.1108/03321640610634461.

[88] R. Szczepanski, T. Tarczewski, and L. M. Grzesiak, "Adaptive state feedback speed controller for PMSM based on Artificial Bee Colony algorithm," *Applied Soft Computing Journal*, vol. 83, Oct. 2019, doi: 10.1016/j.asoc.2019.105644.

[89] B. K. Bose, "Fuzzy logic and neural networks in power electronics and drives," *IEEE Industry Applications Magazine*, pp. 57–63, 2000.

[90] Z. Ibrahim and E. Levi, "A comparative analysis of fuzzy logic and PI speed control in high-performance AC drives using experimental approach," *IEEE Trans Ind Appl*, vol. 38, no. 5, pp. 1210–1218, Sep. 2002, doi: 10.1109/TIA.2002.802993.

[91] L. A. Oscar P Henriques, L. G. B Rolim, W. I. Suemitsu, and P. J. Costa Branco, "DEVELOPMENT AND IMPLEMENTATION OF A NEURO FUZZY TECHNIQUE FOR POSITION SENSOR ELIMINATION IN A SRM."

[92] X. Liu and B. Wang, "ANN Observer of Permanent Magnet Synchronous Motor Based on SVPWM," 2006.

[93] M. N. Uddin and R. S. Rebeiro, "Online efficiency optimization of a fuzzy-logic-controller-based IPMSM drive," *IEEE Trans Ind Appl*, vol. 47, no. 2, pp. 1043–1050, Mar. 2011, doi: 10.1109/TIA.2010.2103293.

[94] D. Sun and Y. He, "Fuzzy Logic Direct Torque Control for Permanent Magnet Synchronous Motors."

[95] E. Levi, F. Barrero, and M. J. Duran, "Multiphase machines and drives-revisited," *IEEE Transactions on Industrial Electronics*, vol. 63, no. 1, pp. 429–432, 2016, doi: 10.1109/TIE.2015.2493510.

[96] A. Salem and M. Narimani, "A Review on Multiphase Drives for Automotive Traction Applications," *IEEE Transactions on Transportation Electrification*, vol. 5, no. 4, pp. 1329–1348, Dec. 2019, doi: 10.1109/TTE.2019.2956355.

[97] E. Levi, "Multiphase electric machines for variable-speed applications," *IEEE Transactions on Industrial Electronics*, vol. 55, no. 5, pp. 1893–1909, May 2008, doi: 10.1109/TIE.2008.918488.

[98] Y. Sui *et al.*, "Multiphase Modular Fault-Tolerant Permanent-Magnet Machine With Hybrid Single/Double-Layer Fractional-Slot Concentrated Winding," *IEEE Trans Magn*, vol. 55, no. 9, pp. 1–6, Jun. 2019, doi: 10.1109/tmag.2019.2917031.

[99] A. Akay and P. Lefley, “Research on Torque Ripple Under Healthy and Open-Circuit Fault-Tolerant Conditions in a PM Multiphase Machine,” *CES Transactions on Electrical Machines and Systems*, vol. 4, no. 4, pp. 349–359, Dec. 2020, doi: 10.30941/CESTEMS.2020.00042.

[100] F. Barrero and M. J. Duran, “Recent advances in the design, modeling, and control of multiphase machines - Part i,” *IEEE Transactions on Industrial Electronics*, vol. 63, no. 1, pp. 449–458, Jan. 2016, doi: 10.1109/TIE.2015.2447733.

[101] M. J. Duran and F. Barrero, “Recent advances in the design, modeling, and control of multiphase machines - Part II,” *IEEE Transactions on Industrial Electronics*, vol. 63, no. 1, pp. 459–468, Jan. 2016, doi: 10.1109/TIE.2015.2448211.

[102] J. Zhang, S. J. He, and K. Wang, “Multi-Harmonic Currents Control Strategy for Five-Phase Permanent Magnet Machine with non-sinusoidal back-EMF,” *IEEE Access*, pp. 1–1, Apr. 2020, doi: 10.1109/access.2020.2989323.

[103] M. JANASZEK, “EXTENDED CLARKE TRANSFORMATION FOR n-PHASE SYSTEMS,” *Proceedings of Electrotechnical Institute*, vol. 63, no. 0, pp. 5–26, Dec. 2016, doi: 10.5604/01.3001.0009.4333.

[104] Iqbal A, Moinoddin S, and Reddy B, *Electrical Machine Fundamentals with Numerical Simulation using MATLAB/SIMULINK*, 1st ed. Wiley, 2021.

[105] Guzinski J, Abu-rub H, and Patryk S, *Variable Speed ac Drives with Inverter Output Filters*, First. 2015 John Wiley & Sons, Ltd, 2015.

[106] E. Levi, R. Bojoi, F. Profumo, H. A. Toliyat, and S. Williamson, “Multiphase induction motor drives - A technology status review,” *IET Electr Power Appl*, vol. 1, no. 4, pp. 489–516, 2007, doi: 10.1049/iet-epa:20060342.

[107] E. E. Ward and H. Harer, “Preliminary investigation of an invertor-fed 5-phase induction motor,” *Proceedings of the Institution of Electrical Engineers*, vol. 116, no. 6, pp. 980–984, 1969, doi: 10.1049/piee.1969.0182.

[108] T. M. Jahns and I. Jul, “Improved Reliability in Solid-State AC Drives by Means of Multiple Independent Phase-Drive-Uiits,” *IEEE Trans Ind Appl*, vol. 16, no. 3, pp. 321–331, 1980.

[109] L. Zhang, X. Zhu, R. Cui, and S. Han, “A Generalized Open-Circuit Fault-Tolerant Control Strategy for FOC and DTC of Five-Phase Fault-Tolerant Permanent-Magnet Motor,” *IEEE Transactions on Industrial Electronics*, vol. 69, no. 8, pp. 7825–7836, Aug. 2022, doi: 10.1109/TIE.2021.3106012.

[110] A. Mohammadpour and L. Parsa, “Global fault-tolerant control technique for multiphase permanent-magnet machines,” *IEEE Trans Ind Appl*, vol. 51, no. 1, pp. 178–186, Jan. 2015, doi: 10.1109/TIA.2014.2326084.

[111] P. Song, W. Li, Z. Li, M. S. Toulabi, and N. C. Kar, “Noise and Vibration Prediction of a Six-Phase IPMSM in a Single Open-Phase Failure Under a Negative Sequence Current Compensated Fault Tolerant Control Mode,” *IEEE Trans Magn*, vol. 58, no. 8, Aug. 2022, doi: 10.1109/TMAG.2022.3146373.

[112] B. Tian, M. Molinas, and Q. An, “PWM Investigation of a Field-Oriented Controlled Five-Phase PMSM under Two-Phase Open Faults,” *IEEE Transactions on Energy Conversion*, vol. 36, no. 2, pp. 580–593, Jun. 2021, doi: 10.1109/TEC.2020.3029264.

[113] F. Wilczyński, P. Strankowski, J. Guziński, M. Morawiec, and A. Lewicki, “Sensorless field oriented control for five-phase induction motors with third harmonic injection and fault insensitive feature,” *Bulletin of the Polish Academy of Sciences: Technical Sciences*, vol. 67, no. 2, pp. 253–262, 2019, doi: 10.24425/bpas.2019.128598.

[114] P. Strankowski, J. Guziński, F. Wilczyński, M. Morawiec, and A. Lewicki, “Open-Phase Fault Detection Method for Sensorless Five-Phase Induction Motor Drives with an Inverter Output Filter,” *Power Electronics and Drives*, vol. 4, no. 1, pp. 191–202, Jun. 2019, doi: 10.2478/pead-2019-0004.

[115] W. Li, G. Feng, Z. Li, M. S. Toulabi, and N. Kar, “Extended Kalman Filter Based Inductance Estimation for Dual Three-Phase Permanent Magnet Synchronous Motors Under the Single Open-Phase Fault,” *IEEE Transactions on Energy Conversion*, vol. 37, no. 2, pp. 1134–1144, Jun. 2022, doi: 10.1109/TEC.2021.3129283.

[116] Z. Liu, Y. Li, and Z. Zheng, “A review of drive techniques for multiphase machines,” *CES Transactions on Electrical Machines and Systems*, vol. 2, no. 2, pp. 243–251, Jun. 2018, doi: 10.30941/cestems.2018.00030.

[117] D. Vyas, M. Morawiec, G. Kostro, A. Jaderko, and J. Baran, “Sensorless Predictive Multiscalar-based Control of the Five-Phase IPMSM,” *IEEE Access*, 2024, doi: 10.1109/ACCESS.2024.3421937.
[118] M. Morawiec, P. Strankowski, A. Lewicki, J. Guzinski, and F. Wilczynski, “Feedback Control of Multiphase Induction Machines with Backstepping Technique,” *IEEE Transactions on Industrial Electronics*, vol. 67, no. 6, pp. 4305–4314, Jun. 2020, doi: 10.1109/TIE.2019.2931236.
[119] Y. Luo, K. Yang, and Y. Zheng, “Luenberger Observer-Based Model Predictive Control for Six-Phase PMSM Motor With Localization Error Compensation,” *IEEE Transactions on Industrial Electronics*, vol. 70, no. 11, pp. 10800–10810, Nov. 2023, doi: 10.1109/TIE.2022.3229340.
[120] M. Ramezani and O. Ojo, “The Modeling and Position-Sensorless Estimation Technique for A Nine-Phase Interior Permanent-Magnet Machine Using High-Frequency Injections,” *IEEE Trans Ind Appl*, vol. 52, no. 2, pp. 1555–1565, Mar. 2016, doi: 10.1109/TIA.2015.2506143.
[121] Z. Krzeminski, “NONLINEAR CONTROL OF INDUCTION MOTOR,” in *Proc. of the 10th IFAC World Congress*, Munich, 1987.
[122] M. Morawiec, A. Lewicki, and C. I. Odeh, “Rotor-Flux Vector Based Observer of Interior Permanent Synchronous Machine,” *IEEE Transactions on Industrial Electronics*, vol. 71, no. 2, pp. 1399–1409, Feb. 2024, doi: 10.1109/TIE.2023.3250851.
[123] Zbigniew KRZEMIŃSKI, “Obserwator prędkości maszyny synchronicznej z zagłębionymi magnesami trwałymi,” *Politechnika Gdańska, Wydział Elektrotechniki i Automatyki, Katedra Automatyki Napędu Elektrycznego*, 2010.
[124] T. Tarczewski and L. M. Grzesiak, “Constrained State Feedback Speed Control of PMSM Based on Model Predictive Approach,” *IEEE Transactions on Industrial Electronics*, vol. 63, no. 6, pp. 3867–3875, Jun. 2016, doi: 10.1109/TIE.2015.2497302.
[125] R. Szczepanski, T. Tarczewski, and L. M. Grzesiak, “PMSM drive with adaptive state feedback speed controller,” *Bulletin of the Polish Academy of Sciences: Technical Sciences*, vol. 68, no. 4, pp. 1009–1017, Oct. 2020, doi: 10.24425/bpasts.2020.134624.
[126] B. M. Wilamowski and J. David Irwin, “Power Electronics and Motor Drives (The Industrial Electronics Handbook),” 2011.
[127] Z. Krzeminski, “Sensorless control of polyphase induction machines,” in *Studies in Systems, Decision and Control*, vol. 75, Springer International Publishing, 2017, pp. 3–26. doi: 10.1007/978-3-319-45735-2_1.
[128] A. Yang and Z. Lu, “Multiscalar Model-Based Predictive Torque Control Without Weighting Factors and Current Sensors for Induction Motor Drives,” *IEEE J Emerg Sel Top Power Electron*, vol. 10, no. 5, pp. 5785–5797, Oct. 2022, doi: 10.1109/JESTPE.2022.3181802.
[129] P. F. C. Goncalves, S. M. A. Cruz, and A. M. S. Mendes, “Disturbance Observer Based Predictive Current Control of Six-Phase Permanent Magnet Synchronous Machines for the Mitigation of Steady-State Errors and Current Harmonics,” *IEEE Transactions on Industrial Electronics*, vol. 69, no. 1, Jan. 2022, doi: 10.1109/TIE.2021.3053885.
[130] Chapman S, *ELECTRIC MACHINERY FUNDAMENTALS*, 4th edition. McGraw-Hill Science/Engineering/Math; , 2004.
[131] Abu-Rub H, Iqbal A, and Guzinski J, *HIGH PERFORMANCE CONTROL OF AC DRIVES WITH MATLAB ® / SIMULINK*, 2nd ed. John Wiley & Sons Ltd, 2021.
[132] L. Parsa and H. A. Toliyat, “Five-phase permanent-magnet motor drives,” *IEEE Trans Ind Appl*, vol. 41, no. 1, pp. 30–37, Jan. 2005, doi: 10.1109/TIA.2004.841021.
[133] P. Zhao and G. Yang, “Torque Density Improvement of Five-Phase PMSM Drive for Electric Vehicles Applications.”
[134] J. Yang, M. Dou, and D. Zhao, “Iterative sliding mode observer for sensorless control of five-phase permanent magnet synchronous motor,” *Bulletin of the Polish Academy of Sciences: Technical Sciences*, vol. 65, no. 6, pp. 845–857, 2017, doi: 10.1515/bpasts-2017-0092.
[135] Katsuhiko. Ogata, *Modern control engineering*. Prentice-Hall, 2010.
[136] A. Glumineau, J. De, and L. Morales, “Advances in Industrial Control Sensorless AC Electric Motor Control Robust Advanced Design Techniques and Applications.” [Online]. Available: http://www.springer.com/series/1412
[137] M. Morawiec and K. Blecharz, “Non-adaptive Speed and Position Estimation of Doubly-Fed Induction Generator in Grid-Connected Operations,” *IEEE Transactions on Industrial Electronics*, 2023, doi: 10.1109/TIE.2023.3279548.

[138] G. Foo and M. F. Rahman, “Sensorless sliding-mode MTPA control of an IPM synchronous motor drive using a sliding-mode observer and HF signal injection,” *IEEE Transactions on Industrial Electronics*, vol. 57, no. 4, pp. 1270–1278, Apr. 2010, doi: 10.1109/TIE.2009.2030820.

[139] Rodriguez J and Cortes P, *Predictive Control of Power Converters and Electrical Drives*. A John Wiley & Sons, Ltd., Publication, 2012.

[140] B. Tian, L. Sun, M. Molinas, and Q. T. An, “Repetitive Control Based Phase Voltage Modulation Amendment for FOC-Based Five-Phase PMSMs under Single-Phase Open Fault,” *IEEE Transactions on Industrial Electronics*, vol. 68, no. 3, pp. 1949–1960, Mar. 2021, doi: 10.1109/TIE.2020.2975502.

[141] Miroslav K, Ioannis K, and Petar K, *Nonlinear and Adaptive Control Design*. John Wiley and Sons, 1995, 1995.

[142] M. Morawiec, “Dynamic variables limitation for backstepping control of induction machine and voltage source converter,” in *Archives of Electrical Engineering*, Sep. 2012, pp. 389–410. doi: 10.2478/v10171-012-0031-1.

[143] H. İrgan and N. Tan, “PI CONTROLLER DESIGN FOR TIME DELAY SYSTEMS USING DIFFERENT MODEL ORDER REDUCTION METHODS,” *Uludağ University Journal of The Faculty of Engineering*, pp. 225–244, Jan. 2024, doi: 10.17482/uumfd.1318643.

[144] J.-S. Kim, S. Doki, and M. Ishida, “Improvement of IPMSM Sensorless Control Performance by Suppression of Harmonics on the Vector Control Using Fourier Transform and Repetitive Control.”

[145] Y. Mao, J. Yang, D. Yin, and Y. Chen, “Sensorless IPMSM control based on an extended nonlinear observer with rotational inertia adjustment and equivalent flux error compensation,” *Journal of Power Electronics*, vol. 16, no. 6, pp. 2150–2161, 2016, doi: 10.6113/JPE.2016.16.6.2150.

APPENDIX – A

Here an overview of the per unit system utilized during the simulation and experimental analysis is provided. In addition, machine parameter of three-phase drive system and five-phase drive system is also provided.

Table A1 Per unit system

Description	Three-Phase	Five-Phase
Base voltage	$U_b = \sqrt{3}\ U_{Nf}$	$U_b = \sqrt{5}\ U_{Nf}$
Base current	$I_b = \sqrt{3}\ I_{Nf}$	$I_b = \sqrt{5}\ I_{Nf}$
Base impedance	$Z_b = U_b / I_b$	
Base torque	$T_b = U_b\ I_b\ p / \omega_0$	
Base flux	$\psi_b = U_b / \omega_0$	
Base mechanical speed	$\omega_b = \omega_0 / p$	
Angular frequency of the supply voltage	$\omega_0 = 2\pi f_N$	
Base inductance	$L_b = \psi_b / I_b$	
Base capacitance	$C_b = 1 / \omega_b\ I_b$	
Base inertia	$J_b = T_b / \omega_b\ \omega_0$	
Phase voltage	U_{Nf}	
Phase current	I_{Nf}	
Pole pair	pn	
Nominal frequency	f_N	

Table A2 Nominal parameters of three-phase IPMSM drive

Parameters	Value	Unit
Nominal power	3.5	kW
Nominal voltage	285	V
Nominal current	7.5	A
Nominal speed	1500	rpm
Stator resistance	0.767	Ω
d-axis inductance	19.5	mH
q-axis inductance	57	mH
Permanent magnet flux linkage	0.8	Wb
Nominal frequency	50	Hz
Number of poles	2	-

Table A3 Nominal parameters of five-phase IPMSM drive

Parameters	Value	Unit
Nominal power	5.5	kW
Nominal voltage	122	V
Nominal current	10.2	A
Nominal speed	1500	rpm
Nominal torque	35	Nm
Stator resistance	0.816	Ω

d-axis inductance in the first plane	10.85	mH
q-axis inductance in the first plane	16.5	mH
d-axis inductance in the second plane	3.61	mH
q-axis inductance in the second plane	5.5	mH
Permanent magnet flux linkage in the first plane	0.51	Wb
Permanent magnet flux linkage in the second plane	0.0769	Wb
Nominal frequency	75	Hz
Number of poles	6	-

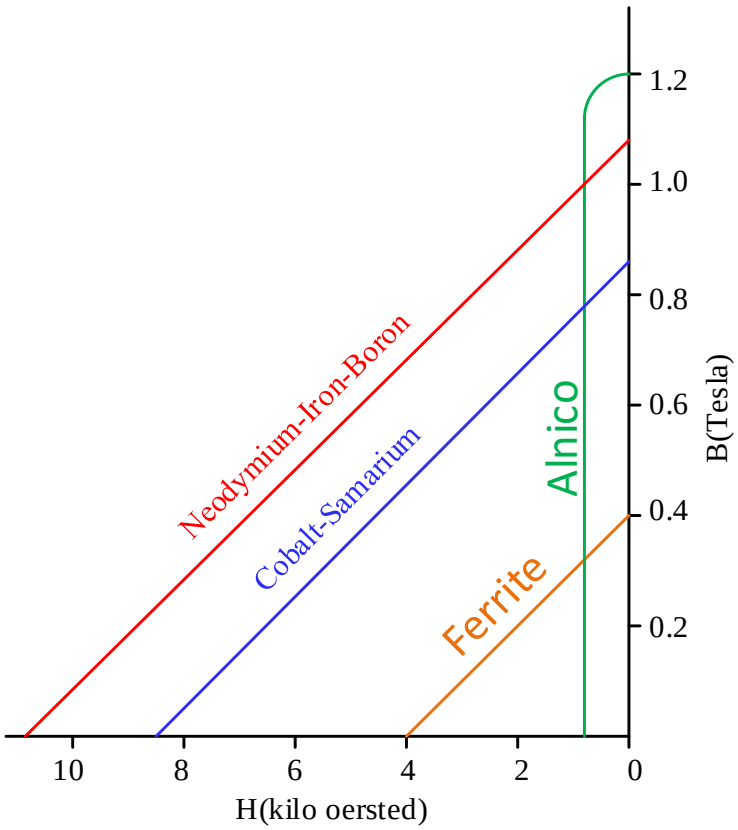

Fig. A1 BH curve of different magnetic material

APPENDIX – B

This appendix shows the three-phase IPMSM drive and five-phase IPMSM drive, utilized in the experimental tests.

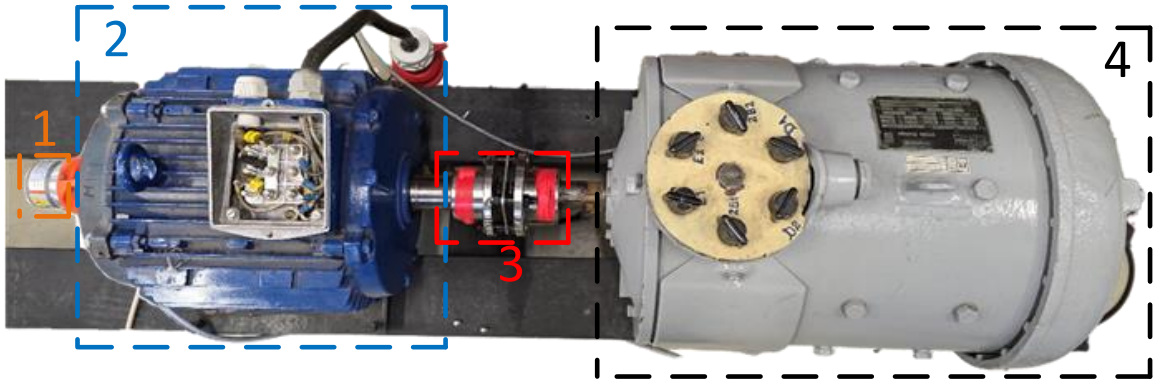

Fig. B1 Three-Phase drive set up

1. Encoder
2. Three-phase IPMSM
3. Mechanical coupling
4. DC machine

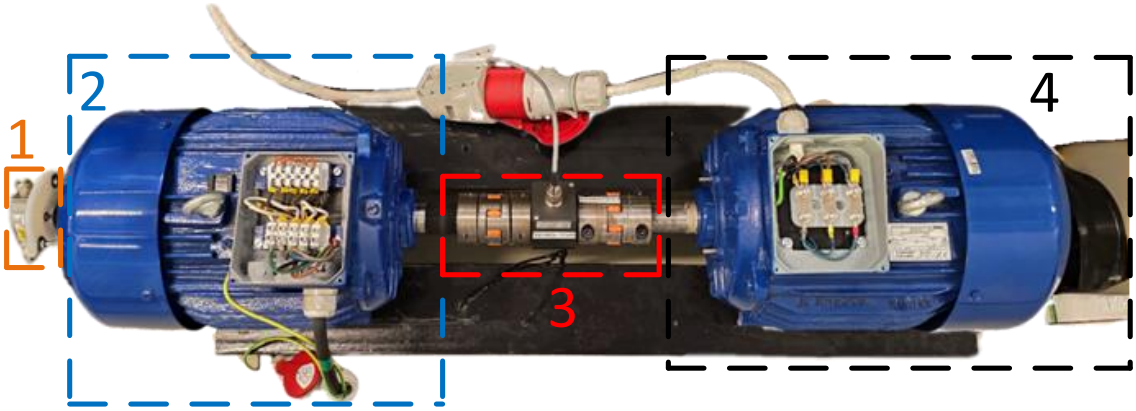

Fig. B2 Five-phase IPMSM drive set up

1. Encoder
2. Five-phase IPMSM
3. Torque meter and Mechanical coupling
4. Three-phase machine with active colling fan

Fig. B3 shows the rotor with permanent magnet inside and signal stator and rotor sheet. Neodymium Iron Boron (NdFeB) type of Permanent magnet was used to complete the constructure of rotor.

(a) (b)

Fig. B3 (a) Rotor structure of five-phase IPMSM (b) A single stator plate

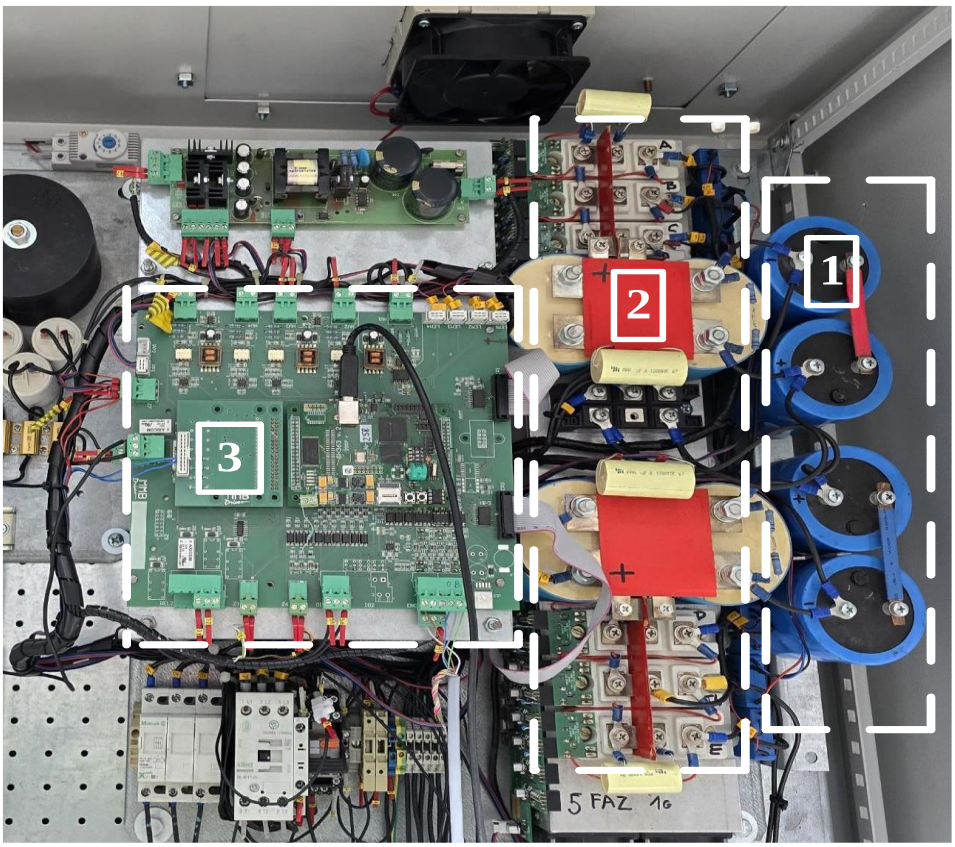

Fig. B4 Five-phase Inverter structure

1. DC link capacitor
2. Transistor array
3. Signal processing unit